

WAVE ENERGETICS OF THE ATMOSPHERE OF MARS

A Dissertation

by

JOSEPH MICHAEL BATTALIO

Submitted to the Office of Graduate and Professional Studies of
Texas A&M University
in partial fulfillment of the requirements for the degree of

DOCTOR OF PHILOSOPHY

Chair of Committee,	Istvan Szunyogh
Co-Chair of Committee,	Mark Lemmon
Committee Members,	Craig Epifanio
	Kim-Vy Tran
Head of Department,	Ping Yang

May 2017

Major Subject: Atmospheric Sciences

Copyright 2017 Joseph Michael Battalio

ABSTRACT

A comprehensive assessment of the energetics of transient waves is presented for the atmosphere of Mars using the Mars Analysis Correction Data Assimilation (MACDA) dataset (v1.0) and the eddy kinetic energy equation. Each hemisphere is divided into four representative periods covering the summer and winter solstices, a late fall period, and an early spring period for each of the three Mars years available. Northern hemisphere fall and spring eddy energetics is similar with some inter-annual and inter-seasonal variability, but winter eddy kinetic energy and its transport are strongly reduced in intensity as a result of the winter solstitial pause in wave activity. Barotropic energy conversion acts as a sink of eddy kinetic energy throughout each year with little reduction in amplitude during the solstitial pause. Baroclinic energy conversion acts as a source in fall and spring but disappears during the winter period as a result of the stabilized vertical temperature profile around winter solstice. Traveling waves are typically triggered by geopotential flux convergence. Individual waves decay through a combination of barotropic conversion of the kinetic energy from the waves to the mean flow, geopotential flux divergence, and dissipation. The southern hemisphere energetics is similar to the northern hemisphere in timing, but wave energetics is much weaker as a result of the high and zonally asymmetric topography. The effect of dust on baroclinic instability is examined by comparing a year with a global-scale dust storm (GDS) to two years without a GDS. In the GDS year, waves develop a mixed baroclinic/barotropic growth phase before decaying barotropically. Though the total amount of eddy kinetic energy generated by baroclinic energy conversion is lower during the GDS year, the maximum eddy intensity is not diminished. Instead, the number of intense eddies is reduced by about 50%.

DEDICATION

To Becca, for equal measures of snark and love.

And to DB and Joe, without your absolute generosity I would not be the person I am today.

And to Bobby, for making me laugh.

ACKNOWLEDGMENTS

I thank Dr. Istvan Szunyogh for the guidance, knowledge, and advice that has contributed in large part to my limited success so far and Dr. Mark Lemmon for the opportunity to operate a car on another planet. I must thank my peers and fellow group members that helped me survive the last five years, including and especially Emily Mason and Dr. Michael Herrera.

Finally, given the state of political discourse at the time of publication of this work, I want to also explicitly thank the citizenry of the United States of America for (most of the time) welcoming, encouraging, and embracing basic scientific research and those who pursue it. It is with your support and trust that the whole of science has advanced so far, so quickly in the last 241 years. We must remember that for our country to continue to prosper, everyone – every single person in our great nation – must have access to knowledge, accept expertise, and be willing to fund scientific inquiry at the highest possible levels, regardless of the political expediency or outcome. Facts and scientific advances are not to be feared but put to good societal use, even if their benefits are not immediately obvious.

CONTRIBUTORS AND FUNDING SOURCES

Contributors

This work was supported by a dissertation committee consisting of Professors Istvan Szunyogh [co-advisor], Mark Lemmon [co-advisor], and Craig Epifanio of the Department of Atmospheric Sciences and Professor Kim-Vy Tran of the Department of Astronomy and Physics.

All other work conducted for the dissertation was completed by the student independently.

Funding Sources

Graduate study was supported by fellowships and scholarships from Texas A&M University and by the Mars Science Laboratory Program through Malin Space Science Systems contract 11-0156 to M.T.L.

TABLE OF CONTENTS

	Page
ABSTRACT	ii
DEDICATION	iii
ACKNOWLEDGMENTS	iv
CONTRIBUTORS AND FUNDING SOURCES	v
TABLE OF CONTENTS	vi
LIST OF FIGURES	viii
1. INTRODUCTION	1
1.1 Mars Background	1
1.2 Waves on Mars	2
1.3 Local Energetics	7
1.4 Solstitial Pause	10
2. METHODS	14
2.1 MACDA Dataset	14
2.1.1 Dust Storms	15
2.1.2 Average Flow Properties	17
2.2 Eddy Kinetic Energy	22
2.2.1 Quasi-Geostrophic Omega	24
2.2.2 Divergence and Geopotential Flux	26
3. NORTHERN HEMISPHERE WAVE ENERGETICS	28
3.1 Pre-Solstitial Pause and MY 25 Global-Scale Dust Storm	28
3.1.1 Pressure-Weighted Vertical Averages	28
3.1.2 Zonal and Meridional Averages	31
3.1.3 Contrasting Prototypical Waves in Clear and Dust Storm Years	38
3.1.4 Intensities	42
3.2 Solstitial Pause and Post-Solstitial Pause	44
3.2.1 Pressure-Weighted Vertical Averages	44

3.2.2	Zonal and Meridional Averages	50
3.2.3	Solstitial Pause Waves	57
3.2.4	Post-Solstitial Pause Waves	60
3.2.5	Inter-Annual Variability	63
3.2.6	Spectral Analysis	65
4.	SOUTHERN HEMISPHERE WAVE ENERGETICS	69
4.1	Integrated EKE Terms	69
4.1.1	Pre-Winter Solstice	69
4.1.2	Solstices	71
4.1.3	Post-Winter Solstice	72
4.2	Zonal and Meridional Averages	73
4.2.1	EKE	73
4.2.2	BCEC	74
4.2.3	Heat Fluxes	75
4.2.4	BTEC	76
4.2.5	GFC	77
4.2.6	ETARANS	78
4.3	Seasonal Variability	79
4.3.1	A Pre-Solstitial Pause Wave	79
4.3.2	A Post-Solstitial Pause Wave	81
4.3.3	A Solstitial Pause Wave	83
4.4	Inter-Annual Variability	84
4.5	Spectral Analysis	85
4.5.1	Pre-Solstitial Pause	85
4.5.2	Solstitial Pause	86
4.5.3	Post-Solstitial Pause	86
4.5.4	Intensities	87
5.	DISCUSSION AND CONCLUSIONS	88
5.1	Discussion	88
5.1.1	Northern Hemisphere Energetics	88
5.1.2	Southern Hemisphere Energetics	92
5.1.3	Anomalous Behavior in the Pause Period	95
5.1.4	Problems with MACDA (v1.0)	96
5.1.5	Possible Causes of Solstitial Pause	98
5.2	Conclusions	100
	REFERENCES	102
	APPENDIX A. FIGURES	113

LIST OF FIGURES

FIGURE	Page
A.1 The Martian topography. [Credit: Mars Orbiter Laser Altimeter (MOLA) Science Team, Mars Global Surveyor, NASA.]	114
A.2 Column optical depth in the visible wavelength range for $L_s = 175^\circ - 255^\circ$ for MY 24 (top), MY 25 (middle), and MY 26 (bottom) from the MACDA dataset. Hatching indicates times of areocentric longitude greater than one degree, when TES retrievals were unavailable, and the analyses are based on a freely running model unconstrained by observations.	115
A.3 The zonal mean temperature field for $L_s = 200^\circ$ (top row) and $L_s = 230^\circ$ (second row), and the mean zonal wind field for $L_s = 200^\circ$ (third row) and $L_s = 230^\circ$ (bottom row) for MY 24 (left), MY 25 (middle), and MY 26 (right).	116
A.4 Time-mean, zonal-mean temperature for the southern hemisphere (left) and northern hemisphere (right) for each of the pre-pause, pause, and post-pause periods. Contours are time-mean and zonal-means of the zonal wind with negative values dashed. Terrain is grayed.	117
A.5 Surface temperature with 5-sol, 30-sol, and 40-sol running means for the period $L_s = 200^\circ - 230^\circ$ for 52.5° N, 175° E in MY 26.	118
A.6 Hovmöller diagram for the eddy component of the meridional wind field at 300 Pa for $L_s = 200^\circ - 230^\circ$ in the $57.5^\circ - 82.5^\circ$ N latitude band. Shown are MY 24 (left), MY 25 (middle), and MY 26 (right). Lines A and B refer to the location of storms discussed in sections 3.1.3.1 and 3.1.3.2. Hatching indicates times of areocentric longitude greater than one degree, when TES retrievals were unavailable, and the analyses are based on a freely running model unconstrained by observations.	119
A.7 As in Fig. A.6 but for $L_s = 255^\circ - 285^\circ$ and at 75 Pa. Lines C – F refer to the location of storms discussed in Section 3.2.3.	120
A.8 As in Fig. A.6 but for $L_s = 330^\circ - 360^\circ$. Lines G and H refer to the location of storms discussed in Section 3.2.4.	121

A.9	Correlation of the two forms of quasi-geostrophic ω and kinematic ω to the Kavulich et al. (2013) GFDL simulation ω between 28° and 80° N for all pressure levels.	122
A.10	The time-mean vertical velocities for $L_s = 200^\circ - 230^\circ$ for the 100-Pa (top) and 400-Pa (bottom) pressure level for MY 24 (left), MY 25 (middle), and MY 26 (right). Contours are surface elevation in 1000 m increments. Values below the mean geoid are dashed, with the mean geoid bolded.	123
A.11	Geopotential flux convergence, $-\overline{\nabla_3 \cdot \mathbf{v}'_3 \phi'}$, at 100 Pa for MY 24 (top), MY 25 (middle), and MY 26 (bottom) for the time-mean $L_s = 200^\circ - 230^\circ$. The geopotential flux convergence is calculated in the advective form (left) and in the flux form (right). Contours are surface elevation in 2500 m increments.	124
A.12	Pressure-weighted vertical averages of the time mean of the terms of the eddy kinetic energy equation for $L_s = 200^\circ - 230^\circ$ for MY 24 (left column), MY 25 (center column), and MY 26 (right column). Shown are the eddy kinetic energy (top), baroclinic energy conversion (second row), geopotential flux convergence (third row), the eddy kinetic energy advection (fourth row), the barotropic energy conversion (fifth row), and the residue (bottom). Contours are surface elevation in 1000 m increments. Values below the mean geoid are dashed, with the mean geoid bolded. . .	125
A.13	Vertical cross sections of the time-mean ($L_s = 200^\circ - 230^\circ$) of the zonal mean (left column) and meridional mean (right column) of baroclinic energy conversion, $-\omega' \alpha'$ and the eddy kinetic energy (J/kg) contoured. The meridional mean is computed for the $57.5^\circ - 82.5^\circ$ N latitude band. Results are shown for MY 24 (top), MY 25 (middle), and MY 26 (bottom).	126
A.14	As in Fig. A.13 but for geopotential flux convergence, $-\overline{\nabla_3 \cdot \mathbf{v}'_3 \phi'}$. Contours show the standard deviation of the geopotential height (gpm).	127
A.15	As in Fig. A.13 but for the zonal mean of the vertical heat flux, $-\overline{T' \omega'}$, (left column) and meridional heat flux, $\overline{T' v'}$, (right column). Contours show temporal mean of vertical motion (10^{-4} Pa/s) (left) and temporal mean of temperature field (K) (right).	128
A.16	As in Fig. A.13 but for the Eady index. Results are shown for MY 24 (top), the difference between MY 25 and MY 24 (middle), and the difference between MY 25 and MY 24 (bottom).	129

A.17 Brunt-Väisälä frequency vertical profile (top), vertical wind shear (middle), and potential temperature gradient (bottom) for the time-mean $L_s = 200^\circ - 230^\circ$ of the $57.5^\circ - 82.5^\circ$ N latitude band.	130
A.18 As in Fig. A.13 but for barotropic energy conversion, $-\mathbf{v}' \cdot (\mathbf{v}'_3 \cdot \nabla_3) \mathbf{v}_m - \mathbf{v}' \cdot \overline{(\mathbf{v}'_3 \cdot \nabla_3) \mathbf{v}'}$. Contours show zonal average zonal wind (m/s) (left) and meridional average zonal wind (m/s) (right).	131
A.19 As in Fig. A.13 but for EKE advection, $-\nabla \cdot \mathbf{v} K_e$. Contours show average total EKE advection, $-\nabla \cdot \mathbf{v} K_e - \nabla_3 \cdot \mathbf{v}'_3 \phi'$ (mJ/kg/s).	132
A.20 Time series of vertical, pressure-weighted averages of eddy kinetic energy (left), with topography contoured as in Fig. A.12, geopotential flux convergence (middle), with baroclinic energy conversion contoured at 0.007 J/kg/s increments and negative values dashed, and eddy kinetic energy advection (right), with barotropic energy conversion contoured at 0.007 J/kg/s increments and negative values dashed for a 4-sol period traveling wave in MY 24 beginning at $L_s = 206.6^\circ$ and continuing at 0.5-sol steps until $L_s = 209.1^\circ$	133
A.21 Time series of the meridional average of eddy kinetic energy (left), with barotropic energy conversion contoured in 0.007 J/kg/s increments and negative values dashed and geopotential flux convergence (right), with baroclinic energy conversion contoured in 0.007 J/kg/s increments and negative values dashed in the $57.5^\circ - 82.5^\circ$ N latitude band for the wave in Fig. A.20.	134
A.22 As in Fig. A.20 but for a 4-sol period traveling wave in MY 25 beginning at $L_s = 201.1^\circ$ and continuing at 0.33-sol steps until $L_s = 202.7^\circ$	135
A.23 As in Fig. A.21 but for the wave in Fig. A.22.	136
A.24 Time series of the volume integrated EKE and EKE equation terms for the $22.5^\circ - 82.5^\circ$ N latitude band for MY 24 (blue), MY 25 (red), and MY 26 (green).	137
A.25 As in Fig. A.12 but for $L_s = 190^\circ - 220^\circ$. The ageostrophic geopotential flux and EKE advection vectors are shown on their respective panels.	138
A.26 As in Fig. A.25 but for $L_s = 255^\circ - 285^\circ$	139
A.27 As in Fig. A.25 but for $L_s = 330^\circ - 360^\circ$	140
A.28 As in Fig. A.25 but for $L_s = 90^\circ - 120^\circ$	141

A.29 Baroclinic energy conversion during three fall (pre: $L_s = 190^\circ - L_s = 220^\circ$), three winter (pause: $L_s = 255^\circ - L_s = 285^\circ$), and three spring (post: $L_s = 330^\circ - L_s = 360^\circ$) periods in the northern hemisphere in the zonal (left column), and meridional (right column) average. Contours are average zonal EKE (J/kg). Terrain is grayed.	142
A.30 As in Fig. A.29 but for vertical heat flux. Contours are average vertical velocity (10^{-4} Pa/s).	143
A.31 As in Fig. A.29 but for meridional heat flux. Contours are average temperature (K) (left column) and average meridional wind (m/s).	144
A.32 As in Fig. A.29 but for geopotential flux convergence. Contours are average zonal EKE (J/kg). Right column shows the ageostrophic geopotential vectors, with the vertical direction scaled by 100.	145
A.33 As in Fig. A.29 but for EKE advection. Right column shows the EKE advection vectors, with the vertical direction scaled by 100.	146
A.34 As in Fig. A.29 but for barotropic energy conversion. Contours are average zonal wind (m/s).	147
A.35 Time series of vertical, pressure-weighted averages of eddy kinetic energy (left), with topography contoured as in Fig. A.12; geopotential flux convergence (middle), with baroclinic energy conversion contoured at 0.006 J/kg/s increments and negative values dashed; and eddy kinetic energy advection (right), with barotropic energy conversion contoured at 0.006 J/kg/s increments and negative values dashed for a 6-sol period traveling wave in MY 26 beginning at $L_s = 281.6^\circ$ and continuing at 0.5-sol steps until $L_s = 284.2^\circ$	148
A.36 As in Fig. A.35 but for a 8-sol period traveling wave in MY 24 beginning at $L_s = 273.3^\circ$ and continuing at 0.5-sol steps until $L_s = 275.8^\circ$	149
A.37 As in Fig. A.35 but for a 16-sol wave in MY 25 beginning at $L_s = 255.0^\circ$ and continuing at 2-sol steps until $L_s = 265.4^\circ$	150
A.38 As in Fig. A.35 but for a stationary wave in MY 24 beginning at $L_s = 276.1^\circ$ and continuing at 0.17-sol steps until $L_s = 277.0^\circ$	151

A.39	Time series of vertical, pressure-weighted averages of eddy kinetic energy (left), with topography contoured as in Fig. A.12; geopotential flux convergence (middle), with baroclinic energy conversion contoured at 0.007 J/kg/s increments and negative values dashed; and eddy kinetic energy transport (right), with barotropic energy conversion contoured at 0.007 J/kg/s increments and negative values dashed for a 5-sol period traveling wave in MY 24 beginning at $L_s = 350.7^\circ$ and continuing at 0.5 sol steps until $L_s = 352.8^\circ$	152
A.40	Time series of the meridional average of eddy kinetic energy (left), with barotropic energy conversion contoured in 0.007 J/kg/s increments and negative values dashed and geopotential flux convergence (right), with baroclinic energy conversion contoured in 0.007 J/kg/s increments and negative values dashed in the $57.5^\circ - 82.5^\circ$ N latitude band for the wave in Fig. A.39.	153
A.41	As in Fig. A.39 but for a 5-sol period traveling wave in MY 24 beginning at $L_s = 336.1^\circ$ and continuing at 0.583-sol steps until $L_s = 338.7^\circ$. . .	154
A.42	Time series of the volume integrated EKE and EKE equation terms for the $22.5^\circ - 82.5^\circ$ N latitude band for MY 24 (blue), MY 25 (red), and MY 26 (green) during the entirety of the northern hemisphere transient wave period ($L_s = 170^\circ - 390^\circ$). Times of areocentric longitude greater than one degree, when TES retrievals were unavailable, and the analyses are based on a freely running model unconstrained by observations are indicated in each plot by thin lines.	155
A.43	As in Fig. A.12 but averaged for MY 24, 25, and 26 during $L_s = 190^\circ - 220^\circ$ for wavenumbers 1, 2, 3, and 4.	156
A.44	As in Fig. A.43 but for $L_s = 255^\circ - 285^\circ$	157
A.45	As in Fig. A.43 but for $L_s = 330^\circ - 360^\circ$	158
A.46	As in Fig. A.42 but for wavenumber 1.	159
A.47	As in Fig. A.42 but for wavenumber 2.	160
A.48	As in Fig. A.42 but for wavenumber 3.	161
A.49	As in Fig. A.42 but for wavenumber 4.	162

A.50	Time-mean, pressure-weighted vertical averages of the terms in the eddy kinetic energy equation in the southern hemisphere for $L_s = 20^\circ - 50^\circ$ for MY 25 (left column), MY 26 (center column), and MY 27 (right column). Shown are the eddy kinetic energy (top), baroclinic energy conversion (second row), geopotential flux convergence (third row), the eddy kinetic energy advection (fourth row), the barotropic energy conversion (fifth row), and the residue (bottom). Contours are surface elevation in 1000 m increments, with dashed values below the mean geoid and the mean geoid in bold.	163
A.51	As in Fig. A.50 but for the winter pause period for MY 25 and MY 26 and the average summer period.	164
A.52	As in Fig. A.50 but for the post pause period ($L_s = 150^\circ - 180^\circ$) for MY 24 (left column), MY 25 (center column), and MY 26 (right column). . .	165
A.53	Baroclinic energy conversion during three fall (pre: $L_s = 20^\circ - L_s = 50^\circ$), two winter (pause: $L_s = 75^\circ - L_s = 105^\circ$), and two spring (post: $L_s = 150^\circ - L_s = 180^\circ$) periods in the zonal (left column), and meridional (right column) average. Contours are average zonal EKE (J/kg). Terrain is grayed.	166
A.54	The zonal average of the vertical (left) and meridional (right) heat fluxes during three fall (pre: $L_s = 20^\circ - L_s = 50^\circ$), two winter (pause: $L_s = 75^\circ - L_s = 105^\circ$), and two spring (post: $L_s = 150^\circ - L_s = 180^\circ$) periods. Contours are average zonal vertical motion (10^{-4} Pa/s) (left) and zonal average temperature (K) (right). Terrain is grayed. .	167
A.55	The meridional average of the vertical (left) and meridional (right) heat fluxes during the time periods in Fig. A.54. Contours are average vertical motion in 2×10^{-4} Pa/s increments, with negative values dashed (left) and average meridional wind in 4 m/s increments, with negative values dashed (right).	168
A.56	As in Fig. A.53 but for barotropic energy conversion in the zonal (left column) and meridional (right column) average. Contours are average zonal wind (m/s).	169
A.57	As in Fig. A.53 but for geopotential flux convergence in the zonal (left column), and meridional (right column) average. Vectors are ageostrophic geopotential flux with motions in the vertical direction multiplied by 10^4 . Contours are average zonal EKE (J/kg).	170

A.58 As in Fig. A.53 but for EKE advection in the zonal (left column), and meridional (right column) average. Vectors are EKE advection flux with motions in the vertical direction multiplied by 10^4 . Contours are average zonal wind (m/s).	171
A.59 Progression of an eddy during MY 27 $L_s = 47.90^\circ - 49.94^\circ$. Each row is 0.5 sol forward in time. Shown are eddy kinetic energy, with topography contoured at 1000 m increments and negative values dashed (left), geopotential flux convergence, with baroclinic energy conversion contoured in 0.00167 (J/kg/s) increments and negative values dashed (middle), and EKE advection, with barotropic energy conversion contoured in 0.00167 (J/kg/s) increments and negative values dashed (right).	172
A.60 Hovmöller diagram of the eddy meridional wind at 300 Pa for three periods in the MACDA dataset averaged between 57.5° S and 82.5° S. Lines I, J, and K refer to the location of storms discussed in Section 4.3.	173
A.61 Time series of the meridionally averaged EKE equation terms of the eddy depicted in Fig. A.59. Shown are eddy kinetic energy, with barotropic energy conversion contoured in 0.00167 (J/kg/s) increments and negative values dashed (left) and geopotential flux convergence, with baroclinic energy conversion contoured in 0.00167 (J/kg/s) increments and negative values dashed (right).	174
A.62 As in Fig. A.59 but for an eddy during MY 24 $L_s = 166.31^\circ - 168.82^\circ$. Baroclinic and barotropic energy conversion are contoured in 0.005 (J/kg/s) increments.	175
A.63 As in Fig. A.61 but for the eddy in Fig. A.62. Baroclinic and barotropic energy conversion are contoured in 0.005 (J/kg/s) increments.	176
A.64 As in Fig. A.62 but for an eddy between MY 25 $L_s = 96.83^\circ - 98.90^\circ$. Baroclinic and barotropic energy conversion are contoured in 0.00125 (J/kg/s) increments.	177
A.65 As in Fig. A.61 but for the eddy in Fig. A.64. Baroclinic and barotropic energy conversion are contoured in 0.00125 (J/kg/s) increments.	178
A.66 Summed, pressure-weighted EKE equation terms in the $57.5^\circ - 82.5^\circ$ S latitude band for MY27 ($L_s = 20^\circ - 60^\circ$) and MY 24 ($L_s = 153.7^\circ - 180^\circ$) in blue, MY 25 in red, and MY 26 in green. Times longer in duration than $L_s = 1^\circ$ when TES retrievals were unavailable and the MACDA GCM ran freely are indicated by thin lines.	179

A.67 As in Fig. A.50 but averaged for MY 25, 26, and 27 during $L_s = 20^\circ - 50^\circ$ for wavenumbers 1, 2, 3, and 4.	180
A.68 As in Fig. A.50 but averaged for MY 25 and 26 during $L_s = 75^\circ - 105^\circ$	181
A.69 As in Fig. A.50 but averaged for MY 24, 25, and 26 during $L_s = 150^\circ - 180^\circ$	182
A.70 As in Fig. A.66 but for wavenumber 1.	183
A.71 As in Fig. A.66 but for wavenumber 2.	184
A.72 As in Fig. A.66 but for wavenumber 3.	185
A.73 As in Fig. A.66 but for wavenumber 4.	186
A.74 Hovmöller diagram of EKE at 10 Pa for $L_s = 180^\circ - 210^\circ$ in the $57.5^\circ - 82.5^\circ$ S latitude band. Shown are MY 24 (left), MY 25 (middle), and MY 26 (right). Hatching indicates times of areocentric longitude greater than one degree, when TES retrievals were unavailable, and the analyses are based on a freely running model unconstrained by observations.	187
A.75 The meridional wind, vertical wind, and temperature signal with the associated heat fluxes for the stationary wave in the northern hemisphere at 300 Pa for $L_s = 190^\circ - 220^\circ$. The bottom panel is the meridionally averaged meridional wind in the $57.5^\circ - 82.5^\circ$ N latitude band.	188
A.76 As in Fig. A.75 but for $L_s = 255^\circ - 285^\circ$	189
A.77 As in Fig. A.75 but for $L_s = 330^\circ - 360^\circ$	190

1. INTRODUCTION*

Traveling waves on Mars are present in both the northern and southern hemispheres, with the maximum amplitude occurring on either side of the winter solstice. These waves evolve in both time and space, indicating that the processes behind their creation also depend on space and time. While facets of these waves have been described by multiple papers, no comprehensive study of the energetics of these waves has been completed. It is the goal of the present work to provide a description of the low-level traveling waves of Mars.

Interest in traveling waves on Mars stems from a desire to test terrestrial theories on a differing flow regime. More saliently, the ability to forecast weather on Mars grows in importance as further robotic missions are launched to explore the surface, and a reliable forecast must be in place to ensure the safety of any future manned missions. Finally, while it will be shown that global-scale dust storms (GDS) drastically affect baroclinic waves, baroclinic waves themselves can initiate regional dust storms. Thus, the ability to predict and understand these features is of great importance to future missions.

1.1 Mars Background

In some ways, Mars is remarkably similar to Earth. Both planets share many of the same defining characteristics. The rotation period of Mars is only 39 minutes longer than Earth, and the axis of rotation of Mars is similar to Earth. The scale height and Rossby radius of deformation are roughly the same compared to Earth, so the planets share many of the same synoptic-scale features. However, Mars is approximately half the size, with a

*Parts of Section 1 are reprinted with permission from "Energetics of the martian atmosphere using the Mars Analysis Correction Data Assimilation (MACDA) " by M. Battalio, I. Szunyogh, and M. Lemmon, 2016. *Icarus*, 276, 1-20, Copyright 2016 by the American Astronomical Society Division of Planetary Science.

third of the surface gravity of Earth. The surface pressure on Mars is just under 1% that of the Earth, and its main constituent is carbon dioxide ($\sim 95\%$). Mars receives half the solar radiation and has a much faster radiative timescale compared to Earth (Read and Lewis, 2004; Read et al., 2015).

For reference, Fig. A.1 shows the topography of the surface of Mars. The southern hemisphere has much higher topography than the northern and is very zonally asymmetric, with strong wave number 1 and 2 components to the topography. The northern hemisphere is dominated by wave number 2 features. Generally, topography increases in height from the north to the south pole. In the southern hemisphere, three features will be referenced repeatedly in the proposal: the Hellas impact basin, centered at 40° S, 70° E; the smaller Argyre Planitia at 50° S, 330° E; the Tharsis Plateau that extends 40° N – 40° S and 220° – 300° E. Besides Tharsis, the main high altitude feature in the northern hemisphere is Arabia Terra, which is an extension of the southern hemisphere highlands into the northern hemisphere around 50° N, 330° E. Several low-lying, northern hemisphere planitias will be referenced: Utopia Planitia to the northwest of Arabia Terra at 60° N, 120° E, Amazonis Planitia 40° N, 190° E, and Acidalia Planitia 70° N, 330° E.

1.2 Waves on Mars

Baroclinic disturbances on Mars have been a subject of intense study in the last few decades. Leovy (1969) first asserted zonal wave number 2–4 to be the most unstable baroclinic modes, and Blumsack and Gierasch (1972) found that topography would reduce the growth rates of the most unstable baroclinic modes. The early observational studies, which began with the analysis of observations from the Viking landers (Barnes, 1980, 1981), found that baroclinic instability played a key role in the development of waves in the northern hemisphere. The results confirmed wave number 2–4 as prevalent with phase speeds of $10\text{--}15\text{ m s}^{-1}$. Dust was found to dramatically alter the characteristics of traveling

waves, warming the mid-levels and cooling the surface (Conrath, 1975). Dust was found to reduce the amplitude of waves at low wave number (1–2) and increase it at higher wave number (3–4) by weakening static stability (Barnes, 1981).

Further insight was gained with the first global climate models (e.g. Pollack et al., 1981; Barnes, 1984), which corroborated the flow favoring wave number 2–4. Continued refinement of the models allowed for the exploration of the vertical structure of baroclinic waves (Barnes et al., 1993). The flow at high altitudes was dominated by waves of wave number 1–2, with waves of wave number 1–4 at the surface. The wave number of the dominant waves also increased with optical thickness. Southern hemisphere waves were present at reduced amplitudes but slightly higher wave numbers (>3) compared to the NH, and topography seemed to play a role in suppressing eddy activity. Collins et al. (1996) demonstrated that the atmospheric flow flipped between two wave number regimes due to diurnal forcing. Hollingsworth and Barnes (1996) anticipated the existence of storm tracks in the northern hemisphere due to the strong zonal inhomogeneity of the surface topography. Using the NASA Ames Mars Global Circulation Model (MGCM) simulation, Hollingsworth et al. (1996) determined that storms would be preferred in the lowland planitias and would be guided by a topographically forced, wave number 2 stationary wave.

Traveling waves have been identified using observations from Mars Global Surveyor. Hinson and Wilson (2002) focused on the southern hemisphere and found such waves at wave number 3 in limb retrievals from from the Thermal Emission Spectrometer (TES). A 2-sol period, wave number 3 wave was found to dominate the signal after winter solstice ($L_s = 134^\circ - 148^\circ$). Additionally, a global circulation simulation corroborated this finding, with the wave amplitude zonally modulated so the waves had the most energy between 180° and 330° E and suggested that the waves were baroclinically forced. Wilson et al. (2002) identified wave number 1 traveling waves in the northern hemisphere during

winter in both TES observations and Geophysical Fluid Dynamics Laboratory (GFDL) MGCM simulations. Banfield et al. (2003, 2004) analyzed forced and traveling waves in TES data, concluding that wave number 1 wave had the highest amplitude. Wave number 2 and 3 waves prevailed during fall and spring, with a lull around the winter solstice. Wave number 1 – 3 eddies were present both before and after the winter solstice. Wave number 1 waves in the southern hemisphere were found to be weaker than the northern hemisphere in general but had indications of a relatively strong wave number 1 eddy during the initiation of the Mars year (MY) 25 global-scale dust storm. Wave number 3 eddies were somewhat weaker and confined to the lowest scale height. Eddies were limited to the storm tracks between 190° and 320° E, just to the south of the Tharsis Plateau and near Argyre Planitia and near 60° E, due south of Hellas Planitia. Unlike the northern hemisphere where areas of maximum eddy amplitude were collocated with the lowland planitias (Hollingsworth and Barnes, 1996), the origin of the southern hemisphere tracks was unclear (Banfield et al., 2004). Both the northern and southern hemisphere waves were found to extract energy from the jet above 2 scale heights (the low limit of TES nadir observations).

During the spring period, the strongest transient wave from TES observations of the southern hemisphere was found to be wave number 1, with an intensification of wave number 1 during global dust events (Imamura and Kobayashi, 2009). These transient waves were still weaker than their northern hemisphere counterparts and weaker still than the southern hemisphere wave number 1 stationary wave. Imamura and Kobayashi (2009) hypothesized that wave number 1 was the strongest due to an energy cascade from higher wave numbers, specifically 2 and 3.

There were strong indications that the instabilities that feed the southern hemisphere waves were similar to those of the northern hemisphere waves. Greybush et al. (2013) identified a region of strong baroclinic energy conversion poleward of the southern hemisphere polar vortex that extended to the surface at 60° S and a negative region of barotropic

energy conversion poleward of the westerly jet using the GFDL MGCM around southern spring equinox. Eddies also were preferred downstream of elevated terrain due to lee cyclongensis, specifically around 30°, 180°, and 270° E. Wave numbers 3 and 4 seemed to be the more prevalent in the southern hemisphere with the GFDL MGCM (Greybush et al., 2012, 2013).

Subsequent work described the relationship between GDS's and traveling waves. Basu et al. (2006) defined two categories of GDS: storms that began in Hellas Planitia and northern hemisphere storms initiated by traveling waves. The superposition of waves provided a sufficiently large surface wind stress to trigger dust lifting. "Flushing" dust storms that transported dust from the polar ice cap to the lower latitudes were primarily baroclinic fronts associated with waves of period 2-3 sol and wave number 3 (Wang et al., 2005). Hinson and Wang (2010) defined three key factors that influenced the flushing storms: baroclinic mode transitions, storm zones that strongly modified the zonal amplitude of baroclinic eddies, and stationary waves.

Evidence of stationary waves has been found in both hemispheres. Early modeling studies found the wave number 1 mode to be the strongest, with strong indications of a sizable, barotropic wave number 2 component (Barnes et al., 1996). Interestingly, even though there is a strong wave number 3 component to the southern hemisphere topography, the stationary wave number 3 component in the southern hemisphere is no stronger than the northern hemisphere (Hollingsworth and Barnes, 1996). Observations have since verified these predictions (Hinson et al., 2003).

Work has been done on the variation of baroclinic waves induced by the seasonal variation of dust opacity (Kuroda et al., 2007). In northern hemisphere autumn, waves weakened as solstice approached due to the tilt of the polar front becoming poleward with height from equatorward with height. Increased dust loading was found to modify baroclinic activity by intensifying the westerly jet due to strengthening of the meridional

temperature gradient in the mid-levels. This stabilized the jet stream to low wave number disturbances. Lewis et al. (2016) further elucidated the solstitial pause in baroclinic wave activity, which occurs within $L_s = 240^\circ - 300^\circ$ period in the northern hemisphere, using the Mars Analysis Correction Data Assimilation (MACDA) reanalysis. Energy conversion was explored by Greybush et al. (2013) that found that baroclinic energy conversion took place near the surface, and baroclinic and barotropic conversions were important in the westerly jets aloft. Additionally, topography played a key role in the development of storm tracks due to lee cyclogenesis.

With the development of reanalysis datasets, a more detailed survey of transient eddies in both the northern and southern hemispheres of Mars was completed by Mooring and Wilson (2015) using the MACDA dataset. After segmenting the dataset into four periods, the northern hemisphere waves were found to have a zonal wave number spectra based on the eddy temperature field that peaked at wave numbers 2 and 3, but the northern hemisphere waves never had an average wave number above 2.75. A tendency for stronger eddy activity in low lying areas was noted with peaks in the eddy fields around 90° , 180° , and 330° E. For the eddy kinetic energy, if years that were affected by dust storms were removed, the pre-pause period had stronger eddy kinetic energy than the post-pause period.

The southern hemisphere waves in MACDA were found to have a zonal wave number spectra that peaked at wave number 3 for most of the periods in each Mars year with an average zonal wave number that never dropped below 3, which was much higher than the northern hemisphere. Pre-winter solstice southern hemisphere waves exhibited great inter-annual variability in the MACDA dataset and had a strong wave number 4 component. Post-winter solstice activity appeared in similar areas as the pre-winter solstice, but the post-solstice eddy activity was stronger than before the solstice in both eddy kinetic energy and poleward heat fluxes. The spatial organization of the eddies echoed that found in previous studies, with two areas of strong eddy kinetic energy near Hellas Planitia and

south of the Tharsis Plateau. The Hellas Planitia maximum in eddy activity also showed a tendency for eddies to propagate cyclonically at the surface around the crater rim.

1.3 Local Energetics

The nature of baroclinic instability and its role in the development of synoptic-scale waves have been well understood in the terrestrial atmosphere for several decades. The models of Charney (1947) and Eady (1949) established baroclinic instability as the prime driver of midlatitude, synoptic-scale atmospheric dynamics. Since the first formulation of the theory of baroclinic instability, much effort has been expended in investigating the initiation and development of waves caused by baroclinic energy conversion. Traveling waves in the midlatitudes have been found to grow baroclinically and decay barotropically (Simmons and Hoskins, 1978, 1979, 1980). The leading edge of an initially localized disturbance propagated as a packet of traveling waves at the associated group velocity, while the trailing end stabilized with no further upstream motion (Swanson and Pierrehumbert, 1994).

The establishment of the local energetics method began with the work of Orlanski and Katzfey (1991) that studied the evolution of cyclones in terms of a local kinetic energy budget. In particular, a common form of cyclogenesis was examined in which storms were triggered by upper tropospheric wave packets through the convergence of geopotential height fluxes, grew by baroclinic conversion of potential energy to eddy kinetic energy (EKE), transported kinetic energy downstream via the background flow and via geopotential flux divergence, and lost kinetic energy to the background flow through barotropic energy conversion. In principle, baroclinic energy conversion can occur spontaneously, but in practice, it is usually triggered by upper-tropospheric traveling waves. A follow-up study (Orlanski and Sheldon, 1993) defined the process as downstream baroclinic development, as the convergence of geopotential fluxes was immediately followed by baroclinic energy

conversion. Downstream baroclinic development was explored in an idealized situation by Chang and Orlanski (1993). Baroclinic energy conversion was found to be correlated with maximum baroclinicity, but geopotential flux convergence acted to maintain eddies downstream of the unstable baroclinic regions, extending the storm tracks downstream into weakly unstable areas. Chang (1993) provided observational evidence of the role of geopotential fluxes in the Pacific storm track.

Orlanski and Sheldon (1995) applied local energetics to cyclone development to create a model of downstream baroclinic evolution. In this conceptual model, an EKE center dispersed energy downstream through geopotential flux divergence, generating a new EKE center. Next, the second EKE center grew baroclinically as geopotential fluxes began to diverge. Lastly, the second EKE center decayed via geopotential fluxes and barotropic conversion. The group velocity of the resulting packets of traveling waves was greater than the phase speed of the individual troughs and ridges, so troughs grew on the downstream side of the wave packet and decayed on the upstream side. Downstream development was found to often lead to development at the surface (Chang, 2000). Decker and Martin (2005) showed that the location of the development within the downstream expanding packet can determine the lifetime of the cyclone. The further downstream within a wave packet that an EKE center develops, the longer the lifetime of a cyclone.

Energetics analyses of this type have been applied to the Pacific storm track (Hakim, 2003; Danielson et al., 2004, 2006), the North Atlantic storm track (Ahmadi-Givi et al., 2014; Rivière et al., 2015), and across the continental United States (Decker and Martin, 2005). In each instance, baroclinic eddies followed the same downstream development, baroclinic growth, and barotropic decay, modulated by the individual circumstances of their particular storm track such as topography and the strength of temperature gradients.

Much of the recent work on transient eddies in the atmosphere of Mars has been to investigate the structure of their energy transport and conversion. Kavulich et al. (2013)

first used the EKE diagnostics of Orlanski and Katzfey (1991) to investigate the energetics of northern hemisphere waves before the winter solstice using the GFDL MGCM. These eddies behaved in a similar way to those on Earth in that they were initiated via geopotential flux convergence, grew through baroclinic energy conversion, and decayed through barotropic energy conversion and dissipation. The main role of baroclinic energy conversion was to maintain already existing downstream propagating packets of waves rather than starting a new chain of baroclinic developments. The role of barotropic energy conversion in the downstream propagating packet depended on the local topography: it was a sink of EKE on the leeward side of topographic features, but in a channel north of the Tharsis Plateau, it enhanced the kinetic energy of the wave packet and extended the region where eddies can exist south. Barotropic energy conversion served as a sink of kinetic energy elsewhere. However, the GFDL simulation was found to have weaker waves above wave number 2 than MACDA.

The Lorenz energy cycle for transient waves was computed by Tabataba-vakili et al. (2015) using MACDA in both the global and temporal means. Contrary to findings of Kavulich et al. (2013) and Wang and Toigo (2016) and to the nature of terrestrial waves, the barotropic conversion of energy from the zonal wind to the eddies was found to be positive so that the only sink of EKE was friction. Also, Tabataba-vakili et al. (2015) found that the diurnal contribution to the EKE exceeded the contribution from longer timescales like those of transient, baroclinic eddies.

Battalio et al. (2016) studied the energetics of transient waves in the northern hemisphere just before the winter solstice ($L_s = 200^\circ - 230^\circ$) during the GDS of MY 25 and during two non-GDS years from the MACDA dataset. The energetics of the transient waves during the low opacity years of MY 24 and 26 were very similar to those reported by Kavulich et al. (2013). However, during the MY 25 GDS, the number of transient eddies was substantially reduced to roughly half the number of those in MY 24 or 26. The

reduction in the number of waves was caused by the altered mean state of the atmosphere due to increased dust that warmed the mid-levels and cooled the surface, stabilizing the atmosphere to baroclinic instability. The increased opacity also decreased the vertical wind shear in the lowest levels (between 500 and 800 Pa), further stabilizing the atmosphere against near-surface baroclinic energy conversion. The intensity of individual waves during the dusty period did not decrease, as the loss of baroclinic energy conversion was offset by barotropic energy conversion from the time-mean flow to the waves.

Higher in the Martian atmosphere, Wang and Toigo (2016) found the energetics of waves to be different than the energetics of waves found by Battalio et al. (2016). At altitudes higher than 20 km, there were two main regimes (Wang and Toigo, 2016): near the poles at high altitudes, waves acted as they did near the surface, generating energy baroclinically and losing it barotropically, but near the equator, the opposite situation held – waves lost energy baroclinically but gained energy barotropically. This could possibly explain how transient eddies crossed the equator from the north to south hemispheres where baroclinic instability is negligible. Furthermore, wave number 3 was found to have the strongest temperature signal and energy conversions below 20 km, and wave number 1 had the strongest energy conversions above 20 km. Using the MarsWRF MGCM, Wang and Toigo (2016) also found times where wave-wave interactions contributed to the EKE budget at high altitudes. EKE transfer between waves occurred when the dominant wave mode transitions from one wave number to another and was negligible when the dominant wave mode was stable.

1.4 Solstitial Pause

The solstitial pause of transient waves in the atmosphere of Mars is a regular phenomenon that occurs in both hemispheres around the winter solstice and was first identified in the modeling study of Barnes et al. (1993). Further modeling work has sought to refine

and match observations using specified dust distributions (Hourdin et al., 1995). Observationally, Banfield et al. (2004) noted the decrease in activity in the northern hemisphere in wave numbers 2 and greater around the winter solstice. In a recent study, Guzewich et al. (2015) identified minima in both the summer and winter solstices of dust lifting activity. The reduction in the intensity of waves was more pronounced in the southern than the northern hemisphere, but the northern hemisphere reduction were more easily observable as the northern hemisphere transient waves are stronger outside of the pause period (Mulholland et al., 2016). The northern hemisphere pause began around $L_s = 240^\circ$ and continued to $L_s = 300^\circ$. The southern hemisphere pause started approximately at $L_s = 60^\circ$ and ended around $L_s = 120^\circ$. The reduction of transient wave activity occurred regardless of the presence of large regional dust storms or a GDS, though there was inter-annual variability in the timing, duration, and intensity of the solstitial pause, especially in the northern hemisphere of Mars.

The behavior of waves in the MACDA dataset during and around the solstitial pause was thoroughly investigated by Lewis et al. (2016). Their results showed that transient waves generally form along the strong thermal boundary at the edge of the polar ice cap that migrates between 40° and 90° N. That is, the region where eddies formed was nearest the pole just after summer solstice, moved southward and slowly disappeared by the winter solstice pause. After the pause, eddies resumed, and the area of development migrated back toward the pole. For most years in the northern hemisphere, the period on either side of the pause was mostly symmetric, but in the southern hemisphere, waves in the early spring were stronger than in the late autumn. In the vertical, the solstitial pause mostly altered the behavior of waves near the surface. Waves aloft were not affected by the pause. The root-mean-square of the temperature was reduced during the pause below 300 Pa, but above 100 Pa, there were still multiple maxima in the root-mean-square temperature. Kuroda et al. (2007) suggested that the upper-level maxima were due to

the middle atmosphere polar warming. The background flow also changed during the solstitial pause period: zonally averaged temperature increased above 10 Pa and north of 60° N during the pause, and the zonal, westerly jet tilted upward toward the pole during the pause, in addition to strengthening and migrating northward.

There are several possible causes of the Martian solstitial pause. Mulholland et al. (2016) investigated the causes in a modeling study using the UK version of the LMD/UK Mars Global Climate Model. Using a number of simulations under a MY 24 dust scenario, the effect of dust opacity and water ice clouds was found to be a prime reason for the initiation of the solstitial pause. Their results indicated that an increase in global dust loading as solstice approached and the presence of water ice clouds contributed to the generation of a pause in eddy activity. The water ice clouds affected transient waves by altering the baroclinicity in the low levels of the atmosphere. This result was corroborated by Guzewich et al. (2016).

In what follows, the EKE equation (Orlanski and Katzfey, 1991) is applied to three years of the MACDA global reanalyses, beginning with the $L_s = 200^\circ - 230^\circ$ period, which intersects the GDS of MY 25. The development and decay of baroclinic waves is compared to that observed in previous work, both on Mars and on Earth. In particular, the focus is on the impact of the MY 25 GDS on baroclinic activity compared to the varying dustiness of MY 24 and 26 and inter-annual variability of the flow. Then, the periods of interest are expanded to cover four times of activity: the pre-solstitial pause (pre-pause) $L_s = 190^\circ - 220^\circ$, the solstitial pause (pause) $L_s = 255^\circ - 285^\circ$, the post-solstitial pause (post-pause) period $L_s = 330^\circ - 360^\circ$, and the summer solstice $L_s = 90^\circ - 120^\circ$ of the northern hemisphere to compare how eddies change seasonally and annually. Finally, attention is directed towards the equivalent periods in the southern hemisphere: the pre-solstitial pause (pre-pause) $L_s = 20^\circ - 50^\circ$, the solstitial pause (pause) $L_s = 75^\circ - 105^\circ$, the post-solstitial pause (post-pause) period $L_s = 150^\circ - 180^\circ$, and the summer solstice

$L_s = 255^\circ - 285^\circ$. Focus is placed on comparing northern and southern hemisphere waves and to carefully describe southern hemisphere eddies given the lack of previous work.

2. METHODS*

2.1 MACDA Dataset

MACDA (v1.0) (Montabone et al., 2011) is a reanalysis of vertical temperature profile retrievals and column dust optical depth retrievals from $L_s = 141^\circ$ in MY 24 to $L_s = 86^\circ$ in MY 27 (February 1999 to August 2004). The temperature profiles and column optical depths were retrieved from radiance observations by the TES instrument that was flown onboard the Mars Global Surveyor in a sun-synchronous polar orbit. The observations provide information about the vertical temperature profile up to 40 km twice a day at approximately 2 AM and 2 PM local time and total atmospheric column dust optical depth every sol around 2 PM local time for the tropics and midlatitudes. Retrievals were assimilated into the UK version of the LMD-UK MGCM (Montabone et al., 2014), which shares the physical parameterizations with the LMD MGCM (Forget et al., 1999), using an assimilation scheme described by Montabone et al. (2006) and Lewis et al. (2007). The dataset is made available publicly on a 5° by 5° resolution latitude-longitude grid at 25 terrain-following sigma levels every two Mars hours. MACDA has been shown to have some bias during the MY 25 GDS (Montabone et al., 2006), but it is an improvement on free runs of the UK MGCM as it captures the well observed solstitial pause in eddy activity in each Mars year (Mooring and Wilson, 2015; Lewis et al., 2016).

The MACDA dataset has been used in several studies to describe the behavior of the Martian atmosphere. Mitchell et al. (2014) compared polar vortices on Mars to those of Earth, Hurley et al. (2014) used MACDA temperature retrievals to constrain model CO_2 condensation levels, Lovejoy et al. (2014) used MACDA for verification of winds of

*Parts of Section 2 are reprinted with permission from "Energetics of the martian atmosphere using the Mars Analysis Correction Data Assimilation (MACDA) " by M. Battalio, I. Szunyogh, and M. Lemmon, 2016. *Icarus*, 276, 1-20, Copyright 2016 by the American Astronomical Society Division of Planetary Science.

MGCM simulations, and Wang and Mitchell (2014) used MACDA to diagnose the Rossby and Froude numbers in a study of atmospheric superrotation. The MACDA reanalysis has become popular to investigate traveling waves in Martian atmosphere, (Mooring and Wilson, 2015; Lewis et al., 2016). The Lorenz energy budget has also been studied over diurnal, seasonal, and annual time-scales using MACDA (Tabataba-vakili et al., 2015).

2.1.1 Dust Storms

Southern hemisphere transient waves play an important role in the annual dust cycle. Large regional dust storms can form from southern hemisphere transient waves (Basu et al., 2006), and rarely, these storms can develop into a GDS if additional lifting centers across the hemisphere can be activated, for example in Argyre Planitia, to the south of the Tharsis Plateau, or from coincident northern hemisphere transient waves (Wang et al., 2003). The MY 25 GDS was activated in this way (Strausberg, 2005). The MY 28 GDS was also the result of southern hemisphere dust lifting. Usually, these storms develop from waves located in and around the Hellas and Argyre Planitias and during the spring period of southern hemisphere transient activity as opposed to the autumn period. The model of Basu et al. (2006) indicated that there could be weak residual transient wave activity after the usual spring period that contributes to the initiation of a GDS during the usual $L_s = 200^\circ - 300^\circ$ period. Regional dust storms in the southern hemisphere are observed to travel west-east between $L_s = 135^\circ - 180^\circ$, as opposed to the more north-south orientation of northern hemisphere dust storms. Southern hemisphere local dust storms are generally more isolated, of shorter duration (<5 sols), and are smaller scale than their northern hemisphere counterparts (Wang et al., 2013). Frontal, flushing dust storms can also propagate from the northern hemisphere into the southern hemisphere through the channels between Tharsis and Arabia Terra.

The GDS of MY 25 was initiated in the southern hemisphere by a series of local

storms forced by the thermal contrasts between the retreating ice cap and bare ground of Hellas Planitia. It was a merging development in the classification of Wang and Richardson (2015). Just after the spring equinox ($L_s = 177^\circ$), a large storm entered Hellas Planitia, causing a rapid increase of the surface obscured by dust. By $L_s = 185^\circ$, the dust spread rapidly east toward the Tharsis Plateau, where additional dust lifting areas developed, and the dust storm fully encircled the equatorial and midlatitude regions by $L_s = 195^\circ$. Lifting continued until $L_s = 212^\circ$, at which time the dust was uniformly distributed (Strausberg, 2005). Dust slowly precipitated out to seasonal levels by $L_s = 304^\circ$ (Cantor, 2007). Citing the large diurnal variation in temperature and modified latitudinal temperature structure, Smith (2002) noted that the dynamics of the atmosphere was changed by the dust storm. The northern hemisphere polar vortex served as a boundary to the dust storm (Mitchell et al., 2014); south of the polar vortex, vertical temperatures increased by over 40 K (Smith, 2002) (see section 2.1.2.1).

The strength of the GDS is juxtaposed to the non-GDS years in Fig. A.2, which shows the optical depth for each Mars year in the MACDA dataset. The general trend of slowly increasing dust approaching northern hemisphere winter is similar in all years up to $L_s = 177^\circ$, then a rapid column optical thickening occurs in MY 25, while the opacities continue to slowly increase in MY 24 and 26. The dust storm rapidly expands out to 40° N, but then the northward expansion slows, only reaching 55° N by $L_s = 230^\circ$.

Beyond the main GDS of MY 25, MY 24 and 26 each had regional dust storms during $L_s = 200^\circ - 230^\circ$: during MY 24, a storm occurred from $L_s = 220^\circ - 230^\circ$ in Acidalia Planitia and $L_s = 202^\circ - 205^\circ$ also in Acidalia (Cantor et al., 2001; Wang et al., 2005); while in MY 26, a storm traveled north to south through Utopia Planitia during $L_s = 205^\circ - 219^\circ$ (Cantor, 2007; Wang and Richardson, 2015). Montabone et al. (2005) compared the evolution of total dust optical depth in these regional dust storms to the GDS in MY 25 and found that the northern hemisphere had much lower optical depth than the

southern hemisphere in general, particularly in MY 25. Returning to MACDA in Fig. A.2, it can be seen that MY 24 has smaller column optical depth than MY 26. The total average optical depth between 57.5° and 82.5° N over the $L_s = 220^\circ - 230^\circ$ period is 0.53, 1.15, and 0.74 for MY 24, 25, and 26, respectively. In several ways, MY 26 was more similar to MY 25 than MY 24 in the $L_s = 200^\circ - 230^\circ$ as a result of the increased dustiness from regional storms, which temporarily modified the local energetics as they traveled and dissipated.

Dust events were not observed during the solstitial pause period in either the northern or southern hemisphere. Intermediately sized dust storms resumed after the solstitial pause, around $L_s = 305^\circ$ (Wang and Richardson, 2015). In the post-pause period, one particularly large intermediate dust storm was observed around $L_s = 313^\circ - 322^\circ$ in MY 26 in Acidalia (Cantor, 2007; Wang, 2007). In the southern hemisphere, the main interval for dust storms was in $L_s = 135^\circ - 185^\circ$, which falls into the post-pause period (Wang and Richardson, 2015).

2.1.2 Average Flow Properties

2.1.2.1 Zonal-mean Temperature and Winds

The zonal mean temperature fields at $L_s = 200^\circ$ (Fig. A.3 top row) and 230° (Fig. A.3 second row) are shown for MY 24 (left column), MY 25 (middle column), and MY 26 (right column). The key feature of the zonal-mean temperature fields is the meridional temperature gradient located near 60° N. At the initial time, MY 24 and 26 have a structure in their polar front that supports baroclinic instability, with a tilt of the gradient away from the pole with increasing height, agreeing with Kavulich et al. (2013) and the studies based on TES observations (e.g. Banfield et al., 2004; Hinson et al., 2012). In MY 25, the tilt is in the opposite direction, which is unfavorable for baroclinic instability at lower levels.

Also evident at $L_s = 200^\circ$ is the effect of dust on the lower latitudes in MY 25. The

100 to 10 Pa layer between 30° N and 30° S is approximately 40 K warmer, and the surface is approximately 10 K cooler on average. This is a result of the higher optical thickness absorbing solar radiation in the upper-levels at the expense of surface. Increased dust also affects the meridional circulation (e.g. Montabone et al., 2005) by strengthening the Hadley cells, which explains the polar warming in the mid-levels via adiabatic processes and the maintenance of the strong meridional temperature gradient. At the later time of $L_s = 230^\circ$, all years display a poleward tilt of the polar front, inhibiting baroclinic instability. Kuroda et al. (2007) found a similar suppression of baroclinic activity due to the increased poleward tilt at $L_s = 280^\circ - 300^\circ$. The meridional temperature gradient decreases at the surface, limiting the sensitivity of the flow to baroclinic instability as the winter solstice approaches. The temperature of the upper-levels in MY 25 still indicates increased warming over the clear years, but the low-level cooling disappears.

All three Mars years show an intensifying westerly jet from $L_s = 200^\circ$ (Fig. A.3 third row) to 230° (Fig. A.3 bottom row) in the northern hemisphere and a weakening jet in the southern hemisphere as Mars approaches northern hemisphere winter. The stronger westerly jet is consistent with the increased meridional temperature gradient through geostrophic balance. The increased vertical shear shifts the most unstable wave number to smaller values (Kuroda et al., 2007). The subtropical jet increases in strength as the Hadley circulation strengthens. The stronger subtropical jet in MY 25 is due to a positive feedback mechanism between the Hadley circulation and dust lifting centers. Haberle et al. (1993) and Murphy et al. (1995) showed that as dust is entrained into the Hadley circulation, the circulation strengthens, intensifying the subtropical jet. The stronger jet increases the likelihood of dust lifting via enhanced surface wind stress, possibly further increasing the optical depth (Basu et al., 2006).

The average zonal properties are briefly discussed for each period and for each hemisphere. Within each hemisphere and for each of the three seasons, there is some inter-

annual variability in the time-mean flow, but mostly, the key differences are between the seasons (Fig. A.4). The left column shows periods of transient wave activity in the southern hemisphere, and the right column shows the respective periods for the northern hemisphere. For the first three pre-pause rows, two years are referenced, because the three pre-pause years from the southern hemisphere (MY 25, 26, 27) are different from the three pre-pause years in the northern hemisphere (MY 24, 25, 26). The northern hemisphere (right column) shows a strong westerly jet at all times. The jet is the strongest during the pause periods, with roughly the same magnitude in the pre- and post-pause periods. For the northern hemisphere pause periods, there is a strong easterly jet in the southern hemisphere. The most important feature in the northern hemisphere is the orientation of the isotherms along the edge of the polar front. As was indicated in Fig. A.3 for the GDS, the isotherms are tilted towards the pole in the pause periods below 10 Pa between 40° and 75° N. Such a signature was also noted by Kuroda et al. (2007) to inhibit baroclinic instability in the northern hemisphere at $L_s = 280^\circ$. The inhibition of baroclinic energy conversion by the vertical temperature profile was also established by Battalio et al. (2016) during the MY 25 GDS.

Focusing on the southern hemisphere (left column), there is a strong westerly jet at all times of roughly the same magnitude (zonal wind contoured in Fig. A.4), but the tilt of the jet is directed towards the pole with height during the pause seasons. The jet during the post-pause period is also broader than the pre-pause jet. The mean temperature profile shows a cold south polar region near the surface and warm equator and northern hemisphere. The meridional transition between the two areas is different between the seasons. During the pre- and post-pause seasons, the vertical temperature profile in the southern midlatitudes (between 60° and 80° S) below 10 Pa is favorable for baroclinic development (i.e. tilted away from the pole with height). However, during the pause period, the isotherms are tilted toward the poles, and along the ground in the same area,

there is tilt of the isotherms also towards the pole, suggesting that the baroclinic instability is not based at the surface.

2.1.2.2 Eddy Components

To remove the diurnal signal from the state variables, a Hamming window digital filter was used to remove the frequency band $0.95 - 1.05 \text{ sol}^{-1}$ and frequencies higher than 1.82 sol^{-1} from each variable of the MACDA dataset as in Kavulich et al. (2013). Filtering in this way removed the diurnal and semidiurnal tides, respectively; the value $1.82/\text{sol}$ was specifically chosen to remove signals from the time step immediately preceding local noon to prevent any semidiurnal tide signal as $10/12 = 0.833$. To obtain the mean state, a 30-sol running mean was calculated for all variables. A 30-sol mean was chosen as it was sufficiently long to capture the seasonal signal while also removing any signal from the baroclinic waves themselves. Figure A.5 shows an example of different running means for surface temperature for MY 26. While the 5-sol mean is clearly affected by the baroclinic waves, the 30-sol average smoothly follows the seasonal trend. The 40-sol mean shows that further averaging does not provide any additional smoothing. The filtered variables will be distinguished from the average with a superscripted prime.

A Hovmöller diagram (Fig. A.6) of the eddy component of the meridional wind in the $57.5^\circ - 82.5^\circ$ N latitude band shows the variations in the propagation of transient waves in the westerly jet at 300 Pa. Waves primarily have a wave number between 2 and 3 with periods between 4 and 5 sols. Waves occur throughout the study period in MY 24 and MY 26; however, their amplitude decreases as time advances. MY 24 displays a decreasing transient wave amplitude after $L_s = 225^\circ$, and MY 26 shows decaying amplitude beginning after $L_s = 215^\circ$, with the primary contribution from flushing dust storms in the eastern hemisphere beforehand. This reduction in wave activity at the end of the study period is reflective of the reversed tilt of the polar front toward $L_s = 230^\circ$ (Fig.

A.3) and the regional dust storms occurring at this time in each year, particularly in MY 26. In MY 25, amplitudes are substantially reduced due to the GDS limiting baroclinic development. The primary growth regions of the waves also differ between years. The amplitude of the MY 24 and 25 waves increase near 180° E, while the amplitude of the MY 26 waves grows upstream near 60° E. Two waves to be compared in Section 3.1.3 are labeled A and B.

The Hovmöller diagram for the pause period for each of the three northern hemisphere years is shown in Fig. A.7. The most obvious features are the slowly propagating waves that occur at the beginning of MY 24 and throughout MY 25. The wave in MY 25 circles the planet twice between $L_s = 255^\circ$ and $L_s = 275^\circ$ before dissipating. These very slow waves are the exception to the usually faster waves of the pre-pause period. The faster waves are also found in the MY 26 pause period and the second half of the MY 24 pause period. Three waves that will be investigated individually later are labeled C, D, E, and F.

Finally, the Hovmöller diagram for the post-pause period in the northern hemisphere is shown in Fig. A.8. Like the pre-pause period, the entirety of the post-pause period is characterized by distinct transient waves of varying amplitude and wave number. Some waves only travel one to two hundred degrees of longitude, while others successfully circumnavigate the planet multiple times without losing coherence. The waves of the beginning of the MY 26 post-pause period are weaker than the others and will be explained in Section 3.2.5. Two waves are individually examined during the post-pause period and are labeled G and H.

2.2 Eddy Kinetic Energy

The Eddy Kinetic Energy Equation (Orlanski and Katzfey, 1991) is

$$\begin{aligned} \frac{\partial}{\partial t} \langle K_e \rangle = & \overbrace{-\langle \nabla \cdot \mathbf{v} K_e \rangle}^1 \overbrace{-\langle \nabla \cdot \mathbf{v}' \phi' \rangle}^2 \\ & \overbrace{-\langle \omega' \alpha' \rangle}^3 \overbrace{-\langle \mathbf{v}' \cdot (\mathbf{v}'_3 \cdot \nabla_3) \mathbf{v}_m - \mathbf{v}' \cdot (\mathbf{v}'_3 \cdot \nabla_3) \mathbf{v}' \rangle}^4 \\ & \overbrace{-[\omega' K_e]_s + [\omega' K_e]_t}^5 \overbrace{-[\omega' \phi']_s + [\omega' \phi']_t}^6 \overbrace{\langle (Residue) \rangle}^7, \end{aligned} \quad (2.1)$$

where the kinetic energy per unit mass is defined as $K_e = \frac{1}{2}(u'^2 + v'^2)$, ϕ is the geopotential height, $\alpha = 1/\rho$ is the specific volume, $\mathbf{v}' = (u', v')$, and $\mathbf{v}'_3 = (u', v', \omega')$. Primed variables indicate the eddy components, and \mathbf{v}_m is the time-mean flow. The overbar indicates a time average, angle brackets denote a mass-weighted vertical average where pressure is the vertical coordinate, and square brackets indicate surface integrals over the surface (s) or top of the atmosphere (t).

Each term on the right-hand-side of Eq. (2.1) describes a process that can change the EKE. Term 1 describes EKE advection by the total flow (ETRANS). Term 2 is the ageostrophic, geopotential flux convergence (GFC) term. When this term is positive, height fluxes are converging, the potential energy of the eddy decreases, and EKE increases. It must be noted that terms 1 and 2 are transport terms, as their integral for the entire atmosphere is zero; thus, they cannot be an ultimate source or sink of EKE.

Term 3 is the baroclinic energy conversion (BCEC) term. When BCEC is positive, EKE is generated from the eddy available potential energy. Term 4 is the barotropic energy conversion (BTEC) term and is positive when kinetic energy is transferred from the background flow and negative when kinetic energy is transferred to the basic flow.

Terms 5 describes vertical fluxes of EKE and can be considered the vertical part of the

ETRANS term. It is neglected in our calculations because it is approximately two orders of magnitude smaller than the other terms. Term 6 is the vertical potential energy flux at the top and bottom of the atmosphere and can be considered the vertical contribution from the GFC term. We consider 1 Pa to be the top of the atmosphere as the top three sigma levels in the MACDA MGCM are sponge levels and are consequently neglected. In the terrestrial atmosphere, term 6 is usually small and can be neglected, but it was found that for the Martian atmosphere, term 6 was only one order of magnitude smaller than the other terms. Throughout the rest of the study, references to the GFC term will refer to the sum of terms 1 and 2, as $-\overline{[\omega'\phi']_s} + \overline{[\omega'\phi']_t} = \frac{\partial(\overline{\omega'\phi'})}{\partial p}$ so that

$$-\overline{\nabla_3 \cdot \mathbf{v}'_3 \phi'} = -\overline{\nabla \cdot \mathbf{v}' \phi'} - \frac{\partial(\overline{\omega'\phi'})}{\partial p}. \quad (2.2)$$

It should also be noted that ideally the surface integral $-\overline{[\omega'\phi']_s}$ is zero, as the boundary condition for vertical motion in a GCM with a horizontal surface is $\omega = 0$. However, we interpolate the data to constant pressure levels, so at the bottom-most level of the analysis, the condition $\omega = 0$ does not necessarily apply.

Term 7 is the residue term and is a catch-all for sources and sinks not accounted for by the EKE equation. Errors collected by this term include frictional effects, sub-grid processes, errors introduced by the temporal filtering, data assimilation, and interpolation errors. Term 7 is calculated by comparing the right hand side of Eq. (2.1) to the left hand side by calculating the change of EKE directly using the product rule:

$$\frac{\partial}{\partial t} \langle K_e \rangle = \mathbf{v}' \cdot \frac{\partial \mathbf{v}'}{\partial t} \quad (2.3)$$

2.2.1 Quasi-Geostrophic Omega

The MACDA dataset does not include vertical velocity, $\omega = dp/dt$, so a method of computing ω from temperatures, heights, and horizontal winds is required. Three trials were performed: a kinematic solution, a quasi-geostrophic (QG) solution with homogeneous boundary conditions, and a QG solution with kinematic boundary conditions. To estimate the effectiveness of various methods of calculating ω , trials of each method were run on data from the MGCM simulation of Kavulich et al. (2013) during the same $L_s = 200^\circ - 230^\circ$ period as to be investigated for MACDA, and the estimated ω was compared to the model provided ω , which is considered the true ω .

The kinematic estimation of vertical motion depends on the horizontal divergence and mass continuity:

$$\omega = \int_p^{p_s} \nabla_h \cdot \mathbf{V} dp, \quad (2.4)$$

where $\nabla_h \cdot \mathbf{V}$ is the horizontal divergence, and p_s is the surface pressure. A second order correction following O'Brien (1970) required nonzero values of omega at the top of the atmosphere to be linearly distributed throughout the column.

The initial kinematic solution was found to be inadequate in describing the structure of the vertical motion. The correlation between the estimated ω and the true ω was 0.21 between 10° and 80° N over the entire $L_s = 200^\circ - 230^\circ$ period. The inability of the method to produce well-behaved estimates of ω was expected based on the poor estimation of divergence from horizontal winds via finite differencing. Instead, the traditional form of the QG- ω equation was used to evaluate vertical motion:

$$\left[\nabla_h^2 + \frac{f_0^2}{\sigma} \frac{\partial^2}{\partial p^2} \right] \omega = \frac{f_0}{\sigma} \frac{\partial}{\partial p} [\mathbf{V}_g \cdot \nabla_h (\zeta + f)] + \frac{1}{\sigma} \nabla_h^2 \left[\mathbf{V}_g \cdot \nabla_h \left(\frac{RT}{p} \right) \right], \quad (2.5)$$

where ω is the vertical velocity, \mathbf{V}_g is the geostrophic wind, σ is the static stability, ζ is

the relative vorticity, p is the pressure, and f_0 is the Coriolis parameter. Sequential over-relaxation was used to invert the left-hand side Laplacian. Static stability was calculated using the relation $\sigma = \frac{\partial\theta}{\partial p}(RT)/(p\theta)$ and was averaged over each level.

A uniform, homogeneous boundary condition across the entire planet was first attempted and compared to a boundary condition supplied by the kinematic solution. It was found that the homogeneous boundary condition solution outperformed the kinematic boundary condition solution. Figure A.9 shows the correlation between the GFDL MGCM ω and QG- ω with homogeneous boundary condition between 28° and 80° N for $L_s = 200^\circ - 230^\circ$. The oscillating pattern in the correlations in Fig. A.9 is the result of the progression of the packets of EKE themselves. The correlation between the QG- ω and the true ω is lower when the pressure-averaged EKE is high, and the correlation is high when the average EKE is low. The correlations between the non-pressure-weighted true ω field and the kinematic boundary condition solution and the homogeneous boundary condition solution for the entire $L_s = 200^\circ - 230^\circ$ time series between 10° and 80° N are 0.55 and 0.62, respectively.

While the correlation of QG- ω to the true ω is somewhat low during the beginning and end of the study period, the correlations between terms of the EKE equation computed using QG- ω and true ω fields are considerably higher. The GFC, BCEC, BTEC, and residual terms are correlated at 0.96, 0.80, 0.91, and 0.93, respectively. Thus, it is the quasi-geostrophic part of ω that dominates the processes described by the EKE equation. We therefore use the QG- ω with homogeneous boundary conditions as the vertical velocity for the rest of this study.

The time-mean vertical motion during the period $L_s = 200^\circ - 230^\circ$ for two levels is shown in Fig. A.10. Shown are MY 24 (left), MY 25 (middle), and MY 26 (right) at the 100-Pa level (top) and 400-Pa level (bottom). Note that the figure is in pressure coordinates, so the negative values indicate upward motion. A stationary, wave number

2 structure is clearly visible at the 100-Pa level, with ascending motions to the west of Arabia Terra and the Tharsis Plateau and descending motions on the eastern slopes. A strong wave number 2 pattern is also present in the TES retrievals (Banfield et al., 2003). A wave number 2 structure remains at 400 Pa, but the descending branches are much stronger than the ascending branches, possibly as a result of the Hadley circulation.

2.2.2 Divergence and Geopotential Flux

A final obstacle to the implementation of the EKE equation to the MACDA dataset was the lack of data for the horizontal divergence of the wind in the dataset. Initially, the divergence was calculated via finite differencing of the horizontal winds. As with ω , control tests were performed on data from the Kavulich et al. (2013) MGCM simulation. Second, fourth, and sixth-order finite differencing proved inadequate to capture smaller scale patterns in the divergence. The effect was amplified by the lower resolution of the MACDA dataset.

The problem was eliminated by rearranging vector products in the EKE equation. In particular, the GFC term (term two in Eq. 2.1) was rewritten as

$$-\langle \nabla \cdot \mathbf{v}' \phi' \rangle = -\langle \phi' (\nabla \cdot \mathbf{v}') + \mathbf{v}' \cdot \nabla \phi' \rangle. \quad (2.6)$$

This expression involves the horizontal divergence of eddy velocities. Explicitly writing out each term yields an advective form:

$$-\langle \phi' (\nabla \cdot \mathbf{v}') + \mathbf{v}' \cdot \nabla \phi' \rangle = -\langle \phi' \frac{\partial u'}{\partial x} + \phi' \frac{\partial v'}{\partial y} + u' \frac{\partial \phi'}{\partial x} + v' \frac{\partial \phi'}{\partial y} \rangle. \quad (2.7)$$

Alternatively, the GFC can be written before the product rule is used to obtain a flux form:

$$-\langle \nabla \cdot \mathbf{v}' \phi' \rangle = -\langle \frac{\partial (u' \phi')}{\partial x} + \frac{\partial (v' \phi')}{\partial y} \rangle. \quad (2.8)$$

In this way, the horizontal divergence is no longer required in the calculations (Xue and Lin, 2001). Only products of heights and winds are necessary to evaluate the GFC term. The flux form method of calculating GFC using Eq. 2.8 is superior as it requires only one finite difference calculation as opposed to the two finite differences required by the advective form (Eq. 2.7). The use of divergence in evaluating the ETRANS term is avoided in a similar way.

The GFC tests for MY 24 (top), MY 25 (middle), and MY 26 (bottom) are shown in Figure A.11 at the 100 Pa level for the $L_s = 200^\circ - 230^\circ$ period in advective form (left) and in flux form (right). The GFC calculated in advective form is close to that found in the flux form, though the latter is reduced in magnitude. There are differences in the field in MY 26 near 60° N by 60° E. GFC in the flux form is positive, while the advective form is negative. Due to the extreme local maxima and minima, the advective form is discarded, leaving calculation of ETRANS and GFC by the method in Eq. 2.8 as the only viable option.

3. NORTHERN HEMISPHERE WAVE ENERGETICS*

3.1 Pre-Solstitial Pause and MY 25 Global-Scale Dust Storm

3.1.1 Pressure-Weighted Vertical Averages

The temporally averaged terms of the EKE equation for each Mars year are shown in Fig. A.12. Shown are the temporal means of the EKE (top), BCEC (second row), GFC (third row), ETRANS (fourth row), BTEC (fifth row), and residue (bottom). The left, middle, and right columns are MY 24, 25, and 26, respectively. The strongest EKE and its sources and sinks are found away from the equator. The EKE in each Mars year is at a maximum in a band between 50° and 80° N, with the highest values between 100° and 200° E and a secondary maximum in MY 24 and 26 near 330° E. This pattern can be explained by stationary waves caused by high topography directly upstream of the favored EKE areas that modulate the propagation of the wave packets (Chang and Orlanski, 1993). The EKE maximum in MY 25 is approximately half the value of the two non-GDS years. The EKE average can most closely be compared to Fig. 4 (top) of Mooring and Wilson (2015) that shows an inter-annual mean of EKE for all three MACDA years at one level during their PRE season ($L_s = 155^\circ - 235^\circ$) and to their Fig. 10, which shows the MY 24/26 average compared to MY 25 during the dust period ($L_s = 186^\circ - 275^\circ$). The Mooring and Wilson (2015) figures show that EKE is favored in certain meridional areas, namely the Planitias, and that eddy activity is reduced in MY 25 during the GDS.

We find the cause for the decreased maximum in EKE in MY 25 to be the reduction of BCEC, which shows a structure similar to the EKE. Positive BCEC is contained in

*Section 3 is reprinted in part with permission from "Energetics of the martian atmosphere using the Mars Analysis Correction Data Assimilation (MACDA) " by M. Battalio, I. Szunyogh, and M. Lemmon, 2016. *Icarus*, 276, 1-20, Copyright 2016 by the American Astronomical Society Division of Planetary Science.

the $50^{\circ} - 80^{\circ}$ N latitude band and in MY 24 and 25 has a maximum collocated with the EKE maximum. The reduced BCEC in MY 25 is due to the GDS throughout the time studied. MY 26 has a bifurcated BCEC maximum on either side of the EKE maximum. The westerly maximum is displaced to 70° E, and the location upstream is explained by orographic effects due to stronger subsidence on the leeward side of Arabia Terra (see Fig. A.10). These zonal differences in the placement of BCEC between MY 24 and 26 to are most likely due inter-annual variability.

As stated earlier, the GFC and ETRANS are transport terms. Thus, they cannot be the ultimate sources or sinks of EKE, but they can contribute to local changes in the EKE. The GFC is the strongest local source and sink of all generation terms and shows a structure dependent on topography. Minima of geopotential flux occur, in general, in the Planitias and downwind of high topography. Maxima of GFC exist over the Plateaus and upstream of topography. The primary minimum occurs around 180° E in the band of highest EKE and carries energy downstream to the north of the Tharsis Plateau, where it is deposited to help extend the storm track to the east away from the strongest BCEC, in agreement with Banfield et al. (2004) and Hinson and Wang (2010). [This phenomenon also exists terrestrially over the Pacific Ocean (Chang, 1993; Chang and Orlanski, 1994).] The mechanism of extending the EKE band eastward occurs in all three years but is strongest in MY 24.

The ETRANS plays an important role in MY 26 in transporting the energy generated by the westerly shifted BCEC maximum to the channel of maximum EKE in Utopia Planitia. A sink of energy occurs north of Arabia Terra, with a source to the east in Utopia Planitia, depositing the EKE generated by the BCEC maximum at the lower elevation. A similar arrangement of sources and sinks is also present in MY 24 and MY 25, but in those years, the western BCEC maximum is much weaker. In MY 24, the maximum of transport is collocated with the EKE maximum near 330° E, which along with the stronger maximum in GFC could explain why the eastern EKE maximum is stronger in MY 24 than in

MY 26.

BTEC acts mostly as a sink of EKE. There are two main areas of negative BTEC: a primary minimum over the Tharsis Plateau and a secondary area between 100° and 120° E near 60° N. MY 25 has a weaker sink of BTEC. As will be explained in more detail later, both of these areas are near the locations of the strongest westerly jet. This suggests that the conversion of eddy potential energy into EKE by BCEC strengthens the jet via BTEC. Finally, the residue is large in magnitude near the pole. The large negative values of the residue must be due to frictional effects, but the positive values at some locations suggest that other factors must also contribute. One such potential source is computational errors in the GFC, as the GFC and residue terms are highly (negatively) correlated with coefficients of -0.89, -0.86, and -0.84 for each year, respectively (a similar observation was reported terrestrially by Ahmadi-Givi et al. 2014). Also, large errors could be caused by the data assimilation scheme that forces the MGCM to alter the atmospheric temperature profile, which in turn modifies the EKE. Although the residual is the same order of magnitude as the other terms in the EKE equation, the overall EKE budget should remain intact as the errors primarily contributing to the residue seem to be due to features unrelated to the EKE equation itself (Ahmadi-Givi et al. 2014).

In comparing Fig. 11 of Kavulich et al. (2013), which used a zonally averaged dust scenario from MY 24, to the left column of Fig. A.12, several differences emerge. The BCEC maximum is shifted to the east in MACDA MY 24 compared to the Kavulich et al. (2013) simulation, and the GFC term has a stronger relative magnitude compared to the other terms. To explain these differences, we first note that the dust scenario in Kavulich et al. (2013) is forced zonally to the MY24/25 scenario, so longitudinal details like particular regional dust storms are lost. Individual regional dust storms can be connected to the transient eddies we investigate, and by smoothing these out zonally, the free-running model of Kavulich et al. (2013) could be missing specific events during the $L_s = 200^\circ$

– 230° period that contribute to the pressure-weighted averages. Free-running simulations can deviate substantially from observations, so if the simulation used by Kavulich et al. (2013) incorrectly modeled the strength, number, or location of transient events, the averages could have been shifted. Further corroborating this possibility is a comparison of the Hovmöller of Kavulich et al. (2013) (their Fig. 10) to the MACDA MY 24 (Fig. A.6). While the frequency of waves is similar, the coherence and relative strength differ. Waves in the Kavulich et al. (2013) simulation are strikingly more coherent than those prescribed by MACDA. Indeed, MY 26 BCEC and GFC are closer to that of Kavulich et al. (2013) than the MY 24 scenario, suggesting that their simulation, while forced by a particular dust scenario, is only one possible scenario for the evolution of the Martian atmosphere.

3.1.2 Zonal and Meridional Averages

3.1.2.1 EKE

Zonal (left column) and meridional (right column) means for the EKE for the $L_s = 200^\circ - 230^\circ$ period are shown in Fig. A.13. The EKE is at a maximum near 10 Pa in the $50^\circ - 80^\circ$ N latitude band. The location of the highest EKE in the region of the westerly jet agrees with Kavulich et al. (2013) and other studies, including Barnes et al. (1993). This corroborates the assertion that the EKE contributes to the maintenance of the westerly jet through BCEC and BTEC. [However, we note that the jet is strongest in MY 25 (see Fig. A.3) when EKE is weakest. This is due to the jet becoming more thermally driven as a result of the stronger meridional temperature gradient in the mid-levels, which is a positive feedback mechanism between dust loading and the strength of the Hadley cell (Haberle et al., 1993; Basu et al., 2006).] The effect of dust on EKE in MY 25 is evident as the maximum is below 325 J/kg. In the meridional average, there are two main areas of EKE. In MY 24, the maximum occurs near 300° E with a secondary maximum near 100° E, while in MY 26 a more elongated maximum is located near 100°

E. In MY 25, the maximum is weaker and located at 150° E and 250° E. The dissimilar meridional distributions of EKE in the non-GDS Mars years are a result of the different energy conversion processes, as will be discussed below.

3.1.2.2 GFC

The total geopotential flux convergence, $-\overline{\nabla_3 \cdot \mathbf{v}'_3 \phi'}$, is shown in Fig. A.14, with the zonal average on the left and meridional average on the right for $L_s = 200^\circ - 230^\circ$. In the zonal average, three main areas of geopotential flux convergence and divergence are prominent. Geopotential flux divergence occurs north of 40° N and below 40 Pa, is strongest in MY 26, and is weakest and lower in height in MY 24. A second divergent area exists generally south of 40° N, above 40 Pa, and is strongest and slightly further north in MY 24 and weakest and further south in MY 26. Between these divergent areas, convergence of geopotential fluxes occurs at 20 Pa near 60° N, which is weakest in MY 25. As the geopotential flux term is neither a global source nor a global sink of EKE, it is expected that the reduction in magnitude during MY 25 should be not as great as for the terms that can be affected by changes in opacity, since the geopotential flux term would transport EKE that already exists prior to the onset of increased optical depth.

Geopotential flux is weak at the surface and stronger above 10 Pa (not shown). Meridionally, convergence is favored between 100° and 150° E in all years, while the strongest divergence occurs just to the west between 0° and 100° E. These features can be understood by considering the atmospheric column shrinking due to strong ascent over Arabia Terra followed by the atmospheric column stretching to the east of that plateau. As the atmospheric column shrinks on ascending over Arabia Terra, divergence must take place to preserve mass, and the converse is true as parcels descend on the leeward side of the plateau. The convergence on the downstream side of the high topography is reflective of the lee cyclogenesis found by Greybush et al. (2013). In MY 24, this pattern repeats over

the Tharsis Plateau: there is strong convergence west of 240° E with strong divergence just to the east.

3.1.2.3 BCEC

BCEC plays a key role in sustaining synoptic-scale systems in the Martian atmosphere and is characterized by the upward and poleward transport of heat. The zonal (left) and meridional (right) averages of $-\omega'\alpha'$ are shown in Fig. A.13. Zonally, there exists a single maximum in each Mars year centered along 60° N. The vertical placement differs between years: in MY 24, the maximum is located near 500 Pa but is above 100 Pa in MY 26. The MY 25 maximum is so weak as to not have a well defined absolute maximum. A minimum in BCEC exists in the upper-levels near 40 Pa in MY 24 and 25, but the feature is weaker in MY 26. This low-dust-loading behavior for the baroclinic conversion was found by Greybush et al. (2013). As in Kavulich et al. (2013), this minimum can be partially explained by GFC in those regions; convergence of heights in those areas forces subsidence. The BCEC term becomes negligible at all latitudes and longitudes above 10 Pa (not shown).

In the meridional direction, the preferred regions of BCEC occur mainly between 0° and 200° E (throughout Utopia Planitia and Amazonis Planitia), with a second area near 320° E (along the southern edge of Acidalia Planitia) below 100 Pa. The height of the maximum areas of BCEC again differs between years. In MY 24, the conversion area is much shallower and is located below 200 Pa. In MY 25 and 26, maxima occur along and above 10 Pa, with a maximum in MY 26 at 100° E and 30 Pa, which is located where the strongest minimum occurs in MY 24. The upper-level minimum in BCEC in MY 24 can be explained again by considering the GFC term. The results for MY 25 and 26 agree with those of Kavulich et al. (2013) on a secondary maximum of BCEC above 100 Pa near 100° E.

BCEC is substantially reduced in MY 25 compared to MY 24 and 26, with the MY 25 maximum at 60° N reduced by an order of magnitude compared to the clear years. Additionally, the positive energy conversion in the meridional average west of 200° E in MY 24 and 26 is absent in MY 25.

3.1.2.4 Heat Fluxes

Baroclinic instability is characterized by poleward and vertical transport of heat. The reduction in heat flux in MY 25 (middle row) compared to MY 24 (top) and MY 26 (bottom) is shown in Fig. A.15. The vertical heat flux, $-\overline{T'\omega'}$, is at left, and the meridional flux, $\overline{T'v'}$, is at right. Each year contains areas of coincident vertical and poleward heat flux between 40° and 70° N. MY 24 contains the strongest vertical fluxes, followed by MY 26; MY 25 has substantially weakened vertical fluxes, suggesting that some mechanism is suppressing the conversion of eddy available potential energy into EKE. The vertical flux is confined to between the surface and 100 Pa, and no downward flux is observed. The meridional flux displays the same reduction in strength from MY 24 to 26 to 25, with the strongest flux confined between 800 and 100 Pa. MY 26 has slightly stronger vertical and meridional fluxes above 200 Pa, which explains the height of the BCEC maximum in MY 26. The decreasing trend of the heat flux below 100 Pa from MY 24 to 26 to 25 can be attributed to the increasing dustiness from one year to the next, which alters the vertical temperature profile.

3.1.2.5 Eady Index

To help explain the underlying cause of the reduced heat fluxes, and thus the reduced BCEC, the structure of the baroclinic instability itself must be explored. There are three reasons that BCEC could be reduced: (i) the static stability of the atmosphere is increased, (ii) the vertical wind shear is weakened, or (iii) some other mechanism prevents the development of perturbations that could efficiently convert available potential energy into

EKE.

The Eady index, σ , (Hoskins and Valdes, 1990) is often used to quantify the sensitivity of the flow to baroclinic instability. It is defined as the ratio between the vertical shear in the zonal wind and the Brunt-Väisälä frequency (N), a measure of static stability, such that

$$\sigma = 0.31f \left(\frac{\partial u}{\partial z} \right) (N)^{-1}, \quad (3.1)$$

where u is the zonal wind component, and f is the Coriolis parameter. N is defined as

$$N = \left(\frac{g}{\theta_{va}} \frac{\partial \theta_{va}}{\partial z} \right)^{\frac{1}{2}}, \quad (3.2)$$

where g is the gravitational constant, and θ_{va} is the ambient virtual potential temperature. A higher Eady index indicates a stronger sensitivity of the flow to baroclinic instability.

The left column of Fig. A.16 shows a vertical cross section of the zonal average of the Eady index, and the right column is a meridional average for a latitudinal band of $57.5^\circ - 82.5^\circ$ N. Shown are MY 24 (top), the difference between MY 25 and 24 (middle), and the difference between MY 26 and 24 (bottom). The meridional cross section is restricted to the $57.5^\circ - 82.5^\circ$ N latitude band as that is the latitude belt where a vertical average of the Eady index (not shown) and BCEC (Fig. A.12, second row) are at a maximum. In the zonal direction, all three years show large-scale similarity with the absolute maximum in a narrow band at the surface extending from 40° to 80° N. Large index values protrude vertically from the surface at 50° N polewards to 60° N at ~ 70 Pa. In MY 26, the Eady index is slightly lower below 300 Pa and slightly higher above 300 Pa near the pole but does not deviate substantially from the MY 24 average. In MY 25, the Eady index is larger above 300 Pa between 60° and 80° N but much weaker below 300 Pa. This lower atmospheric layer is responsible for the reduced heat fluxes in Fig. A.15.

To further investigate the inhibition of energy conversion, the time-mean vertical Brunt-Väisälä frequency profile (top), vertical wind shear (middle), and potential temperature gradient (bottom) for $L_s = 200^\circ - 230^\circ$ for each MY are shown in Fig. A.17. Above 300 Pa, both the static stability and the vertical wind shear are increased in MY 25 compared to MY 24 and 26. [Note that the increased vertical wind shear above 300 Pa in MY 25 is the result of the strengthened westerlies, which keep an approximate thermal wind balance with the increased meridional temperature gradient (Fig. A.3).] Below 300 Pa, which is the area of greatest eddy heat flux (Fig. A.15), both the static stability and vertical wind shear act together in lowering the Eady index in MY 25. Between 500 and 300 Pa, the Brunt-Väisälä frequency is larger in MY 25, with MY 26 falling between those of MY 24 and 25. The higher stability is due to the altered vertical temperature profile. Potential temperatures are lower in the 500 to 200 Pa layer in MY 25, and consequently, the potential temperature gradient is larger above 500 Pa in MY 25 (Fig. A.17 bottom panel). The stability profile of MY 26 that falls between those of MY 24 and MY 25 is the result of a regional dust storm at $L_s = 215^\circ$ that leads to a warmer temperature profile in MY 26 compared to MY 24. Between 500 and 800 Pa, the vertical wind shear is reduced in MY 25 from MY 24, with MY 26 between. The reduction in shear is the result of increased surface winds in dust storm years (Haberle et al., 1993), which reduce the difference between the wind speeds at the top of the boundary layer and below the westerly jet, limiting the shear. Above 200 Pa, the Brunt-Väisälä frequency is smaller in MY 26, which explains the increased heat fluxes aloft compared to MY 24.

3.1.2.6 BTEC

BTEC is found to be a major sink of EKE, especially near 10 Pa. Figure A.18 displays the zonal (left panels) and meridional ($57.5^\circ - 82.5^\circ$ N band) (right panels) averages of the time-mean of barotropic energy conversion for the $L_s = 200^\circ - 230^\circ$ period. Zon-

ally, there are two separate minima: one between 30° and 60° N above 50 Pa and another near 70° N between 10 and 100 Pa. The secondary minimum is collocated with the axis of highest EKE (Fig. A.13 contours). This suggests that the baroclinic eddies transfer kinetic energy to the basic flow, strengthening the jet, similarly to that found by Kavulich et al. (2013) and terrestrially (Orlanski and Katzfey, 1991), with the rate of growth baroclinically similar to the rate of decay barotropically as found by Simmons and Hoskins (1978). The meridional areas of negative BTEC coincide with the strongest zonal winds (contoured). Each Mars year has two areas where BTEC transfers kinetic energy from the eddies to the flow that strengthens the westerly jet. These areas are located near 90° E and 290° E, with the western MY 25 maximum shifted to 150° E. An exception is the eastern maximum in MY 26 that has positive BTEC located on the upstream side of the zonal wind maximum, but the zonal wind maximum associated with that area is the weakest of the maxima. Here, kinetic energy is being transferred from the jet to the eddies, weakening that jet maximum in MY 26.

3.1.2.7 ETRANS

Finally, ETRANS does contribute to the transport of EKE across the hemisphere, as shown in Fig. A.19. In the meridional average, ETRANS redistributes the EKE similarly to the GFC term. That is, energy is transported from the main BCEC areas, namely near 60° E and 200° E (Fig. A.13) downstream to 150° E and 300° E, mostly near the 10 Pa pressure level. ETRANS and GFC elongate the region of highest EKE to the east, so much so that in MY 24, a strong band of EKE (>120 J/kg) exists around the entire 70° N latitude circle (see top left panel of Fig. A.12). The eastward stretching of the high EKE region is well known from terrestrial studies (e.g. Chang, 1993). Zonally, ETRANS and GFC reinforce each other. The role of the transport processes becomes even more transparent when the two transport terms are combined (Fig. A.19 contours). In the zonal

average, the combined transport terms have a maximum near 10 Pa in the regions south of the highest EKE, between 40° and 50° N. Energy is taken out of the main generation area and deposited to the south, extending the area of EKE southward. Closer to the surface, the negative region extends equatorward with a region of weakly positive ETRANS near the pole, but the combined transport (Fig. A.19 contours) shows no such near surface secondary maximum as the GFC is weak near the pole in the zonal average.

3.1.3 Contrasting Prototypical Waves in Clear and Dust Storm Years

3.1.3.1 MY 24 Example Wave

To further elucidate the differences on Fig. A.6 between EKE generation processes in dust and clear periods, a typical wave from each MY 24 and 25 is contrasted. The two waves are indicated by lines A and B on Fig. A.6, respectively. We begin with an investigation of the MY 24 EKE center, which is generated from downstream development between $L_s = 206.6^\circ$ and $L_s = 209.1^\circ$ (Fig. A.20 left column). Each panel advances time by 0.5 sol compared to the panel above. The EKE packet is initiated to the northeast of Arabia Terra and propagates eastward at a rate of approximately $90^\circ \text{ sol}^{-1}$ until it dissipates after completing nearly one circumnavigation. This evolution is typical for storms in the clear years. The preferred areas of such developments are locations of lee cyclogenesis (Greybush et al., 2013) and are the storm tracks noted by Hollingsworth and Barnes (1996), Banfield et al. (2004), Wang et al. (2005), Basu et al. (2006), and Hinson and Wang (2010).

The two transport terms are also shown in Fig. A.20: GFC is the middle column, and ETRANS is the right column. GFC is the largest local contributor to the transport of EKE. As in the terrestrial atmosphere, the geopotential flux is the initiator of EKE generation. In the initial phase of development, the generation of EKE is preceded by GFC (top row). At the next step (row two), the GFC maximum has an EKE maximum slightly

downstream, and they travel together as time progresses, following the downstream development paradigm of Orlandi and Sheldon (1995). As the positive region of GFC grows, the EKE grows slightly downstream. However, as the region of positive GFC grows in size and magnitude, an upstream region of geopotential flux divergence intensifies concurrent with the decay of the geopotential flux convergence in the initial upstream region. The couplet changes in magnitude and size proportionally so that their net contribution to the change in EKE is approximately zero. An additional, weaker couplet of GFC forms downstream of the main couplet that helps to disperse energy downstream to trigger further downstream development (Orlandi and Katzfey, 1991). This is consistent with the numerical study of Orlandi and Chang (1993) that found multiple downstream regions of GFC that developed after the initial upstream disturbance. ETRANS is weaker and has the opposite sign in areas of strongest GFC with a correlation of -0.62 between the ETRANS and GFC at the middle time-step. ETRANS propagates the energy eastward from the upstream to the downstream side of the wave as the GFC accumulates energy on the upstream side of the wave.

The generation terms are contoured in Fig. A.20. BCEC (middle column contours) is a source of EKE during the growth phase of the wave packet. BTEC (right column contours) acts as a sink during the decay phase of the storm. Both of these processes are smaller in magnitude than either of the transport terms. The growth of the EKE maximum occurs due to the input of energy through baroclinic conversion, though the geopotential flux initiates that baroclinic conversion. The top row shows only a weak area of BCEC at the initial time-step. Once BCEC begins, the center of BCEC grows quickly as it crosses Utopia Planitia, intensifying the EKE maximum. The baroclinic growth explains the strengthening couplet of GFC, which increases in magnitude as the transport of EKE increases. Thus, GFC initiates BCEC, but the baroclinic growth of the EKE is why the geopotential flux increases in magnitude. The BCEC intensifies until the BTEC begins increasing to

the north of the Tharsis Plateau (row three). In row five, the BTEC reaches a minimum, and the EKE packet begins to dissipate.

The baroclinic growth of EKE is dependent on the ability of waves to simultaneously transport heat towards the pole (converting available potential energy of the mean flow to eddy available potential energy) and vertically (converting the eddy available potential energy to EKE). Next, the continually increasing EKE must be transported downstream. This is not accomplished by the mean flow (Orlanski and Katzfey, 1991) but via propagation by the GFC (Chang, 2001). Convergence of geopotential heights behind the eddy converts EKE into potential energy, and divergence of geopotential heights ahead of the eddy converts that potential energy back into EKE. [Note that in the text we have referred to positive values of the GFC term as convergence and negative values as divergence due to the minus sign in front of the GFC term.] The wave propagates to the east towards the Tharsis Plateau. The direction of horizontal and vertical heat fluxes reverse as the flow reaches Acidalia Planitia, but from Fig. A.13, the longitudinal average of BCEC is still positive at 300° E: instead of transporting warm perturbations north and up, the topography helps transport cold perturbations southward and down.

The vertical structure of the wave is shown in Fig. A.21. The strongest EKE (Fig. A.21 left column), GFC (Fig. A.21 right column), and BCEC (Fig. A.21 right column, contours) are collocated during the strengthening phase of the eddy. GFC and BCEC both have westward tilts with height, as expected of a wave converting potential energy into EKE (e.g. Orlanski and Sheldon, 1995). BCEC takes place mostly in a layer between 300 and 10 Pa but also extends below 500 Pa. GFC precedes the development of strong BCEC, and the GFC maximum precedes the EKE maximum by about 0.5 sol, similarly to that found by Ahmadi-Givi et al. (2014). The most negative BTEC (Fig. A.21 left column, contours) is confined to the layer above 300 Pa, which is expected as this is the height of the westerly jet. Once BTEC stops, the geopotential flux convergence, which sustains the

system, turns to geopotential flux divergence as the wave continues to dissipate.

3.1.3.2 MY 25 Example Wave

We now contrast the MY 24 disturbance, which shows a similar structure to that of the storm in Kavulich et al. (2013) and to terrestrial waves, to a local storm during the GDS of MY 25. The disturbance examined below is similar in form and duration to several other systems in MY 25 including a storm from $L_s = 211^\circ - 214^\circ$, another $L_s = 218^\circ - 221^\circ$, and several other weaker systems. A local EKE maximum is initiated in the same region as in the MY 24 case, northeast of Arabia Terra (Fig. A.22 left column) at $L_s = 201.1^\circ$. The EKE maximum propagates eastward at a speed of approximately $80^\circ \text{ sol}^{-1}$ (note each panel advances at 0.33 sol). The wave dissipates after $L_s = 202.7^\circ$, just west of Arabia Terra.

GFC and ETRANS terms exhibit similar shapes and magnitudes relative to the EKE maximum as the MY 24 storm. GFC (Fig. A.22 middle column) precedes any BCEC or BTEC. Once the wave packet is initiated, the GFC grows in concert with the EKE, and additional couplets develop upstream and downstream of the main GFC couplet. As in MY 24, ETRANS (Fig. A.22 right column) serves mostly as a local sink of EKE in the main area of EKE, with a maximum directly downstream.

The primary differences between the MY 25 and 24 waves are in the growth and decay mechanisms. BCEC plays a lesser role in the strengthening of the EKE in MY 25 (Fig. A.22 middle column, contours), though there are weak areas of BCEC throughout the growth period of the wave. BCEC only becomes a major factor well into the development of the storm (sixth panel from top). This is not surprising, as temperatures aloft are much warmer even at the beginning of the study period in MY 25 (Fig. A.3), which has the effect of suppressing baroclinic instability by increasing static stability. Despite the reduced BCEC, EKE attains a similar maximum magnitude as in the MY 24 storm. The reason

for this is BTEC (Fig. A.22 right column, contours), which unlike in the MY 24 case, is positive during the development of the EKE packet. EKE attains a magnitude similar to that for the MY 24 case, because the level of EKE depends on the difference between BCEC and BTEC rather than the magnitudes of each term (Simmons and Hoskins, 1980). However, BTEC does become a sink of EKE once the EKE packet reaches the Tharsis Plateau, as in the MY 24 case. This pattern of weaker BCEC compensated by positive BTEC during development is a characteristic of storms in the GDS year.

EKE has a deeper vertical structure in the MY 25 case than in the MY 24 case (Fig. A.23 left column). An amplifying pattern of EKE descends from 30 Pa at the second time-step to 300 Pa at the sixth time-step, 2.66 sols later, which coincides with the one BCEC maximum (Fig. A.23 right column, contours). GFC (Fig. A.23 right column) exhibits a weaker tilt with height, a consequence of the reduced baroclinicity, and time-step seven shows an easterly tilt with height just before the barotropic decay begins. Also strong geopotential flux divergence remains throughout the existence of the eddy, unlike in the MY 24 case, where divergence only occurred once the eddy began to decay. The left column of Fig. A.23 (contours) corroborates the aforementioned finding that the wave is a mixed barotropic/baroclinic wave; that is, the wave grows by both barotropic and baroclinic energy conversion. A tongue of positive BTEC grows from near 10 to 400 Pa during the growth phase of the eddy. As the wave progresses, a downstream region of negative BTEC takes over to accelerate the decay of the wave.

3.1.4 Intensities

The global-scale dust storm has a profound effect on the amount of EKE generated by the baroclinic waves. Figure A.24 shows the volume-integrated EKE and its generation terms for each MY in the $22.5^\circ - 82.5^\circ$ N latitude band. MY 24 (blue) and MY 26 (green) maintain higher background levels of EKE throughout the $L_s = 200^\circ - 230^\circ$ period

than MY 25 (red). However, MY 26 does show reduced EKE similar to MY 25 after $L_s = 220^\circ$. Though the background levels are reduced in MY 25, the maximum intensity of the storms is not diminished. The number of strong EKE generation events is reduced instead so that the EKE is generated in short bursts in MY 25. Three major events are clear: $L_s = 201^\circ - 203^\circ$, $L_s = 214^\circ$, and $L_s = 227^\circ - 228^\circ$, with other smaller events. This is contrasted to the two other years that have a higher background EKE level with more frequent major EKE generation events. There were three major events in MY 25 and six major events in both MY 24 and 26. Thus, the frequency of major EKE events is roughly halved in MY 25. A power spectrum (not shown) of the EKE time series indicates a peak at frequencies of $5-6 \text{ sol}^{-1}$ for MY 24 and 26 and a dominant peak at 3 sol^{-1} for MY 25.

The MY 25, $L_s = 214^\circ$ event is unusual. The EKE spikes sharply and then falls to its background level equally as quickly. Concurrent spikes are recognized in the transport, BCEC, GFC, and BTEC terms. This storm defied energetics analysis as the associated residue (not pictured) was larger than sum of the energy conversion and transport terms, and the EKE appeared to spontaneously develop across a large latitudinal and longitudinal swath simultaneously ($30^\circ - 70^\circ \text{ N}$ and $180^\circ - 270^\circ \text{ E}$). The timing of the system does not fall in a gap of TES retrievals, but retrievals are unavailable north of 30° N (Fig. 2 Montabone et al., 2014). In an attempt to explain this storm, the aforementioned analysis was duplicated on a beta-version of the EMARS reanalysis (Greybush et al., 2012). This particular storm was not present in the EMARS reanalysis. Thus, the MY 25, $L_s = 214^\circ$ storm may be an artifact of the MACDA reanalysis as a result of the bias found by Montabone et al. (2006) in MY 25

The two transport terms remain close to zero at almost all times for all three years. This is expected as ETRANS and GFC only move EKE and cannot be ultimate sources or sinks. Integrating the plots of Fig. A.24 across time gives values of GFC and ETRANS

one to two orders of magnitude smaller than that of the energy conversion terms.

The BCEC term is nearly always positive for all three years but never exceeds 0.75 J/kg/s during MY 25. Conversely, MY 24 and 26 show periodic BCEC events with the volume integrated BCEC correlated to the volume integrated EKE with correlation values 0.67, 0.51, and 0.77 for years 24, 25, and 26, respectively, at a zero time-step lag. Also note that in all years near $L_s = 230^\circ$, BCEC is reduced compared to $L_s = 200^\circ$, reflective of the reversal of the tilt of the polar front between the two time periods and the decrease of the meridional temperature gradient, stabilizing the atmosphere to baroclinic instability (see Fig. A.3).

BTEC has similar values and fluctuations in each year. The average values are negative but occasionally become positive during large EKE generation events. During MY 25, BTEC experiences a reduced number of positive events and is closer to zero on average. The reduced magnitude of BTEC is attributable to two causes. One, a sink of EKE becomes smaller if less EKE is generated, and two, the relatively higher average of BTEC during MY 25 is due to these periodic episodes of positive BTEC events.

3.2 Solstitial Pause and Post-Solstitial Pause

We now investigate the energetics over the course of the entirety of the MACDA dataset.

3.2.1 Pressure-Weighted Vertical Averages

3.2.1.1 Pre-Solstitial Pause

For completeness, the pre-pause period is repeated to introduce the ageostrophic geopotential flux (AGF) and ETRANS vectors for the period $L_s = 190^\circ - 220^\circ$ (Fig. A.25). This period corresponds to the peak of pre-pause activity and shows an earlier time during the GDS in MY 25 (Fig. A.2); thus, the averages for MY 25 are closer to those for MY 24 and 26. Furthermore, during this period of MY 26, the wave activity is higher than

in MY 24, so the temporal averages of the terms in the EKE equation are much higher (Wang, 2007). The strength and positioning of terms in MY 24 for this period are similar to those that were shown in Section 3.1.1. For MY 25, all terms have larger magnitudes during $L_s = 190^\circ - 220^\circ$ than during $L_s = 200^\circ - 230^\circ$. EKE, and BCEC in particular, have larger magnitude, and the BCEC center to the northwest of Arabia Terra is stronger. Each term of the EKE equation is substantially larger magnitude in $L_s = 190^\circ - 220^\circ$ compared to $L_s = 200^\circ - 230^\circ$ in MY 26, and this pre-pause period has the highest magnitude EKE shown. The residue is more negative during this period, indicating increased friction as a sink of EKE.

In row three, we also show the ageostrophic geopotential flux vectors, which are defined by:

$$(\mathbf{v}'\phi')_a = \mathbf{v}'\phi' - \mathbf{k} \times \nabla \frac{\phi'^2}{2f(y)}, \quad (3.3)$$

where $f(y)$ is the latitudinal varying Coriolis parameter (Orlanski and Sheldon, 1993). The AGF vectors are shown in each GFC panel. All three years show a pattern of circulation in both Utopia and Amazonis Planitia. Vectors are directed west to east between 60° and 80° N, and upon approaching Tharsis, a segment of the fluxes are directed southwesterly along the windward side of Tharsis into Amazonis. The flux vectors are pointed in a retrograde direction between 40° and 60° N, back to Arabia Terra and then across into Acidalia in MY 24. In MY 26, the vectors are westward across Tharsis. In MY 25, they have a similar but weaker pattern than in either MY 24 or 26. The magnitude of the vectors south of 40° N is not large enough to be shown. The equivalent flux vectors for the ETRANS term are also shown ($\mathbf{v}K_e$). The ETRANS vectors are more uniform and are strictly directed from west to east in all locations. Vectors in MY 25 have the smallest magnitude, with MY 24 and 26 having larger magnitude. Vectors curve around Tharsis and somewhat around Arabia Terra.

3.2.1.2 Solstitial Pause

The terms of the EKE equation for the solstitial pause period are shown in Fig. A.26. [Note that the scale for the EKE has been changed.] The EKE retains larger values in the zonal band between 50° and 80° N; however, the EKE during the pause period in MY 24 and 26 is highest in Acidalia Planitia instead of Utopia Planitia as during the pre-pause period. There are also indications of flushing storms in MY 25 close to the equator around 120° E. MY 25 has the strongest EKE during the pause period in a nearly continuous band around 70° N, with a gap in the band around 200° E. The stronger EKE during the MY 25 pause is due to the waves that result from the large meridional temperature gradients that form as a result of the middle atmosphere polar warming from the MY 25 GDS (Kuroda et al., 2007; McCleese et al., 2008).

The BCEC has small magnitude in all three years and has a wave number 2 structure, with negative BCEC northwest of Tharsis and Arabia Terra. Of the three years, MY 25 has the area of strongest BCEC in Acidalia Planitia. GFC also has a wave number 2 structure between 60° and 80° N in each year that is roughly in phase with the wave in BCEC. The phase is reversed between 40° and 60° N so that there are areas of positive (negative) GFC north of negative (positive) GFC. In the 40° – 60° N latitude band, there are higher wave number features, while in the 60° – 80° N latitude band there is only the wave number 2 feature. The GFC is strongest in MY 25 during the pause period. The AGF vectors are much weaker in the pause period than the pre-pause period but have the same directionality as in the pre-pause period.

ETRANS has a structure similar to that of GFC in the 60° to 80° N latitude band, but it does not reverse phase south of that band, so that between 40° and 60° N, ETRANS and GFC are out of phase and partially cancel each other out. ETRANS also has some higher-order wave number features in the 40° – 60° N band. For GFC and ETRANS, there

are no features south of 40° N. The ETRANS vectors are similarly weaker in the pause period. They are predominantly directed from west to east and are largest in magnitude between 40° and 60° N. BTEC also has a wave number 2 pattern, but it is out of phase with the other terms by about 60° of longitude. The negative areas of BTEC are larger in area and in magnitude than the positive areas. BTEC does not show the two-banded structure of the GFC or ETRANS and is coherent meridionally. The magnitude of BTEC is strongest just downstream of the areas of high topography, around 120° E and 300° E. The residue during the pause period is mostly positive and shows the same wave number 2 pattern as GFC. The widespread positive values of the residue might be attributable to the presence of clouds over the northern hemisphere pole in winter (Pettengill and Ford, 2000). Combined with the deposition of CO_2 onto the northern pole, these could be the source of diabatic effects that are not captured by the EKE equation.

3.2.1.3 Post-Solstitial Pause

The EKE equation terms for the period after the solstitial pause period are shown in Fig. A.27. During $L_s = 330^\circ - 360^\circ$, EKE returns to pre-pause levels. EKE is strongest during this time in MY 24 and 25 compared to the pre-pause times, while the EKE in MY 26 experiences somewhat weaker levels than the pre-pause average. EKE during the post-pause period in MY 24 is the strongest of all periods examined, with values above 200 J/kg/s over a wide region in Amazonis Planitia. Furthermore, EKE extends in a wider latitudinal band close to the north pole in all three years. Longitudinally, EKE is still largest in the three northern hemisphere Planitias. The values of EKE in MY 25 are also comparable to those of MY 24 and 26, as the GDS of MY 25 has ended by the post-pause time, and opacity values have decreased to nearly normal levels (Fig. A.2). The EKE in MY 26 has values that are lower than those in either MY 24 or 25. We attribute the reduction to inter-annual variability and regional dust activity. However, the EKE of MY

26 still shows the preferred areas of Utopia and Acidalia Planitias.

BCEC is again only positive in the post-pause average. In all three years, the maximum BCEC is in Amazonis Planitia. This location is shifted slightly downstream of the maximum in the pre-pause period. The other two maxima of BCEC in the post-pause period are in Acidalia Planitia and Utopia Planitia. MY 24 has the strongest BCEC, followed by MY 26, and MY 25 with the least BCEC. GFC in the post-pause period is similar to that of the pre-pause time, with a strong wave number 2 component in two separate latitude bands, $40^{\circ} - 60^{\circ}$ N and $60^{\circ} - 80^{\circ}$ N. Negative areas are located upstream of topography, and positive areas are located downstream of topography. The AGF convergence vectors also show a wave number 2 structure in the $60^{\circ} - 80^{\circ}$ N latitude band and are directed from the upstream negative area of GFC to the downstream positive side, so just as in the pre-pause period, the GFC works to transport energy around high topography. This process is strongest over Tharsis in MY 24 and 25 and strongest around Arabia Terra in MY 26. A secondary feature operates in the $40^{\circ} - 60^{\circ}$ N latitude band. On the windward side of Tharsis, in all three years, some of the AGF vectors are directed equatorward and then towards the west, explaining where the GFC convergence upstream of Tharsis originates. The AGF vectors are directed east to west in the $40^{\circ} - 60^{\circ}$ N latitude band and recirculate GFC upstream. This process is strongest in MY 25, where the circulation is maintained between 100° and 240° E, and it is weakest in MY 26, where there is almost no recirculation in Utopia and Amazonis. This could explain why average EKE in MY 25 is stronger than in MY 26, even though the BCEC is stronger in MY 26. The process of GFC recirculation was noted terrestrially by Chang (2000).

ETRANS has a stronger wave number 1 pattern in the $60^{\circ} - 80^{\circ}$ N latitude band in the post-pause period than during the pause or pre-pause. ETRANS has considerable inter-annual variability, but it is broadly positive between 120° and 240° E and negative upstream of Arabia Terra. In the $40^{\circ} - 60^{\circ}$ N latitude band, ETRANS retains the wave

number 2 structure noted at previous times. The ETRANS vectors are larger and more uniform in direction than the AGF vectors and have larger magnitude post-pause than pre-pause. The vectors are strongest in each year between 40° and 60° N, with small magnitudes south of that latitude band. BTEC in the post-pause period is quite similar to that of the pre-pause period. The most positive area of BTEC is located at 240° E and 50° N, with the most negative area to the northwest. The wave number 2 pattern is evident in the BTEC, with negative values downstream and weaker positive values upstream of topography. The residue is of comparable magnitude to GFC and also has the two-banded, wave number 2 structure noted in the pause period. Between 60° and 80° N, the residue is negative downstream of topography, and between 40° and 60° N, the residue is negative upstream of topography. This is most evident in MY 24 when the residue is strongest, but this pattern is also noticeable in MY 26.

3.2.1.4 Summer Solstice

For completeness, the pressure-weighted averages for the summer solstice period ($L_s = 90^\circ - 120^\circ$) for MY 25 and 26 are provided in Fig. A.28. All energetics terms for the period are weaker than even for the winter solstice period. [Note that the colorbar scales have been changed.] EKE is highest over the Tharsis Plateau, with only minimal amounts of EKE found in the planitias. The high EKE over topography during the summer period can be attributed to orographic effects. BCEC is minimal during both years, with a negative of BCEC over Tharsis. GFC and the associated AGF vectors are also very weak, but there are areas of nonzero GFC around the pole. Here, the magnitude of GFC is less than one quarter of that of the pre- or post-pause periods. ETRANS and its vectors are similarly weak, but they do exhibit the same wave number 1 pattern found at other times. BTEC also has a wave number 1 pattern but is mostly negative in both years. The residue is positive for most regions, which can be attributed to diabatic heating during the warmest

time of the year. Combining these results, there is no indication of traveling wave activity during the summer period from the energetics.

3.2.2 Zonal and Meridional Averages

3.2.2.1 EKE

The zonal and meridional averages of EKE during each of the nine periods of interest in the northern hemisphere are shown in Fig. A.29. EKE increases with height more quickly near the pole and slowly near the equator in all periods. In the zonal average (left column) between 55° and 85° N, EKE is the strongest near the surface, with values at or above 100 J/kg/s at 600 Pa . The six pre- and post-pause periods are quite similar, with some inter-annual variability. As noted in previous sections, EKE is weakest in the MY 25 pre-pause, but it is also very weak in the MY 26 post-pause. The other four non-pause periods have similar values of EKE in the jet core, with values between 150 and 200 J/kg/s . In all periods, the highest EKE is constrained above 100 Pa , so it does not contribute strongly to the pressure-weighted vertical average. The three pause periods have considerably weaker EKE below 100 Pa , and the zonal band of higher EKE in the mid-levels is shifted slightly equatorward due to the southward shift of transient waves during the pause period. The magnitude of EKE below 200 Pa during the pause period is roughly one quarter of that of the pre- and post-pause periods. Above 100 Pa though, the EKE still reaches the same large values (above 200 J/kg/s) as in the non-pause periods, which is evidence of upper-level waves during the pause, as noted in Kuroda et al. (2007).

In the meridional average (between 57.5° and 82.5° N), EKE is the largest in the $120^\circ - 240^\circ$ E longitude band for all six non-pause periods. These preferred areas of wave activity are locations of lee cyclogenesis (Greybush et al., 2013) and are the storm tracks noted by Hollingsworth and Barnes (1996), Banfield et al. (2004), Wang et al. (2005), Basu et al. (2006), and Hinson and Wang (2010). This is particularly true for the MY 24

and 26 pre-pause period and the MY 24 post-pause period. There are smaller values of EKE in the mid-levels, around the longitudes for Arabia Terra and Tharsis. During the pause periods, there appear to be no favored longitudes for EKE, and each period shows little zonal change in EKE amplitude.

3.2.2.2 BCEC

BCEC for the northern hemisphere is shown in colored contours in Fig. A.29. All six non-pause periods show the same BCEC behavior. All post-pause periods and MY 24 pre-pause have BCEC maxima around 400 Pa and 60° N. The pre-pause MY 25 and 26 period have maxima closer to 100 Pa and shifted slightly north. The meridional extent of BCEC is the same in the six non-pause periods between 35° and 80° N. BCEC never reaches the surface in any period but is closest to the surface in the post-pause period. In each non-pause period, there is a small area of negative BCEC above 100 Pa and located at 50° N. This will be shown to correspond to an area of strongly positive GFC. The zonal average of EKE during the pause period is very different. In the MY 24 and 26 pause periods, there is a weak positive area of BCEC south of 60° N. The largest magnitude feature in BCEC during the pause period is a negative region located above 200 Pa between 60° and 70° N. This region will be further discussed in Section 3.2.2.3. Finally, a second area of positive BCEC lies above 50 Pa, with a maximum around 70° N.

There are three longitudes favored for BCEC in the non-pause times: 60 – 100°, 140 – 210°, and 310 – 350° E. These correspond to the longitudes of Utopia, Amazonis, and Acidalia Planitias. There is no single favored region for BCEC in all six periods, though in each individual year there is one basin where BCEC is preferred. Amazonis is preferred pre-pause in MY 24 and post-pause in MY 24 and 26. Utopia is preferred pre-pause in MY 26. The three basins are equally preferred post-pause in MY 25. Acidalia is not the region of strongest BCEC in any season despite being a preferred region for flushing type

dust storms (Wang and Richardson, 2015), and it may have lower BCEC because of the prevalence of dust storms. Negative regions of BCEC are limited to two non-pause periods and are located above 200 Pa: MY 26 pre-pause above Acidalia and MY 24 post-pause above Utopia. Interestingly, these two years experience the strongest areas of positive BCEC in the other basins, while the negative BCEC aloft tends to limit the positive BCEC located beneath these regions. As will be shown later, these two regions correspond to locations of downward heat fluxes and positive GFC. In the pause periods of MY 24 and 26, weak local maxima of BCEC remain at mid-levels in the three basins, but the upper-level negative BCEC located above those positive regions is of much larger magnitude. All three years also have two positive regions of BCEC located at 150° and 290° E. These somewhat align with regions of strong negative GFC (see Section 3.2.2.4).

3.2.2.3 Heat Fluxes

To further investigate the nature of BCEC across the transient wave season, the vertical (Fig. A.30) and meridional (Fig. A.31) heat fluxes are shown. In the zonal average of the temperature fluxes (left columns), the flux is strongly directed towards the pole and upward during the non-pause periods between 40° and 70° N. The vertical heat flux is not based at the surface; instead it starts at around 600 Pa. The meridional heat flux is strongest closest to the surface. The combination of these fluxes indicates strong BCEC. In the pause period, the heat fluxes are substantially reduced. The meridional heat flux is pushed southward over the strongest meridional temperature gradients. The zonal mean temperature (Fig. A.31 left column, contours) becomes strongly tilted towards the poles, which also suppresses baroclinic instability (Kuroda et al., 2007). The vertical heat flux has the same location, but it is weaker in magnitude. Additionally, there is a downward flux of heat above 400 Pa. This location corresponds to negative BCEC and partially explains why BCEC serves to remove EKE during the pause period.

The meridional average of the vertical heat flux shows the same spatial distribution as the BCEC itself. The meridional average of the meridional heat flux is more zonally homogeneous, though there is a gap in each post-pause season around 150° E. This suggests that the preferred regions of BCEC are dictated by the location of the vertical heat flux and not the meridional heat flux. The average vertical (Fig. A.30 right column, contours) and meridional (Fig. A.31 right column, contours) wind components are much stronger in the pause period than the non-pause periods, indicating that the stationary waves are much stronger during the pause. However, in the non-pause periods, there is no discernible trend between the strength of the heat fluxes and the strength of the mean flow. In the pause period, the meridionally averaged meridional heat flux is very weak, but there is a strong region above 100 Pa. This has no associated vertical heat fluxes, so it does not contribute to BCEC. This region might be a result of upper-level waves in the pause period (Lewis et al., 2016).

3.2.2.4 GFC

There is great uniformity in the GFC above the surface between each of the six non-pause seasons (Fig. A.32 left column). There exists a broad area of geopotential flux divergence extending from 10 Pa to near the surface from 50° to 80° N. In the middle of this broad area is a pocket of GFC centered at 400 Pa and 65° N. A second area of GFC is located around 40° N and above 300 Pa. This strong, positive area of GFC is aligned with the region of negative BCEC in many of the non-pause years. The GFC explains why there is negative BCEC, as if there is convergence aloft, heat fluxes will be forced downward. The pause periods have substantially different GFC. There is strong geopotential flux divergence above 100 Pa from 80° N south to the equator, and there is a patch of GFC below that at 50° N.

Despite the uniformity in the zonally averaged GFC, there is great inter-annual vari-

ability of the meridionally average GFC (Fig. A.32 right column). In general, there is strong GFC along and downstream of the longitude of Tharsis. There is also strong geopotential flux divergence located at 180° E. At all other longitudes, there is year to year variability. At all longitudes where the BCEC (Fig. A.29) is at a maximum for the period, the GFC is at a minimum. This coincidence can be explained by the reverse of the argument applied to the upper-level BCEC minima. Divergence in the upper or mid-levels draws air from below to fill in the horizontal removal of mass. The rising air forces baroclinic instability. However, not all regions of strong geopotential flux divergence correspond to strong BCEC. Thus, while a strong geopotential flux is not a sufficient condition for strong BCEC, it is a necessary one. The pause period has reduced GFC except above 100 Pa, and there is no broad trend to the GFC field, which is ruled by inter-annual variability.

The vertical AGF vectors are also shown in the meridional average. [Note that the vertical direction has been scaled by a factor of 100 to bring out the vertical flow patterns.] One feature is prominent in all nine periods. There are strong downward fluxes at 240° E that converge just west of Tharsis. This suggests that Tharsis acts as a dam to the propagation of transient eddies from Amazonis to Acidalia. All non-pause periods have upward directed fluxes in Acidalia. The pause periods have fluxes directed downward at all levels and all longitudes. Again, this is indicative of wave activity above 10 Pa.

3.2.2.5 ETRANS

ETTRANS zonal average shows great uniformity between the non-pause seasons (Fig. A.33 left column). There is a column of positive ETRANS just south of 80° N that spreads south and downward to around 700 Pa. At 60° N, there is a column of negative values that is tilted towards the pole and extends to 700 Pa and 30° N. Finally, there is a second positive area around 10 Pa at 50° N. These features indicate that EKE is removed from the area south of the westerly jet and transported aloft and poleward. There is some inter-annual

variability. For example, in the MY 26 pre-pause period, there is a third, weak area of positive ETRANS values in the middle of the negative column. Also, the negative column of ETRANS is stronger in the post-pause period than in the pre-pause period. ETRANS in the pause period is quite different from the non-pause periods. Large values of ETRANS are relegated above 100 Pa. The sign of ETRANS is reversed from the non-pause periods. The values are negative at 70° N and positive at 55° N, meaning that EKE is transported to the south, which does correspond to the preferred regions of transient wave activity during the pause period (Lewis et al., 2016).

ETRANS maintains two patterns in the meridional average (Fig. A.33 right column). In each of the six non-pause seasons, there is a strong, vertically uniform wave number 1 component to the field, but in half of those periods, there is an equally strong wave number 2 component as well. Wave number 1 dominates in the MY 25 and 26 pre-pause period and in the MY 25 post-pause period. ETRANS is negative between 300° and 100° E and is positive between 120° and 270° E. In the other three non-pause periods, the wave number 1 negative pattern remains, but it is somewhat weaker, while a second negative pattern emerges around 180° E. In the three years that lack a strong wave number 1 component, the ETRANS areas are much stronger. The meridional average of ETRANS is much weaker in the pause period, with almost no contribution below 200 Pa. There is a wave number 1 component to the ETRANS, but like the zonal average, it is reversed from the non-pause periods. Values are negative between 120° and 240° E and are positive between 300° and 100° E. This suggests that EKE is removed from the Utopia and Amazonis Planitias and deposited above Tharsis and Arabia Terra.

Finally, the meridional average of the ETRANS vectors is investigated. [Note that the vertical direction has been scaled by a factor of 100 to bring out the vertical flow patterns.] Despite the three distinct patterns of the ETRANS (non-pause wave number 1, non-pause wave number 2, and pause wave number 1), the directionality of the ETRANS vectors

is the same in all periods. Vectors are pointed from west to east at all times. There is a wave number 2 structure in the vertical direction that aligns with topography. Vectors are directed upward upstream of Tharsis and Arabia Terra and are downward downstream. The downward directed vectors around 120° E are the strongest in all non-pause periods, while the downward vectors in Acidalia are strongest in the pause period. Unsurprisingly, the vectors are stronger in the non-pause periods. The similarity in the direction and magnitude of the ETRANS vectors indicates that the vectors are most influenced by the flow and not the strength of the ETRANS term itself.

3.2.2.6 BTEC

The zonal average of BTEC trends negative for all periods (Fig. A.34 left column). All nine periods have negative BTEC above 500 Pa and between 50° and 70° N that extends above 100 Pa and south to 20° N. The areas of negative BTEC during the pause period have a magnitude about twice that of the non-pause periods. The non-pause periods do have some preferred regions of positive BTEC at 180° N and 600 Pa and south of the main area of negative BTEC. This indicates that outside of the main jet (Fig. A.34 left column, contours), BTEC can work to extract energy from the mean flow. However, inside the jet, the waves feed the mean flow, so the westerly jet stream on Mars is eddy-driven as opposed to subtropical (Panetta and Held, 1988; Panetta, 1993; Lee, 1997). The increased magnitude of the BTEC during the pause period also lends credence to the effect of the barotropic governor on the generation of the solstitial pause, which was identified by Mulholland et al. (2016) as a possible contributor. In effect, the pause is so pronounced because BTEC acts as a stronger sink of EKE, while at the same time the baroclinic source is weakened (Fig. A.29).

The topography forces a strong wave number 2 structure in the meridional average of BTEC (Fig. A.34 right column). BTEC is negative downstream and positive upstream

of topography. BTEC extends from 10 to 600 Pa in the non-pause periods, but during the pause, BTEC never reaches below 400 Pa. The zonal wind (Fig. A.34 left column, contours) is largest at the longitudes of high topography as well, which can be partially explained by the contribution of BTEC converting energy from the eddies to the mean flow. In the pause period, there is also stronger positive BTEC at the upper-most levels. This corresponds to the upper-level wave activity that occurs during the pause. These waves are not investigated here due to the lack of vertical resolution in the TES observations assimilated into the MACDA dataset.

3.2.3 Solstitial Pause Waves

To provide further examples of wave activity in the northern hemisphere of Mars, an eddy from the pause period is investigated in detail, and three others are provided as differing examples of the type of EKE generation observed in the pause period.

3.2.3.1 Example 1

We begin by considering a pause period wave from MY 26 during $L_s = 281.6^\circ - 284.2^\circ$ (Fig. A.35). This 6-sol traveling wave begins in Acidalia just before $L_s = 281.6^\circ$ [labeled C in Fig. A.7]. In the first three panels, the wave experiences little or no growth. In the first panel in particular, there is no positive energy conversion and only weak transport. In the second time-step, a GFC dipole (middle column) has grown around 30° N, but there is also negative BCEC (middle column, contours). This continues to be the case for the following time-step. At time-step four, the GFC dipole increases in amplitude, and EKE begins to grow. However, also during this time, BTEC (right column, contours) and BCEC become more negative. ETRANS (right column) experiences little to no activity above the background level noise in the field, though there are scattered areas of negative ETRANS around the location of EKE. The strengthening of GFC and EKE continues in time-step five, while BTEC remains negative. EKE at time-step five develops into a torus, which

happens with some regularity in waves that travel across Utopia. BCEC shows a tri-pole feature in time-steps four and five, where positive values are up and downstream of the EKE maximum, but over the EKE maximum itself, BCEC is negative. The tri-pole feature can also be seen in the GFC, so that the GFC takes the opposite sign than BCEC. In time-step six, GFC, which appears to be the main source of EKE for the wave, experiences a reduction in magnitude, so the EKE decreases as well. The pattern of positive GFC continues decreasing in magnitude more quickly than the pattern of negative GFC in time-steps seven and eight. In time-step nine, the pattern of positive GFC has disappeared, leaving only a sink of energy as the EKE has reduced to almost background levels. This wave provides a case of GFC being both the main source and sink of EKE, with secondary roles played by ETRANS and the energy conversion terms. It is important to note that the GFC providing the main EKE sources and sinks is possible, because the GFC can be a local source/sink of EKE. It is only prohibited from being a global source/sink of EKE.

3.2.3.2 Example 2

A second example of wave activity during the pause period is taken from MY 24 during $L_s = 273.3^\circ - 275.8^\circ$ (Fig. A.36) [labeled D in Fig. A.7]. This wave follows a somewhat similar track to the wave of the first example. It is initiated by GFC just upstream of Arabia Terra in the first time-step. This eddy shows a strong BCEC/GFC tri-pole feature just as the first eddy, but the tri-pole feature is much stronger in this instance. Additionally, the ETRANS term shows clear activity of transport. A difference is that BTEC, while mostly a sink of EKE during this wave, is briefly a source in the second, third, and seventh time-steps. An additional difference is that the GFC remains even through the decay phase of the eddy. It is the two energy conversion terms that serve to remove EKE. These first two example waves serve to demonstrate that while there are transient waves in the pause period, the waves behave quite differently from the pre- and post-pause waves.

3.2.3.3 Example 3

The very slow moving wave in MY 25 shown in Fig. A.7 [labeled E] during the pause period is depicted in Fig. A.37 for the period $L_s = 255.0^\circ - 265.4^\circ$. This long period, isolated wave number 1 eddy circumnavigated the planet in approximately 16 days, which is much longer than the usual, shorter period traveling waves seen elsewhere in the northern hemisphere. BCEC played almost no role in this system, which is unsurprising given that the wave did not extend to the surface nor had a westward tilt with height, indicating that this was not a baroclinic wave but of the type described in Kuroda et al. (2007) and Wang and Toigo (2016) that occurs in the upper-levels during the pause. Instead, the wave grew primarily by BTEC, especially over the longitudes of Tharsis. However, there were extensive areas of negative BTEC at other times. The wave also had strong GFC and ETRANS couplets, but unlike all other wave investigated in the northern hemisphere, the GFC and ETRANS couplets were in phase at all times, which is opposite to what is found in the low-level traveling waves, regardless of the contribution of BTEC or BCEC to their growth. It should be recalled that while TES retrievals were available for the period of this wave, they are reliable only below 40 km (10 Pa). It has been shown that other analysis datasets generated with the help of different models deviate from MACDA above this level (Vaugh et al., 2016).

3.2.3.4 Example 4

A final example of strong EKE is taken from MY 24 during $L_s = 276.1^\circ - 277.0^\circ$ (Fig. A.38) [labeled F in Fig. A.7]. This example serves to demonstrate the source of the weak EKE and residue shown near the equator in Fig. A.26. A short lived, stationary pocket of EKE is generated spontaneously in the absence of positive energy conversion, GFC, or ETRANS. [Note that for this example, the time-step between rows is 0.167 sol or 4 Mars hours.] In the second time-step, just as the EKE begins to grow, there is strong

geopotential flux divergence, which continues for the entirety of the EKE event. ETRANS becomes very strong, but as it describes merely the advection of already generated EKE, it does not explain the source of EKE. The decay of the EKE event can be attributed to negative BCEC and BTEC, as well as to geopotential flux divergence. Over the course of the 90° of areocentric longitude investigated during the three pause seasons, an event of this nature occurred only at one other time, also in MY 24 at the same location but with less intensity. As the event occurs along the equator, the energetics of the same time period in the southern hemisphere was investigated with similarly inconclusive indications for the source of the event (not shown).

3.2.4 Post-Solstitial Pause Waves

The interpretation of the energetics of individual waves continues with a detailed investigation of two waves from the MY 24 post-pause period. [Note that for the post-pause eddy figures, the color scale has changed from the pause eddies.]

3.2.4.1 Example 1

The post-pause wave to be investigated in detail is from MY 24, $L_s = 350.7^\circ - 352.8^\circ$ [labeled G in Fig. A.8]. Figure A.39 shows the terms of the EKE equation at 12 hour intervals for a 4.5 sol time period. The wave evolution shown is a clear example of downstream development in the paradigm of Orlanski and Sheldon (1993).

Beginning at time-step one, there is a broad, weak wave number 1 structure in EKE (left column), with a minor wave number 2 component. These areas are the remnants of a previous wave shearing out over Arabia Terra (not shown). The same wave number structure is found in GFC (middle column) and ETRANS (right column). There is positive ETRANS north of Arabia Terra and negative ETRANS north of Tharsis, and the opposite is true for the GFC term, though there are several other minor areas of nonzero GFC as well. There is essentially no BCEC (middle column, contours) and only a small area of

positive BTEC (right column, contours) north of Arabia Terra associated with the remnant wave. The first indication of the initial eddy is visible in the EKE field at 30° E and 60° N. In the second time-step, this area of enhanced EKE has grown and strengthened along with two areas of BCEC that straddle the EKE center. The GFC, ETRANS, and BTEC fields have propagated eastward but have maintained their spatial extent. In the third time-step, the initial EKE center continues to strengthen with increased BCEC and small areas of negative BTEC. An area of EKE downstream of the initial area has developed from the remnant EKE. The ETRANS and GFC fields have split into multiple areas as a result of the new EKE center. The GFC now has two dipoles, one for each EKE center. This continues in the fourth time-step, where both waves strengthen along with the GFC dipoles. In the fifth time-step, the strengthening of the upstream EKE center ceases, while the downstream EKE center continues to grow. The downstream GFC dipole propagates ahead of the two EKE centers and weakens, but the downstream ETRANS dipole strengthens. BCEC consolidates into two areas, one for each wave. There are areas of smaller scale BTEC scattered throughout the domain. At time-step six, EKE is being passed from the upstream wave to the downstream development. The downstream EKE center weakens, while the upstream strengthens. The upstream GFC dipole has markedly increased in magnitude and shifted relative to the EKE centers so that the convergent area is collocated with the downstream EKE, and the divergent area is collocated with the upstream area. BCEC is stronger over the upstream area, but that source of EKE is immediately transported downstream. Also in the sixth time-step, BTEC has developed a dipole, with the negative values encompassing a larger area. The ETRANS dipole is strongest at the downstream EKE center. These processes continue through time-step seven. In time-step eight, the barotropic decay continues and baroclinic conversion ceases, while GFC and ETRANS continue to propagate the weakening EKE over Tharsis. In the final time-step, BCEC has stopped completely, and negative BTEC is collocated with the remaining areas of EKE.

Additionally, a new GFC dipole and EKE center have developed over Arabia Terra.

The meridional averages for the same wave are shown in Fig. A.40. Several features are worth noting. Both waves have EKE (left column) with westerly tilts that extends to 100 Pa, just as all other pre- or post-pause waves in the northern hemisphere. The upstream wave appears to be more surface based as it has a local maximum of EKE adjacent to the surface. The downstream wave has no such feature and has all of its energy located above 500 Pa. The surface-based nature of the upstream wave is further indicated by BCEC (right column, contours). The upstream wave has BCEC closer to the surface and in the first few time-steps has a negative region of BCEC aloft, while the downstream wave only has positive BCEC values above 500 Pa. The shift of GFC (right column) noted in the zonal averages at step six is more transparent in Fig. A.40. In the first five time-steps, GFC couplets straddle BCEC, so the highest BCEC falls between adjacent areas of positive and negative GFC. However, in time-step six, the GFC shifts slightly downstream so that the positive (negative) area is collocated with the downstream (upstream) EKE center. Finally, the higher wave number activity in BTEC in the vertical average is shown to be contained around and above 100 Pa for all locations not associated with an EKE center. It is only when eddies interact with the mean flow that BTEC (left column, contours) extends below 300 Pa. The BTEC activity above 100 Pa is associated with non-baroclinic waves (Kavulich et al., 2013; Lewis et al., 2016).

3.2.4.2 Example 2

A final northern hemisphere example is from MY 24, $L_s = 336.1^\circ - 338.7^\circ$ (Fig. A.41) [labeled H in Fig. A.8]. Most waves during the pre- or post-pause periods behave as in Example 1 or as in the non-GDS eddy detailed in Section 3.1.3.1. The following example shows an exception to this typical growth and decay of waves on Mars and Earth. The wave starts as most do, by initiation via GFC downstream of Arabia Terra that is the

result of downstream development from a wavetrain undergoing BTEC around Tharsis. BCEC immediately starts in the following step; however, an area of negative BCEC is also initiated. The EKE, GFC, and BCEC couplet continue strengthening through time-step four. In time-step five, the wave attains its maximum EKE, but the BCEC couplet has weakened. BTEC serves as an additional source of EKE to reinforce the wave, which continues through time-step seven, even though the BCEC that provided the initial growth mechanism has ceased. In the final two time-steps, BTEC switches sign and becomes the final sink of EKE. Furthermore, in the final three time-steps, the next wave is seen to undergo the same processes. These two waves are a minority of cases during the pre- and post-pause periods where BCEC is reinforced by BTEC. It should be noted that this is similar to but not completely comparable to the behavior of waves during the GDS in the MY 25 pre-pause period. The waves during the GDS (e.g., Fig. A.23) experience positive BTEC immediately from initiation and only become baroclinic at the end of the lifecycle. The reverse occurs for these waves.

3.2.5 Inter-Annual Variability

The pressure-weighted, integrated intensities between 57.5° and 82.5° N for the entirety of the transient wave period in the martian northern hemisphere are shown in Fig. A.42. The period $L_s = 170^\circ$ to 390° of the following year is shown for MY 24 (blue), 25 (red), and 26 (green). The periods when TES observations were unavailable for assimilation and the model was free-running are indicated by thin lines. The solstitial pause is noticeable in all EKE terms except the BTEC. EKE activity quickly ramps up after $L_s = 180^\circ$ in all three years. As discussed in Section 3.1, MY 25 has reduced EKE during the pre-pause period compared to MY 24 and 26 but still has higher values of EKE than during the pause period of any year. The peak of the pre-pause EKE is around $L_s = 205^\circ$ in MY 24 and 26 and is earlier in MY 25. Activity decreases after $L_s = 220^\circ$ and reaches

a nearly constant lower level around $L_s = 240^\circ$. With some exceptions for individual waves during the pause period, no activity occurs above the lower background level, and no waves approach the magnitude of EKE during the pre- or post-pause periods. EKE activity remains low until $L_s = 310^\circ$, when values quickly increase for MY 24 and 25. MY 26 experiences increasing wave activity similarly to MY 24 and 25, which is briefly interrupted between $L_s = 320^\circ$ and $L_s = 330^\circ$. This decrease in activity just as the post-pause period begins is the result of a large regional dust storm (Wang and Richardson, 2015) that increases opacity enough to alter the vertical temperature in a similar way to the GDS of MY 25. Being only a regional storm, opacity decreases quickly, so the MY 26 post-pause wave activity resumes quickly. Wave activity remains high in all three years until after $L_s = 360^\circ$, when values again decrease until $L_s = 390^\circ$. EKE returns to the pause levels after this time. The post-pause period of EKE is shifted slightly closer in time to the actual time of the winter solstice ($L_s = 270^\circ$) than the pre-pause period. This could be due to the very short radiative timescales of the Mars atmosphere.

The solstitial pause is evident in the two transport terms. Outside of the pause period, ETRANS and GFC experience irregular fluctuations that have a somewhat smaller amplitude than the signals in the energy conversion terms. In the pre- and post-pause, the GFC term has larger, instantaneous peaks than ETRANS, and GFC is also slightly larger during the pause as well. The pause period occurs at roughly the same time in EKE, ETRANS, and GFC, and the pre-pause period starts, and the post-pause period ends at the same time for the three terms.

The magnitude of BCEC is the most positive of the four right-hand-side terms of the EKE equation. It also shows the signal of the solstitial pause more strongly than EKE. BCEC increases concurrently with, or shortly after, the increase in EKE during the pre-pause period and maintains large values until the end of the pre-pause period. BCEC in MY 25 is reduced more than the EKE due to the suppression of baroclinic instability by

the large optical depths in the MY 25 GDS. During the solstitial pause, BCEC has some minor peaks of intensity, but on average, it falls below zero with some larger dips. This is a result of the BCEC dipoles shown in Section 3.2.4. BCEC returns to positive values and larger peaks somewhat earlier than EKE after the pause period and continues to have larger positive values until $L_s = 370^\circ$. The exception to this behavior is MY 26, in which BCEC ramps up at the same time as in MY 24 and 25, but then it abruptly decreases to pause levels during the $L_s = 325^\circ - 335^\circ$ period. This time corresponds to a period of reduced EKE and is the reason for the post-pause pressure-weighted averages being smaller for MY 26 (Fig. A.27).

BTEC shows the weakest signs of the solstitial pause. In MY 24 and 26, it shows a slight decrease in magnitude during the pause, and in MY 25, it shows almost no indication of a reduction. Values throughout the entirety of the transient wave period tend towards the negative, with brief events of positive values during the pre- and post-pause periods. The removal of EKE by BTEC at all times could be a contributor to the solstitial pause phenomena itself. The strongest negative BTEC events line up with the strongest BCEC and EKE events. The intensity plot demonstrates that the contribution of BTEC to EKE is occasionally positive as some positive values align with positive EKE events, including EKE events that lack concurrent BCEC.

3.2.6 Spectral Analysis

We conclude the analysis of the energetics of the northern hemisphere by spectrally decomposing the transient waves into their constituent wave numbers.

3.2.6.1 Pre-Solstitial Pause

As has been discussed previously, wave numbers 1 and 2 are the strongest transient modes in the northern hemisphere. The energetics analysis bares that out as a whole. The EKE equation terms decomposed by wave number for the yearly averaged pre-pause

period are shown in Fig. A.43. The strongest EKE is found in wave number 2, which is closely followed by wave number 1. [Note the colorbar scales have changed from previous pressure-averaged figures.] Several features are worth noting. EKE for wave number 1 is closest to the pole, and EKE for wave number 3 is closest to the equator, at around 65° N. [This is due to a reduction in the actual wavelength of the wave and in the β -effect (Hartmann, 1979; Barnes, 1984), which pushes the neutral curve for the Charney-type baroclinic instability to smaller zonal wavenumbers.] Despite the slightly differing latitudes of EKE for each wave number, BCEC is confined to the same band for all wave numbers. Also, BCEC is stronger for wave number 3 than wave number 1, even though the EKE is much weaker for wave number 3 than wave number 1. For the wave number 1 waves, a wave number 2 pattern is embedded in the BTEC field. This feature arises as the wave number 1 wave at each time-step is averaged over many time-steps for the pre-pause period, so as the wave number 1 propagates eastward, the BTEC magnitude is increased when the wave interacts with topography. This means that wave number 1 waves transfer energy to the mean flow when interacting with the wave number 2 topography. The residue, on average, is negative for wave numbers 2 and greater and positive for wave number 1. This suggests that higher wave number components are the most affected by friction and dissipation.

3.2.6.2 Solstitial Pause

During the pause period, wave number 1 is the dominant wave number (Fig. A.44). This is mostly due to the MY 25 wave number 1 feature that was identified in previously. Again, for the wave number 1 waves, there exists a wave number 2 pattern to the resulting BTEC. We attribute this to forcing from the wave number 2 topography that causes wave number 1 waves to lose energy upon passing the wave number 2 topography. The weakest of all EKE terms at all wave numbers is the BCEC, but there are some positive areas for

wave numbers 1 and 3, while there are none for wave numbers 2 and 4. Wave number 3 and especially wave number 4 are comparatively much weaker during the pause period than wave numbers 1 and 2.

3.2.6.3 Post-Solstitial Pause

The post-pause energetics is again strongest in wave number 2 (Fig. A.45), with wave number 1 slightly weaker. GFC is the strongest for wave number 1, with the other terms being much smaller. BCEC in wave number 1 is almost nonexistent, with even wave number 4 having stronger BCEC. This suggests that much of the eddy energy at wave number 1 is the result of energy cascading from higher wave numbers (Imamura and Kobayashi, 2009). The wave number 2 components are the strongest for GFC, ETRANS, and BTEC. Wave number 3 is much stronger post-pause than any other period and has the strongest BCEC of any time. Additionally, EKE and BCEC have a sizable contribution from wave number 4 components.

3.2.6.4 Intensities

The summed intensities of the EKE terms for each wave number are shown in Figs. A.46 (wave number 1), A.47 (wave number 2), A.48 (wave number 3), and A.49 (wave number 4). The wave number 1 intensities do not exhibit a clear pause signal in EKE or the energy conversion terms. There is a brief period of low EKE around $L_s = 325^\circ$, but at other times, the wave number 1 EKE component is comparable to that in the pre- and post-pause seasons. Given the result of Mulholland et al. (2016) that the solstitial pause is partly the result of increased opacity due to dust and cloud cover, this contradicts the finding of Barnes et al. (1993) that established that wave numbers increase during higher opacity conditions. Instead, the nearly uniform energetics for wave number 1 could possibly result from the strengthening of upper-level waves (Wang and Toigo, 2016).

The pause signal is evident in all terms at wave number 2. EKE and BCEC are

strongest at wave number 2, but the BTEC is strongest at wave number 1. The pause signal in the energetics is the most pronounced at wave number 3, so the majority of the solstitial pause originates in the energetics through a reduction of the intensity of the wave number 3 traveling waves. This result was not evident in previous studies, including Mooring and Wilson (2015) that did not find an appreciable difference in activity between the non-pause and pause times at wave number 3 in the eddy temperature or eddy meridional velocity fields. Mooring and Wilson (2015) instead found wave number 2 to be the most affected by the pause. EKE during the post-pause period is strongest at wave number 3; however, because EKE is stronger over the entire transient wave period at wave number 1 and is stronger, on average, at wave number 2 in the pre-pause period, the total EKE at wave number 3 is not as intense. There is a strong solstitial pause signal at wave number 4. In general, EKE enters the waves via BCEC at all wave numbers but only exits the eddies via BTEC at wave numbers 1 and 2.

4. SOUTHERN HEMISPHERE WAVE ENERGETICS

Each of the four periods investigated here cover four different regimes of transient eddy activity in the southern hemisphere. The pre-winter and post-winter periods contain the largest eddy amplitudes, with the winter and summer periods much lower. Three pre-pause, two pause, and two post-pause periods are considered. The post-pause MY 25 period is neglected due to the long period where observations were not retrieved and due to the altered energetics of the GDS.

4.1 Integrated EKE Terms

4.1.1 Pre-Winter Solstice

The EKE equation terms for the pre-winter solstice season are shown in Fig. A.50. Some inter-annual variability is present, but EKE is contained throughout the southern hemisphere highlands in the upper and midlatitudes and is present closer to the equator over Tharsis. A track of EKE exists from about 40° S, 120° E to the southeast to 70° S, 270° E. The poleward side of Hellas is also a preferred area of EKE, but the equatorward side of the basin is devoid of EKE. Argyre Planitia is also generally lacking in EKE. In MY 25, EKE in Hellas Planitia is strong enough so that there is a continuous band of EKE around the hemisphere as is present in the northern hemisphere pre-solstice period (Battalio et al., 2016), but this continuous band does not exist in MY 26 and 27. The activity in MY 25 in Hellas Planitia has been noted previously as a precursor to the GDS later that Mars year (Strausberg, 2005).

BCEC (Fig. A.50 second row) shows less inter-annual variability compared to the EKE. The main area of BCEC exists in a crescent-shaped feature to the south of Tharsis and is strongest from 150° to 300° E, just upstream of Argyre. There exists a second, smaller area of BCEC between the Hellas and Argyre Planitias. Inside or downstream of

both basins exist areas of negative BCEC. These regions are contained between 40° and 70° S, which is slightly more equatorward than the BCEC during the pre-solstice period of the northern (Battalio et al., 2016).

GFC (Fig. A.50 third row) is the strongest in MY 25, with the strongest GFC around the southern pole. In all years, there is GFC upstream of Tharsis and on the eastern flank of Hellas Planitia, with geopotential flux divergence on the western flank of the basin. The AGF vectors are also shown. The strong GFC near the south pole in MY 25 is connected to anomalous AGF vectors compared to MY 26 and MY 27. Between 120° and 180° E, AGF vectors are away from the pole and converge south of 70° S, but in MY 26 and 27, vectors are more zonal near the pole, with some circulation around the southern side of Tharsis and into Argyre. In all three years, there is convergence of fluxes from the south to north, west of Argyre, and convergence over Tharsis itself is associated with northwesterly vectors. The dipole in Hellas Planitia is due to strong divergence directed toward the convergence on the eastern side.

ETRANS (Fig. A.50 fourth row) is weaker than the GFC term. The strongest areas of ETRANS are in Hellas Planitia, with a positive area on the eastern side and a negative area on the western side. The ETRANS flux ($\mathbf{v}K_e$) is mostly zonal and strongest between 40° and 70° S. Terrain again plays a role in modifying the flux from being strictly zonal. The ETRANS flux dips southward and accelerates around Tharsis, and more importantly, EKE is removed from the southwestern side of Hellas, accelerated through the basin, then deposited on the southeastern side.

BTEC shows less inter-annual variability compared to the GFC or ETRANS terms, but like the GFC and ETRANS terms, BTEC (Fig. A.50 fifth row) has a negative region on the western side and a positive region on the southeastern side of Hellas Planitia. There is also a second negative region on the northeast side of Hellas. A weak positive area of BTEC exists between Hellas and Tharsis from 150° to 240° E, but there is a negative

region along and poleward of Tharsis itself. The areas of negative BTEC associated with topography indicate a result similar to the pattern found in the northern hemisphere – that eddies traveling around topography lose energy to the mean flow.

The residue term (Fig. A.50 bottom row) shows great variability near the south pole but less inter-annual variability in the midlatitudes. There are positive regions of the residue on the western and northeastern flanks of Hellas, and negative regions on the southeast side of Hellas and throughout flat highlands of Daedalia (150° to 300° E). The residue is positive near 20° S in each year. In MY 25 at the pole, the residue is negative between 120° to 300° E and positive elsewhere. The residue is weaker in magnitude near the pole in MY 26 and 27. The broad swaths of negative residue indicate that dissipation and friction are key sinks of EKE.

4.1.2 Solstices

The EKE equation terms are the weakest during the solstice periods. The EKE during the winter solstice (Fig. A.51 left and middle columns, top row) is confined to Tharsis and near the equator, while during the summer solstice (Fig. A.51 right column, top row), there exists a band of EKE south of 60° S, between 150° and 360° E as well as over Tharsis. The qualitative shape of the EKE field in the summer average is more the like the fall and spring than winter; however, the magnitude is far less.

BCEC (Fig. A.51 second row) has a weak positive area along the southern edge of Tharsis in winter and a positive area over Tharsis in summer. In winter, Hellas Planitia has prevalent negative BCEC. BTEC (Fig. A.51 fifth row) is negative throughout the southern hemisphere in winter and is negligible in the midlatitudes in summer.

Inter-annual variability dominates GFC and ETRANS. There are no specific areas of GFC or ETRANS common to all three years, as would be expected for periods when the energetics is weak (Chang, 2001). In the summer average and both winter years, any given

midlatitude zonal band alternates between positive and negative areas chaotically. GFC is larger in magnitude than the ETRANS term for all three periods. The AGF fluxes in the pause period are similar to those in the pre-pause period but are weaker. The AGF fluxes during the summer solstice are quite different. They are constrained to near the pole and are directed from east to west across all longitudes. The pause period ETRANS fluxes are also similar to the pre-pause fluxes, but the summer fluxes are outside of the midlatitudes, close to and directed towards the equator or near the pole.

The residue term is the largest in magnitude of the five EKE equation terms during the solstices and is mostly positive in winter midlatitudes and is negative in summer midlatitudes. In winter, the residue is largest along the southern rim of Hellas Planitia and on the southeastern tip of Tharsis. The large areas of positive residue indicate that some process not captured by the EKE equation is a source for some of the energy of the winter waves. The most likely source is diabatic effects (Chang, 2001), as friction or dissipation cannot be sources of EKE. The MACDA reanalysis does not include data to estimate either dissipation or diabatic processes.

4.1.3 Post-Winter Solstice

The EKE equation terms during the post-winter solstice period are shown in Fig. A.52. There is great variability between the three years, noting that the MY 24 average begins at $L_s = 153.7^\circ$, and that MY 25 contains roughly 10 degrees of areocentric longitude where the model ran freely, as well as the GDS. EKE in the post-solstice period is highest in the same areas as the pre-solstice period, but the EKE in the $50^\circ - 70^\circ$ S latitude band is the strongest. In MY 24 and 26, the highest EKE is just south of Tharsis and upwind of Agyre, abruptly stopping at the edge of the basin. There is also EKE directly upstream of Hellas Planitia in both years, while MY 26 only has EKE over Tharsis. For none of the three times shown is there a track of EKE from near the equator to the southeast as in the

pre-solstice period.

BCEC during the post-solstice period (Fig. A.52 second row) is similar to the pre-solstice period, with a maximum aligned with the EKE maximum south of Tharsis and a second area upstream of Hellas. BTEC (Fig. A.52 fifth row) is much weaker than BCEC, is the weakest of all the terms, and like the pre-solstice period, is at its most negative south of Tharsis in the same region that BCEC is strongest.

GFC (Fig. A.52 third row) is strongest in Hellas Planitia, with divergence on the western side and convergence on the eastern side. A weak area of geopotential flux divergence resides at the southern tip of Tharsis, with GFC on the eastern side of Argye in MY 24. ETRANS (Fig. A.52 second row) is spatially similar to but weaker than the GFC term. The AGF vectors consist of mostly a broad area of counterclockwise circulation trapped between Hellas to the west and Tharsis and Argyre to the east. The strongest area of the circulation is the eastern side. The ETRANS flux vectors are still zonal as in the other two periods and are pushed closer to the pole due to the jet stream migration closer to the pole and a tightened polar vortex (Waugh et al., 2016).

The residue term is the strongest sink of EKE on average, with broadly negative areas in both MY 24 and 26 south and east of Tharsis and in the Argyre and Hellas Planitias. This indicates that friction and dissipation are the largest sinks of EKE in the southern hemisphere post-solstice period. The residue is weakly positive near the equator and at the southern pole, with small scattered regions in the midlatitudes between 120° and 200° E.

4.2 Zonal and Meridional Averages

4.2.1 EKE

EKE is contoured for each of the seven periods in Fig. A.53, with the zonal average at left and the meridional average at right. The EKE during the pre-pause period for MY 25, 26, and 27 (top three rows) is of intermediate intensity. There is uniform EKE at the upper-

levels throughout the midlatitudes, with values up to 100 J/kg at 10 Pa. Only weak EKE is found below 200 Pa, with a magnitude of no more than 25 J/kg, but there are indications of a protrusion of EKE at 60° S where the 25 J/kg contour dips below 200 Pa. The EKE during the pause periods of MY 25 and 26 (rows four and five, respectively) is the weakest, with the 10 J/kg contour never dropping below 250 Pa. The EKE increases monotonically with height at all longitudes and latitudes. The post-pause period (bottom two rows) has the strongest EKE average, with values of 10 J/kg extending to the surface and a tongue of 50 J/kg protruding to 200 Pa at 60° S. The zonal maximum of EKE poleward of 60° S lines up with the area of the westerly jet maximum. The post-pause time has stronger EKE than the pre-pause period.

4.2.2 BCEC

BCEC is shown in the colored contours in Fig. A.53, with the zonal average (left) and meridional average (right) for each of the seven periods. BCEC is a strong source of EKE in the pre- and post-pause periods. Like the EKE, BCEC is strongest in the post-pause period, followed by the pre-pause period, with the pause period showing the least BCEC. Positive BCEC is found in the pre- and post-pause periods in an area between 30° and 75° S. BCEC during the post-pause period is positive between 400 and 50 Pa but is shallower and much weaker in the pre-pause period with values between 450 and 250 Pa. This leads to the BCEC maxima being roughly the same height above the ground, as the surface pressure is less during the post-pause period. For all times, there is negative BCEC directly aloft of the positive BCEC, with the negative BCEC being the largest magnitude in the pre-pause period. There are only weak indications of BCEC in the area 40° – 60° S and 400 – 200 Pa during the pause period, above which exists an area of negative BCEC extending towards the pole.

Meridionally, there are two preferred regions of positive BCEC in each of the seven

periods. The larger and stronger area lies between 120° E, 300° E, 400 Pa, and 100 Pa. The weaker area is just east of Hellas Planitia between 20° and 60° E. These two areas are nearly continuous during the post-pause period. During the pause period, there is a strong area of negative BCEC near 100 Pa above Hellas, and in non-pause times, this area of negative BCEC is smaller and weaker. There is great inter-annual variability in the three seasons. During the pre-pause period, the strongest BCEC is found in MY 27, and the strongest BCEC during the post-pause period occurs in MY 24.

4.2.3 Heat Fluxes

As the primary source of energy for the eddies is baroclinic instability, the strength of the averaged heat fluxes for each of the seven study periods is now considered. The zonally averaged heat fluxes are shown in Fig. A.54. The zonally averaged fluxes are strongest during the post-pause period and weakest during the pause period. Where there are strong heat fluxes, they are aligned with the strongest BCEC. The strongest vertical heat flux (Fig. A.54, left column) is beneath and poleward of the strongest vertical motion (left column, contours), and there is no area of strong ascent except along the terrain near the pole. In each period, there is an area of strong descent associated with the descending branch of the Hadley circulation. In no period, though, are the vertical heat fluxes negative. The zonally averaged meridional heat flux, however, is negative above 100 Pa in each of the pre-pause, pause, and the MY 26 post-pause period. This suggests that the negative BCEC at those levels is caused by the transport of heat away from the pole.

The meridionally averaged heat fluxes are shown in Fig. A.55, with the average vertical motion contoured at left and the average meridional wind contoured at right. All meridionally averaged heat fluxes are positive in all periods between Hellas and Argyre. Following Mooring and Wilson (2015), the meridional heat fluxes are strongest in the post-pause period. The negative area in the vertical flux on the eastern side of Hellas appears

to be the main contributor to the negative BCEC in that area, as the pattern is not echoed in the meridional heat fluxes, but the negative meridional heat flux is the contributor to the negative BCEC above 100 Pa in all periods except the post-pause in MY 24. While there are strong meridional heat fluxes in the Hellas and Argyre Planitias, there are no vertical heat fluxes in either basin, suggesting that heat is not transported out of nor in to the largest basins.

4.2.4 BTEC

BTEC is usually found to be a sink of EKE in both the northern hemisphere of Mars (Kavulich et al., 2013; Wang and Toigo, 2016; Battalio et al., 2016) and terrestrially (e.g. Orlanski and Sheldon, 1995; Decker and Martin, 2005). The same is found during most periods in the southern hemisphere (Fig. A.56). During the pre-pause period, there is a strong, negative area of BTEC near 10 Pa between 20° and 50° S. This corresponds to the time of the most equatorward extent of the highest jet winds (Fig. A.56 contours), suggesting that BTEC is giving energy to the mean flow. During the pause, this area is further south, between 40° and 60° S, and the fastest winds are confined closer to the pole at this time. The area of negative BTEC in the post-pause period is much weaker and smaller post-pause. During the post-pause period, the strongest feature of BTEC is a positive region from 10 to 200 Pa and around 55° S. There are also weaker positive areas in this region during two of the pre-pause periods (MY 25 and 27). In all seven periods, there is a weak area of negative BTEC – strongest in the pause period – close to pole between 10 and 200 Pa.

The meridional distribution of BTEC is fairly uniform across all seven periods. In all years, a barotropic sink of EKE occurs upstream of Argyre Planitia above 400 Pa; this feature is strongest in the post-pause period. BTEC is also a sink of EKE just upstream of Hellas Planitia in all years but is strongest at the surface in the post-pause period and

strongest aloft in the pre-pause and pause periods. BTEC is a source of EKE in the region between the two deep basins and above 300 Pa in the pre- and post-pause periods; BTEC remains a sink of EKE throughout that area in the pause period. The strongest barotropic source region lies above the eastern flank of Hellas Planitia in the pre- and post-pause periods. These results suggest that interactions with a column undergoing convergence or divergence cause energy to leave the eddies during all periods, but a vertical column unaffected by large terrain changes will pull energy out of the flow in the pre- or post-pause periods.

4.2.5 GFC

GFC is moderately stronger in magnitude than the two energy conversion terms (Fig. A.57), which is similar to northern hemisphere (Battalio et al., 2016). As with BCEC and BTEC, GFC during the two post-pause periods is the strongest in magnitude. However, the vertical arrangement of GFC is the same in the pre- and post-pause periods. Near the surface and south of 60° S, there is a shallow layer of positive GFC. Above that and between 300 and 150 Pa, there is a layer of geopotential flux divergence that extends both towards the pole and towards the equator, reaching to 50° S. Immediately above that is another layer of GFC extending up to 10 Pa. In the post-solstice periods, the upper-level GFC extends from 40° to 80° S but is not as zonally broad in the pre-pause periods. Additionally, there are indications of a second area of geopotential flux divergence higher in the atmosphere in the pre-pause period. In the pause period, the layers of alternating GFC are lifted upwards, and the top-most GFC below 10 Pa is missing. Closer to the equator, there are areas of positive GFC near the surface in the pre-pause period, a near-surface area of divergence in the pause period, and only very weak activity near the equator in the post-pause period. Within each season, there is strong uniformity in the GFC from year to year. Important to note is that the strongest BCEC (Fig. A.53) is collocated with

the areas of geopotential flux divergence, and the areas of negative BCEC correspond to GFC.

In the meridional average, there is GFC near the surface on the eastern side of Hellas Planitia and just upstream of Argyre Planitia in all seven periods. Both of these regions have AGF flux vectors that are directed towards the surface, with the strongest fluxes in the pause periods. [Note: to indicate vertical direction of the fluxes, the vertical component of the vectors has been multiplied by 10^4 .] Also, there is strong geopotential flux divergence in all seven periods along the surface in the highlands between the two large impact basins, and in these areas, the AGF vectors are directed upwards into the top layer of positive GFC. This layer of negative GFC extends over the regions of positive GFC in the basins during the post-pause period, but pre-pause, the positive areas above the basins extend into the mid-levels. The strong positive and negative GFC bands exist across nearly all longitudes and through all depths in the post-pause period, are weaker but still layered during the pre-pause period, and are limited near the surface in the pause period. In the pause period, the strongest magnitude GFC is closest to 10 Pa.

4.2.6 ETARANS

ETRANS is generally the weaker of the two transport terms. For the pre-pause and pause periods, the zonal mean of the ETRANS term is very small except above 100 Pa (Fig. A.58 left column). Positive transport is indicated north of 40° S in the pre-pause periods and further north during the pause. During the post-pause periods, ETRANS has a couplet between 10 and 400 Pa, with negative advection at 70° S and positive advection at 55° S, meaning that in the meridional direction this term serves to move EKE equatorward and out of the main westerly jet, like in the northern hemisphere.

The small magnitude of the zonal mean is due to the near cancelation of terms in each zonal band, as the meridional mean shows vertical alignment of positive and negative ar-

eas, unlike the GFC term, which has vertical layering. In the pre-pause and pause periods, there is a wave number 2 pattern to the ETRANS. The strongest negative area extends from the surface to 10 Pa on the westward side of Hellas, with a weaker area between 120° and 240° E. The strongest positive ETRANS is on the eastern side of Hellas and above Argyre. The post-pause period follows the same general pattern of the pre-pause and pause periods, but the negative area on the eastern side of Hellas is accompanied by an adjacent positive area. The ETRANS fluxes are highly influenced by terrain, and the flux directions show a general wave number 1 pattern, with a weaker wave number 2. [Again, the vertical component of the vectors has been multiplied by 10^4 .] There is strong descending motion on the leeward side of Tharsis and into Hellas from the west. There are ascending fluxes east of Hellas and into the western side of Tharsis. The strongest fluxes are found in the pre-pause season, with the post-pause season having relatively weaker fluxes. There is a wave number 2 structure to the sign of ETRANS but a wave number 1 pattern in the direction of the ETRANS fluxes because of acceleration in the vertical direction of the winds. For example, the vertical fluxes in the mid-levels at 240° E become larger with height, and so there is negative ETRANS. But to the west, the vertical fluxes are high in the mid-levels but weaker above, so ETRANS is positive in that area.

4.3 Seasonal Variability

Only the mean values of the EKE equation for the southern hemisphere have been discussed up to this point. Typical eddies from the pre-pause, pause, and post-pause periods are compared to contrast intensity and evolution.

4.3.1 A Pre-Solstitial Pause Wave

The pre-pause wave is taken from MY 27 during $L_s = 47.90^\circ - 49.94^\circ$, with the EKE equation terms shown in Fig. A.59. The time-step between rows is 0.5 sol, with time increasing downward. The evolution of this wave is very similar across multiple

waves during the pre-pause period as shown in a Hovmöller diagram of v' (Fig. A.60) [The present wave is labeled I.]. The wave initiates around 160° E from GFC (middle column). At time-step two, a weak area of BCEC (middle column, contours) has arisen along with the consolidation of EKE (left column) into a focused area at 180° E and 50° S. The couplet of GFC has grown in magnitude and area, and a couplet of stronger ETRANS (right column) has also developed. During the third time-step, there is a lull in all terms, and an area of EKE separates away from the main area much closer to the equator, along with the strengthening of a weak region of positive BTEC (right column, contours), which is the singular abnormal behavior of this wave compared to others in the pre-pause period. The fourth time-step shows the strongest BCEC and positive BTEC, as the primary EKE center finally begins to develop at 50° S. The positive BTEC propagates to the east with the piece of EKE, onto the Tharsis Plateau. Another feature at this time is the negative BCEC on the western flank of Hellas, which occurs as a result of the eastward wind flowing downwards into the basin. In the fifth time-step, GFC has restrengthened concurrent with the dissipation of the barotropically generated EKE near Tharsis. The eastward propagation, baroclinic growth, and transport through GFC continue in time-steps six, seven, and eight. In time-steps seven and eight, BTEC becomes a sink of energy along with the redevelopment of the ETRANS couplet around 240° E. By time-step nine, BCEC has substantially weakened, and the wave is dissipating. In time-step ten, BCEC has ceased completely, and the ETRANS and GFC couplets have weakened to a background level. However, the beginnings of the next eddy are evident at 180° E, along with a small region of BCEC.

In the meridional direction, the pre-pause eddy is easily identifiable by the extension of EKE down towards the surface, while other activity remains confined to the upper-levels (Fig. A.61). The wave shows the classic westerly tilt of a baroclinic wave throughout its life cycle and slowly propagates across the relatively uniform topography between Hellas

and Argyre. GFC (Fig. A.61 right column) is also tilted and exhibits the strong couplet behavior near the surface and does not extend aloft; though away from the main eddy, there are pockets of GFC aloft. BCEC (Fig. A.61 right column, contours) extends to the surface and has a westerly tilt like the EKE. For all times, the positive BCEC lines up with the negative GFC, which can be qualitatively explained by the horizontal divergence forcing air to ascend, following both Kavulich et al. (2013) and Battalio et al. (2016). BCEC that was shown near Hellas in Fig. A.59 corresponds to areas above 100 Pa, so the only BCEC associated with the main wave is near Tharsis. BTEC (Fig. A.61 left column, contours) remains confined above 100 Pa except in time-steps seven and eight where a negative area drops down to 250 Pa, serving to initiate the decay stage of the wave.

4.3.2 A Post-Solstitial Pause Wave

The post-pause wave evolves during $L_s = 166.31^\circ - 168.82^\circ$ in MY 24 (Fig. A.62) [labeled J in Fig. A.60]. This particular wave is an example of strong baroclinic downstream development and was one of the stronger MY 24 waves. In the initial time, there are several EKE packets in the highland plains, but the strongest is just to the east of Argyre (Fig. A.62 left column). What becomes the main EKE packet is located to the west of Hellas. Each of these packets is associated with couplets of both GFC (Fig. A.62 middle column) and ETRANS (Fig. A.62 right column); however, the energy conversion terms are both weak. In the second and third time-steps, EKE has consolidated into one packet in the highlands, and the stronger packet approaches Hellas. Energy conversion remains weak, and the transport terms have focused into two sets of couplets around the EKE packets. At time-step four, downstream baroclinic development begins as the GFC, and to a lesser extent the ETRANS, transport energy from the western to the eastern sides of Hellas. A nascent center of EKE begins growing around 90° E, with a small area of BCEC (middle column, contours). Time-step five shows the EKE center continuing to grow and

propagate eastward. BCEC has started to grow quickly and is collocated with the strongest area of negative GFC, while downstream a new couplet of GFC has developed. This new couplet initiates a new downstream development in time-step six, which shows two main BCEC areas, with a third still around Hellas. Additionally in time-step six, ETRANS has taken on a higher wave number pattern, and BTEC (right column, contours) begins acting as a sink of energy. All four EKE equation terms and the EKE itself all strengthen in time-step seven, with the wave furthest downstream taking over with very high BCEC and also higher BTEC. As the waves approach Argyre and the southern extent of Tharsis in time-step eight, the upstream wave begins to weaken along with the BCEC and transport terms, but the downstream eddy continues to have strong BCEC. As the downstream eddy crosses Argyre, it, too, drops in intensity, with a reduction in BCEC, and by the final time-step, both eddies have dissipated, along with the energy conversion and ETRANS. In time-step nine, a new eddy begins in the same area as before with GFC on the eastern side of Hellas, which continues propagating eastward in the final time-step, though no BCEC has yet been triggered.

The baroclinic downstream development is made more transparent looking in the meridional direction (Fig. A.63). The first eddy is initiated to the west of Hellas and is transported across the basin, though interestingly never extends into the basin and appears to shrink in vertical extent during transit. Upon reaching the eastern side, BCEC (right column, contours) begins and continues through time-steps four and five, and simultaneously, the tilt of the associated EKE (left column) increases. During the strong BCEC in the western eddy, concurrent geopotential flux divergence (right column) transports energy downstream to a region of GFC, where second and third waves are initiated in timestep five and strengthen through time-step eight. A second region of BCEC is initiated, which is partially transported downstream to the third wave that lacks positive BCEC. The absence of any BTEC in the western eddy (left column, contours) indicates that the removal

of energy by GFC causes its demise, which is similar to the wave packet composites of Chang (2001). The subsequent wave does show strong negative BTEC in time-steps six through eight.

4.3.3 A Solstitial Pause Wave

Finally, in contrast to the two coherent and vigorous waves in the pre- and post-pause periods, one of the stronger waves from the pause period is shown from MY 25, $L_s = 96.83^\circ - 98.90^\circ$, which is representative of how waves interact with Tharsis (Fig. A.64) [labeled K in Fig. A.60]. At time-step one, there is widespread, weak EKE (left column) and an EKE center north of Hellas as well as negative BCEC (middle column, contours) and a couplet of ETRANS (right column) in Hellas Planitia. At the second time, there is more organization in the GFC field (middle column) and long streak of EKE at 50° S and 180° E and on the western flank of Tharsis. Energy conversion and ETRANS are still weak. The EKE over Tharsis intensifies in the third time-step, and a third area of EKE develops at 75° S and 180° E. GFC becomes stronger with the highland EKE center, but there is still only sporadic energy conversion and ETRANS. In the fourth step, all three EKE areas along with the GFC have weakened, and the two, parallel EKE areas propagate eastward. However, BCEC has been triggered just south and west of Tharsis, which leads to strengthening of the EKE areas south of Tharsis in the fifth time-step. The positive BCEC is collocated with geopotential flux divergence as was found in the pre-pause storm. The more northern of the two EKE packets wraps around the eastern edge of Tharsis in time-step six, as a couplet of ETRANS arises north of Argyre. By time-step seven, the organization in the GFC field is lost and eddy activity and BCEC is reduced. EKE flairs again in two places in time-step eight: one area directly over Tharsis, with associated positive BCEC and negative BTEC (right column, contours), and an area west of Hellas, which has strong geopotential flux divergence and negative BCEC, BTEC, and

ETRANS. The area west of Hellas dissipates in the following time-step, but the Tharsis region retains large values of EKE. Furthermore, BCEC slowly dies and BTEC continues to be a main sink of energy. Time-step ten shows further dissipation of the EKE and a return to background levels of GFC and ETRANS.

Though there are some aspects of the pause wave that are similar to the pre- and post-pause waves regarding the horizontal placement of EKE and its transport and conversion, the vertical distribution of EKE is quite different (Fig. A.65). EKE (Fig. A.65 left column) for the pause wave is confined mostly above 300 Pa and is strongest above 100 Pa, though some does extend to the surface. Unlike the pre- and post-pause storms, BCEC (Fig. A.65 right column, contours) shows equally strong positive and negative regions, all of which are further aloft than the pre- and post-pause storms. BTEC (Fig. A.65 left column, contours) has negative but also positive regions, unlike the pre- and post-pause storms, which helps to compensate for the negative BCEC. GFC (Fig. A.65 right column) is also relegated to the upper-levels and only briefly extends to near the surface during the time of the peak intensity of the wave.

4.4 Inter-Annual Variability

One key feature demonstrated in each of the four seasons investigated is large inter-annual variability. The integrated, pressure-weighted terms of the EKE equation and the EKE itself are shown in Fig. A.66. The largest EKE and BCEC in the pre-pause period, both in a background average value and in the intensity of EKE peaks is found in MY 25. ETRANS, GFC, and BTEC are all comparable in intensity between each year. Both MY 25 and 26 transition to the pause-period level of activity around the same time ($L_s = 60^\circ$). The pause period has little variability between the two years available in the MACDA dataset, with only minor exceptions, but wave activity resumes at a higher level much sooner in MY 26 than in MY 25, approximately $L_s = 20^\circ$ sooner.

After $L_s = 150^\circ$, EKE activity rapidly increases and again has the strongest average in MY 25, with the exception of one eddy during MY 24. EKE in the post-solstice period is increased in MY 26 over the pre-pause or pause periods but is weaker than in either MY 24 or 25. Stronger, longer-duration EKE activity in the post-pause period in MY 25 is due to the MY 25 GDS that formed in the southern hemisphere at this time. Unfortunately, the MACDA GCM ran freely during a long portion of the GDS intensification period but was able to capture the time immediately preceding the intensification and the time directly afterwards, and both EKE and BCEC are higher in these periods. Interestingly, ETRANS, GFC and BTEC during the GDS are not substantively increased above that of other years.

4.5 Spectral Analysis

Finally, the spectral decomposition of the energetics of the southern hemisphere waves is investigated.

4.5.1 Pre-Solstitial Pause

Just like the northern hemisphere pre-pause period, the strongest EKE and GFC in southern hemisphere is found in wave number 1 (Fig. A.67). However, unlike the northern hemisphere periods, there is substantial power contained in the higher wave numbers, with higher power in wave numbers 3 and 4 than in 2. BCEC is strongest at wave numbers 3 and 4, followed by 2. BCEC in wave number 1 has a negative region upstream of Tharsis, so the source of EKE in wave number 1 must be from other wave numbers. BTEC is weakly negative at all wave numbers except 4 but has the highest magnitude in wave number 2. GFC is strongest in wave number 1, with a strong positive area poleward of Tharsis. Because GFC is so strong in wave number 1, the residue is also large because the other EKE terms are all small.

4.5.2 Solstitial Pause

Unsurprisingly, there is little activity at higher wave numbers in the pause period (Fig. A.68). The wave number 4 energetics is considerably weaker than other wave numbers. The strongest EKE is in wave number 2, with little signal at higher wave numbers. The only source of BCEC is in wave number 3, and wave numbers 1 and 2 have negative BCEC. GFC again has the highest magnitude in wave number 1, but wave number 2 also contains relatively strong GFC. BTEC is negative at all wave numbers, with wave number 2 having the highest magnitude values. The residue is largest at the longer wave numbers and is mostly positive, as indicated in Section 4.1.2.

4.5.3 Post-Solstitial Pause

The energetics during the post-pause period is dominated by wave number 3 (Fig. A.69) for all EKE equation terms. The post-pause wave number 3 EKE and BCEC are the strongest of any wave number for the southern hemisphere. There is also a positive contribution to EKE from BTEC, leading to a strongly negative residue in wave number 3. Wave number 4 also has large, positive BCEC and negative residue, but EKE is weaker in wave number 4 than in wave number 2. There is also intense BCEC and EKE in wave number 2. The lower wave numbers (1 and 2) have negative BTEC, so as in the northern hemisphere, EKE enters via the shorter wave numbers and leaves at the longer wave numbers. As was the case in the pre-pause and pause periods, GFC is strongest in wave number 1, and there is little signal from the other EKE equation terms in wave number 1. However, as the post-pause period has the strongest transient waves, there is high magnitude GFC at all wave numbers. The residue is negative in wave numbers 2 and greater, especially so in wave number 3, with wave number 1 exhibiting some positive features.

4.5.4 Intensities

The integrated intensities for each wave number have been compiled in Figs. A.70 (wave number 1), A.71 (wave number 2), A.72 (wave number 3), and A.73 (wave number 4). Unlike in the northern hemisphere, the southern hemisphere exhibits the signs of the solstitial pause at all wave numbers, though more strongly at some wave numbers than others. The energetics in the post-pause period is stronger in all wave numbers compared to the pre-pause period. The strongest wave number 1 activity is in MY 26 post-pause; however, the initiation of activity around $L_s = 130^\circ$ coincides with a lack of assimilated observations (indicated by the plot line becoming thin). Similarly, the strongest activity in MY 25 also occurs when observations are unavailable. There is little wave number 1 activity in MY 24/27. Additionally, near the end of the time series, EKE and GFC experience a sharp increase in MY 25. This is associated with strong westward moving waves above 1 Pa (for more information, see Section 5.1.4). The two strongest wave number 2 EKE events are the same as the wave number 1 events; however, BCEC for the MY 26 event comes from wave number 1, while BCEC for the MY 25 event originates in wave number 2. BCEC is larger in wave number 2 than 1, but BTEC is about equal in magnitude in both. The strongest BCEC of any period or in any wave number occurs at wave number 3. BCEC is also strongest in MY 24 during the pre-pause period in wave number 1. Compared to the northern hemisphere, wave number 4 is much stronger in the southern hemisphere, being only slightly weaker than wave number 3 activity. There are substantial contributions to BCEC and GFC in wave number 4, with the pre-pause period BCEC in wave number 4 being of comparable magnitude as in wave number 1 and 2. BTEC in wave numbers 3 and 4 is much weaker in magnitude than in wave numbers 1 and 2. ETRANS is almost negligible in wave number 4.

5. DISCUSSION AND CONCLUSIONS

5.1 Discussion

5.1.1 Northern Hemisphere Energetics

The transient wave energetics of the northern hemisphere during the fall and spring season is similar to that of the terrestrial atmosphere. There are a variety of growth and decay mechanisms for individual waves (see Sections 3.2.3 and 3.2.4), but most waves, especially during non-dusty periods away from the winter solstice, experience the same general energetics. Most waves grow through a combination of BCEC and BTEC, initiated by GFC. Waves propagate by ETRANS and GFC, only to decay by friction, dissipation, geopotential flux divergence, and BTEC. This development cycle was established by Orlanski and Katzfey (1991); Orlanski and Sheldon (1993); Orlanski and Chang (1993); Chang (1993, 2001) and fits with the downstream development paradigm of Orlanski and Sheldon (1995). The prime areas of transient wave growth are the planitias of Mars, namely, Utopia, Amazonis, and Acidalia, in roughly that order of preference. These areas have been identified as favored regions for transient waves both observationally and via modeling studies (Hollingsworth and Barnes, 1996; Banfield et al., 2004; Wang et al., 2005; Basu et al., 2006; Hinson and Wang, 2010; Wang et al., 2013; Mooring and Wilson, 2015).

Several exceptions are found to the regular energetics. The GDS of MY 25 provides the most striking example of a period where waves deviate from their usual behavior. During the GDS, waves struggle to grow by BCEC and instead almost solely extract EKE from the mean flow by BTEC (Fig. A.22), which was corroborated in the Lorenz energy cycle by Tabataba-vakili et al. (2015). The recurrence of waves is reduced, but the intensity of EKE remains roughly the same. This behavior is a result of the vertical temperature profile stabilizing (Fig. A.17) due to the absorption of insolation by dust and a stronger poleward

tilt to the westerly jet (Battalio et al., 2016; Guzewich et al., 2016).

The second main alteration to the usual wave behavior is during the solstitial pause. Like GDS waves, individual pause waves are substantially different, not necessarily in amount of generated EKE, but in duration, propagation, and generation and decay processes. Shorter wave number pause waves are not as coherent as non-pause waves and do not travel long distances before decaying (Fig. A.7). Pause waves also rely primarily on BTEC to grow but also utilize some BCEC. Pause waves also show indications of negative BCEC, which serves as a sink of EKE. This is seen in the zonal and meridional averages of BCEC during the pause period as compared to the non-pause periods (Fig. A.29).

However, there are isolated examples of anomalous waves even within the non-pause periods. One example was described in Section 3.2.4.2. This wave, and others like it, behave in a similar way to the GDS waves where they add BTEC at certain times during their lifecycle. In these waves though, the order of energy conversion is reversed. In the non-pause waves that grow by BTEC, they begin as other non-pause waves do by GFC initiating BCEC; however, before the BTEC becomes negative, they feed off the mean flow via positive BTEC. This usually occurs just before the waves begin interacting with the Tharsis Plateau, and the meridional BTEC averages indicate positive barotropic conversion (Fig. A.34). This is the reverse of what happens during the GDS period, where waves feed off of BTEC first, then BCEC once the BTEC becomes negative.

The effect of dust on baroclinic waves is not limited to only occasions where there is a dust storm that reaches global scale. Wang (2007) showed that there is a feedback between the wave number 3 traveling waves and flushing dust storms. If there are occasions where the traveling waves do initiate waves that cross the equator and trigger further dust lifting, the dust can shut down the growth of traveling waves. This effect is most obvious in the post-pause period in MY 26. Two flushing storms developed before and during the post-pause period. The strongest of which occurred during the post-pause timeframe at

$L_s = 310^\circ - 320^\circ$ (Wang, 2007). The result of this process was a reduction in the zonal and meridional BCEC averages (Fig. A.29 bottom row) and a reduction in the EKE for that time (Fig. A.42). A series of storms also impacted the pre-pause MY 24 energetics (Wang et al., 2005), so the BCEC and EKE are slightly reduced from the less dusty times.

Even though the average energetics of each year are fairly uniform, other inter-annual variability is paramount in describing the small differences between the energetics between each year. The EKE is stronger in the post-period for MY 24, as the type “C” storm that originates in the southern hemisphere from Kass et al. (2016) was very weak. The MY 26 post-pause period is weaker compared to its pre-pause period. This is partly due to the aforementioned flushing dust storms, but it is also indirectly due to the direction of the storms that move towards the equator, because the AGF vectors are also directed equatorward. In MY 24 and 25 that did not have obvious flushing storms in the post-pause period, AGF vectors recirculate energy back to the area of cyclogenesis on the leeside of Arabia Terra (Greybush et al., 2013), so EKE is larger during these periods. This recirculation of AGF vectors was noted terrestrially by Chang (2000).

Regarding BCEC, Kavulich et al. (2013) and Battalio et al. (2016) found that in the upper-levels, pockets of negative BCEC that otherwise lack an explanation in baroclinically unstable regions are caused by strong GFC forcing downward motions. The same is found at all periods in the northern hemisphere; however, an additional constraint is placed on the BCEC. Longitudes where BCEC (Fig. A.29) is at a maximum for a given period have GFC (Fig. A.32) that is at a minimum. If the geopotential flux divergence is in the upper or mid-levels, as is usually the case, the positioning of the BCEC maxima can be explained by using a similar argument to why negative BCEC is associated with positive GFC. If there is divergence in the upper or mid-levels, then air must be drawn from below as a replacement. The rising air forces positive baroclinic instability. Not all regions of strong geopotential flux divergence correspond to strongly positive BCEC. Thus, it is the

case that while strong geopotential flux is not a necessary case for strong BCEC, they are closely related in the meridional average. It was also found that negative BCEC can also be caused by negative vertical heat fluxes as well, even if GFC is not strongly positive in the upper-levels (Fig. A.30). Furthermore, there is a strong connection between the strongest positive BCEC and the strongest vertical heat flux. The meridional heat flux does not have such a close association.

BTEC is mostly negative in the time averages over each period (Fig. A.34). In the wave number analysis of BTEC, there is a wave number 2 structure even for the wave number 1 waves (Fig. A.43 and A.44), meaning that wave number 1 waves transfer energy to the mean flow via the wave number 2 topography. This is corroborated by the summed intensities of wave number 1 that demonstrated that the BTEC does not show a large signal from the solstitial pause (Fig. A.46). Furthermore, the spectrally decomposed pressure-averages show a uniform lack of BCEC at wave number 1, but wave number 1 has consistently high values of EKE (Mooring and Wilson, 2015). The ETRANS term for the total wave activity during the pause period also has a strong wave number 1 structure. Thus, wave number 1 clearly plays a large role in the energetics of the northern hemisphere, but there is no source of EKE at wave number 1 except for an energy cascade from higher wave numbers. This was shown to be consistent with the usual $-5/3$ slope for the inertial range of the energy spectra (Imamura and Kobayashi, 2009). In MarsWRF simulations, Wang and Toigo (2016) found periods where EKE left wave numbers 2 and 3 and entered wave number 1, and wave-wave interactions were also found to contribute sinks to the higher wave number EKE at some times. It appears that in the MACDA dataset, the source of much of the power in wave number 1 comes from the upscale propagation of EKE from higher wave numbers.

5.1.2 Southern Hemisphere Energetics

As noted previously, southern hemisphere transient waves have not been as thoroughly investigated in the literature as the northern hemisphere for a variety of reasons but mostly because the southern hemisphere waves are the weaker. The zonally asymmetric terrain has been repeatedly cited as the reason for the southern hemisphere having weaker transient wave activity compared to the northern hemisphere (e.g. Blumsack and Gierasch, 1972; Hollingsworth and Barnes, 1996), but the results presented here point to a second, equally simple explanation for the suppression of baroclinic activity: a shortened vertical column. The vertical stability profile does not change above 10 Pa between the southern and northern hemispheres (see Fig. A.4), but the terrain is much higher on average in the southern hemisphere. This reduces the amount of vertical column available for energy conversion. The BCEC occurs at roughly the same height above the surface in both hemispheres (see Figs. A.29 and A.53), so the reduced vertical column limits the amount of unstable vertical profile that can undergo baroclinic conversion. The combination of these two causes is why the EKE equation terms are smaller in the southern hemisphere (Figs. A.50, A.51, and A.52).

The growth of waves in the southern hemisphere is again predicated on BCEC. Waves grow in the flat highlands and decay on approaching the basins. The post-pause period shows positive BCEC between 400 and 50 Pa, but the pre-pause period has shallower and much weaker BCEC between 450 and 250 Pa. This leads to the BCEC maxima being roughly the same height above the ground, as the surface pressure is lower during the post-pause season. Most non-pause waves have upper-level BCEC that is collocated with negative geopotential fluxes, and negative upper-level BCEC is collocated with GFC. Waves grow when the geopotential flux divergence and BCEC are collocated, but waves decay when GFC is collocated with BCEC. A prime example can be seen in Fig. A.61.

There are many more areas of negative average BCEC in the southern hemisphere than in the northern hemisphere (Fig. A.53). The negative areas in the vertical heat flux on the eastern side of Hellas appear to be the main contributors to the negative BCEC, as the pattern is not present in the meridional heat fluxes (Fig. A.55), but the negative meridional heat flux is the cause of the negative BCEC above 100 Pa in all periods, except the post-pause in MY 24. This is similar to what is found for the northern hemisphere, where it is the negative vertical heat fluxes that correspond to negative BCEC.

Storm tracks in the southern hemisphere are distinct as opposed to the continuous tracks in the northern hemisphere, and frontal dust storms are more separated and shorter in duration (Wang and Richardson, 2015). The topography of the southern hemisphere could cause stationary waves to modulate the amplitudes of the eddies, which leads to a localization of wave activity and the zonal extent of the storm track (Chang and Orlanski, 1993). This interference could occur in a similar way to what stationary waves do to energetics with the northern hemisphere pause period (see Section 5.1.5). The post-pause eddy for the southern hemisphere provides an example of this phenomenon (Fig. A.59). The first eddy is initiated to the west of Hellas and is transported across the basin, though interestingly never extends into the basin and appears to shrink in vertical extent during transit as a result of the induced stationary wave. The shallow layer of GFC near the surface in the basins and the AGF fluxes directed towards the surface (Fig. A.57) bring in EKE to where friction can reduce the strength of the eddies.

Inter-annual variability is also quite important in the southern hemisphere. During the post-pause period, EKE is very high in MY 24 and 25. The energetics of MY 25 is strong due to the diabatically forced dust lifting centers during the GDS. The strong energetics of MY 24 is due to the high coherence and repeatability of waves during this period (Fig. A.60). These strong waves in MY 24 were noted by Hinson and Wilson (2002) as 2-sol period, wave number 3 waves from TES limb retrievals.

Hollingsworth et al. (1997) first found that the post-pause waves were the strongest in the southern hemisphere, a finding that was confirmed in subsequent work (Wang and Richardson, 2015; Lewis et al., 2016). There is no settled answer for why this occurs; however, the energetics results suggest a possible cause. It is possible that some EKE that is integrated into the southern hemisphere post-pause averages originates from flushing dust storms in the northern hemisphere during its pre-pause period. Flushing activity in the northern hemisphere does occur during both its pre- and post-pause periods, but the post-pause northern hemisphere period occurs too early (before $L_s = 0^\circ$) to directly affect the southern hemisphere pre-pause period. However, a lingering effect from the flushing storms may serve to suppress southern hemisphere traveling waves during the pre-pause period. MY 26 has lower values of EKE and energetics terms pre-pause because of the effect of a late flushing dust storm that traveled from the northern to southern hemisphere (Wang, 2007). The lingering dust from flushing storms can alter the southern hemisphere temperature profile upon crossing the equator. This flushing activity is possible because upper-level (higher than 20 km) waves act oppositely from surface waves, whereby near the equator, waves lose energy baroclinically but gain energy barotropically (Wang and Toigo, 2016). This explains how transient waves can cross the equator, where baroclinic instability is negligible. The additional dust during the pre-pause period affects the energetics just as the southern hemisphere dust from the GDS affected the MY 25 pre-pause northern hemisphere energetics.

As a secondary consideration, the post-pause period may be intensified by the evaporation of the polar ice cap, which would intensify meridional temperature gradients. This is indirectly established by looking at the zonal average temperature in the Fig. A.54 (right column, contours), which is much tighter post-pause, and by the increased meridional temperature fluxes during the post-pause period, which has a zonally averaged maximum that is stronger and closer to the surface post-pause (Fig. A.54). Forget (1998) noted

that the area of strongest sublimation later in spring is between 160° and 300° E, which corresponds to the largest increase in the meridional heat flux in the post-pause period (Fig. A.55). The reduced magnitude of the southern hemisphere energetics allows for this effect to be observed. This is opposed to the northern hemisphere, where the coherence and higher amplitude of the waves in both the pre- and post-pause periods overwhelms the smaller contribution from the diabatic effect.

5.1.3 Anomalous Behavior in the Pause Period

While the energetics of the pre- and post-pause periods in both hemispheres are uniform, neglecting the effects of dust storm activity, the pause period energetics demonstrate several interesting, anomalous behaviors. The energetics of multiple individual waves were described in Sections 3.2.3 and 4.3.3. Those sections showed that the paradigm of Orlanski and Katzfey (1991), Orlanski and Sheldon (1993, 1995), and Chang (2001) does not necessarily hold for pause waves. For example, the MY 26 northern hemisphere pause wave (Section 3.2.3.1) had low energy conversion terms and was mostly progressed as a result of GFC alone. Growth mostly through GFC is an atypical development pattern but is allowed because GFC can be a local source/sink of EKE. GFC is only prohibited from being a global source/sink of EKE.

The wave number 1 intensities do not exhibit a significant pause signal in EKE or the energy conversion terms. Given the result of Mulholland et al. (2016) that the solstitial pause is partly the result of increased opacity due to dust and cloud cover, this appears to contradict the finding of Barnes et al. (1993) that showed that wave numbers increase during higher opacity conditions. However, Lewis et al. (2016) showed that temperature is reduced during the pause below 300 Pa, but above 100 Pa there are still multiple maxima in the temperature. It is suggested that the upper-level temperature maxima are due to the middle atmosphere polar warming (Kuroda et al., 2007; McCleese et al., 2008) caused by

the GDS and regional dust events like the “B” type storm of Kass et al. (2016). The polar warming event during MY 25 also explains why wave number 1 is so strong in MY 25 during the pause period (see Fig. A.60). Additionally, waves above 20 km have been shown to be dominated by a wave number 1 structure (Banfield et al., 2004), which emerges from barotropic sources (Wang and Toigo, 2016). This also explains why BCEC becomes slightly negative during the pause as well as why the upper-level waves are shown to be lacking in baroclinicity (Wang and Toigo, 2016). The high altitude of these pause waves also causes the downward directed GFC fluxes seen especially in the southern hemisphere, as energy is directed from the upper-levels towards the surface (Fig. A.57).

The residue during the pause period in the southern hemisphere, and to a lesser extent the northern hemisphere, is more positive than negative (Fig. A.26 and A.51). This is opposed to all non-pause periods and what is found terrestrially (e.g. Orlanski and Chang, 1993; Decker and Martin, 2005; Ahmadi-Givi et al., 2014). A positive residue indicates that EKE is generated from some process not accounted for in the EKE equation. Dissipation and friction can only be sinks of energy, while other usual potential sources, such as errors from data assimilation or interpolation, have no reason for existing only during the pause period. Instead, a possible source of the positive residue is diabatic heating (Chang, 2001) caused by the condensation of polar hood clouds (Pettengill and Ford, 2000; Benson et al., 2010, 2011) and from the deposition of CO₂ onto the polar ice cap (Forget, 1998). The heating from the CO₂ condensation provides additional an source of energy that cannot be captured by the EKE equation.

5.1.4 Problems with MACDA (v1.0)

MACDA (v1.0) is the only publicly available reanalysis for any period on Mars. However, because Martian reanalysis is only in its nascent stages of development, the MACDA dataset exhibits several issues, inconsistencies, and deficiencies. One particular issue is

the development of several eddies that have unrealistic energetics, one of which was discussed in Section 3.1.4 at $L_s = 214^\circ$ in MY 25. These waves spontaneously develop without an energy generating mechanism and then subsequently decay equally as suddenly. A beta version of a separate reanalysis dataset (Greybush et al., 2012) did not contain these types of waves, indicating problems with the data assimilation scheme of MACDA. A second type of unrealistic EKE event occurred twice in the pause period of MY 24, where a stationary area of EKE spontaneously erupted and decayed with little change in the EKE equation terms [see Section 3.2.3.4]. Such behavior is not consistent with energetics analysis and is considered an issue with the dataset itself instead of with the analysis methodology.

A second type of anomalous activity was noted at the end of the transient wave period in the southern hemisphere during MY 25 and can be seen after $L_s = 185^\circ$ in Fig. A.66. A Hovmöller diagram of the pressure-averaged (between the surface and 0.1 Pa) EKE for the period is presented in Fig. A.74. At the beginning of each year, there are transient eastward moving waves. However, in MY 25, the waves abruptly switch direction and travel westward. These waves are confined to above 10 Pa and could possibly be westerly traveling Rossby waves. If so, they should be barotropic in nature, as there is little BCEC noted with the activity. It is equally possible, since the phenomena only occurs in the highest levels, that this feature is an anomaly of MACDA itself.

The westward waves of MY 25 highlight a main problem of the MACDA (v1.0) dataset. Because only TES retrievals are available during the period analyzed, any features above 40 km (10 Pa) should be examined with trepidation, as the reliability of TES temperature retrievals is of dubious quality at higher altitudes. In comparisons of MACDA to the only other reanalysis (EMARS), the reanalyses agreed at almost all times at the low-levels, but they showed large differences in the upper-levels, especially in the temperature profiles along the polar front (Waugh et al., 2016). Thus any work to examine the dynamics

of upper-level waves that could occur in the pause period [e.g. Figs 2 and 3 of Lewis et al. (2016)] or at the end of MY 25 should be considered preliminary. However, the dataset is currently undergoing updates to ameliorate these issues (Montabone et al., 2014), and new reanalysis datasets are being developed to compare to MACDA (Greybush et al., 2012, 2013) that include more years and include data that are reliable at higher altitudes.

5.1.5 Possible Causes of Solstitial Pause

The solstitial pause is a phenomena that has been identified and investigated in multiple studies. The zeroth-order explanation for the sudden reduction in transient wave activity is that the tilt of the polar front switches from being tilted away from the pole with increasing height to being tilted towards the pole with increasing height. [Compare the temperature gradient between 40° and 80° N below 10 Pa in Fig. A.4 in the pre- and post-pause panels with the gradient in the pause panels. Similarly, compare the panels between 40° and 80° S in the southern hemisphere.] A tilt of the polar front towards the pole is not an unstable baroclinic field, because in those instances, temperature increases with height, which is a highly statically stable environment. This is similar to the situation during the GDS of MY 25. This is also similar to the Pacific storm track in the northern hemisphere of Earth (Nakamura, 1992). As a general explanation, the polar front tilt is sufficient to describe the climatological reasoning for a lack of waves, but the work presented here provides two explanations for how the solstitial pause is made manifest in individual transient features.

In the terrestrial atmosphere, a barotropic governor has been indicated as an explanation for the Pacific mid-winter minimum in transient wave activity (Deng and Mak, 2005, 2006). Mulholland et al. (2016) investigated the possibility of such a feature altering transient waves in the atmosphere of Mars and found that it could be a contributor to the solstitial pause but was likely not the prime motivator. However, the wave energetics lend credence to the governor as a partial explanation in the mid-levels. In the zonal-mean

BTEC in the northern (Fig. A.34) and southern (Fig. A.56) hemispheres, the BTEC is more negative during the solstitial pause. Additionally, the integrated intensities for both hemispheres (Figs. A.42 and A.66) show that BTEC does not decrease during the pause period, while all other EKE equation terms do. The lack of individual waves during the pause period is so apparent because BTEC acts as a stronger sink of EKE, while at the same time the BCEC is weakened.

Topography is also a frequently cited explanation for the solstitial pause, including for the terrestrial atmosphere (Penny et al., 2010). And indeed for other terrestrial worlds, stationary eddies have been found to control the strength and length of storm tracks by altering the temperature gradients (Kaspi and Schneider, 2013). For Mars, topography is usually invoked as a modifier of solstitial pause activity directly by interfering with the storm track, as the polar ice caps – and thus the gradients for baroclinic eddy initiation – move equatorward (Banfield et al., 2003; Hinson and Wang, 2010; Mulholland et al., 2016). However, an alternative explanation can be found by an investigation of the heat fluxes of the stationary waves in the northern hemisphere that indicate that the stationary waves dramatically strengthen during the pause period [see also Imamura and Kobayashi (2009)]. Fig. A.75 shows the signal of the stationary wave and its associated vertical and meridional heat fluxes during $L_s = 190^\circ - 220^\circ$. These values were found by subtracting the zonal-mean field from the temporal average and then averaging the three Mars years together. The pre-pause wave amplitude and heat fluxes are of comparable intensity to the post-pause period (Fig. A.77), but both are much weaker than the stationary wave signal during the pause period (Fig. A.76). This suggests that the available potential energy during the pause period is used by the stationary waves instead of the transient waves. The reason for this is indirectly related to topography. Modeling work (Guzewich et al., 2016) has indicated that the jet moves equatorward during the pause period, which allows for greater interaction with topography, though this does not appear to be the case in the

MACDA dataset (Fig. A.4). However, as noted in Fig. A.4, the westerly jet is much stronger during the pause period. The increased speed of the jet intensifies the stationary waves. The strengthened stationary eddies make the coherent propagation of transient waves more difficult (Lee and Held, 1993), which is evidenced by a comparison of Figs. A.7 and A.8.

5.2 Conclusions

The dynamics and energetics of transient waves during four seasons in both the northern and southern hemispheres of the atmosphere of Mars were investigated during three Mars years. MACDA provided the reanalysis data for the comparison of the three years, one of which (MY 25) contained a global-scale dust storm. The eddy kinetic energy equation (Orlanski and Katzfey, 1991) was the primary tool used for the analysis of the data. In comparing the three years, the following conclusions can be drawn:

The energetics of transient waves is strongest during two periods that roughly align with the fall and spring seasons in both hemispheres. Except for periods of unusually high opacity, most transient waves of the pre-winter solstice and post-winter solstice periods are quite similar across years. Waves during the winter solstice are weaker than during the fall and spring, and they are the least intense in the summer. The winter energetics is weaker due to a stabilized vertical temperature profile around winter solstice, a barotropic governor, and stronger stationary waves that deprive transient waves of baroclinic energy conversion.

The waves are strongest in the northern hemisphere in comparison to the southern hemisphere due more zonally asymmetric topography and shorter atmospheric column in the southern hemisphere. Waves in the southern hemisphere are stronger after the winter solstitial pause due to the influence of flushing dust storms from the northern hemisphere limiting wave activity during the pre-solstitial pause period and to the strengthening of the

meridional temperature gradient due to the melting of the CO₂ ice cap.

The waves of the clear years of MY 24, 26, and 27 show eddy kinetic energy growth and decay mechanisms similar to those that were described by Kavulich et al. (2013) and Battalio et al. (2016). Below 10 Pa, waves generate eddy kinetic energy primarily by baroclinic energy conversion in wave numbers 2 and higher. Barotropic energy conversion acts mostly as a sink of eddy kinetic energy in wave numbers 2 and below in the regions downstream of the main baroclinic energy conversion, though it can act as a source of eddy kinetic energy directly west of the Tharsis Plateau, extending the storm track downstream of the main baroclinic energy conversion regions. Geopotential flux convergence provides the triggering mechanism for wave development, and barotropic energy conversion and also friction play a role in the decay of waves.

In the global-scale dust storm year of MY 25, the intensity of baroclinic energy conversion is substantially reduced due to decreased vertical wind shear between 500 and 800 Pa. Further inhibition of eddy heat fluxes results from the more isothermal, statically stable atmosphere above 500 Pa. This leads to a weaker sensitivity of the atmosphere to baroclinic instability. This weaker sensitivity reduces the frequency of storms to roughly half of that during non-dust-storm years. However, compared to MY 24 and 26, the absolute intensity of the individual eddy kinetic energy generation events does not decrease. The storms during MY 25 become mixed baroclinic/barotropic: the waves gain energy both baroclinically and barotropically and lose it barotropically. Once a wave begins to lose energy barotropically, it begins to generate energy baroclinically, which compensates for the loss of EKE due to BTEC. Waves during the pause periods take on unusual growth and decay patterns similar to those during the GDS.

REFERENCES

- Ahmadi-Givi, F., M. Nasr-Esfahany, and a. R. Mohebalhojeh, 2014: Interaction of North Atlantic baroclinic wave packets and the Mediterranean storm track. *Quarterly Journal of the Royal Meteorological Society*, **140 (680)**, 754–765, doi:10.1002/qj.2171.
- Banfield, D., B. Conrath, P. Gierasch, R. Wilson, and M. Smith, 2004: Traveling waves in the martian atmosphere from MGS TES Nadir data. *Icarus*, **170 (2)**, 365–403, doi:10.1016/j.icarus.2004.03.015.
- Banfield, D., B. Conrath, M. Smith, P. Christensen, and R. Wilson, 2003: Forced waves in the martian atmosphere from MGS TES nadir data. *Icarus*, **161 (2)**, 319–345, doi:10.1016/S0019-1035(02)00044-1.
- Barnes, J. R., 1980: Time Spectral Analysis of Midlatitude Disturbances in the Martian Atmosphere. *Journal of the Atmospheric Sciences*, **37 (9)**, 2002–2015.
- Barnes, J. R., 1981: Midlatitude Disturbances in the Martian Atmosphere: A Second Mars Year. *Journal of the Atmospheric Sciences*, **38 (2)**, 225–234.
- Barnes, J. R., 1984: Linear baroclinic instability in the Martian atmosphere. *Journal of the Atmospheric Sciences*, **41 (9)**, 1536–1550, doi:10.1175/1520-0469(1984)041<1536:LBIITM>2.0.CO;2.
- Barnes, J. R., R. M. Haberle, J. B. Pollack, H. Lee, and J. Schaeffer, 1996: Mars Atmospheric Dynamics as Simulated by the NASA Ames General Circulation Model 3. Winter quasi-stationary eddies. *Journal of Geophysical Research*, **101 (E5)**, 12 753–12 776, doi:10.1029/92JE02946.
- Barnes, J. R., J. B. Pollack, R. M. Haberle, C. B. Leovy, R. W. Zurek, H. Lee, and J. Schaeffer, 1993: Mars Atmospheric Dynamics as Simulated by the NASA Ames General Circulation. *Journal of Geophysical Research*, **98 (E2)**, 3125–3148.

- Basu, S., J. Wilson, M. Richardson, and A. Ingersoll, 2006: Simulation of spontaneous and variable global dust storms with the GFDL Mars GCM. *Journal of Geophysical Research*, **111** (E9), E09 004, doi:10.1029/2005JE002660.
- Battalio, M., I. Szunyogh, and M. Lemmon, 2016: Energetics of the martian atmosphere using the Mars Analysis Correction Data Assimilation (MACDA) dataset. *Icarus*, **276**, 1–20, doi:10.1016/j.actamat.2015.02.029.
- Benson, J. L., D. M. Kass, and A. Kleinböhl, 2010: Mars' south polar hood as observed by the Mars Climate Sounder. *Journal of Geophysical Research E: Planets*, **115**, 1–22, doi:10.1029/2009JE003554.
- Benson, J. L., D. M. Kass, and A. Kleinböhl, 2011: Mars' north polar hood as observed by the Mars Climate Sounder. *Journal of Geophysical Research E: Planets*, **116** (3), 1–13, doi:10.1029/2010JE003693.
- Blumsack, S. L., and P. J. Gierasch, 1972: Mars: The Effects of Topography on Baroclinic Instability. *Journal of the Atmospheric Sciences*, **29** (9), 1081–1089.
- Cantor, B. A., 2007: MOC observations of the 2001 Mars planet-encircling dust storm. *Icarus*, **186** (1), 60–96, doi:10.1016/j.icarus.2006.08.019.
- Cantor, B. A., P. B. James, M. Caplinger, and M. J. Wolff, 2001: Martian dust storms: 1999 Mars Orbiter Camera observations. *Journal of Geophysical Research*, **106** (E10), 23 653–23 687.
- Chang, E. K. M., 1993: Downstream Development of Baroclinic Waves as Inferred from Regression Analysis. *Journal of the Atmospheric Sciences*, **50** (13), 2038–2053.
- Chang, E. K. M., 2000: Wave Packets and Life Cycles of Troughs in the Upper Troposphere: Examples from the Southern Hemisphere Summer Season of 1984/85. *Monthly Weather Review*, **128** (1), 25–50, doi:10.1175/1520-0493(2000)128<0025:WPALCO>2.0.CO;2.
- Chang, E. K. M., 2001: The Structure of Baroclinic Wave Packets. *Journal of the Atmo-*

- spheric Sciences*, **58**, 1694–1713, doi:10.1175/1520-0469(2001)058<1694:TSOBWP>2.0.CO;2.
- Chang, E. K. M., and I. Orlanski, 1993: On the Dynamics of Storm Track. *Journal of the Atmospheric Sciences*, **50** (7), 999–1015.
- Chang, E. K. M., and I. Orlanski, 1994: On Energy Flux and Group Velocity of Waves in Baroclinic Flows. *Journal of the Atmospheric Sciences*, **51** (24), 3823–3828.
- Charney, J. G., 1947: The Dynamics of Long Waves in a Baroclinic Westerly Current. *Journal of Meteorology*, **4** (5).
- Collins, M., S. R. Lewis, and P. L. Read, 1996: Baroclinic Wave Transitions in the Martian Atmosphere. *Icarus*, **136** (120), 344–357.
- Conrath, B. J., 1975: Thermal structure of the Martian atmosphere during the dissipation of the dust storm of 1971. *Icarus*, **24** (1), 36–46, doi:10.1016/0019-1035(75)90156-6.
- Danielson, R., J. Gyakum, and D. Straub, 2004: Downstream Baroclinic Development Among Forty-one Cold-Season Eastern North Pacific Cyclones. *Atmosphere-Ocean*, **42** (July), 1–16, doi:10.3137/ao.420402.
- Danielson, R. E., J. R. Gyakum, and D. N. Straub, 2006: A Case Study of Downstream Baroclinic Development over the North Pacific Ocean. Part II : Diagnoses of Eddy Energy and Wave Activity. *Monthly Weather Review*, **134** (5), 1549–1567.
- Decker, S. G., and J. E. Martin, 2005: A Local Energetics Analysis of the Life Cycle Differences between Consecutive, Explosively Deepening, Continental Cyclones. *Monthly Weather Review*, **133** (1), 295–316.
- Deng, Y., and M. Mak, 2005: An idealized model study relevant to the dynamics of the midwinter minimum of the Pacific storm track. *J. Atmos. Sci.*, **62** (4), 1209–1225, doi:10.1175/JAS3400.1.
- Deng, Y., and M. Mak, 2006: Nature of the Differences in the Intraseasonal Variability of the Pacific and Atlantic Storm Tracks: A Diagnostic Study. *Journal of the Atmospheric*

- Sciences*, **63** (10), 2602–2615, doi:10.1175/JAS3749.1.
- Eady, B. E. T., 1949: Long Waves and Cyclone Waves. *Tellus*, **1** (3), 33–52.
- Forget, F., 1998: Mars co2 ice polar caps. *Solar System Ices*, Springer, 477–507.
- Forget, F., and Coauthors, 1999: Improved general circulation models of the Martian atmosphere from the surface to above 80 km. *Journal of Geophysical Research*, **104** (E10), 24 155, doi:10.1029/1999JE001025.
- Greybush, S. J., E. Kalnay, M. J. Hoffman, and R. J. Wilson, 2013: Identifying Martian atmospheric instabilities and their physical origins using bred vectors. *Quarterly Journal of the Royal Meteorological Society*, **139** (672), 639–653, doi:10.1002/qj.1990.
- Greybush, S. J., R. J. Wilson, R. N. Hoffman, M. J. Hoffman, T. Miyoshi, K. Ide, T. McConnochie, and E. Kalnay, 2012: Ensemble Kalman filter data assimilation of Thermal Emission Spectrometer temperature retrievals into a Mars GCM. *Journal of Geophysical Research*, **117** (E11), E11 008, doi:10.1029/2012JE004097.
- Guzewich, S. D., A. Toigo, and D. Waugh, 2016: The effect of dust on the martian polar vortices. *Icarus*, **278**, 100–118, doi:10.1016/j.icarus.2016.06.009.
- Guzewich, S. D., A. D. Toigo, L. Kulowski, and H. Wang, 2015: Mars Orbiter Camera climatology of textured dust storms. *Icarus*, **258**, 1–13, doi:10.1016/j.icarus.2015.06.023.
- Haberle, R. M., J. B. Pollack, J. R. Barnes, R. W. Zurek, C. B. Leovy, J. R. Murphy, H. Lee, and J. Schaeffer, 1993: Mars Atmospheric Dynamics as Simulated by the NASA Ames General Circulation Model 1. The Zonal-Mean Circulation. *Journal of Geophysical Research*, **98**, 3093–3124.
- Hakim, G. J., 2003: Developing Wave Packets in the North Pacific Storm Track. *Monthly Weather Review*, **131** (11), 2824–2837, doi:10.1175/1520-0493(2003)131<2824:DWFITN>2.0.CO;2.
- Hartmann, D. L., 1979: Baroclinic Instability of Realistic Zonal-Mean State to Planetary

- Waves. *Journal of the Atmospheric Sciences*, **36** (12), 2336–2349.
- Hinson, D. P., and H. Wang, 2010: Further observations of regional dust storms and baroclinic eddies in the northern hemisphere of Mars. *Icarus*, **206** (1), 290–305, doi:10.1016/j.icarus.2009.08.019.
- Hinson, D. P., H. Wang, and M. D. Smith, 2012: A multi-year survey of dynamics near the surface in the northern hemisphere of Mars: Short-period baroclinic waves and dust storms. *Icarus*, **219** (1), 307–320, doi:10.1016/j.icarus.2012.03.001.
- Hinson, D. P., and R. J. Wilson, 2002: Transient eddies in the southern hemisphere of Mars. *Geophysical Research Letters*, **29** (7), 3–6, doi:10.1029/2001GL014103.
- Hinson, D. P., R. J. Wilson, M. D. Smith, and B. J. Conrath, 2003: Stationary planetary waves in the atmosphere of Mars during southern winter. *Journal of Geophysical Research*, **108** (E1), 5004, doi:10.1029/2002JE001949, URL <http://www.agu.org/pubs/crossref/2003/2002JE001949.shtml>.
- Hollingsworth, J. L., and J. R. Barnes, 1996: Forced Stationary Planetary Waves in Mars's Winter Atmosphere. *Journal of the Atmospheric Sciences*, **53** (3), 428–448.
- Hollingsworth, J. L., R. M. Haberle, J. R. Barnes, A. F. C. Bridger, J. B. Pollack, H. Lee, and J. Schaeffer, 1996: Orographic control of storm zones on Mars. *Nature*, **380**, 413–416.
- Hollingsworth, J. L., R. M. Haberle, and J. Schaeffer, 1997: Seasonal variations of storm zones on Mars. *Advances in Space Research*, **19** (8), 1237–1240, doi:10.1016/S0273-1177(97)00275-5.
- Hoskins, B. J., and P. J. Valdes, 1990: On the Existence of Storm-Tracks. *Journal of the Atmospheric Sciences*, **47** (15), 1854–1864.
- Hourdin, F., F. Forget, and O. Talagrand, 1995: The sensitivity of the martian surface pressure to various parameters: A comparison between numerical simulations and Viking observations. *Journal of Geophysical Research*, **100**, 637–655.

- Hurley, J., N. Teanby, P. Irwin, S. Calcutt, and E. Sefton-Nash, 2014: Differentiability and retrievability of CO₂ and H₂O clouds on Mars from MRO/MCS measurements: A radiative-transfer study. *Planetary and Space Science*, **97**, 65–84, doi:10.1016/j.pss.2014.03.015.
- Imamura, T., and H. Kobayashi, 2009: Wavenumber spectra of planetary-scale disturbances in the Mars atmosphere. *Icarus*, **199** (2), 286–294, doi:10.1016/j.icarus.2008.09.021, URL <http://dx.doi.org/10.1016/j.icarus.2008.09.021>.
- Kaspi, Y., and T. Schneider, 2013: The Role of Stationary Eddies in Shaping Midlatitude Storm Tracks. *The Journal of Climate*, 2596–2613, doi:10.1175/JAS-D-12-082.1.
- Kass, D. M., A. Kleinböhl, D. J. McCleese, J. T. Schofield, and M. D. Smith, 2016: Interannual similarity in the Martian atmosphere during the dust storm season. *Geophysical Research Letters*, **43**, doi:10.1002/2016GL068978.
- Kavulich, M. J., I. Szunyogh, G. Gyarmati, and R. J. Wilson, 2013: Local Dynamics of Baroclinic Waves in the Martian Atmosphere. *Journal of the Atmospheric Sciences*, **70** (11), 3415–3447, doi:10.1175/JAS-D-12-0262.1.
- Kuroda, T., A. S. Medvedev, P. Hartogh, and M. Takahashi, 2007: Seasonal changes of the baroclinic wave activity in the northern hemisphere of Mars simulated with a GCM. *Geophysical Research Letters*, **34** (9), L09 203, doi:10.1029/2006GL028816.
- Lee, S., 1997: Maintenance of Multiple Jets in a Baroclinic Flow. *Journal of the Atmospheric Sciences*, **54** (13), 1726–1738, doi:10.1175/1520-0469(1997)054.
- Lee, S., and I. M. Held, 1993: Baroclinic Wave Packets in Models and Observations. *Journal of the Atmospheric Sciences*, **50** (10), 1413–1428, doi:10.1175/1520-0469(1993)050<1413:BWPIMA>2.0.CO;2.
- Leovy, C. B., 1969: Mars: theoretical aspects of meteorology. *Applied optics*, **8** (7), 1279–86.
- Lewis, S. R., D. P. Mulholland, P. L. Read, L. Montabone, R. J. Wilson, and M. D. Smith,

- 2016: The solstitial pause on Mars: 1. A planetary wave reanalysis. *Icarus*, **264**, 456–464, doi:10.1016/j.icarus.2015.08.039.
- Lewis, S. R., P. L. Read, B. J. Conrath, J. C. Pearl, and M. D. Smith, 2007: Assimilation of thermal emission spectrometer atmospheric data during the Mars Global Surveyor aerobraking period. *Icarus*, **192** (2), 327–347, doi:10.1016/j.icarus.2007.08.009.
- Lovejoy, S., J.-P. Muller, and J. P. Boisvert, 2014: On Mars too expect macroweather. *Geophysical Research Letters*, **41**, 7694–7700, doi:10.1002/2014GL061861.Received.
- McCleese, D. J., and Coauthors, 2008: Intense polar temperature inversion in the middle atmosphere on Mars. *Nature Geoscience*, **1**, 745–749, doi:10.1038/ngeo332.
- Mitchell, D. M., L. Montabone, S. Thomson, and P. L. Read, 2014: Polar vortices on Earth and Mars: A comparative study of the climatology and variability from reanalyses. *Quarterly Journal of the Royal Meteorological Society*, **141** (687), 550–562, doi:10.1002/qj.2376.
- Montabone, L., S. R. Lewis, and P. Read, 2011: Mars Analysis Correction Data Assimilation (MACDA): MGS/TES v1.0. NCAS British Atmospheric Data Centre, doi:10.5285/78114093-E2BD-4601-8AE5-3551E62AEF2B.
- Montabone, L., S. R. Lewis, and P. L. Read, 2005: Interannual variability of Martian dust storms in assimilation of several years of Mars global surveyor observations. *Advances in Space Research*, **36** (11), 2146–2155, doi:10.1016/j.asr.2005.07.047.
- Montabone, L., S. R. Lewis, P. L. Read, and D. P. Hinson, 2006: Validation of martian meteorological data assimilation for MGS/TES using radio occultation measurements. *Icarus*, **185** (1), 113–132, doi:10.1016/j.icarus.2006.07.012.
- Montabone, L., and Coauthors, 2014: The Mars Analysis Correction Data Assimilation (MACDA) Dataset V1.0. *Geoscience Data Journal*, **1**, 129–139, doi:10.1002/gdj3.13.
- Mooring, T. A., and R. J. Wilson, 2015: Transient eddies in the MACDA Mars reanalysis. *Journal of Geophysical Research: Planets*, **120**, 1–26, doi:10.1002/2015JE004824.

- Mulholland, D. P., S. R. Lewis, P. L. Read, J.-B. Madeleine, and F. Forget, 2016: The solstitial pause on Mars: 2 modelling and investigation of causes. *Icarus*, **264**, 465–477, doi:10.1016/j.icarus.2015.08.038.
- Murphy, R., B. Pollack, M. Haberle, B. Leovy, O. B. Toon, and J. Schaeffer, 1995: Three-dimensional numerical simulation of Martian global dust storms. *Journal of Geophysical Research: Planets*, **100 (E12)**, 26 357–26 376.
- Nakamura, H., 1992: Midwinter Suppression of Baroclinic Wave Activity in the Pacific. *Journal of the Atmospheric Sciences*, **49 (17)**, 1629–1642, doi:10.1175/1520-0469(1992)049<1629:MSOBWA>2.0.CO;2.
- O'Brien, J., 1970: Alternative Solutions to the Classical Vertical Velocity Problem. *Journal of Applied Meteorology*, **9 (2)**, 197–203.
- Orlanski, I., and E. K. M. Chang, 1993: Ageostrophic Geopotential Fluxes in Downstream and Upstream Development of Baroclinic Waves. *Journal of the Atmospheric Sciences*, **50 (2)**, 212–225.
- Orlanski, I., and J. Katzfey, 1991: The Life Cycle of a Cyclone Wave in the Southern Hemisphere. Part I: Eddy Energy Budget. *Journal of the Atmospheric Sciences*, **48 (17)**, 1973–1998.
- Orlanski, I., and J. P. Sheldon, 1993: A Case of Downstream Baroclinic Development over Western North America. *Monthly Weather Review*, **121 (11)**, 2929–2950.
- Orlanski, I., and J. P. Sheldon, 1995: Stages in the energetics of baroclinic systems. *Tellus*, **47A (5)**, 605–628.
- Panetta, R. L., 1993: Zonal Jets in Wide Baroclinically Unstable Regions: Persistence and Scale Selection. *Journal of the Atmospheric Sciences*, **50 (14)**, 2073–2106.
- Panetta, R. L., and I. M. Held, 1988: Baroclinic Eddy Fluxes in a One-Dimensional Model of Quasi-geostrophic Turbulence. *Journal of the Atmospheric Sciences*, **45 (22)**, 3354–3365.

- Penny, S., G. H. Roe, and D. S. Battisti, 2010: The Source of the Midwinter Suppression in Storminess over the North Pacific. *Journal of Climate*, **23** (3), 634–648, doi:10.1175/2009JCLI2904.1.
- Pettengill, G. H., and P. G. Ford, 2000: Winter clouds over the North Martian polar cap. *Geophysical Research Letters*, **27** (5), 609–612, doi:10.1029/1999GL010896.
- Pollack, J. B., C. B. Leovy, P. W. Grieman, and Y. Mintz, 1981: A Martian general circulation experiment with large topography. *Journal of the Atmospheric Sciences*, **38** (1), 3–29, doi:10.1175/1520-0469(1981)038<0003:AMGCEW>2.0.CO;2.
- Read, P. L., and S. Lewis, 2004: *The Martian Climate Revisited*. Springer.
- Read, P. L., S. R. Lewis, and D. P. Mulholland, 2015: The physics of Martian weather and climate: a review. *Reports on Progress in Physics*, **78** (12), 125 901, doi:10.1088/0034-4885/78/12/125901.
- Rivière, G., P. Arbogast, and a. Joly, 2015: Eddy kinetic energy redistribution within windstorms Klaus and Friedhelm. *Quarterly Journal of the Royal Meteorological Society*, **141** (688), 925–938, doi:10.1002/qj.2412, URL <http://doi.wiley.com/10.1002/qj.2412>.
- Simmons, A. J., and B. Hoskins, 1979: The Downstream and Upstream Development of Unstable Baroclinic Waves. *Journal of the Atmospheric Sciences*, **36** (7), 1239–1254.
- Simmons, A. J., and B. J. Hoskins, 1978: The Life Cycles of Some Nonlinear Baroclinic Waves. *Journal of the Atmospheric Sciences*, **35** (3), 414–432, doi:10.1175/1520-0469(1978)035<0414:TLCOSN>2.0.CO;2.
- Simmons, A. J., and B. J. Hoskins, 1980: Barotropic Influences on the Growth and Decay of Nonlinear Baroclinic Waves. *Journal of the Atmospheric Sciences*, **37** (8), 1679–1984.
- Smith, M., 2002: Thermal Emission Spectrometer Observations of Martian Planet-Encircling Dust Storm 2001A. *Icarus*, **157** (1), 259–263, doi:10.1006/icar.2001.6797.
- Strausberg, M. J., 2005: Observations of the initiation and evolution of the 2001 Mars

- global dust storm. *Journal of Geophysical Research*, **110** (E2), E02 006, doi:10.1029/2004JE002361.
- Swanson, K., and R. T. Pierrehumbert, 1994: Nonlinear Wave Packet Evolution on a Baroclinically Unstable Jet. *Journal of the Atmospheric Sciences*, **51** (3), 384–396.
- Tabataba-vakili, F., P. L. Read, S. R. Lewis, L. Montabone, T. Ruan, Y. Wang, A. Valeanu, and R. M. B. Young, 2015: A Lorenz / Boer energy budget for the atmosphere of Mars from a “reanalysis” of spacecraft observations. *Geophysical Research Letters*, **42**, 8320–8327, doi:10.1002/2015GL065659.
- Wang, H., 2007: Dust storms originating in the northern hemisphere during the third mapping year of mars global surveyor. *Icarus*, **189** (2), 325 – 343, doi:j.icarus.2007.01.014.
- Wang, H., and M. I. Richardson, 2015: The origin, evolution, and trajectory of large dust storms on Mars during Mars years 24–30 (1999–2011). *Icarus*, **251**, 112–127, doi:10.1016/j.icarus.2013.10.033.
- Wang, H., M. I. Richardson, A. D. Toigo, and C. E. Newman, 2013: Zonal wavenumber three traveling waves in the northern hemisphere of Mars simulated with a general circulation model. *Icarus*, **223** (2), 654–676, doi:10.1016/j.icarus.2013.01.004, URL <http://dx.doi.org/10.1016/j.icarus.2013.01.004>.
- Wang, H., M. I. Richardson, R. J. Wilson, A. P. Ingersoll, A. D. Toigo, and R. W. Zurek, 2003: Cyclones, tides, and the origin of a cross-equatorial dust storm on Mars. *Geophysical Research Letters*, **30** (9), 1488, doi:10.1029/2002GL016828, URL <http://doi.wiley.com/10.1029/2002GL016828>.
- Wang, H., and A. D. Toigo, 2016: The variability, structure and energy conversion of the northern hemisphere traveling waves simulated in a Mars general circulation model. *Icarus*, **271**, 207–221, doi:10.1016/j.icarus.2016.02.005.
- Wang, H., R. W. Zurek, and M. I. Richardson, 2005: Relationship between frontal dust storms and transient eddy activity in the northern hemisphere of Mars as observed by

- Mars Global Surveyor. *Journal of Geophysical Research*, **110** (E7), E07005, doi:10.1029/2005JE002423.
- Wang, P., and J. L. Mitchell, 2014: Planetary ageostrophic instability leads to superrotation. *Geophysical Research Letters*, **41** (12), 4118–4126, doi:10.1002/2014GL060345.
- Waugh, D. W., A. D. Toigo, S. D. Guzewich, S. J. Greybush, R. J. Wilson, and L. Montabone, 2016: Martian polar vortices: Comparison of reanalyses. *Journal of Geophysical Research: Planets*, **121**, 1–16, doi:10.1002/2016JE005093. Received.
- Wilson, R. J., D. Banfield, B. J. Conrath, and M. D. Smith, 2002: Traveling waves in the Northern Hemisphere of Mars. *Geophysical Research Letters*, **29** (14), 3–6, doi:10.1029/2002GL014866.
- Xue, M., and S.-J. Lin, 2001: Numerical Equivalence of Advection in Flux and Advective Forms and Quadratically Conservative High-Order Advection Schemes. *Monthly Weather Review*, **129** (3), 561–565, doi:10.1175/1520-0493(2001)129<0561:NEOAIIF>2.0.CO;2.

APPENDIX A

FIGURES

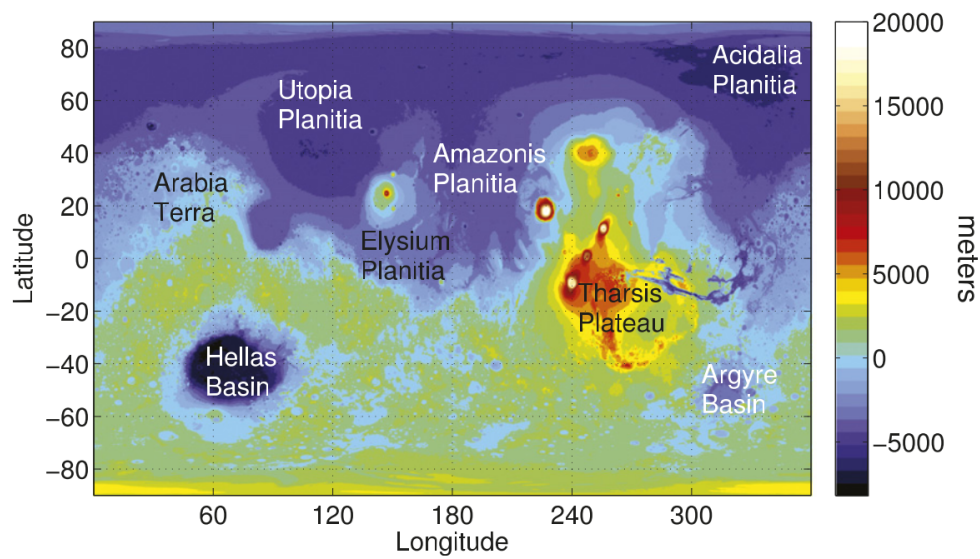


Figure A.1: The Martian topography. [Credit: Mars Orbiter Laser Altimeter (MOLA) Science Team, Mars Global Surveyor, NASA.]

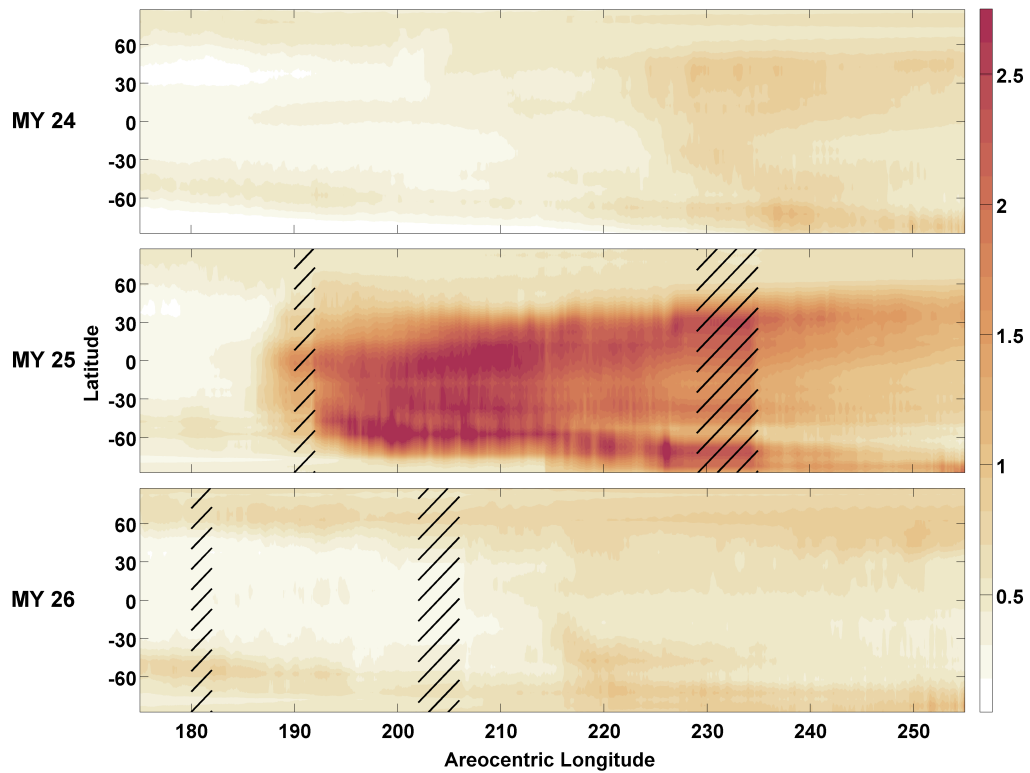


Figure A.2: Column optical depth in the visible wavelength range for $L_s = 175^\circ - 255^\circ$ for MY 24 (top), MY 25 (middle), and MY 26 (bottom) from the MACDA dataset. Hatching indicates times of areocentric longitude greater than one degree, when TES retrievals were unavailable, and the analyses are based on a freely running model unconstrained by observations.

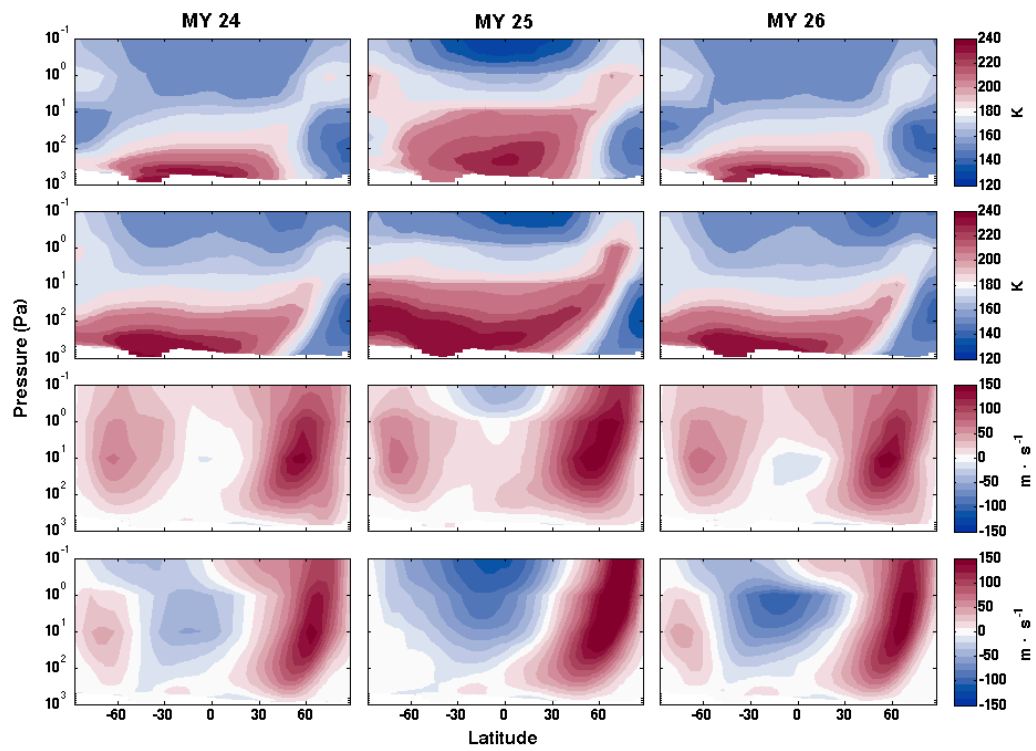


Figure A.3: The zonal mean temperature field for $L_s = 200^\circ$ (top row) and $L_s = 230^\circ$ (second row), and the mean zonal wind field for $L_s = 200^\circ$ (third row) and $L_s = 230^\circ$ (bottom row) for MY 24 (left), MY 25 (middle), and MY 26 (right).

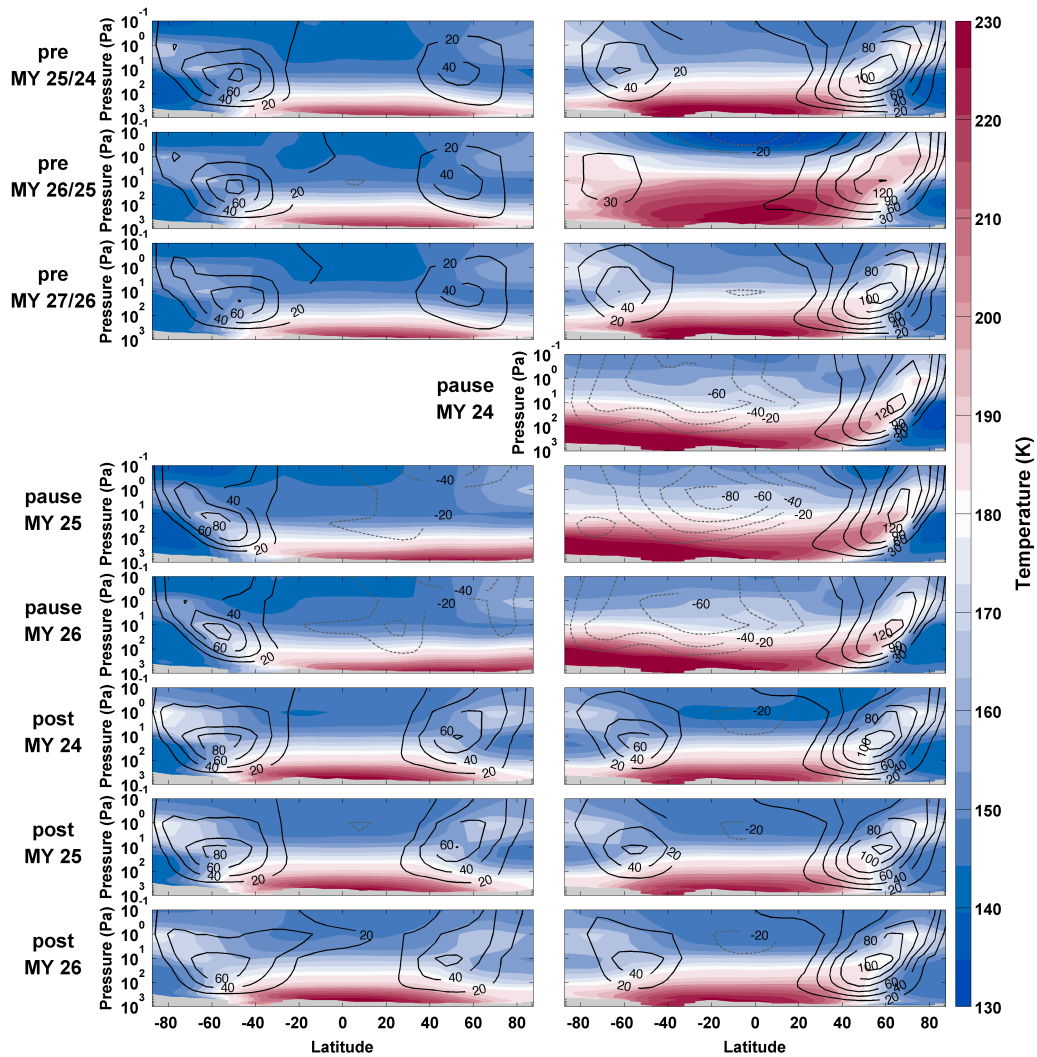


Figure A.4: Time-mean, zonal-mean temperature for the southern hemisphere (left) and northern hemisphere (right) for each of the pre-pause, pause, and post-pause periods. Contours are time-mean and zonal-means of the zonal wind with negative values dashed. Terrain is grayed.

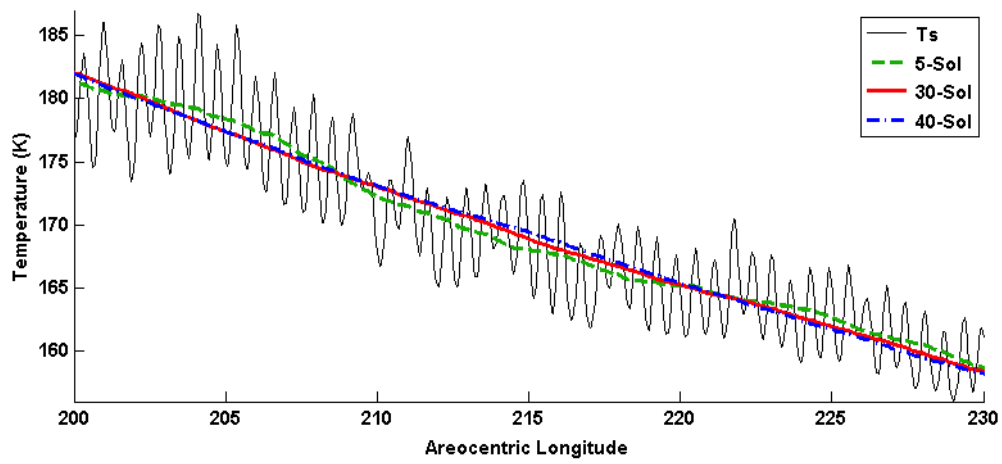


Figure A.5: Surface temperature with 5-sol, 30-sol, and 40-sol running means for the period $L_s = 200^\circ - 230^\circ$ for 52.5° N, 175° E in MY 26.

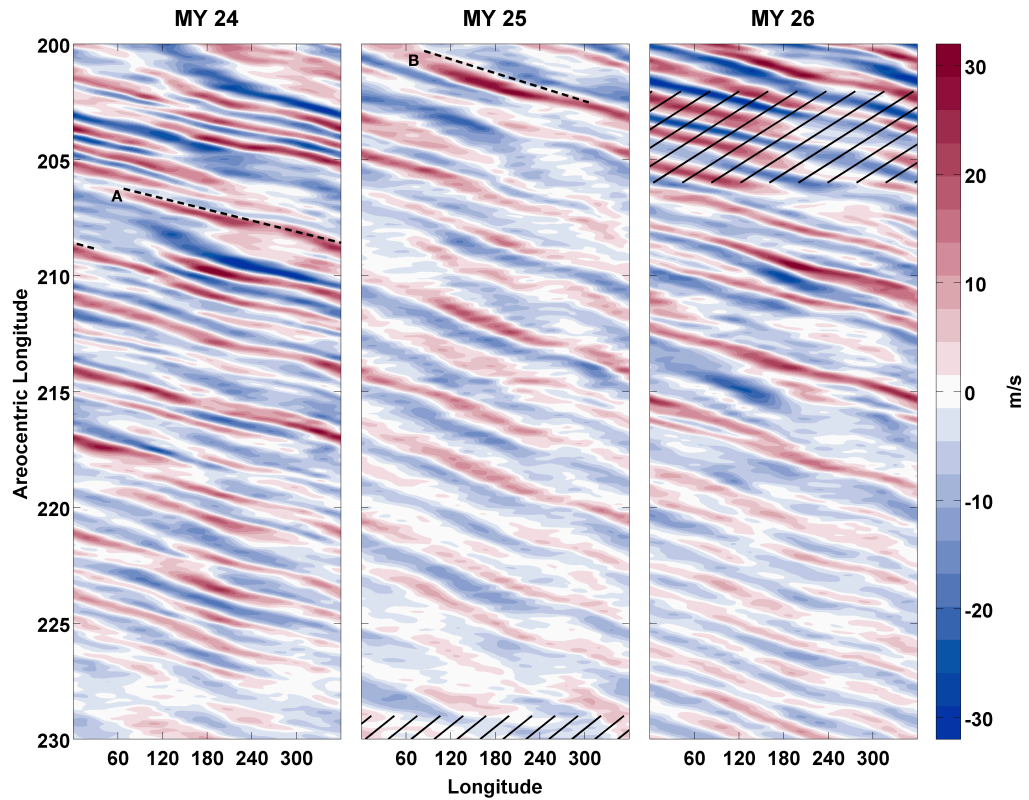


Figure A.6: Hovmöller diagram for the eddy component of the meridional wind field at 300 Pa for $L_s = 200^\circ - 230^\circ$ in the $57.5^\circ - 82.5^\circ$ N latitude band. Shown are MY 24 (left), MY 25 (middle), and MY 26 (right). Lines A and B refer to the location of storms discussed in sections 3.1.3.1 and 3.1.3.2. Hatching indicates times of areocentric longitude greater than one degree, when TES retrievals were unavailable, and the analyses are based on a freely running model unconstrained by observations.

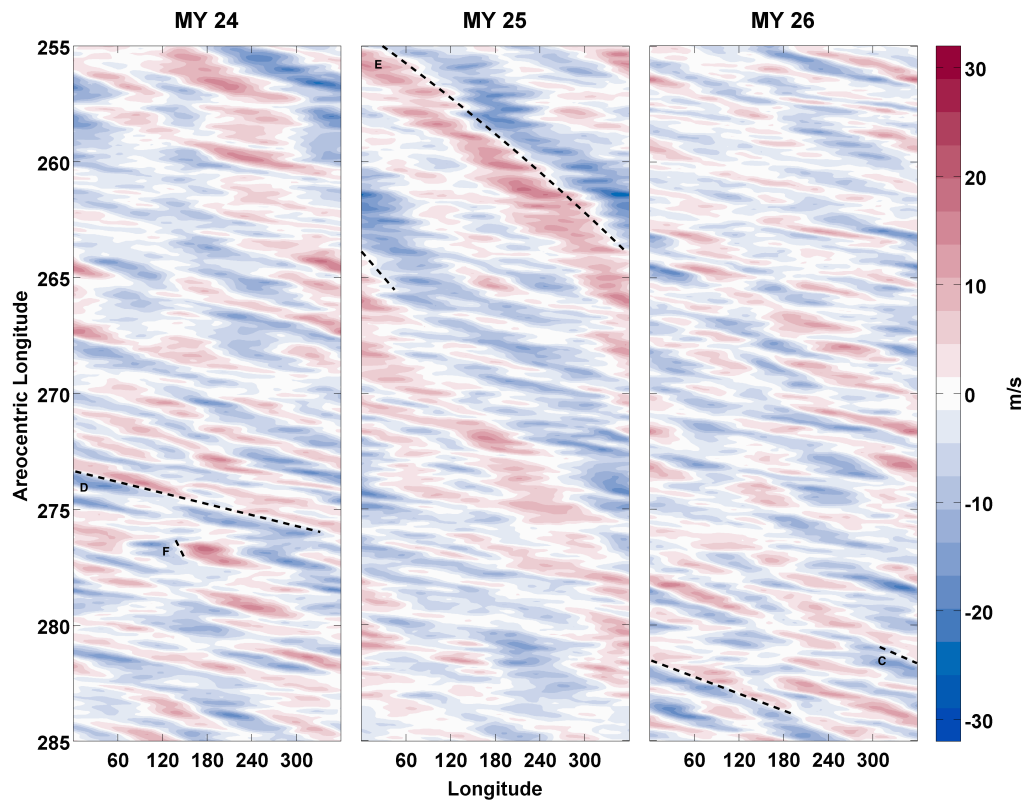


Figure A.7: As in Fig. A.6 but for $L_s = 255^\circ - 285^\circ$ and at 75 Pa. Lines C – F refer to the location of storms discussed in Section 3.2.3.

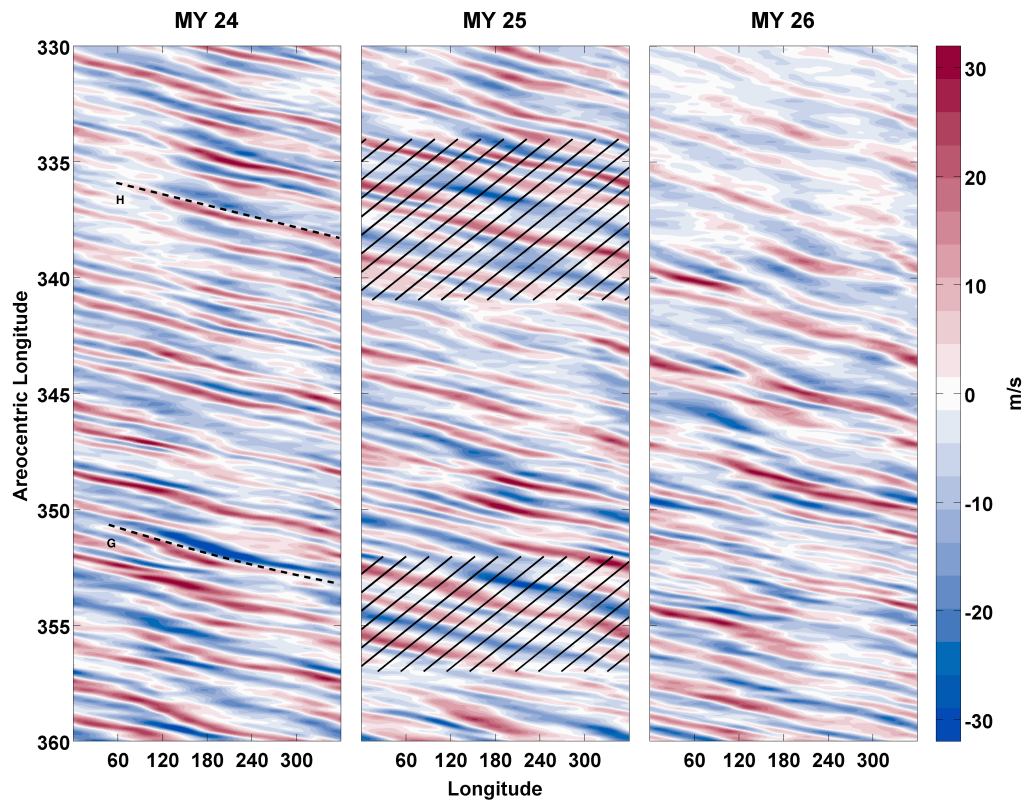


Figure A.8: As in Fig. A.6 but for $L_s = 330^\circ - 360^\circ$. Lines G and H refer to the location of storms discussed in Section 3.2.4.

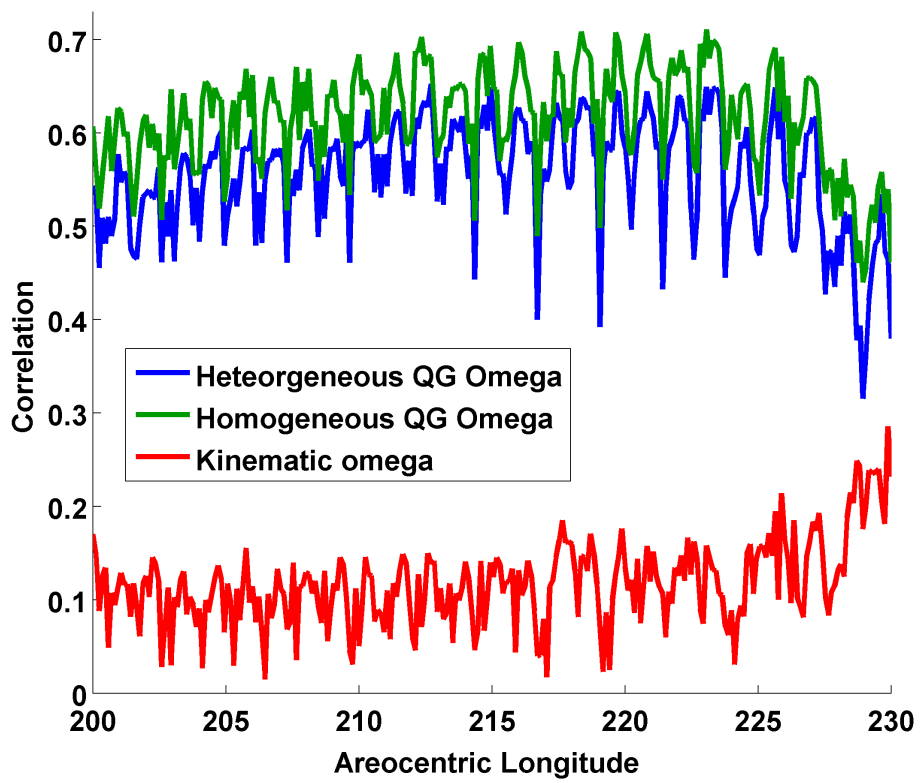


Figure A.9: Correlation of the two forms of quasi-geostrophic ω and kinematic ω to the Kavulich et al. (2013) GFDL simulation ω between 28° and 80° N for all pressure levels.

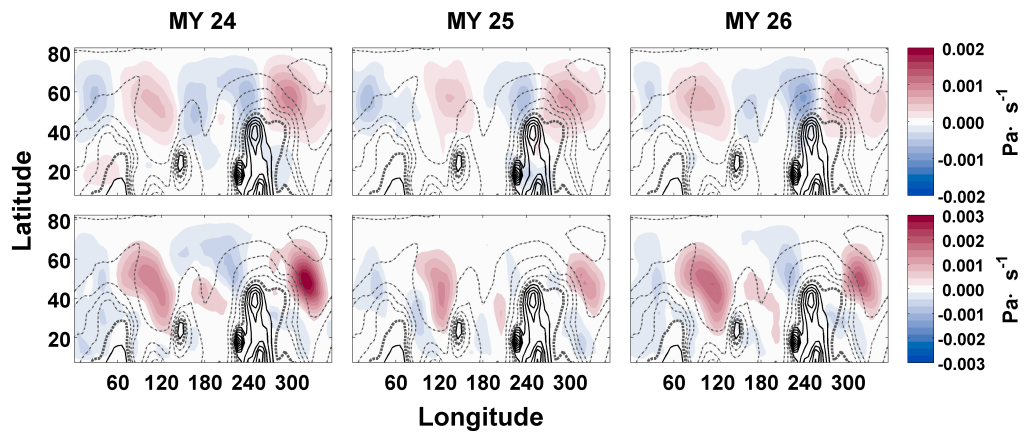


Figure A.10: The time-mean vertical velocities for $L_s = 200^\circ - 230^\circ$ for the 100-Pa (top) and 400-Pa (bottom) pressure level for MY 24 (left), MY 25 (middle), and MY 26 (right). Contours are surface elevation in 1000 m increments. Values below the mean geoid are dashed, with the mean geoid bolded.

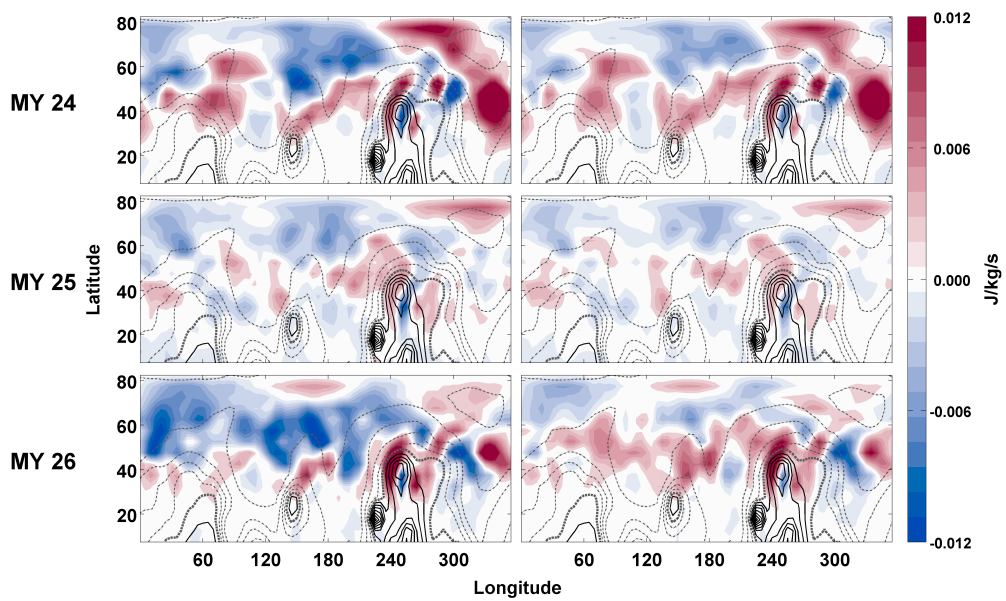


Figure A.11: Geopotential flux convergence, $-\overline{\nabla_3 \cdot \mathbf{v}'_3 \phi'}$, at 100 Pa for MY 24 (top), MY 25 (middle), and MY 26 (bottom) for the time-mean $L_s = 200^\circ - 230^\circ$. The geopotential flux convergence is calculated in the advective form (left) and in the flux form (right). Contours are surface elevation in 2500 m increments.

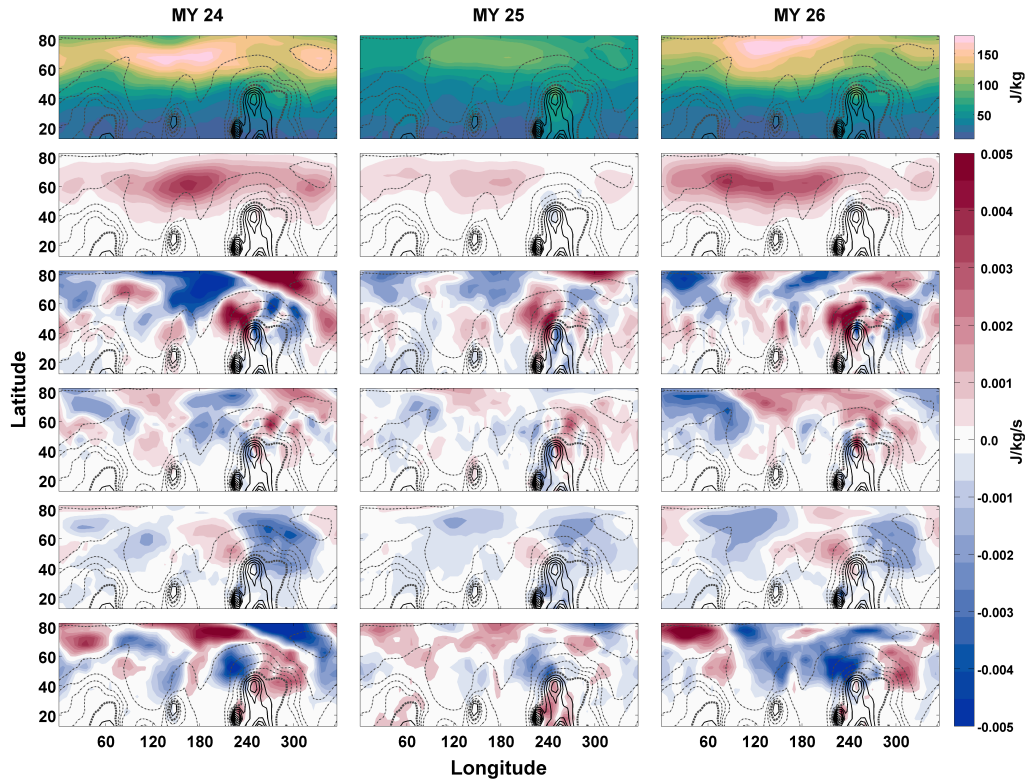


Figure A.12: Pressure-weighted vertical averages of the time mean of the terms of the eddy kinetic energy equation for $L_s = 200^\circ - 230^\circ$ for MY 24 (left column), MY 25 (center column), and MY 26 (right column). Shown are the eddy kinetic energy (top), baroclinic energy conversion (second row), geopotential flux convergence (third row), the eddy kinetic energy advection (fourth row), the barotropic energy conversion (fifth row), and the residue (bottom). Contours are surface elevation in 1000 m increments. Values below the mean geoid are dashed, with the mean geoid bolded.

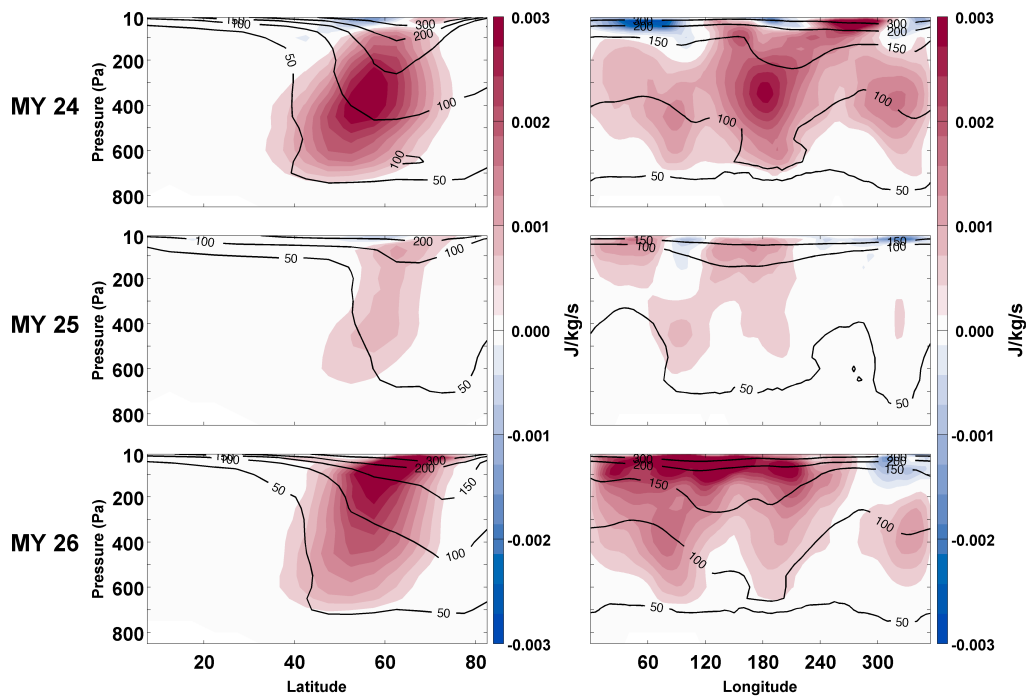


Figure A.13: Vertical cross sections of the time-mean ($L_s = 200^\circ - 230^\circ$) of the zonal mean (left column) and meridional mean (right column) of baroclinic energy conversion, $-\omega'\alpha'$ and the eddy kinetic energy (J/kg) contoured. The meridional mean is computed for the $57.5^\circ - 82.5^\circ$ N latitude band. Results are shown for MY 24 (top), MY 25 (middle), and MY 26 (bottom).

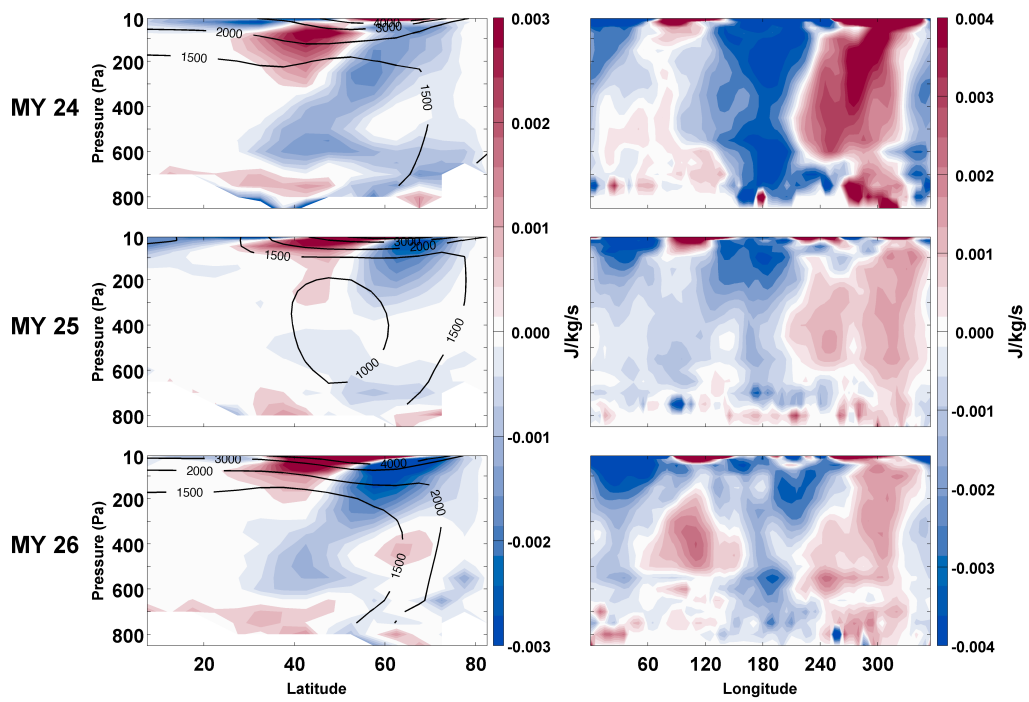


Figure A.14: As in Fig. A.13 but for geopotential flux convergence, $-\overline{\nabla_3 \cdot \mathbf{v}'_3 \phi'}$. Contours show the standard deviation of the geopotential height (gpm).

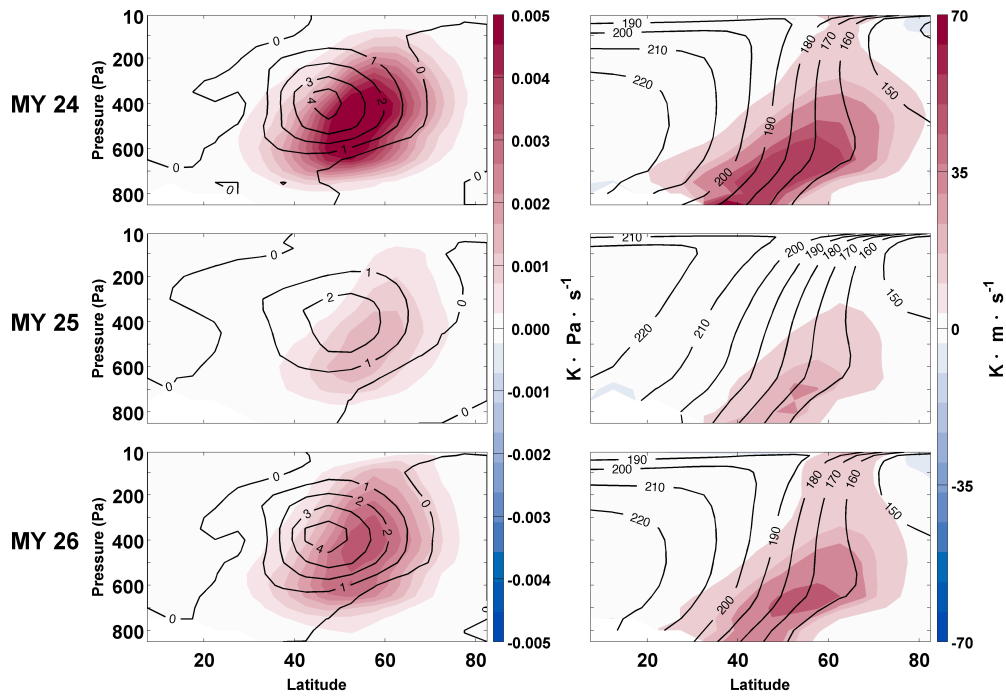


Figure A.15: As in Fig. A.13 but for the zonal mean of the vertical heat flux, $-\overline{T'\omega'}$, (left column) and meridional heat flux, $\overline{T'v'}$, (right column). Contours show temporal mean of vertical motion (10^{-4} Pa/s) (left) and temporal mean of temperature field (K) (right).

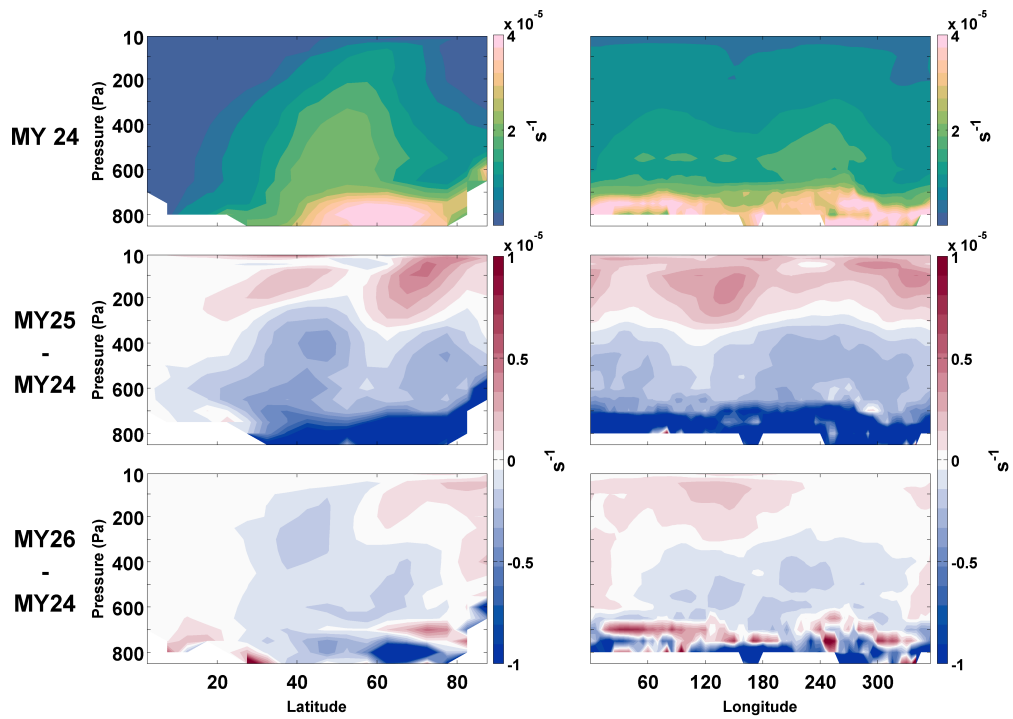


Figure A.16: As in Fig. A.13 but for the Eady index. Results are shown for MY 24 (top), the difference between MY 25 and MY 24 (middle), and the difference between MY 25 and MY 24 (bottom).

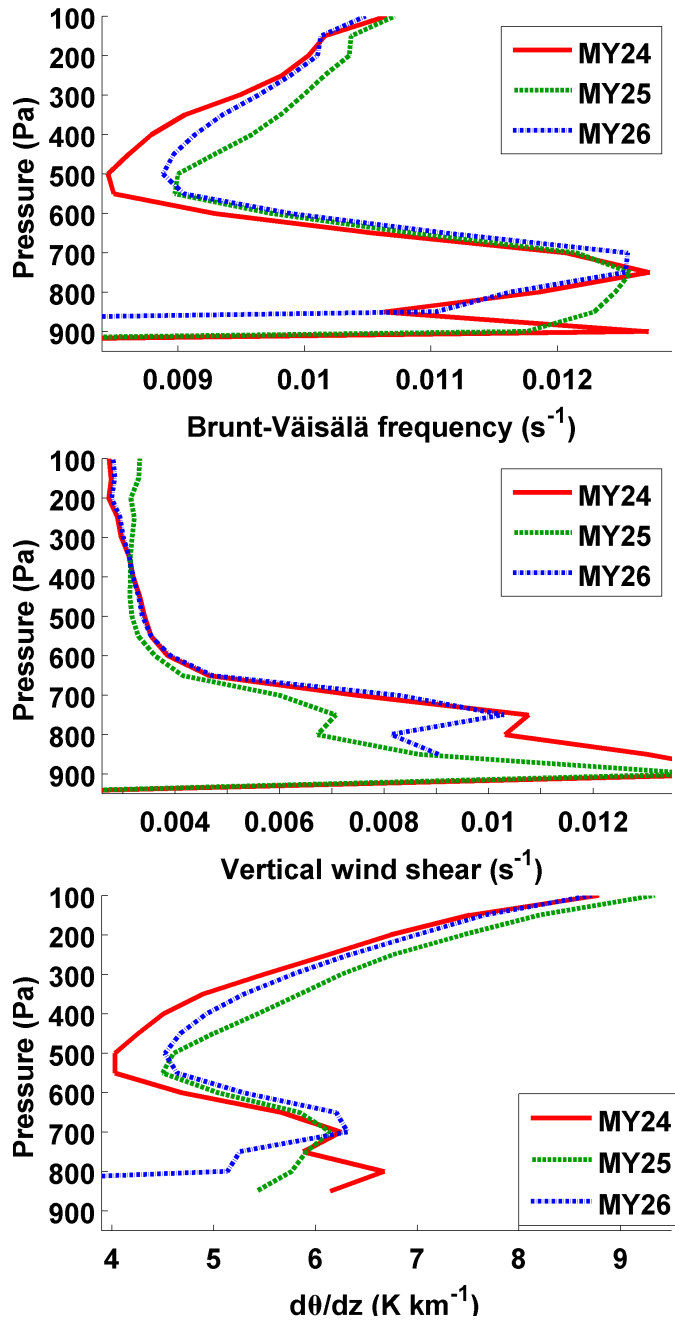


Figure A.17: Brunt-Väisälä frequency vertical profile (top), vertical wind shear (middle), and potential temperature gradient (bottom) for the time-mean $L_s = 200^\circ - 230^\circ$ of the $57.5^\circ - 82.5^\circ$ N latitude band.

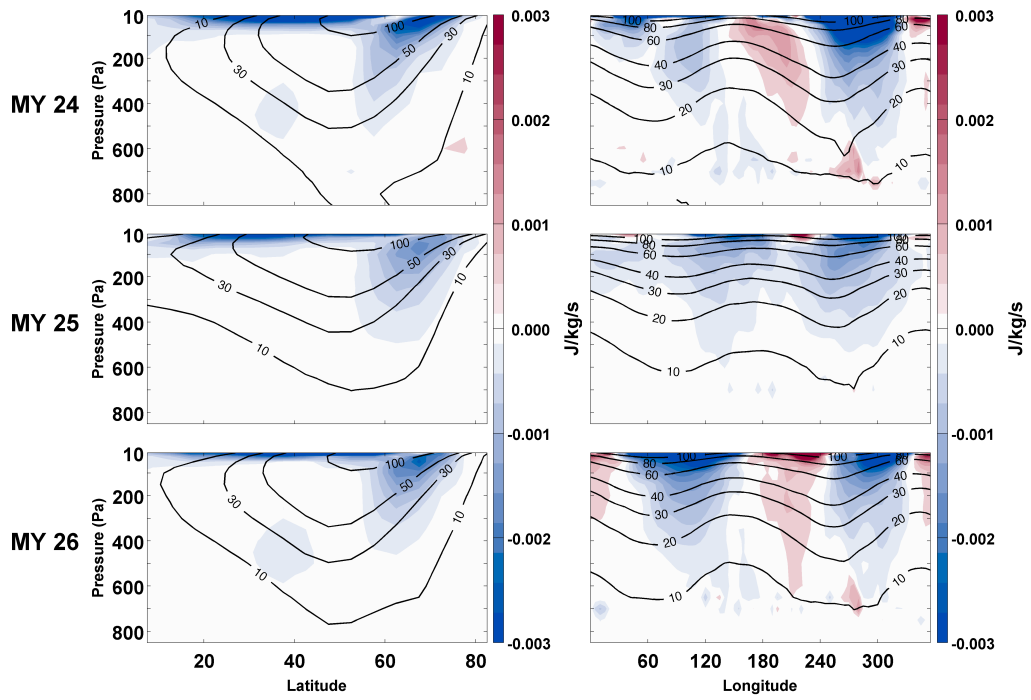


Figure A.18: As in Fig. A.13 but for barotropic energy conversion, $-\mathbf{v}' \cdot (\mathbf{v}'_3 \cdot \nabla_3) \mathbf{v}_m - \mathbf{v}' \cdot (\mathbf{v}'_3 \cdot \nabla_3) \mathbf{v}'$. Contours show zonal average zonal wind (m/s) (left) and meridional average zonal wind (m/s) (right).

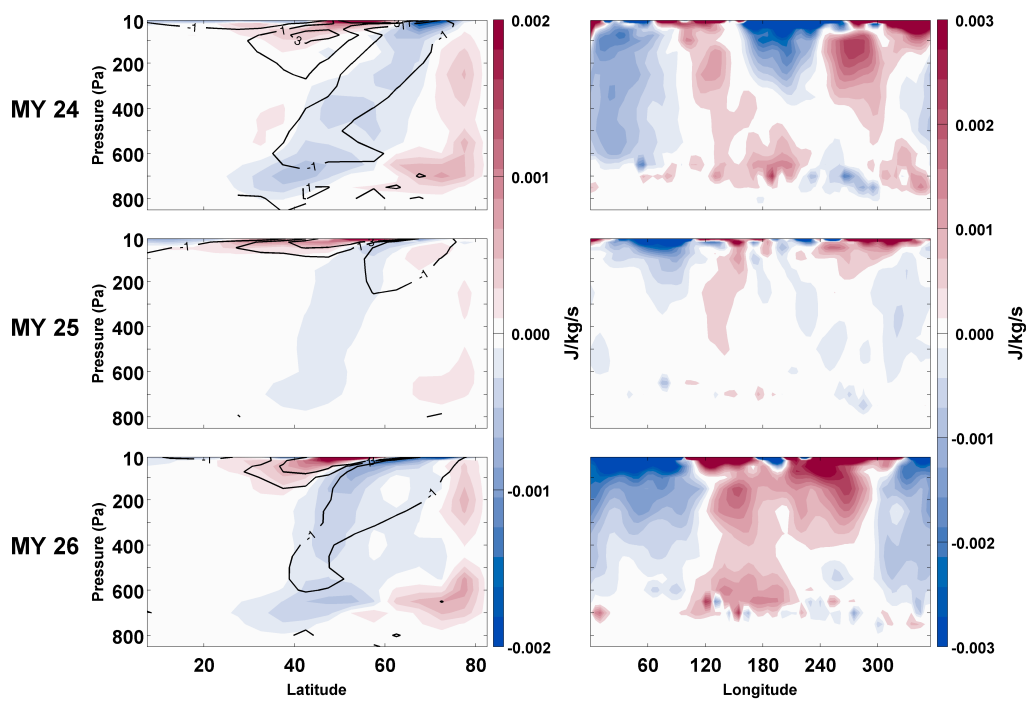


Figure A.19: As in Fig. A.13 but for EKE advection, $-\nabla \cdot \mathbf{v}K_e$. Contours show average total EKE advection, $-\nabla \cdot \mathbf{v}K_e - \overline{\nabla_3 \cdot \mathbf{v}'_3 \phi'}$ (mJ/kg/s).

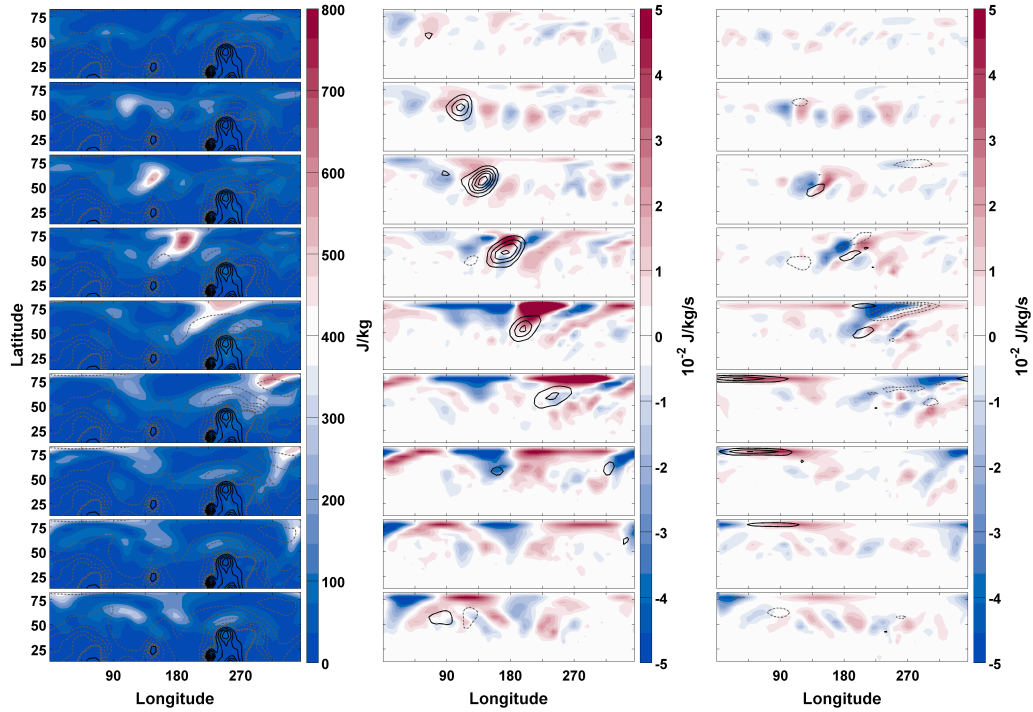


Figure A.20: Time series of vertical, pressure-weighted averages of eddy kinetic energy (left), with topography contoured as in Fig. A.12, geopotential flux convergence (middle), with baroclinic energy conversion contoured at 0.007 J/kg/s increments and negative values dashed, and eddy kinetic energy advection (right), with barotropic energy conversion contoured at 0.007 J/kg/s increments and negative values dashed for a 4-sol period traveling wave in MY 24 beginning at $L_s = 206.6^\circ$ and continuing at 0.5-sol steps until $L_s = 209.1^\circ$.

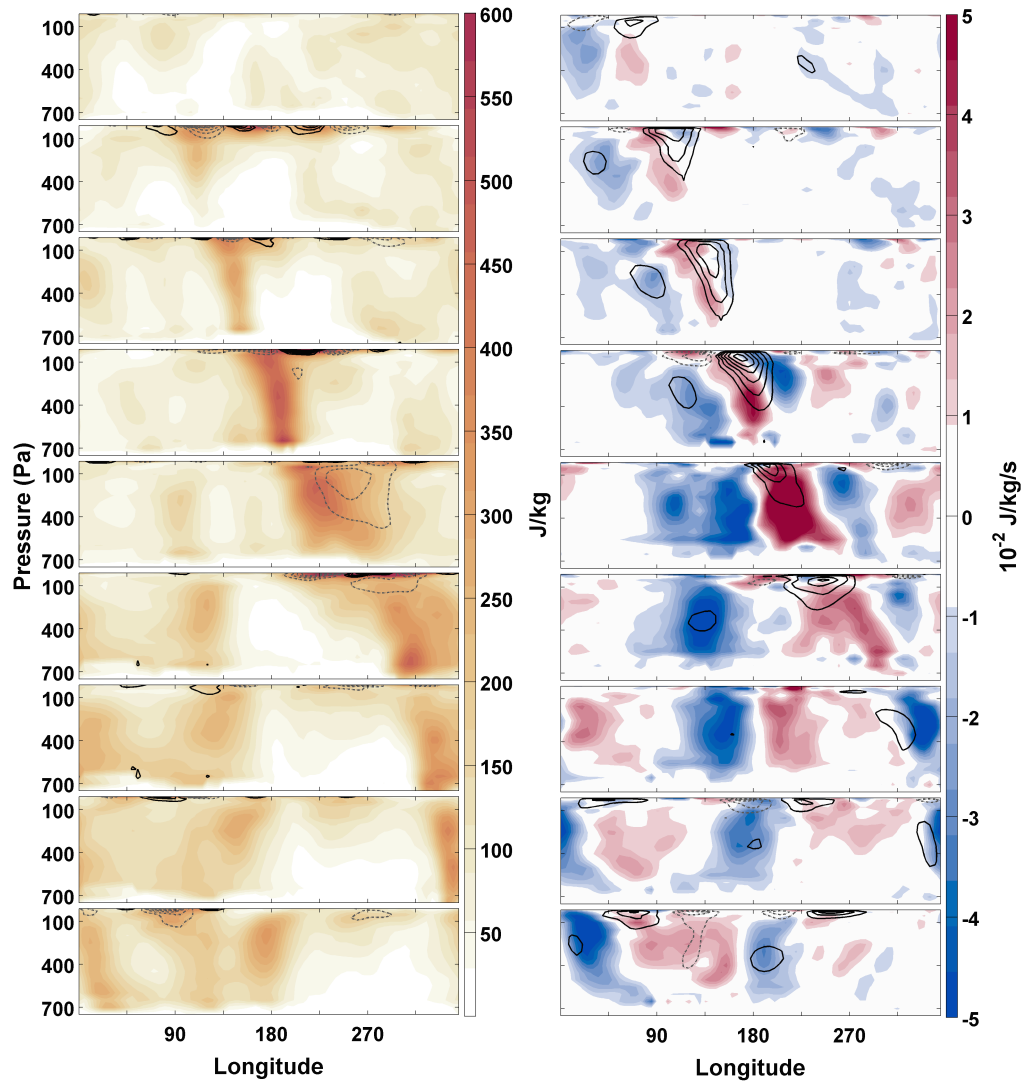


Figure A.21: Time series of the meridional average of eddy kinetic energy (left), with barotropic energy conversion contoured in 0.007 J/kg/s increments and negative values dashed and geopotential flux convergence (right), with baroclinic energy conversion contoured in 0.007 J/kg/s increments and negative values dashed in the $57.5^\circ - 82.5^\circ \text{ N}$ latitude band for the wave in Fig. A.20.

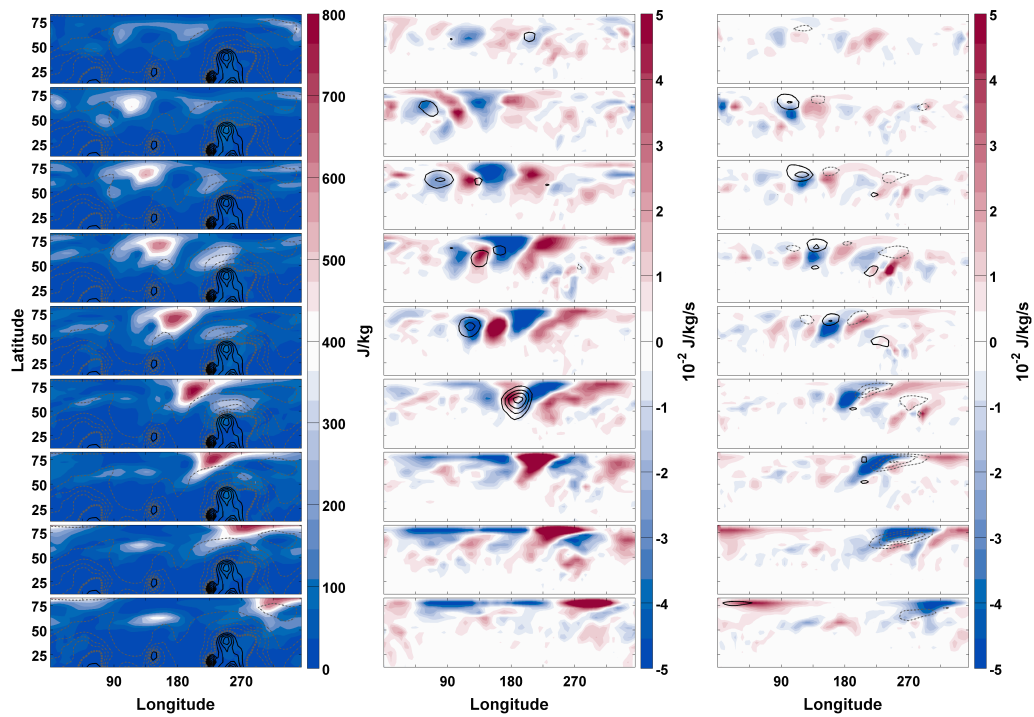


Figure A.22: As in Fig. A.20 but for a 4-sol period traveling wave in MY 25 beginning at $L_s = 201.1^\circ$ and continuing at 0.33-sol steps until $L_s = 202.7^\circ$.

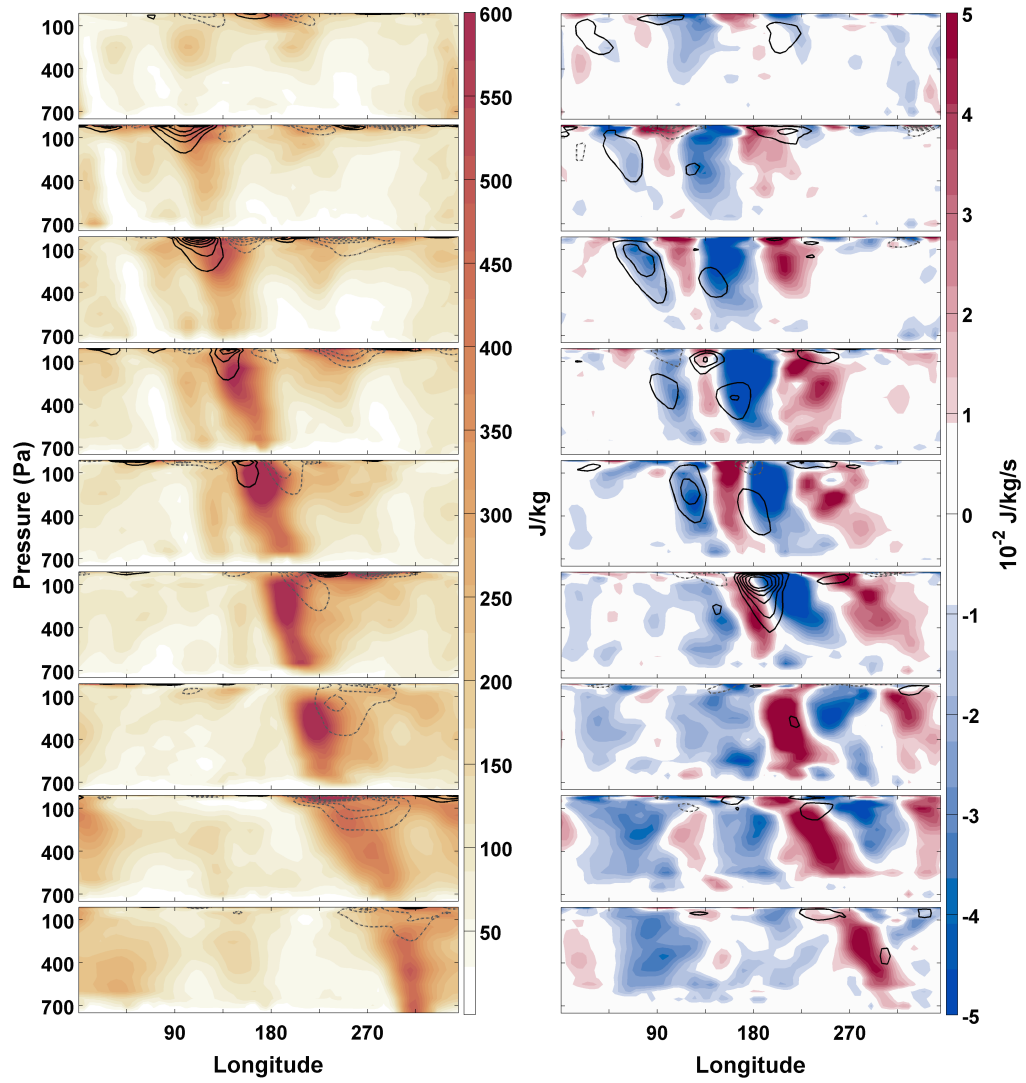


Figure A.23: As in Fig. A.21 but for the wave in Fig. A.22.

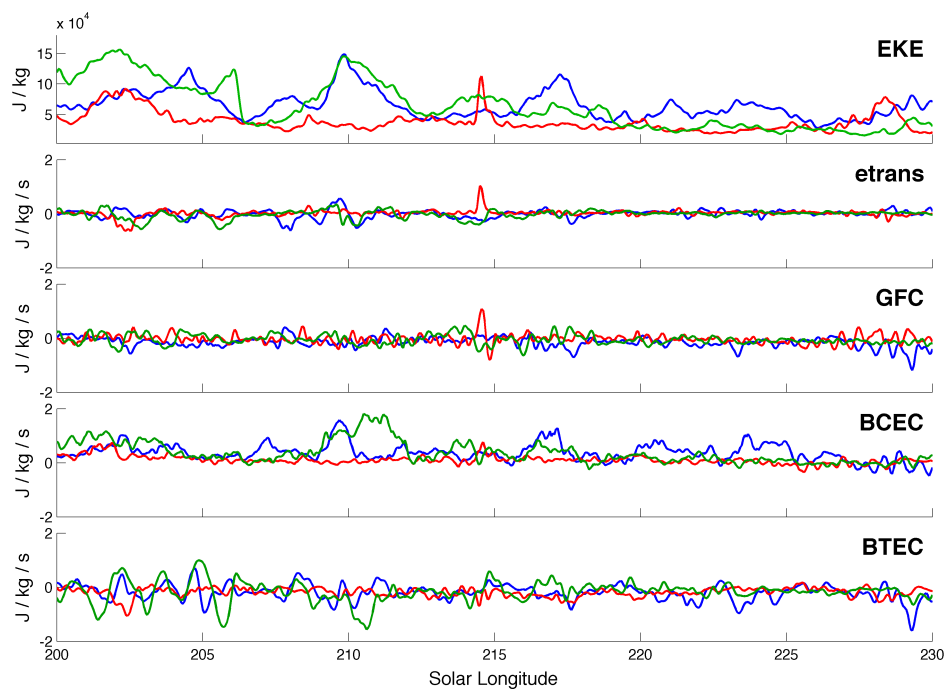


Figure A.24: Time series of the volume integrated EKE and EKE equation terms for the $22.5^{\circ} - 82.5^{\circ}$ N latitude band for MY 24 (blue), MY 25 (red), and MY 26 (green).

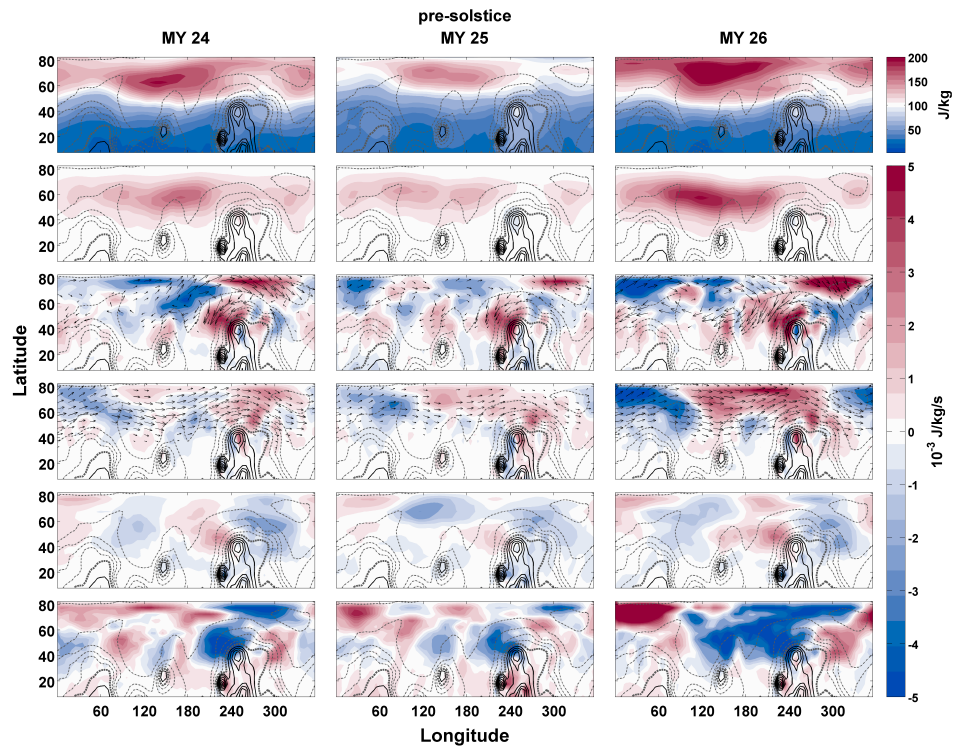


Figure A.25: As in Fig. A.12 but for $L_s = 190^\circ - 220^\circ$. The ageostrophic geopotential flux and EKE advection vectors are shown on their respective panels.

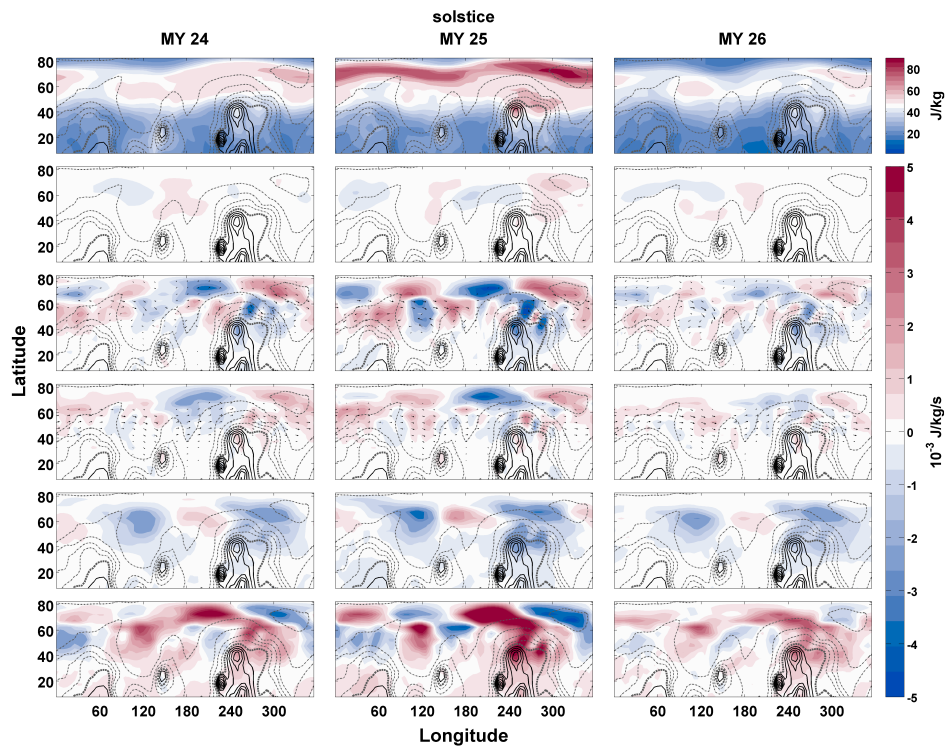


Figure A.26: As in Fig. A.25 but for $L_s = 255^\circ - 285^\circ$.

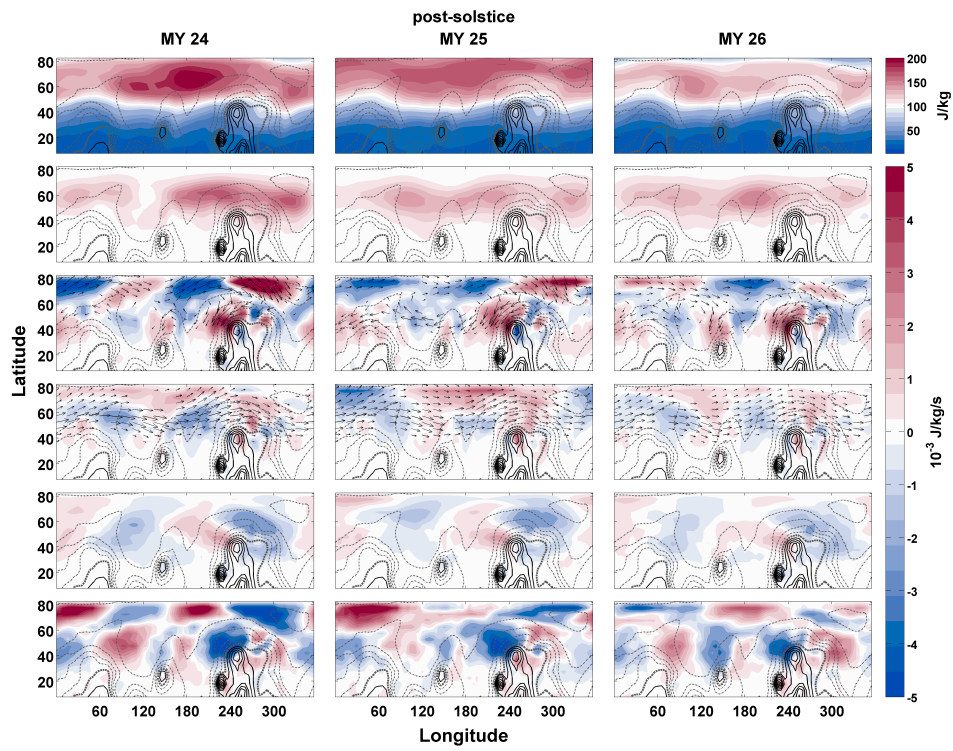


Figure A.27: As in Fig. A.25 but for $L_s = 330^\circ - 360^\circ$.

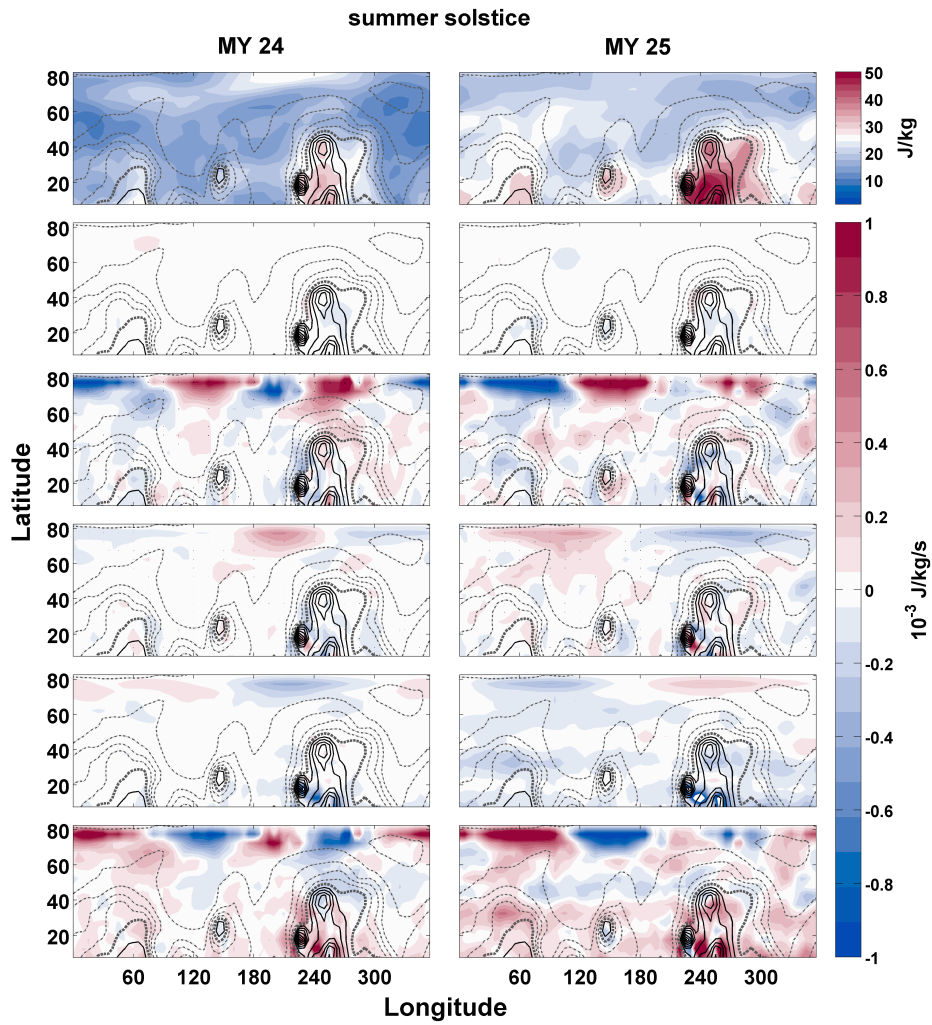


Figure A.28: As in Fig. A.25 but for $L_s = 90^\circ - 120^\circ$.

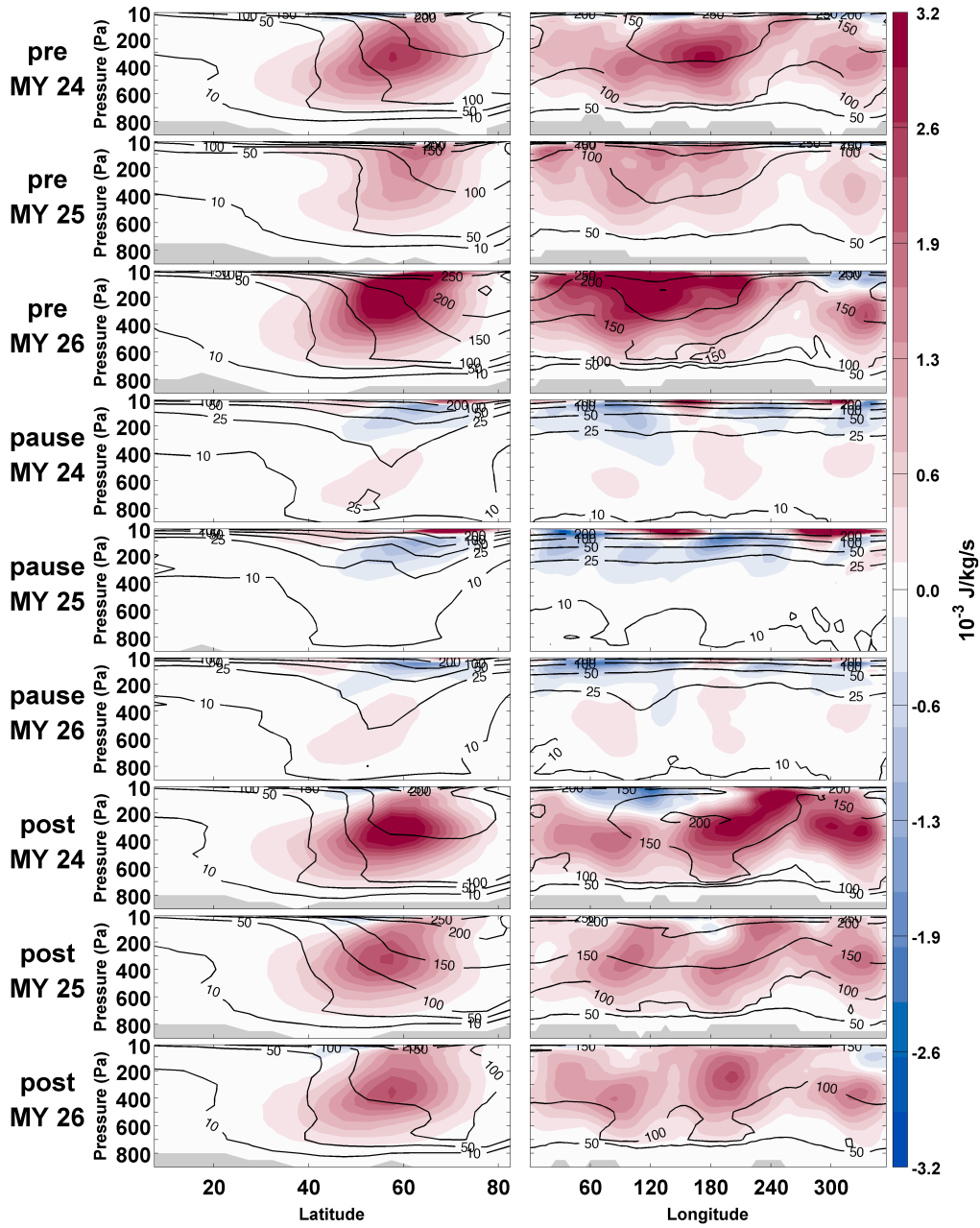


Figure A.29: Baroclinic energy conversion during three fall (pre: $L_s = 190^\circ - L_s = 220^\circ$), three winter (pause: $L_s = 255^\circ - L_s = 285^\circ$), and three spring (post: $L_s = 330^\circ - L_s = 360^\circ$) periods in the northern hemisphere in the zonal (left column), and meridional (right column) average. Contours are average zonal EKE (J/kg). Terrain is grayed.

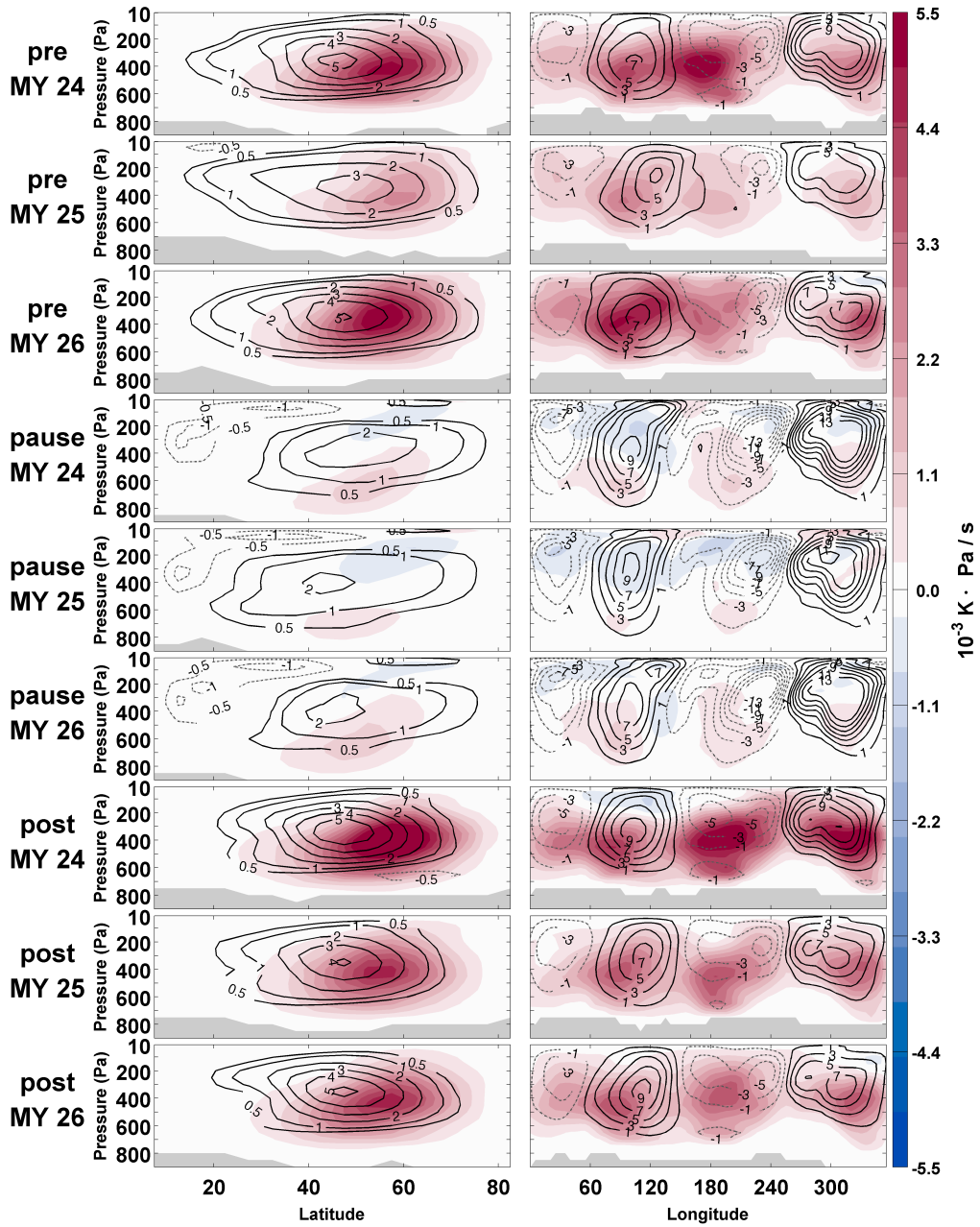


Figure A.30: As in Fig. A.29 but for vertical heat flux. Contours are average vertical velocity (10^{-4} Pa/s).

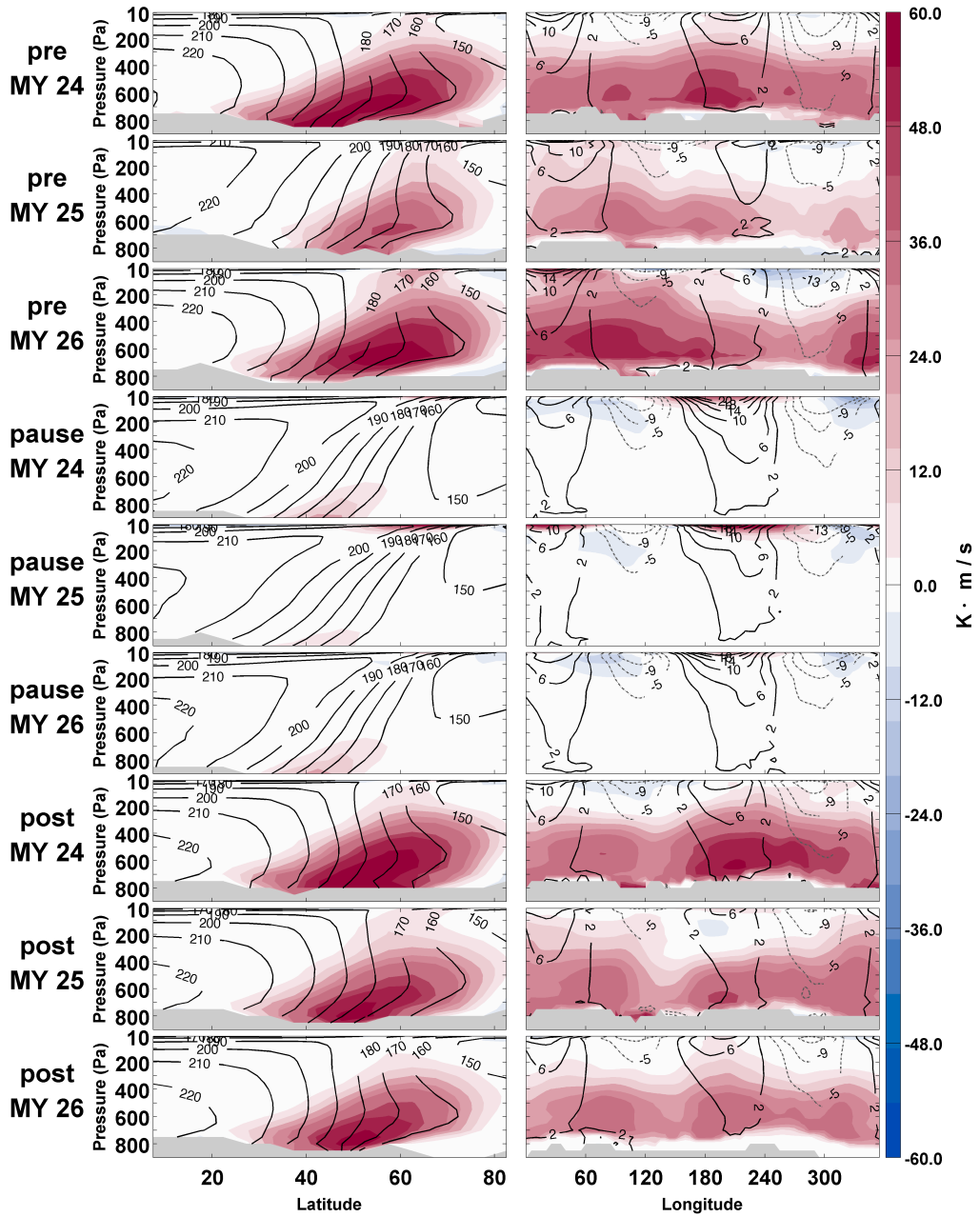


Figure A.31: As in Fig. A.29 but for meridional heat flux. Contours are average temperature (K) (left column) and average meridional wind (m/s).

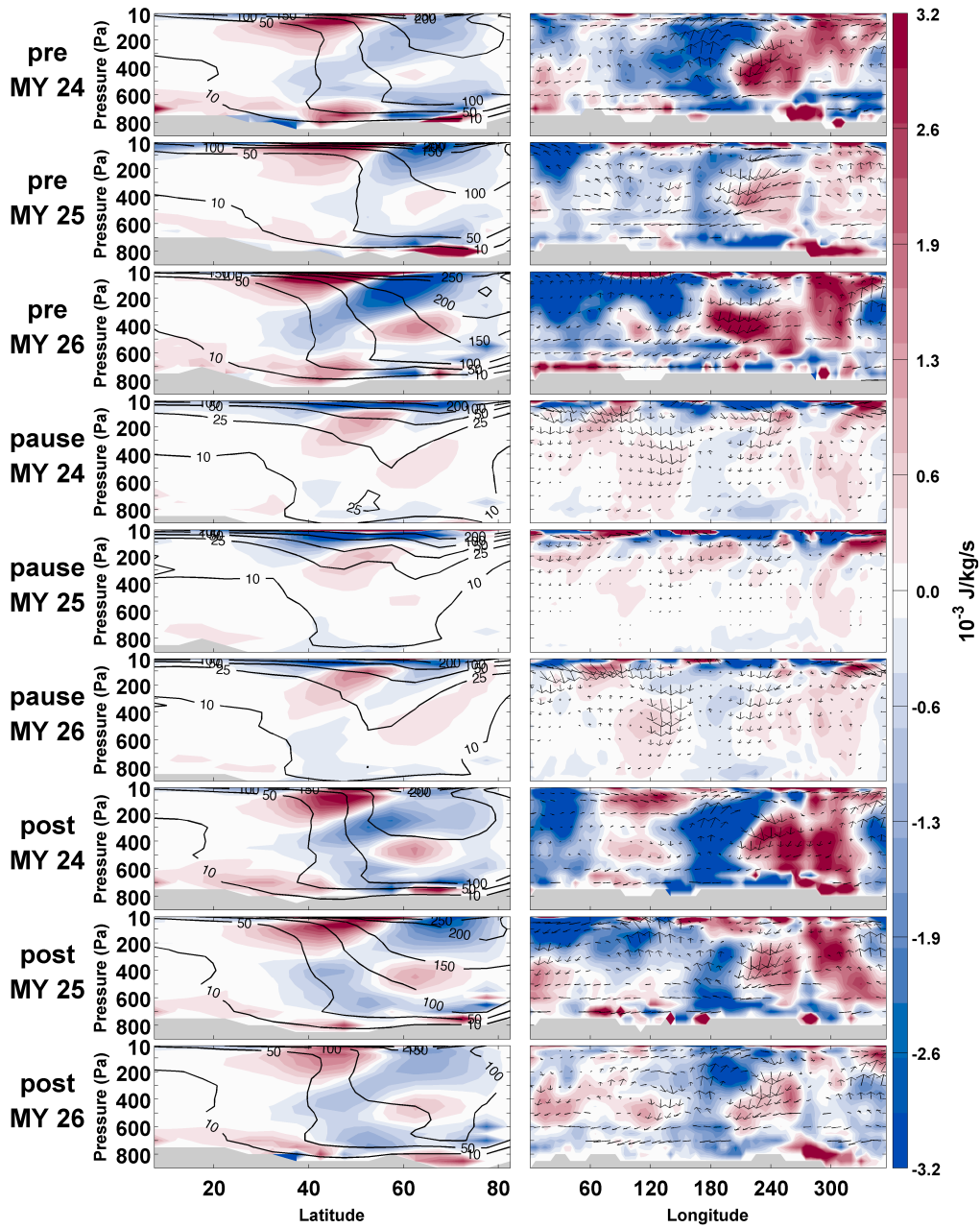


Figure A.32: As in Fig. A.29 but for geopotential flux convergence. Contours are average zonal EKE (J/kg). Right column shows the ageostrophic geopotential vectors, with the vertical direction scaled by 100.

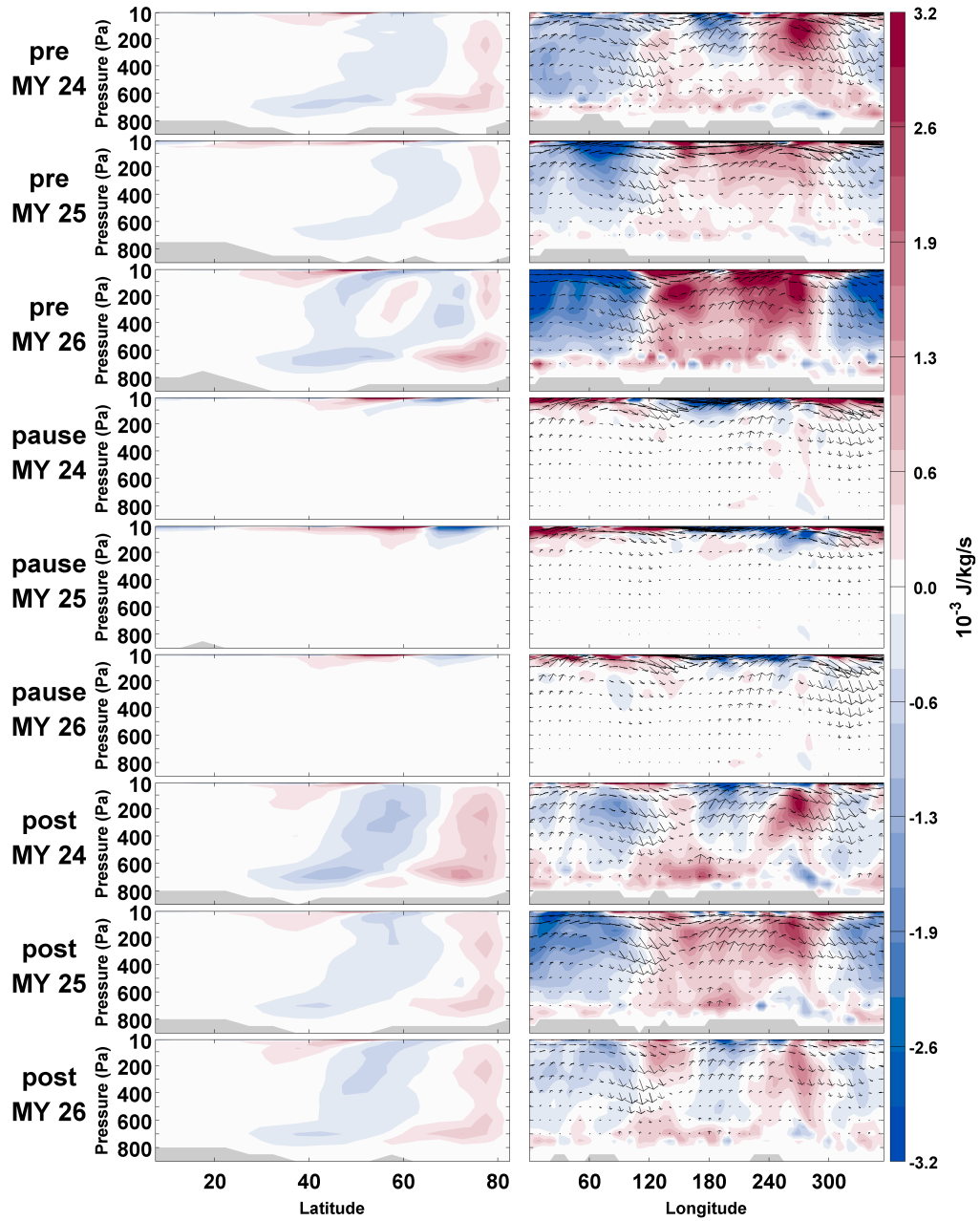


Figure A.33: As in Fig. A.29 but for EKE advection. Right column shows the EKE advection vectors, with the vertical direction scaled by 100.

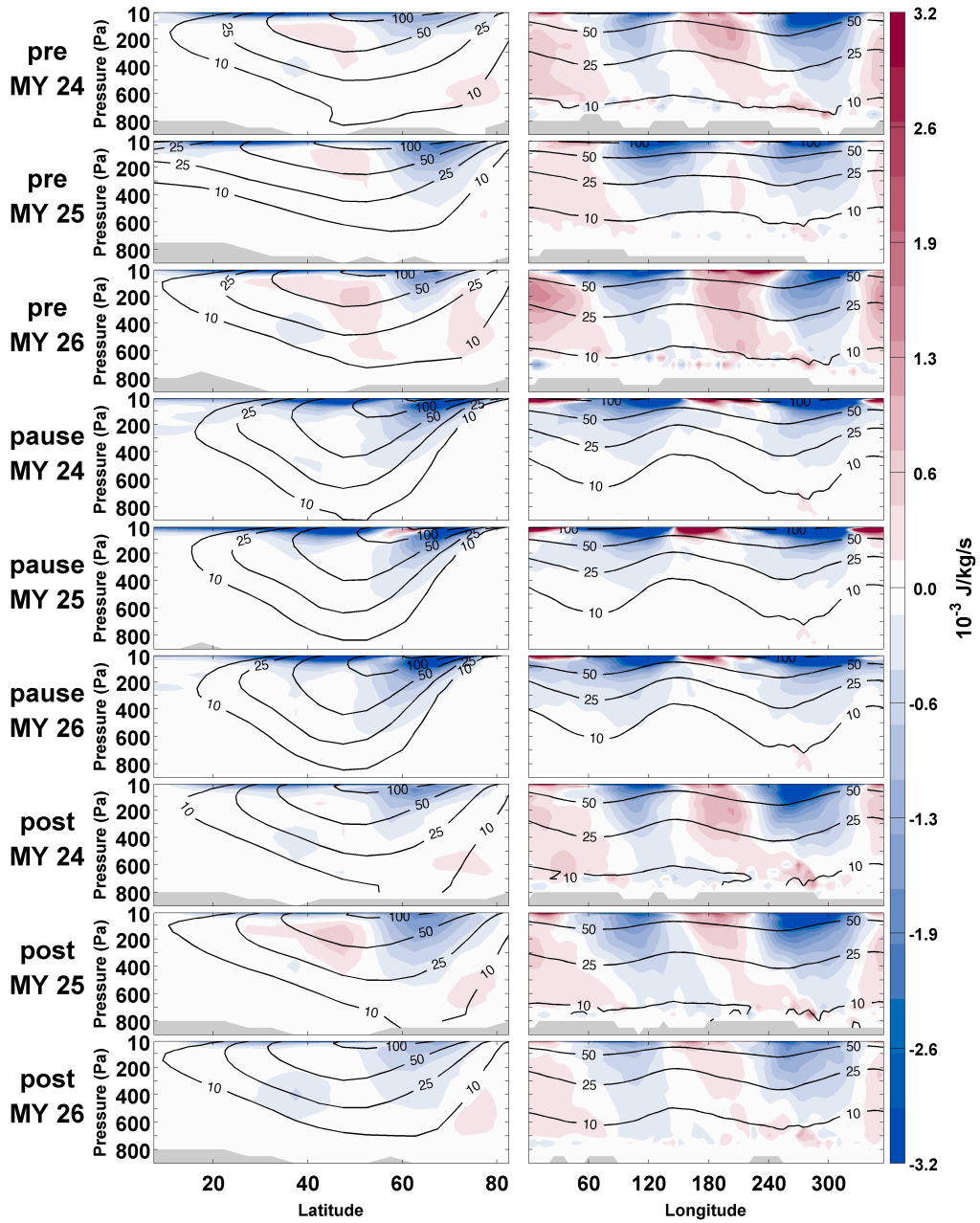


Figure A.34: As in Fig. A.29 but for barotropic energy conversion. Contours are average zonal wind (m/s).

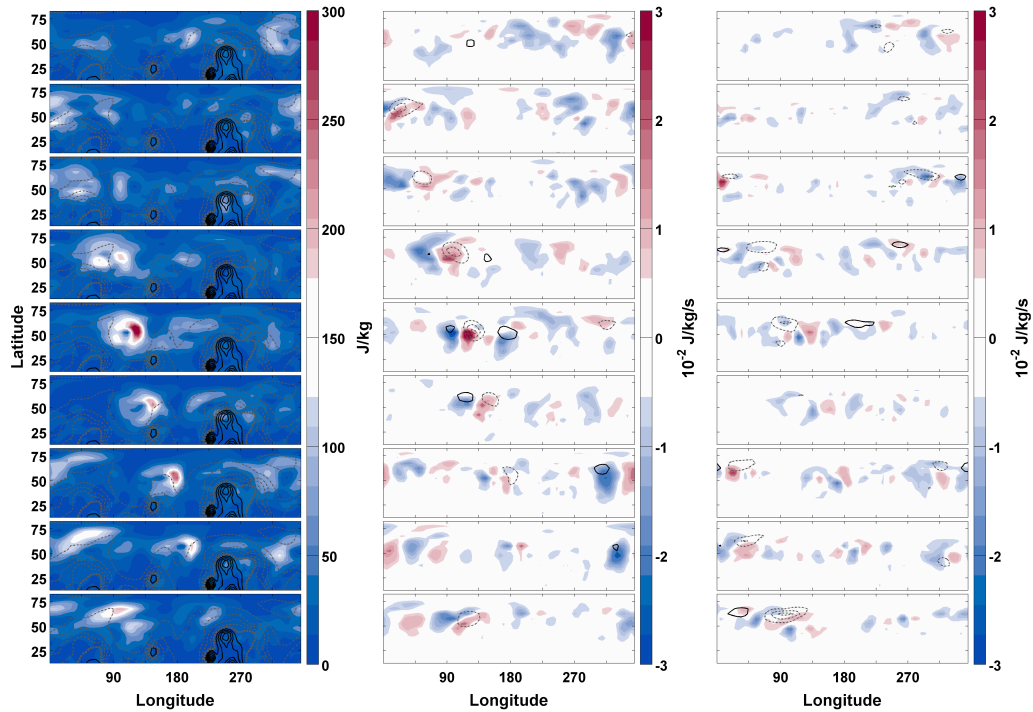


Figure A.35: Time series of vertical, pressure-weighted averages of eddy kinetic energy (left), with topography contoured as in Fig. A.12; geopotential flux convergence (middle), with baroclinic energy conversion contoured at 0.006 J/kg/s increments and negative values dashed; and eddy kinetic energy advection (right), with barotropic energy conversion contoured at 0.006 J/kg/s increments and negative values dashed for a 6-sol period traveling wave in MY 26 beginning at $L_s = 281.6^\circ$ and continuing at 0.5-sol steps until $L_s = 284.2^\circ$.

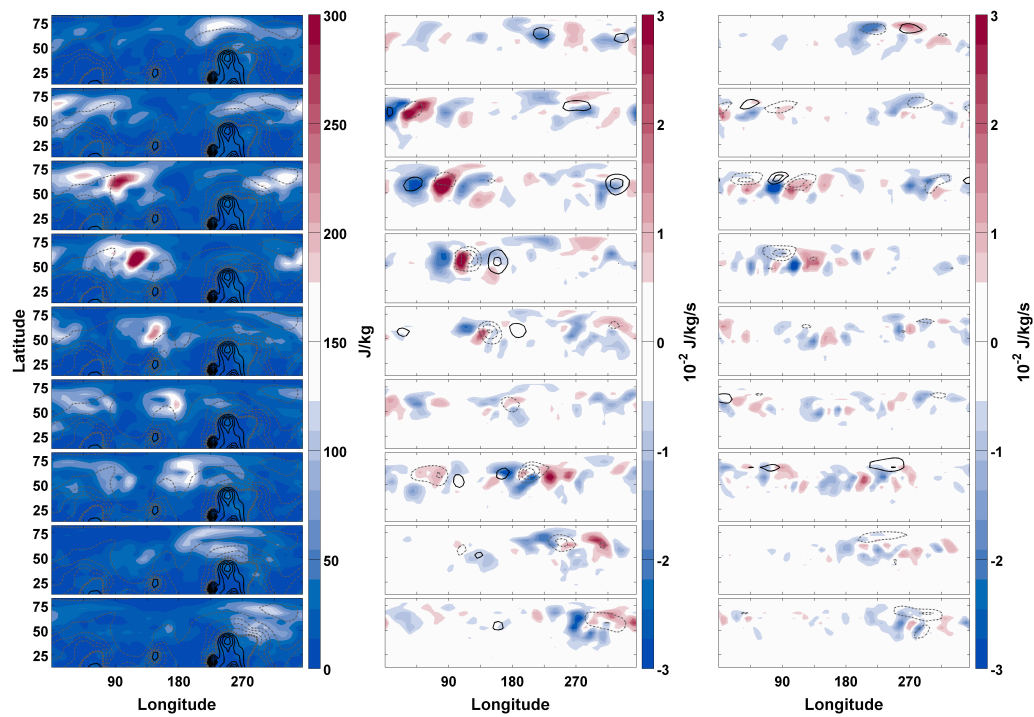


Figure A.36: As in Fig. A.35 but for a 8-sol period traveling wave in MY 24 beginning at $L_s = 273.3^\circ$ and continuing at 0.5-sol steps until $L_s = 275.8^\circ$.

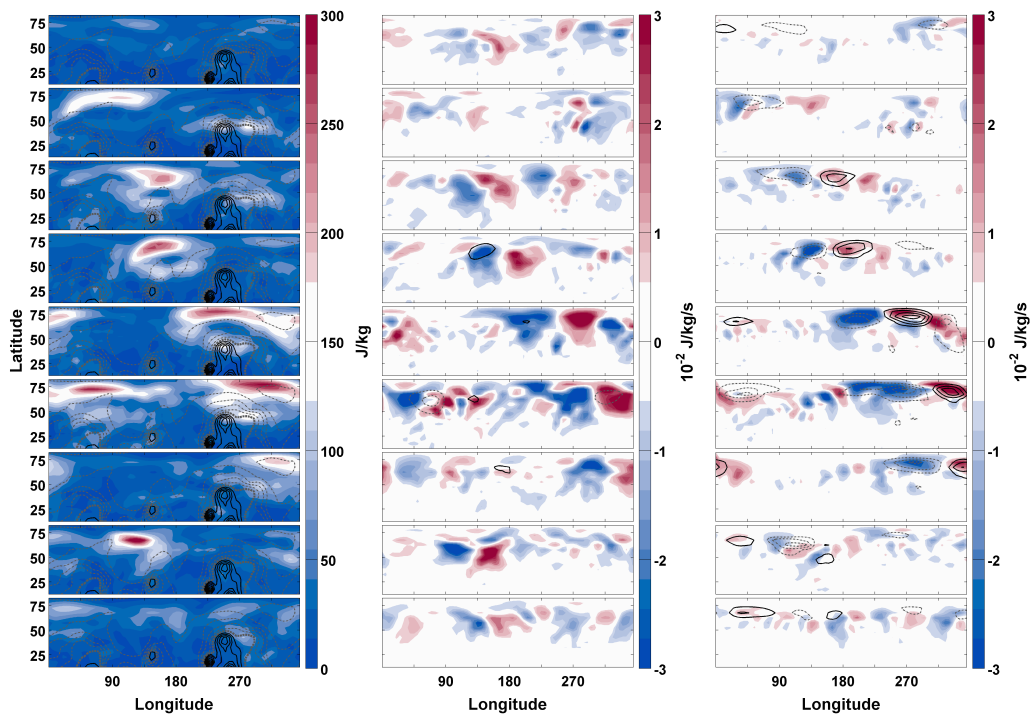


Figure A.37: As in Fig. A.35 but for a 16-sol wave in MY 25 beginning at $L_s = 255.0^\circ$ and continuing at 2-sol steps until $L_s = 265.4^\circ$.

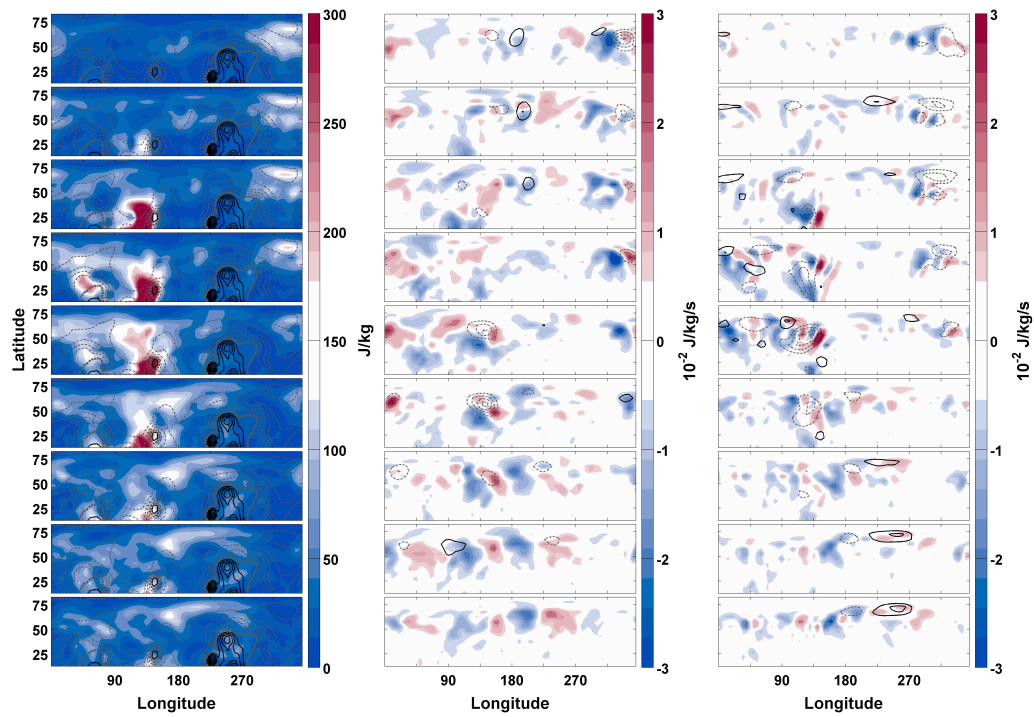


Figure A.38: As in Fig. A.35 but for a stationary wave in MY 24 beginning at $L_s = 276.1^\circ$ and continuing at 0.17-sol steps until $L_s = 277.0^\circ$.

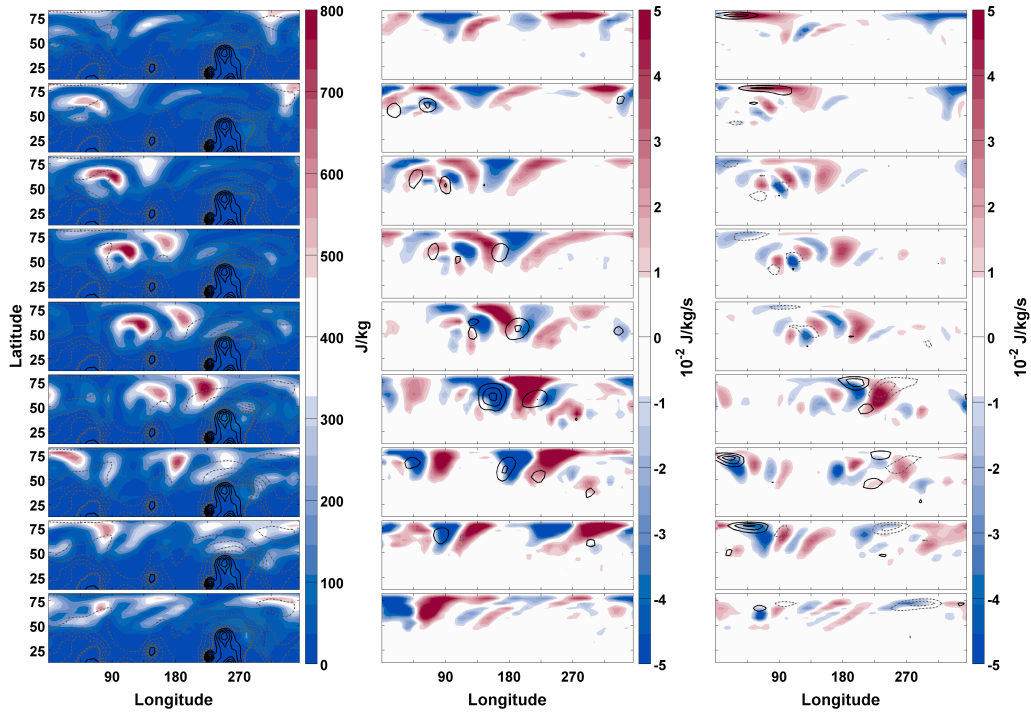


Figure A.39: Time series of vertical, pressure-weighted averages of eddy kinetic energy (left), with topography contoured as in Fig. A.12; geopotential flux convergence (middle), with baroclinic energy conversion contoured at 0.007 J/kg/s increments and negative values dashed; and eddy kinetic energy transport (right), with barotropic energy conversion contoured at 0.007 J/kg/s increments and negative values dashed for a 5-sol period traveling wave in MY 24 beginning at $L_s = 350.7^\circ$ and continuing at 0.5 sol steps until $L_s = 352.8^\circ$.

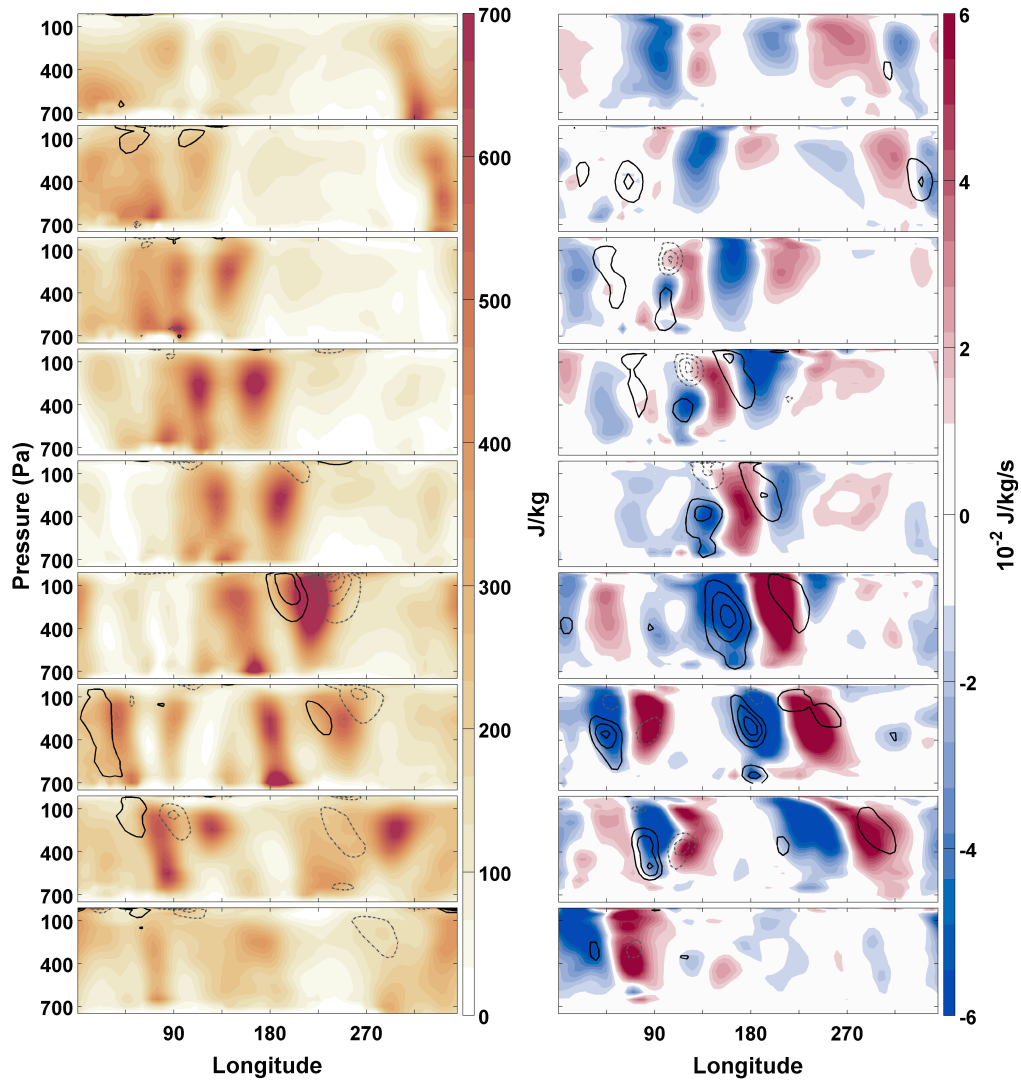


Figure A.40: Time series of the meridional average of eddy kinetic energy (left), with barotropic energy conversion contoured in 0.007 J/kg/s increments and negative values dashed and geopotential flux convergence (right), with baroclinic energy conversion contoured in 0.007 J/kg/s increments and negative values dashed in the $57.5^\circ - 82.5^\circ \text{ N}$ latitude band for the wave in Fig. A.39.

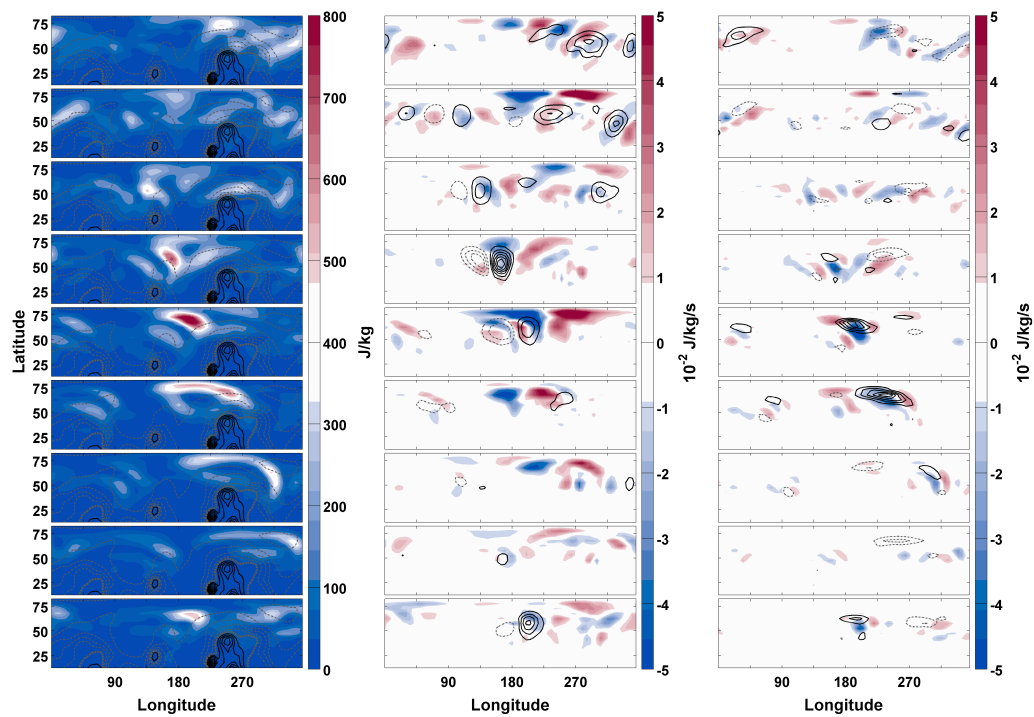


Figure A.41: As in Fig. A.39 but for a 5-sol period traveling wave in MY 24 beginning at $L_s = 336.1^\circ$ and continuing at 0.583-sol steps until $L_s = 338.7^\circ$.

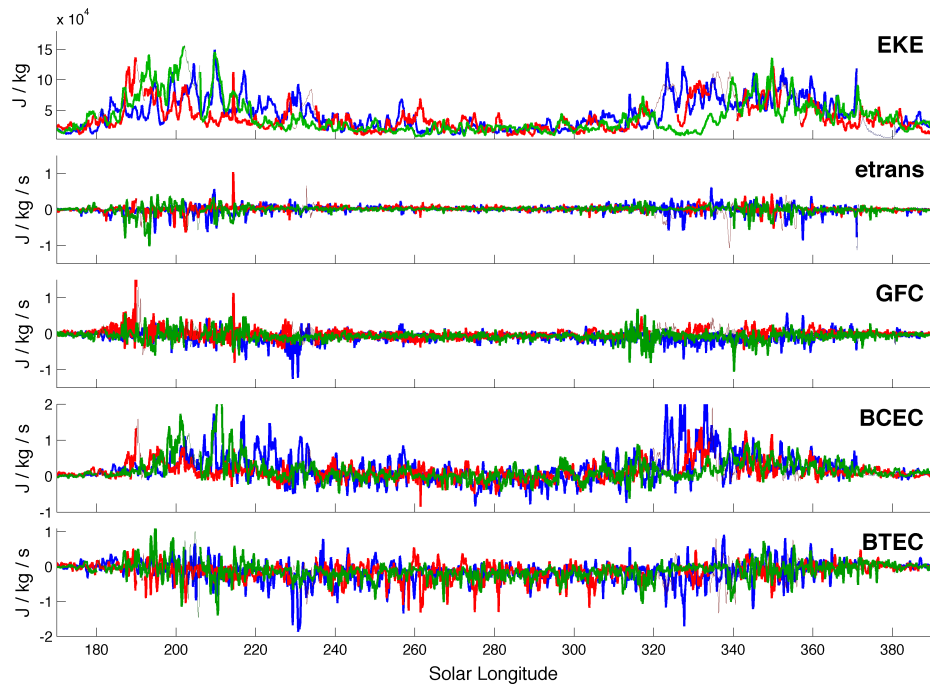


Figure A.42: Time series of the volume integrated EKE and EKE equation terms for the $22.5^\circ - 82.5^\circ$ N latitude band for MY 24 (blue), MY 25 (red), and MY 26 (green) during the entirety of the northern hemisphere transient wave period ($L_s = 170^\circ - 390^\circ$). Times of areocentric longitude greater than one degree, when TES retrievals were unavailable, and the analyses are based on a freely running model unconstrained by observations are indicated in each plot by thin lines.

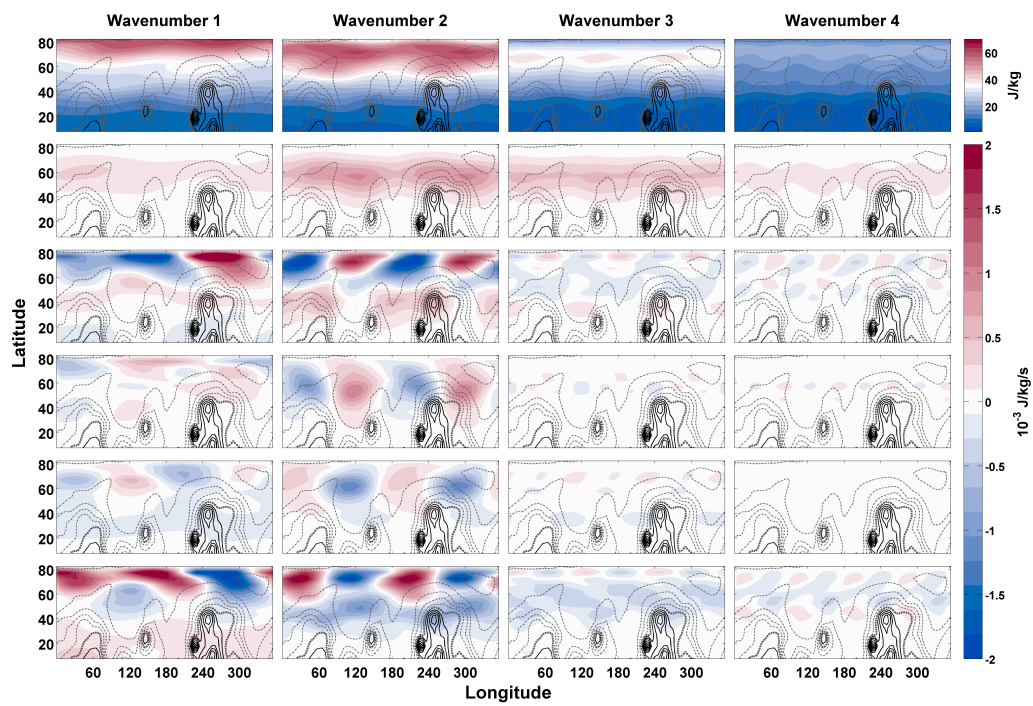


Figure A.43: As in Fig. A.12 but averaged for MY 24, 25, and 26 during $L_s = 190^\circ - 220^\circ$ for wavenumbers 1, 2, 3, and 4.

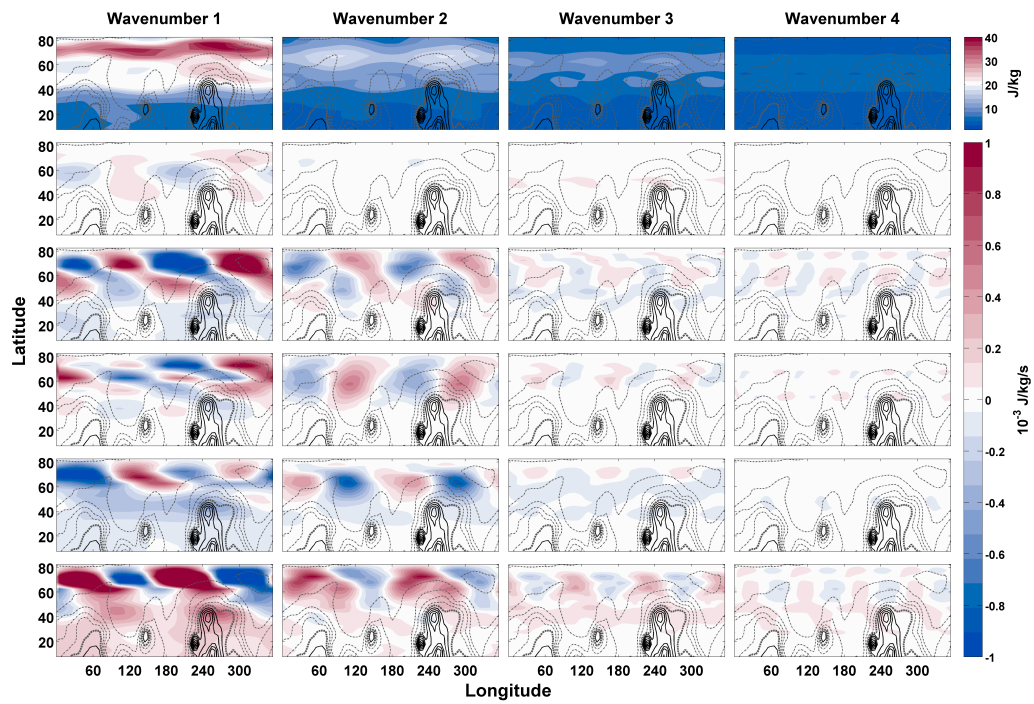


Figure A.44: As in Fig. A.43 but for $L_s = 255^\circ - 285^\circ$.

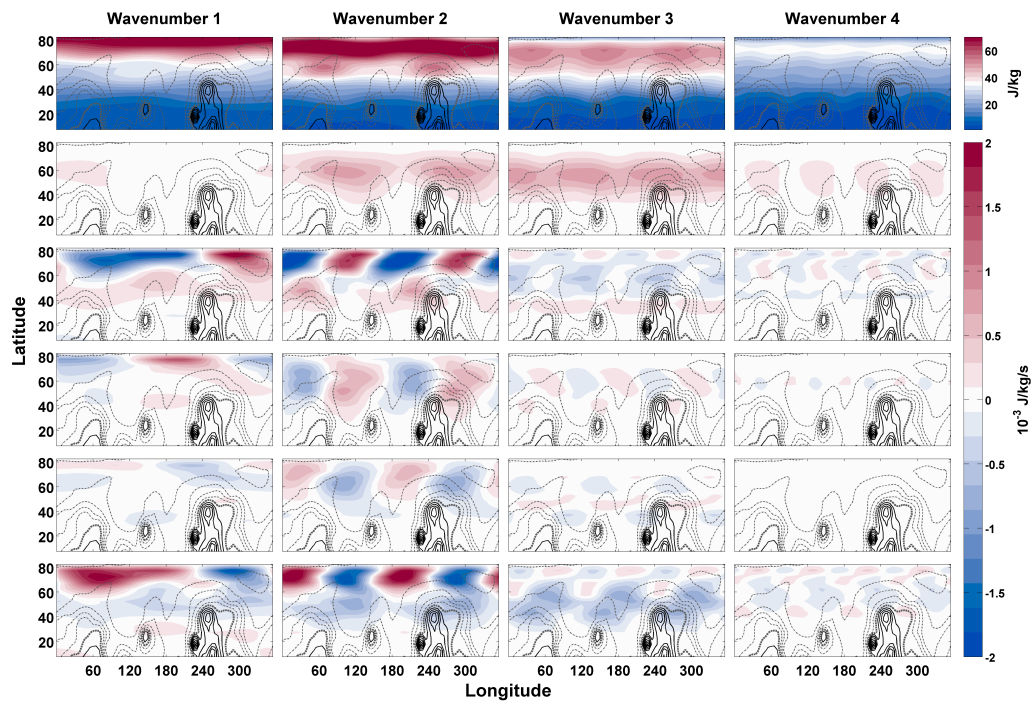


Figure A.45: As in Fig. A.43 but for $L_s = 330^\circ - 360^\circ$.

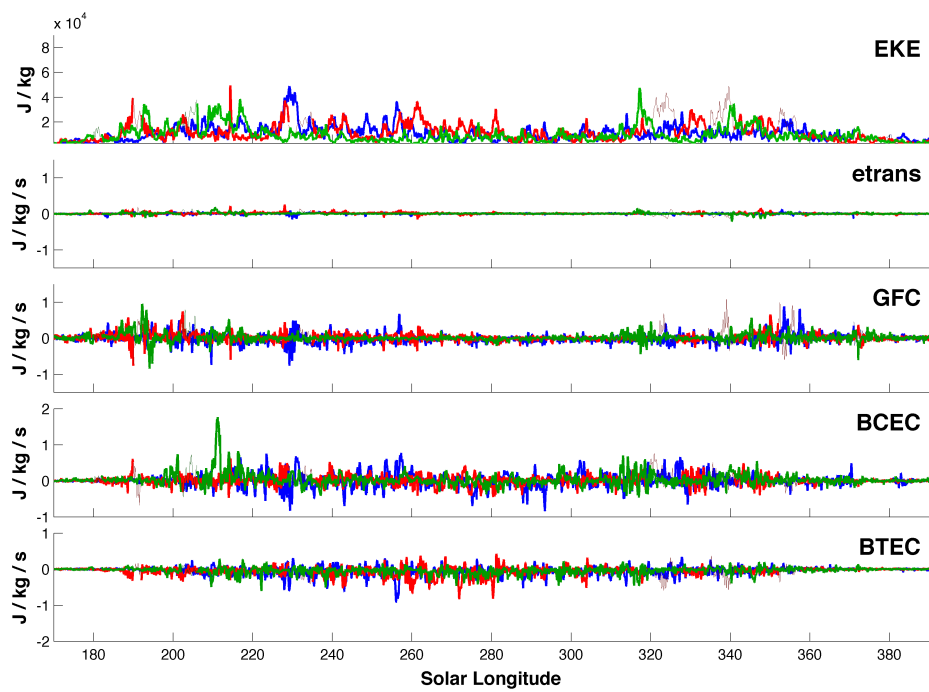


Figure A.46: As in Fig. A.42 but for wavenumber 1.

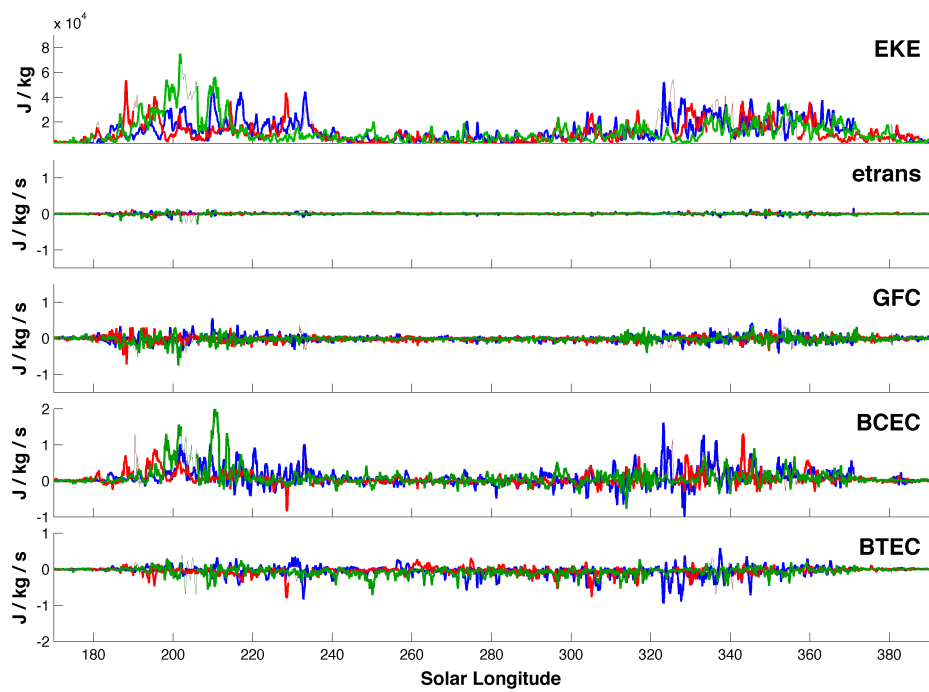


Figure A.47: As in Fig. A.42 but for wavenumber 2.

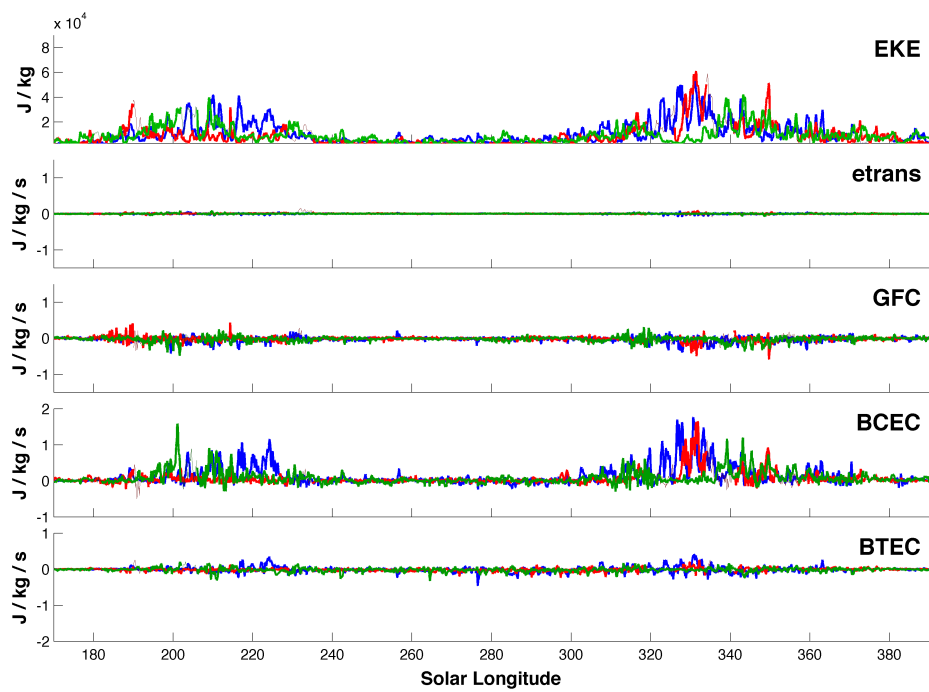


Figure A.48: As in Fig. A.42 but for wavenumber 3.

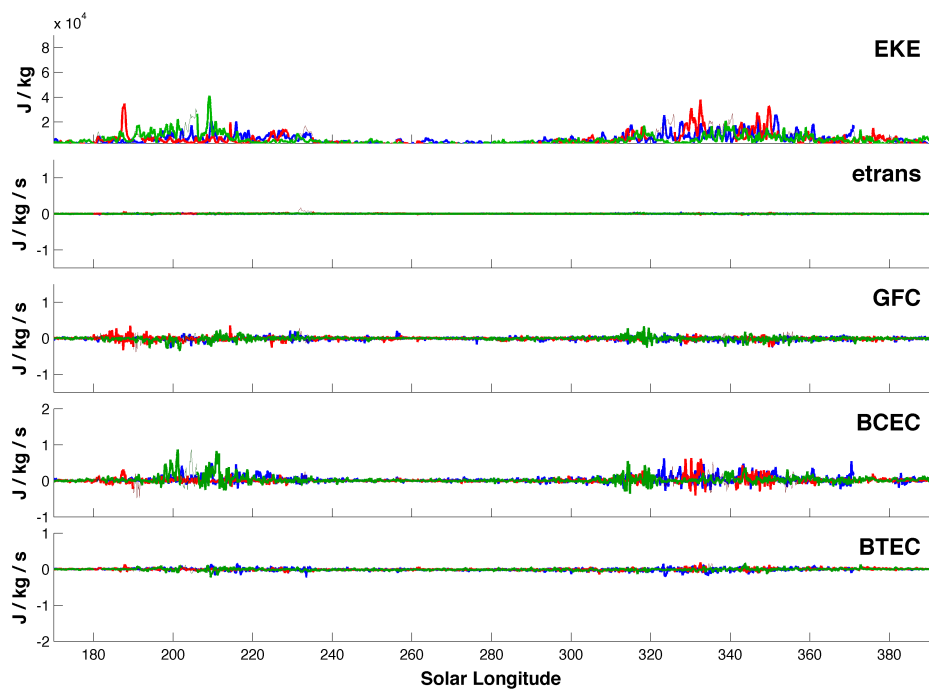


Figure A.49: As in Fig. A.42 but for wavenumber 4.

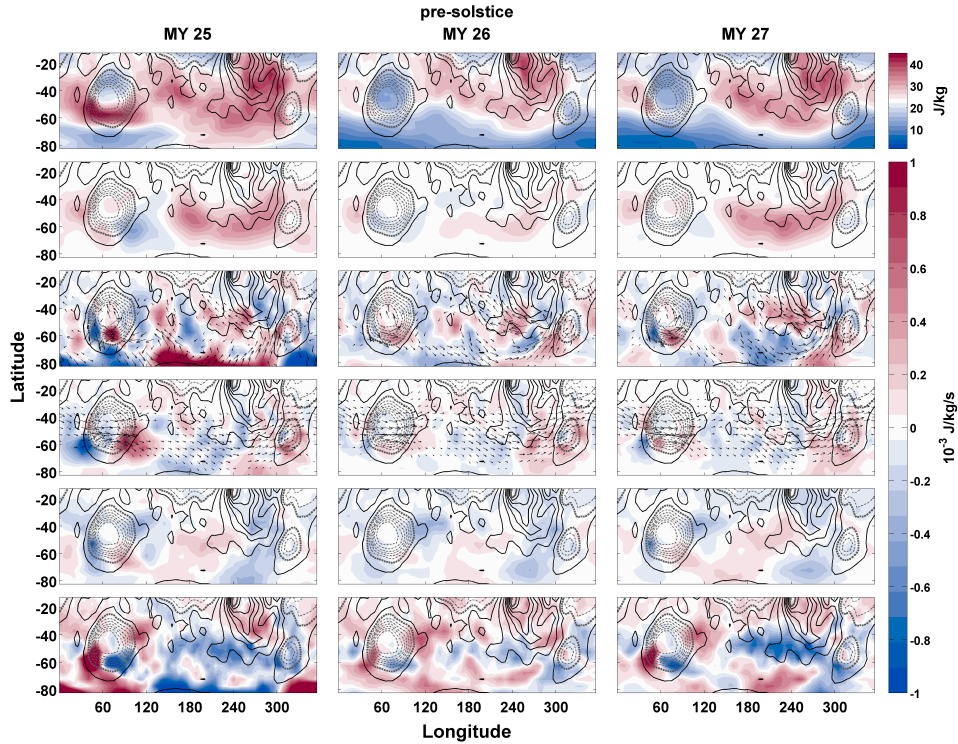


Figure A.50: Time-mean, pressure-weighted vertical averages of the terms in the eddy kinetic energy equation in the southern hemisphere for $L_s = 20^\circ - 50^\circ$ for MY 25 (left column), MY 26 (center column), and MY 27 (right column). Shown are the eddy kinetic energy (top), baroclinic energy conversion (second row), geopotential flux convergence (third row), the eddy kinetic energy advection (fourth row), the barotropic energy conversion (fifth row), and the residue (bottom). Contours are surface elevation in 1000 m increments, with dashed values below the mean geoid and the mean geoid in bold.

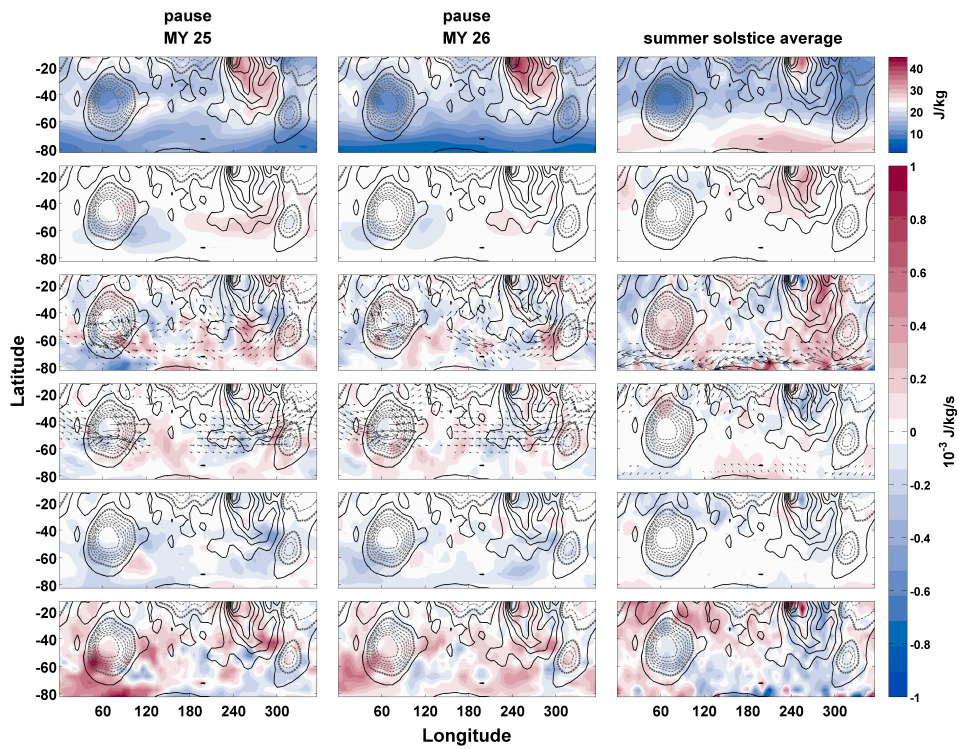


Figure A.51: As in Fig. A.50 but for the winter pause period for MY 25 and MY 26 and the average summer period.

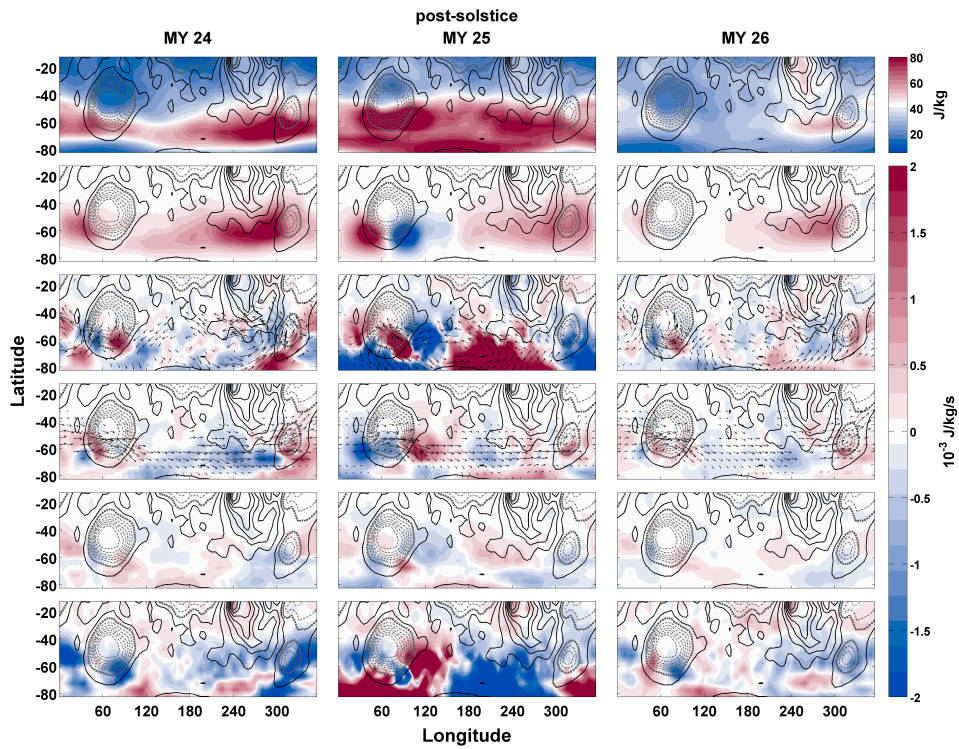


Figure A.52: As in Fig. A.50 but for the post pause period ($L_s = 150^\circ - 180^\circ$) for MY 24 (left column), MY 25 (center column), and MY 26 (right column).

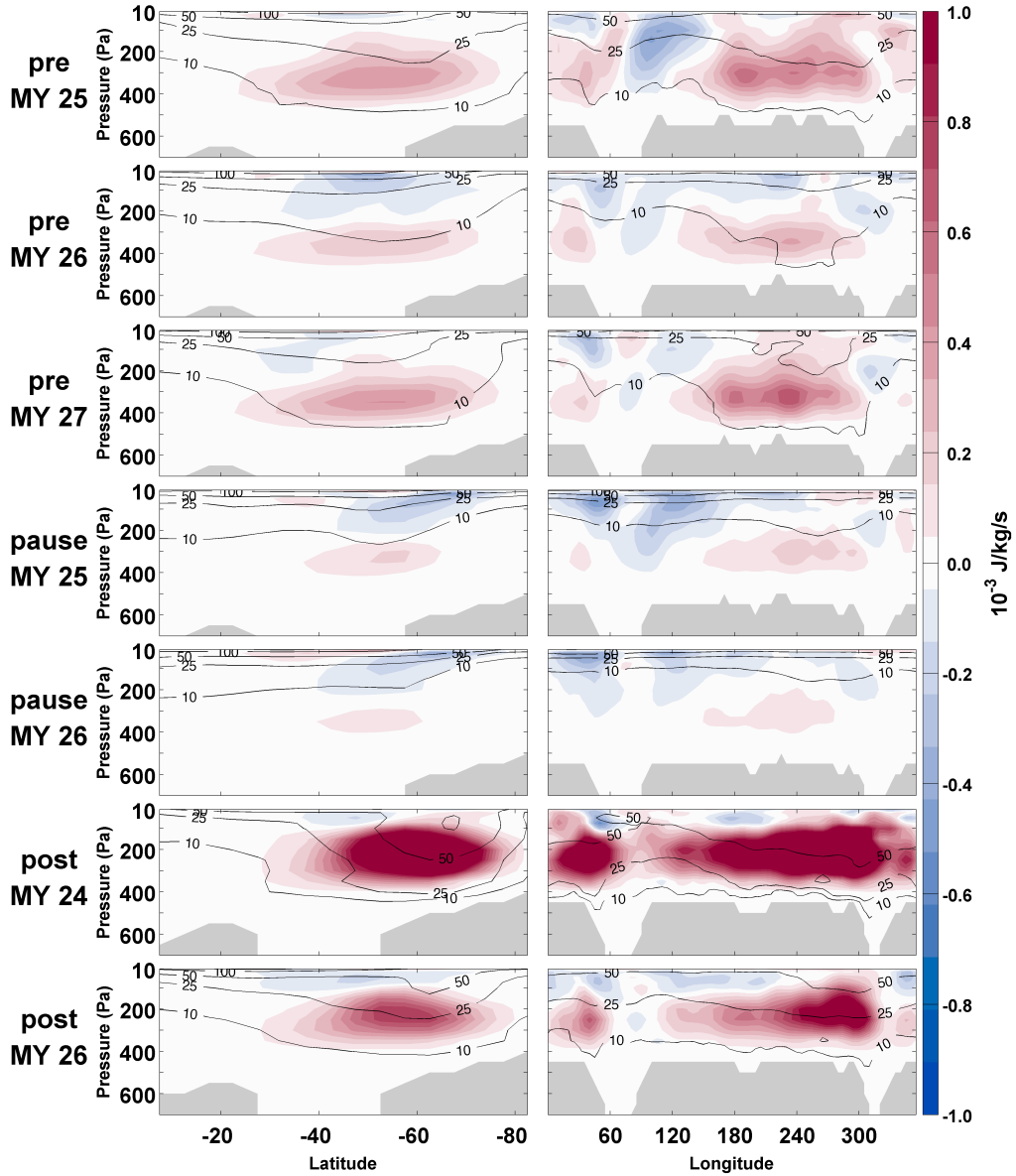


Figure A.53: Baroclinic energy conversion during three fall (pre: $L_s = 20^\circ - L_s = 50^\circ$), two winter (pause: $L_s = 75^\circ - L_s = 105^\circ$), and two spring (post: $L_s = 150^\circ - L_s = 180^\circ$) periods in the zonal (left column), and meridional (right column) average. Contours are average zonal EKE (J/kg). Terrain is grayed.

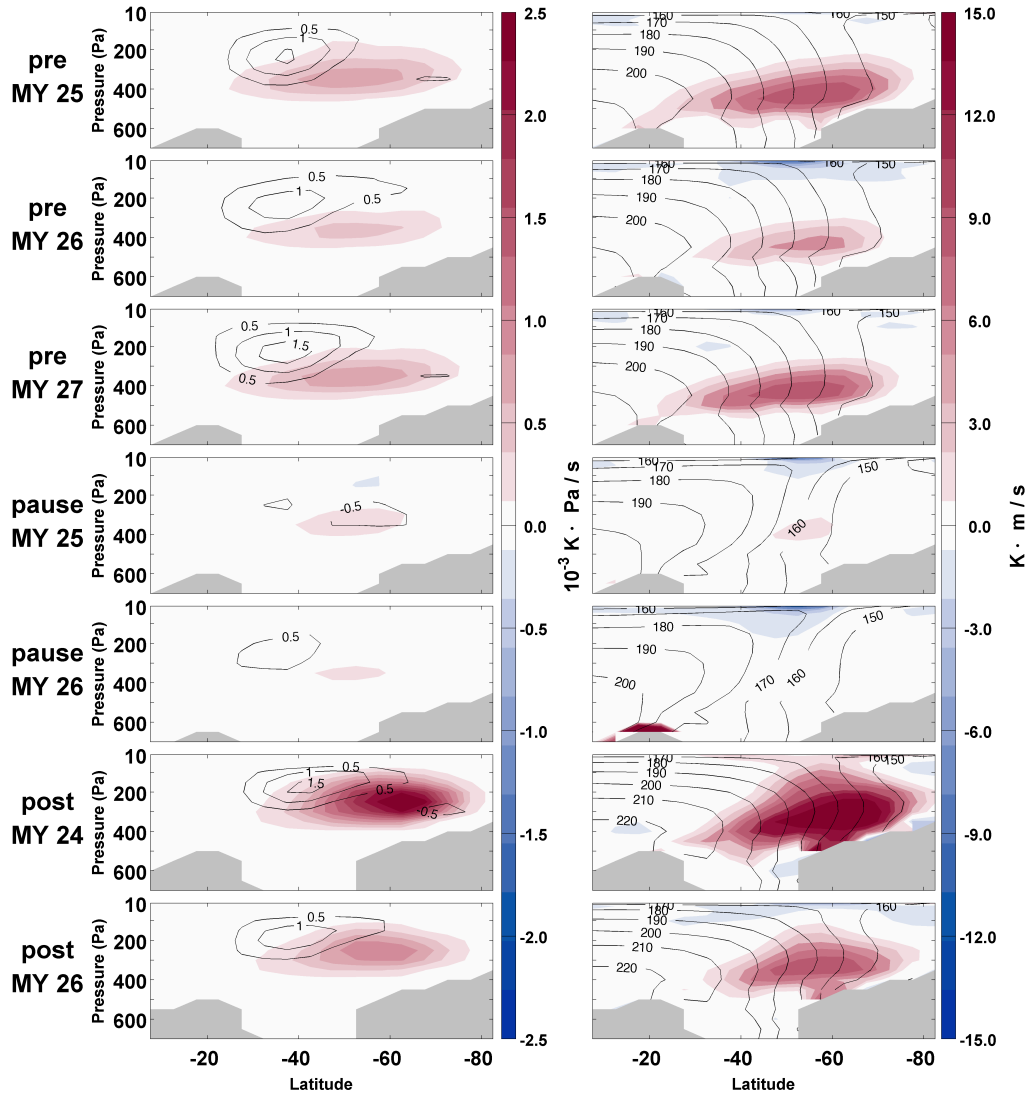


Figure A.54: The zonal average of the vertical (left) and meridional (right) heat fluxes during three fall (pre: $L_s = 20^\circ - L_s = 50^\circ$), two winter (pause: $L_s = 75^\circ - L_s = 105^\circ$), and two spring (post: $L_s = 150^\circ - L_s = 180^\circ$) periods. Contours are average zonal vertical motion (10^{-4} Pa/s) (left) and zonal average temperature (K) (right). Terrain is grayed.

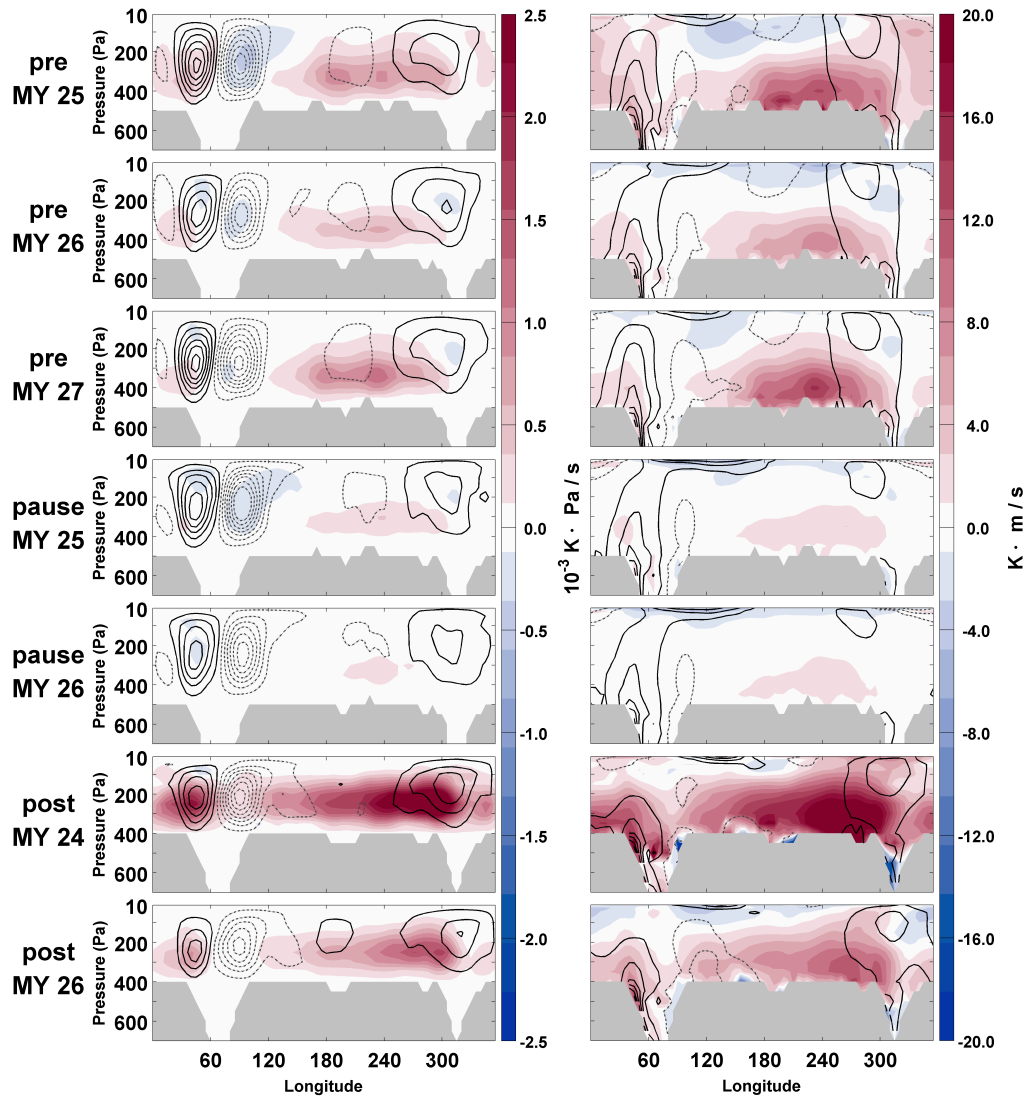


Figure A.55: The meridional average of the vertical (left) and meridional (right) heat fluxes during the time periods in Fig. A.54. Contours are average vertical motion in 2×10^{-4} Pa/s increments, with negative values dashed (left) and average meridional wind in 4 m/s increments, with negative values dashed (right).

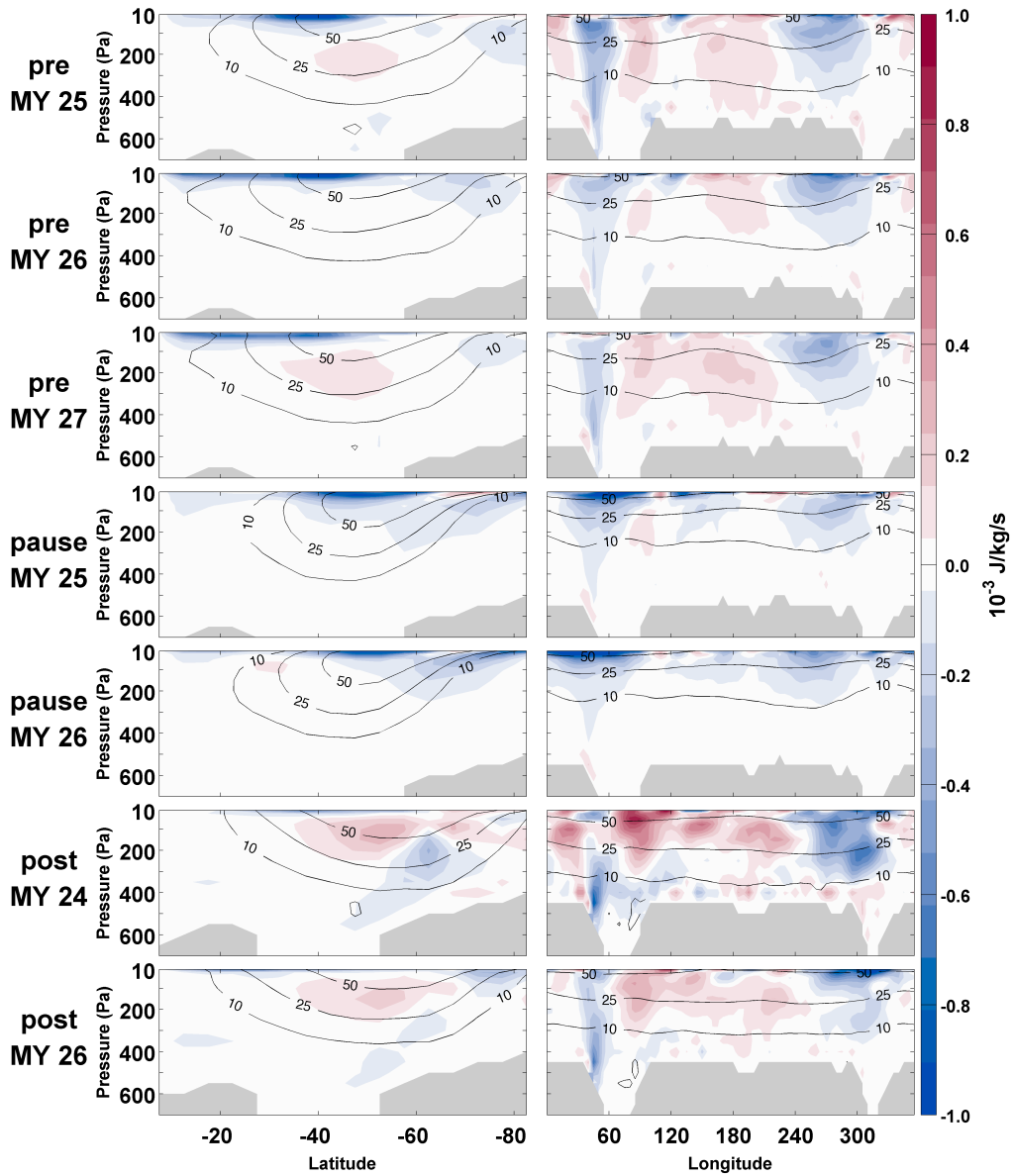


Figure A.56: As in Fig. A.53 but for barotropic energy conversion in the zonal (left column) and meridional (right column) average. Contours are average zonal wind (m/s).

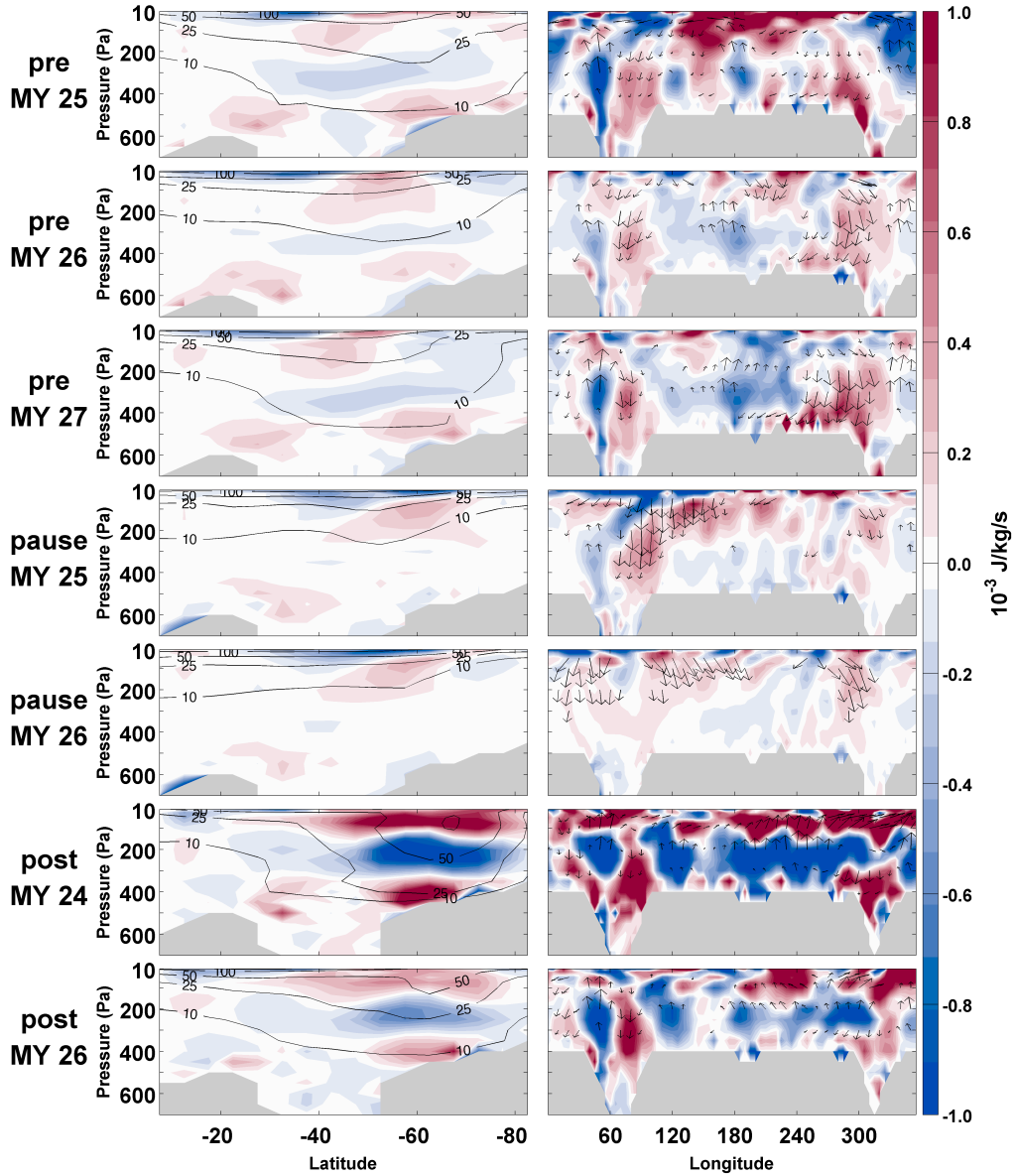


Figure A.57: As in Fig. A.53 but for geopotential flux convergence in the zonal (left column), and meridional (right column) average. Vectors are ageostrophic geopotential flux with motions in the vertical direction multiplied by 10^4 . Contours are average zonal EKE (J/kg).

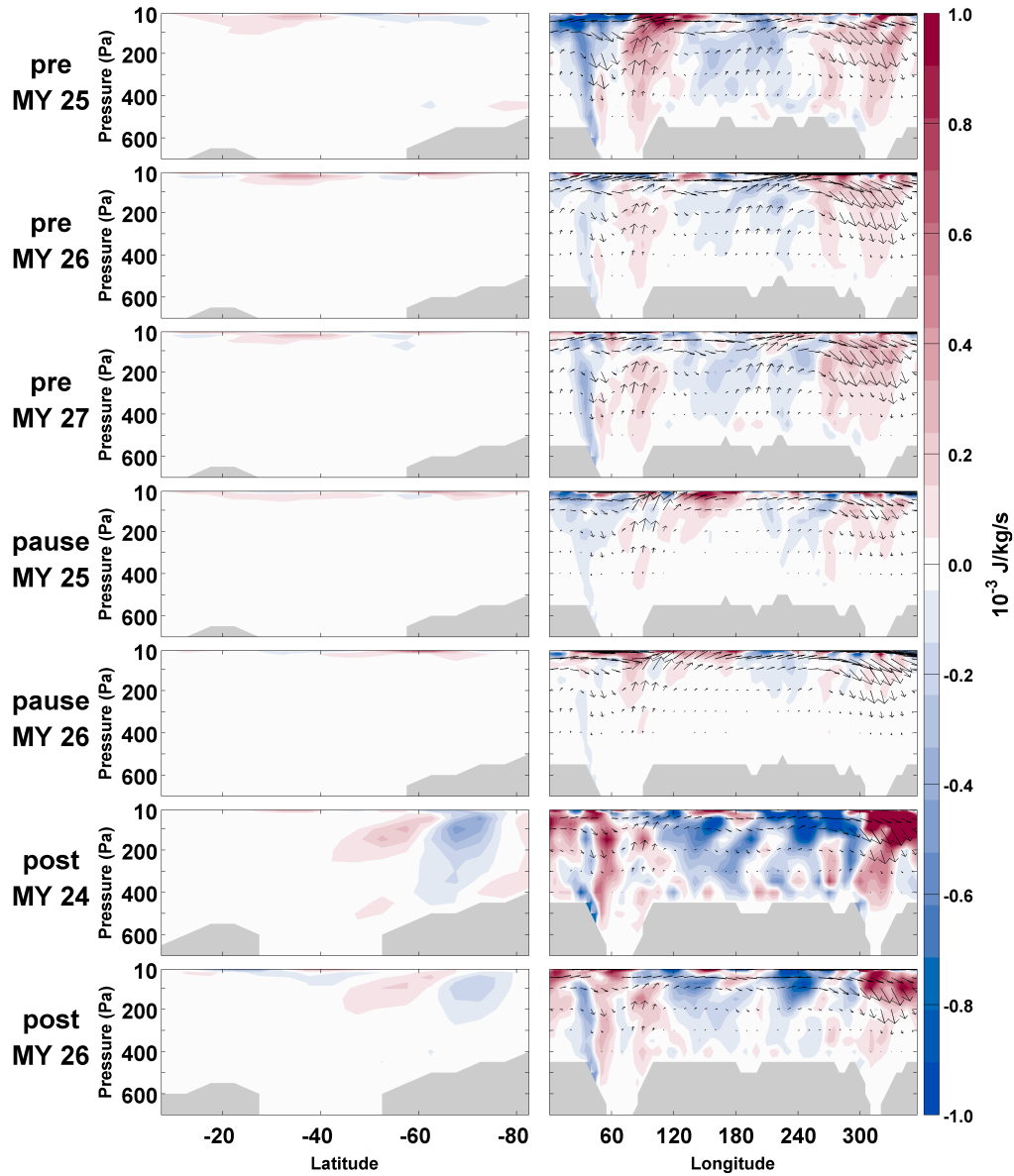


Figure A.58: As in Fig. A.53 but for EKE advection in the zonal (left column), and meridional (right column) average. Vectors are EKE advection flux with motions in the vertical direction multiplied by 10^4 . Contours are average zonal wind (m/s).

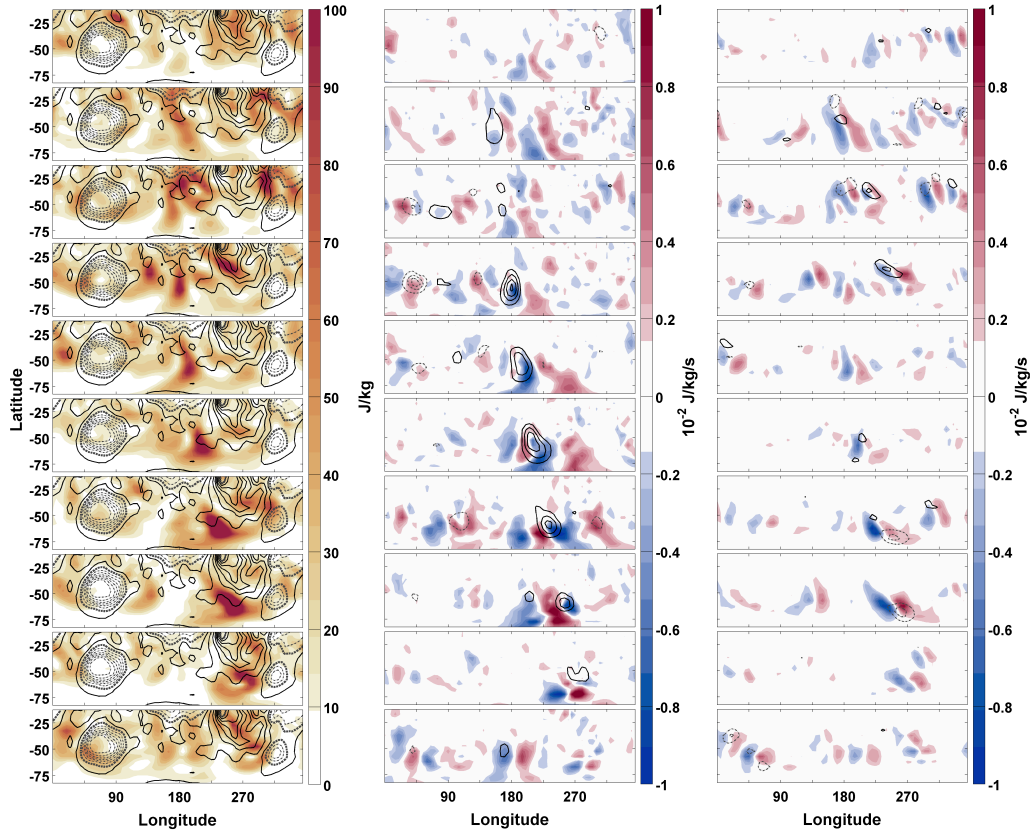


Figure A.59: Progression of an eddy during MY 27 $L_s = 47.90^\circ - 49.94^\circ$. Each row is 0.5 sol forward in time. Shown are eddy kinetic energy, with topography contoured at 1000 m increments and negative values dashed (left), geopotential flux convergence, with baroclinic energy conversion contoured in 0.00167 (J/kg/s) increments and negative values dashed (middle), and EKE advection, with barotropic energy conversion contoured in 0.00167 (J/kg/s) increments and negative values dashed (right).

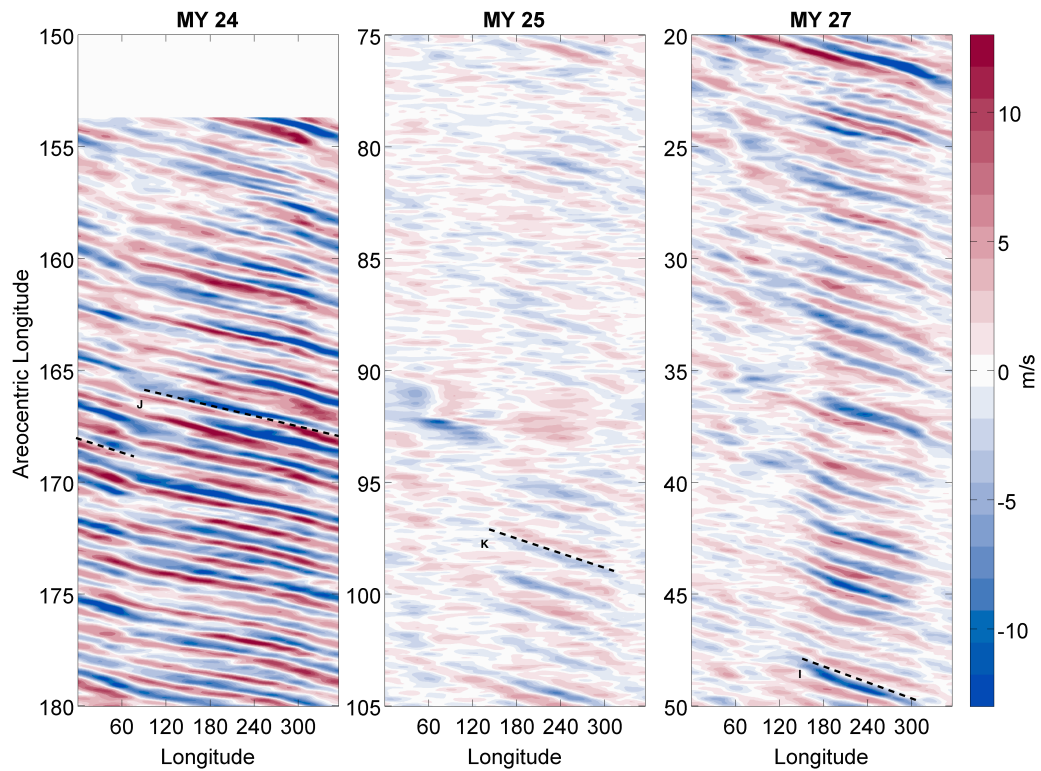


Figure A.60: Hovmöller diagram of the eddy meridional wind at 300 Pa for three periods in the MACDA dataset averaged between 57.5° S and 82.5° S. Lines I, J, and K refer to the location of storms discussed in Section 4.3.

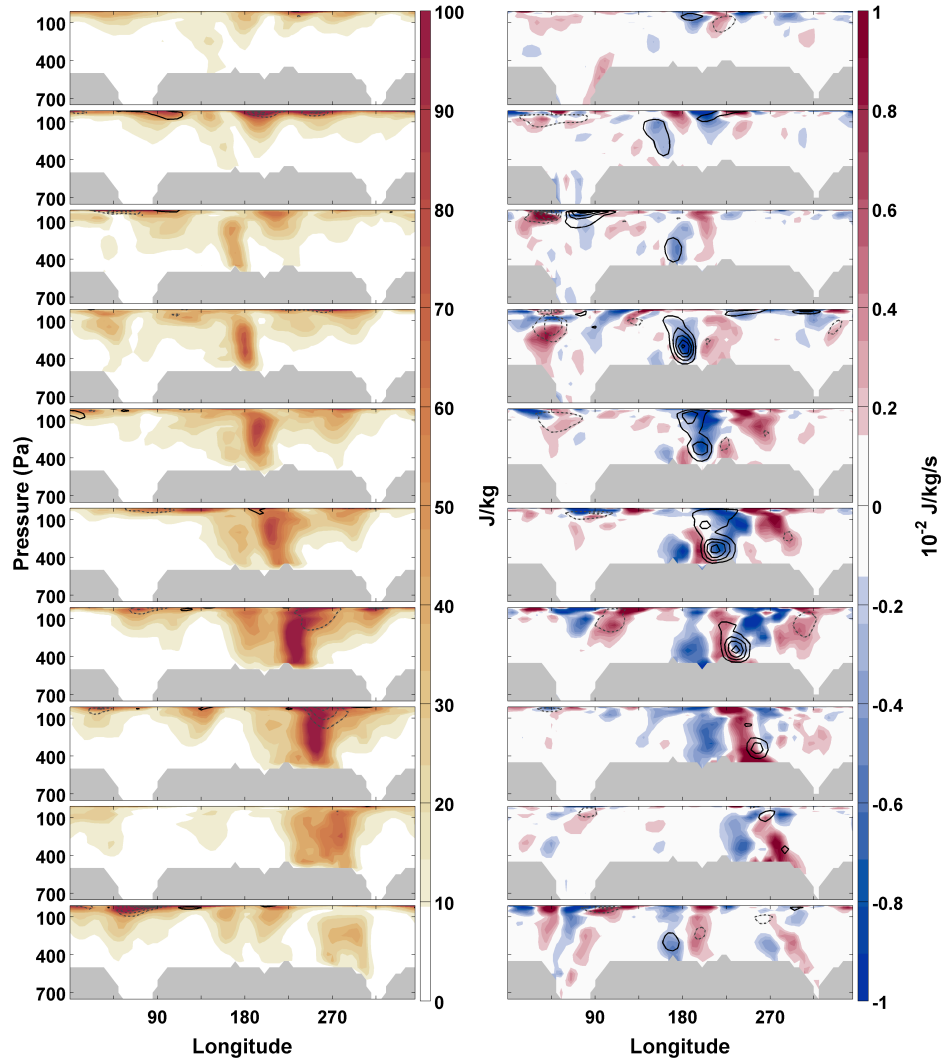


Figure A.61: Time series of the meridionally averaged EKE equation terms of the eddy depicted in Fig. A.59. Shown are eddy kinetic energy, with barotropic energy conversion contoured in 0.00167 (J/kg/s) increments and negative values dashed (left) and geopotential flux convergence, with baroclinic energy conversion contoured in 0.00167 (J/kg/s) increments and negative values dashed (right).

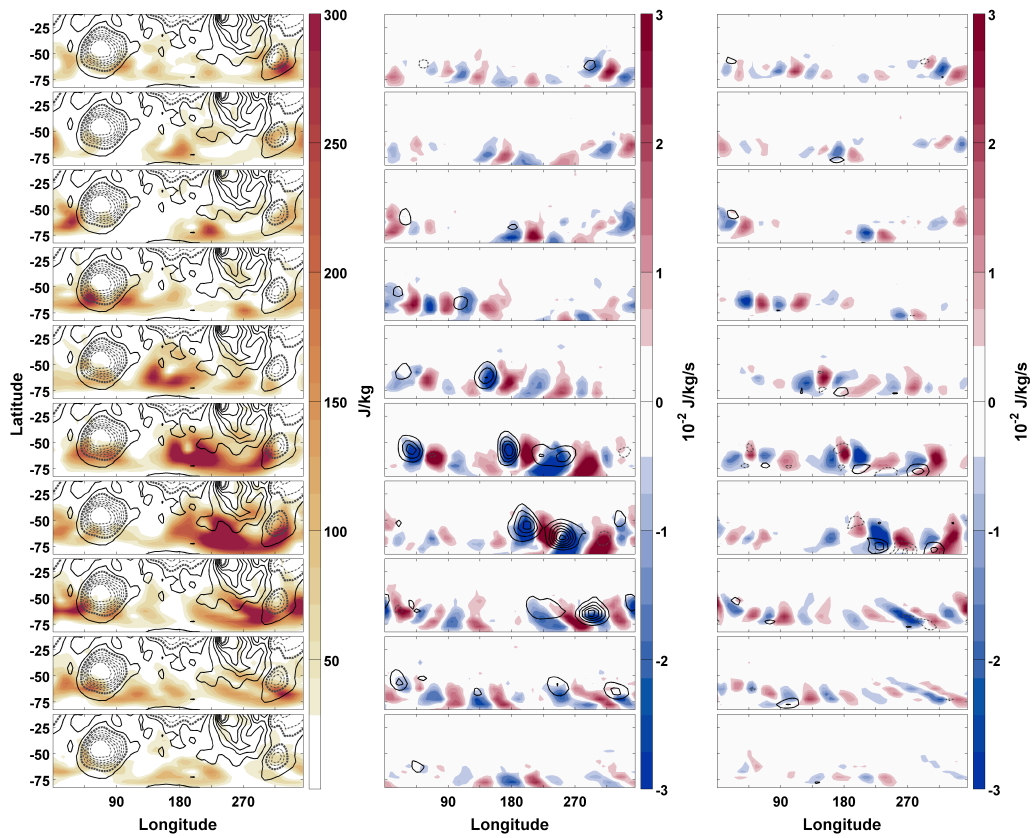


Figure A.62: As in Fig. A.59 but for an eddy during MY 24 $L_s = 166.31^\circ - 168.82^\circ$. Baroclinic and barotropic energy conversion are contoured in 0.005 (J/kg/s) increments.

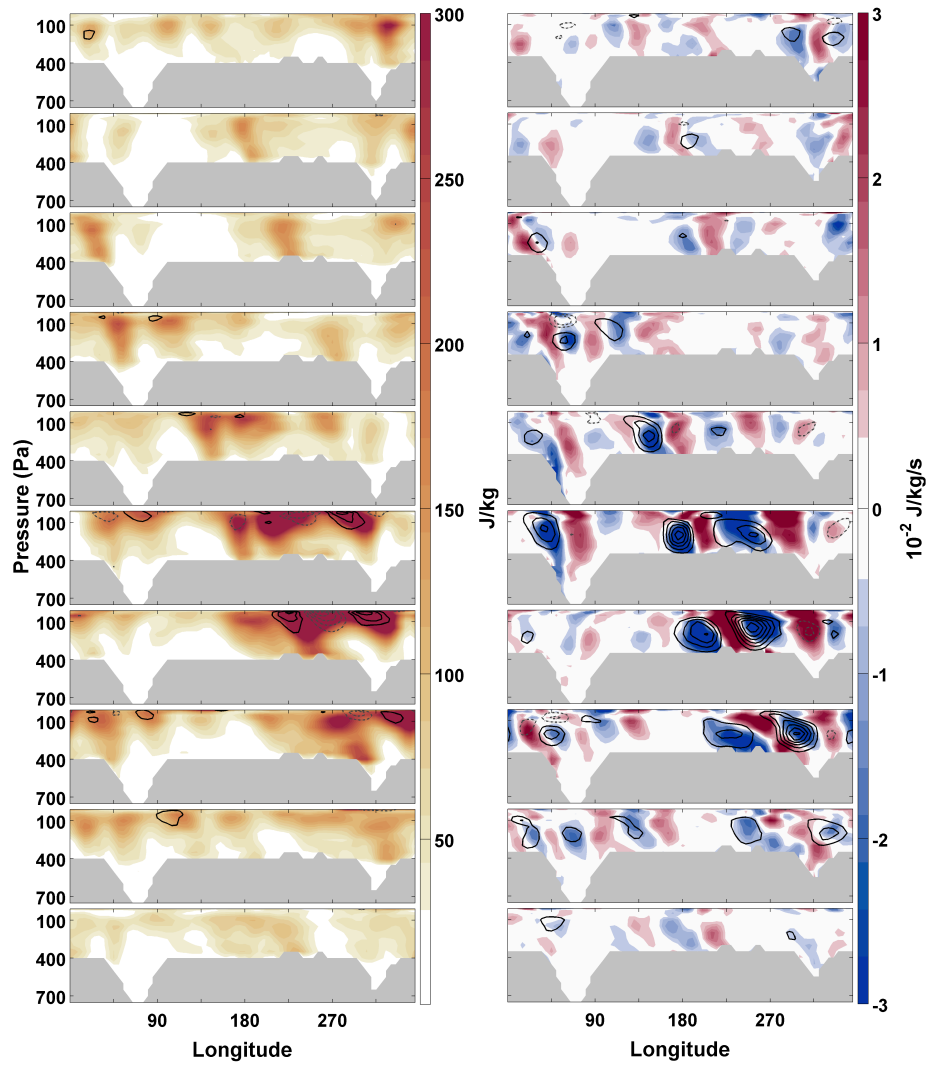


Figure A.63: As in Fig. A.61 but for the eddy in Fig. A.62. Baroclinic and barotropic energy conversion are contoured in 0.005 (J/kg/s) increments.

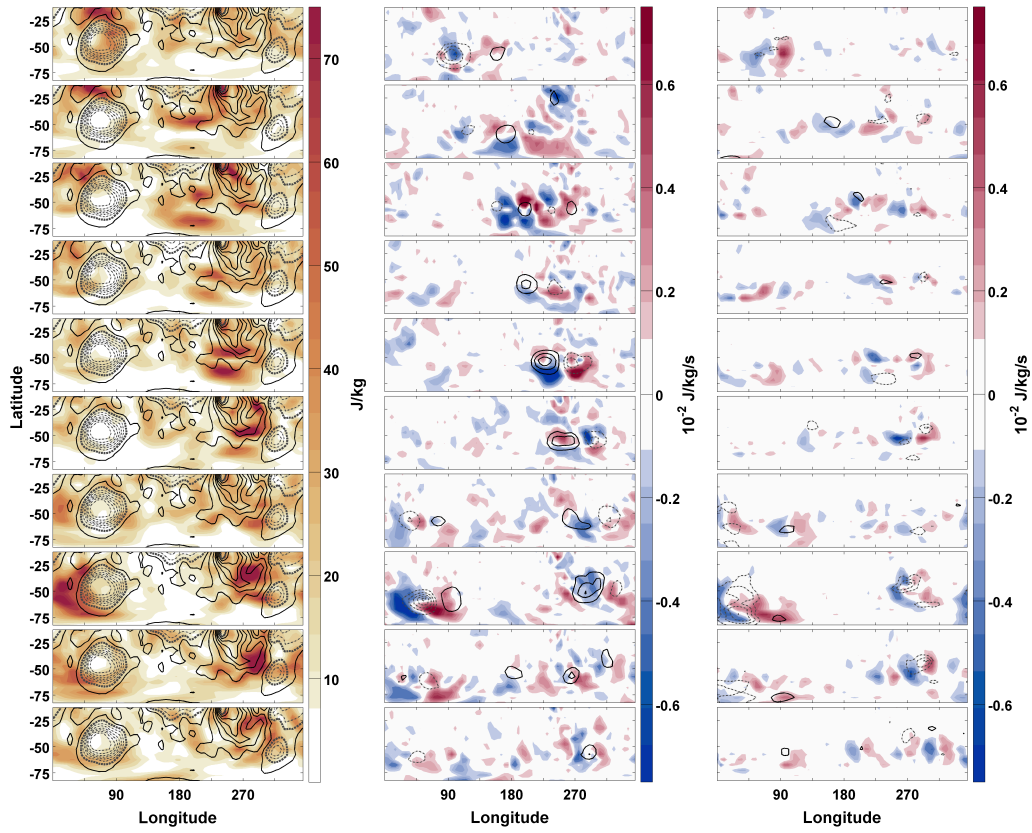


Figure A.64: As in Fig. A.62 but for an eddy between MY 25 $L_s = 96.83^\circ - 98.90^\circ$. Baroclinic and barotropic energy conversion are contoured in 0.00125 (J/kg/s) increments.

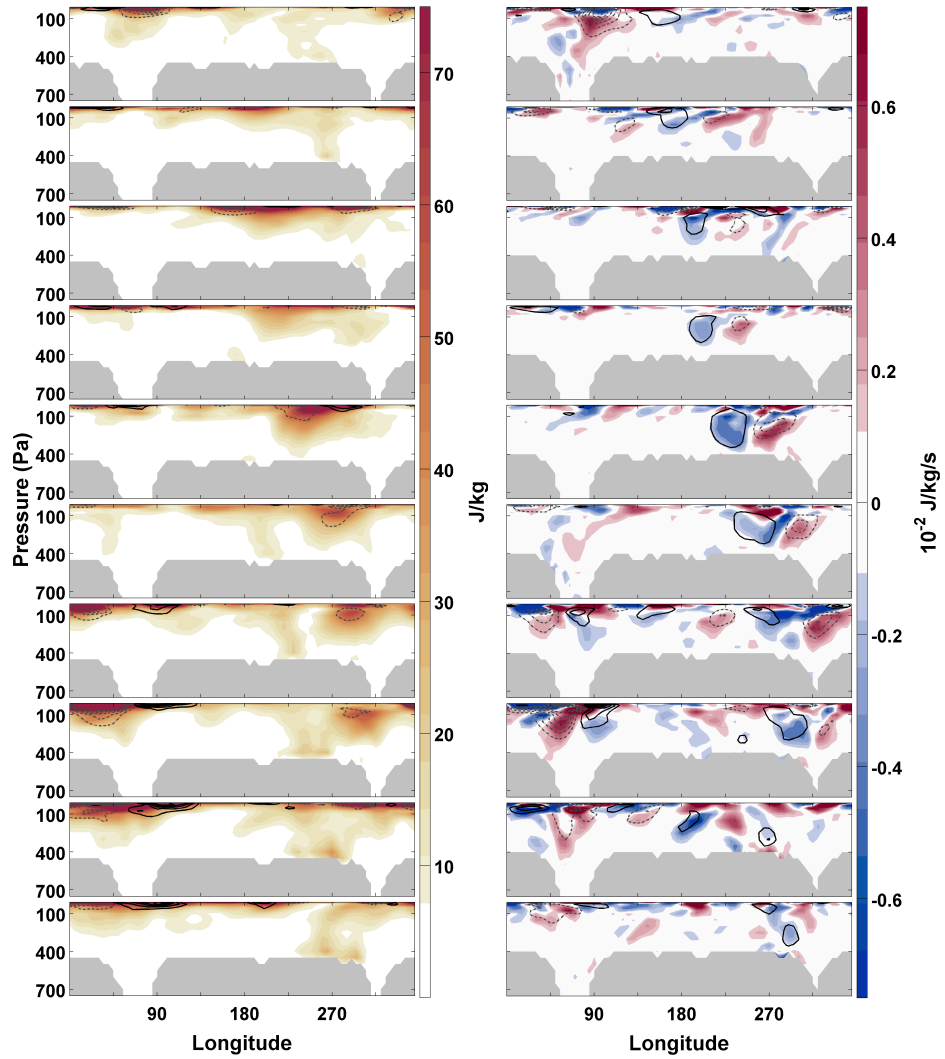


Figure A.65: As in Fig. A.61 but for the eddy in Fig. A.64. Baroclinic and barotropic energy conversion are contoured in 0.00125 (J/kg/s) increments.

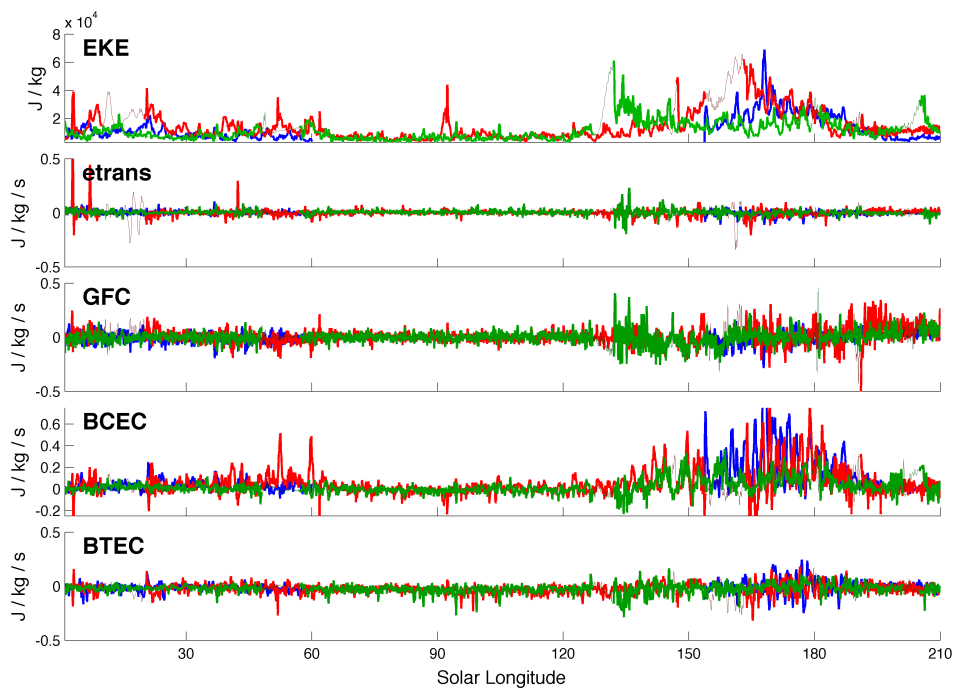


Figure A.66: Summed, pressure-weighted EKE equation terms in the $57.5^\circ - 82.5^\circ$ S latitude band for MY27 ($L_s = 20^\circ - 60^\circ$) and MY 24 ($L_s = 153.7^\circ - 180^\circ$) in blue, MY 25 in red, and MY 26 in green. Times longer in duration than $L_s = 1^\circ$ when TES retrievals were unavailable and the MACDA GCM ran freely are indicated by thin lines.

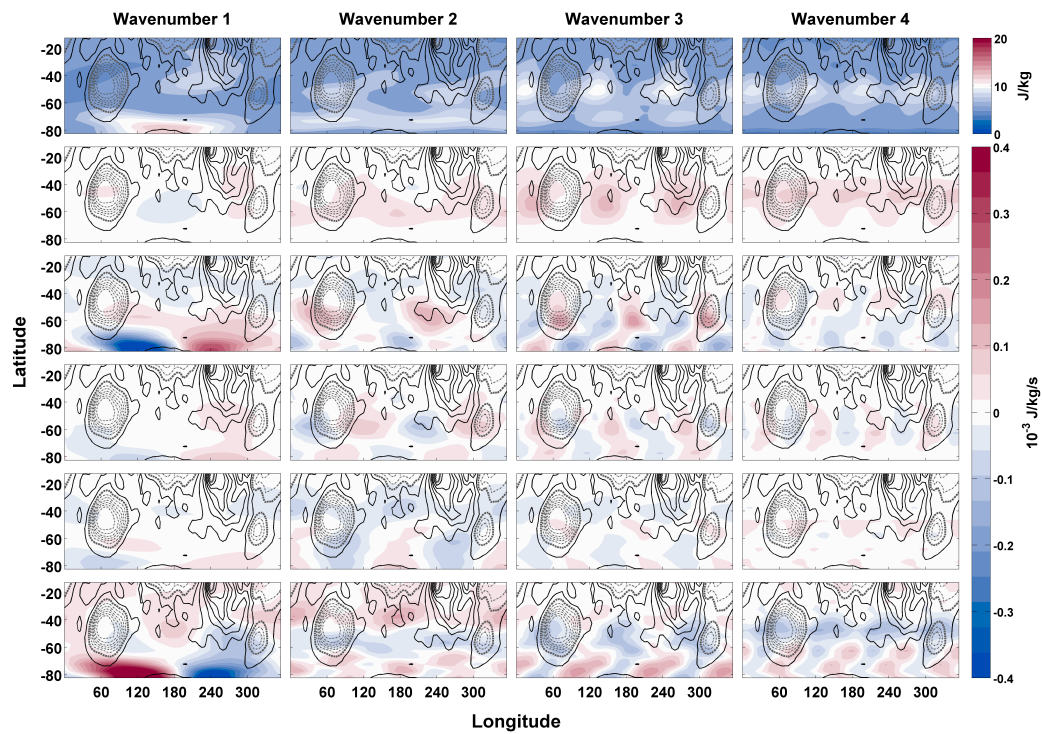


Figure A.67: As in Fig. A.50 but averaged for MY 25, 26, and 27 during $L_s = 20^\circ - 50^\circ$ for wavenumbers 1, 2, 3, and 4.

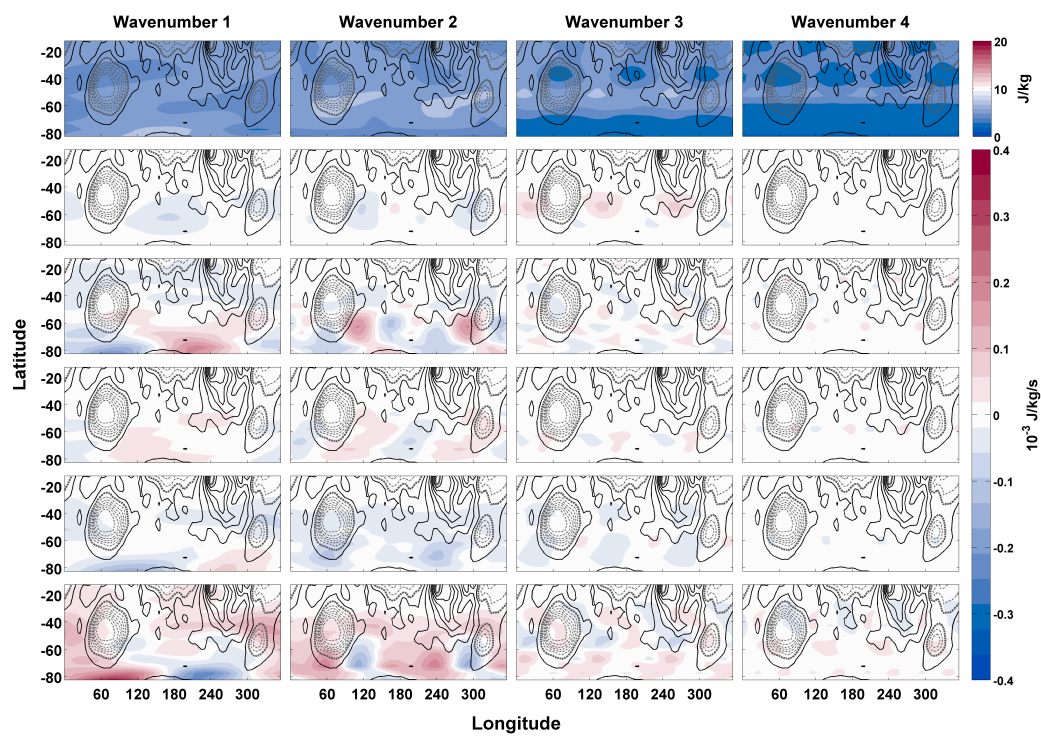


Figure A.68: As in Fig. A.50 but averaged for MY 25 and 26 during $L_s = 75^\circ - 105^\circ$.

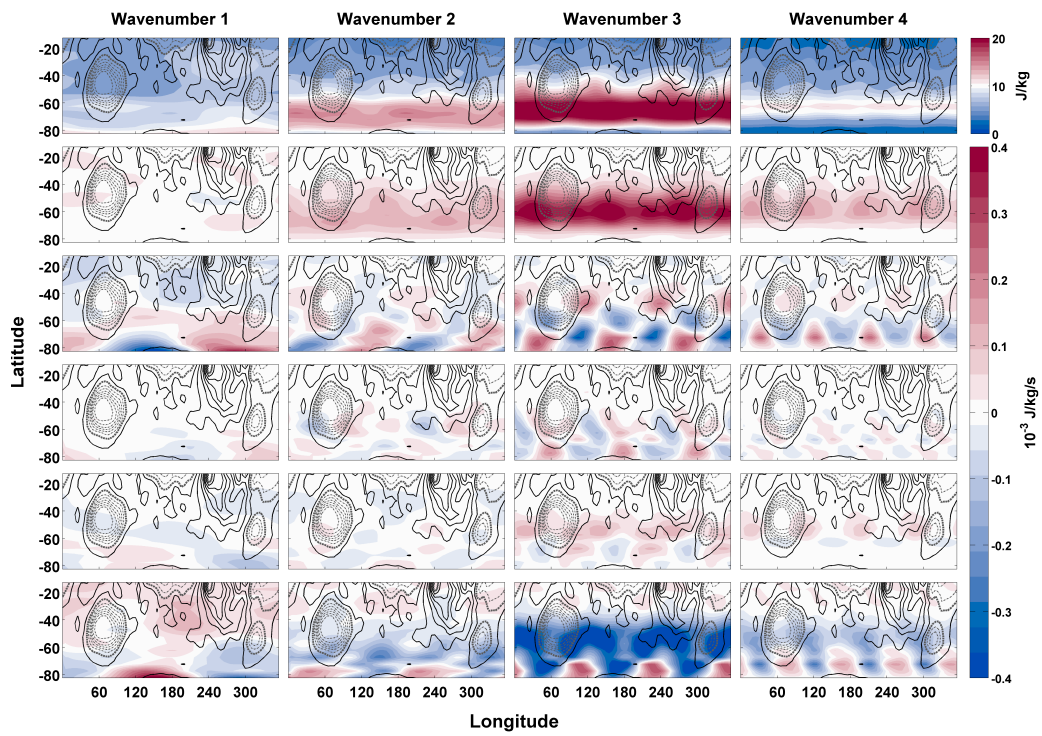


Figure A.69: As in Fig. A.50 but averaged for MY 24, 25, and 26 during $L_s = 150^\circ - 180^\circ$.

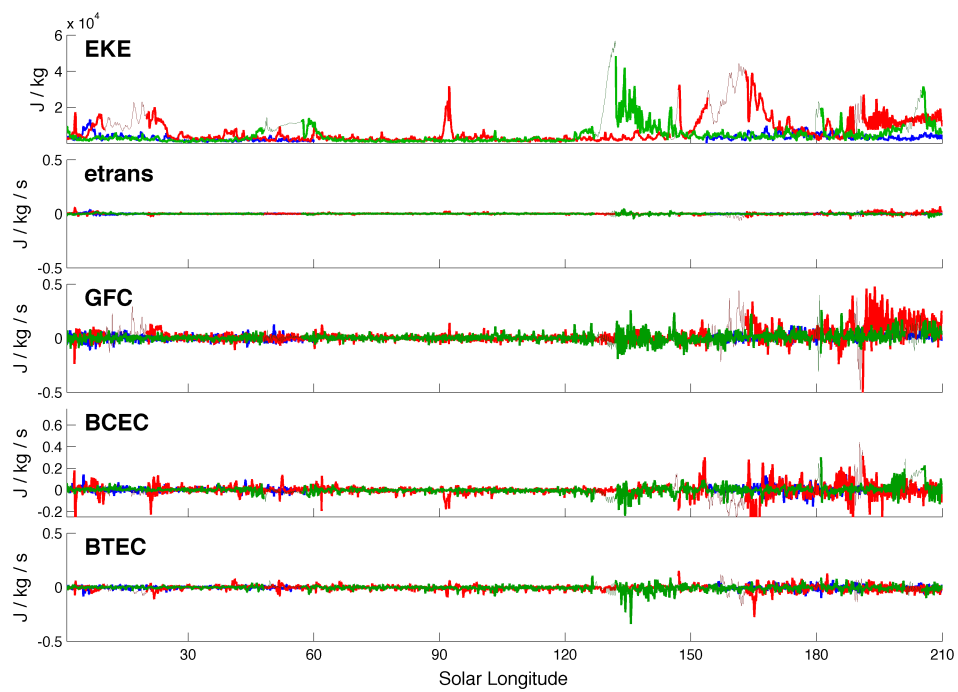


Figure A.70: As in Fig. A.66 but for wavenumber 1.

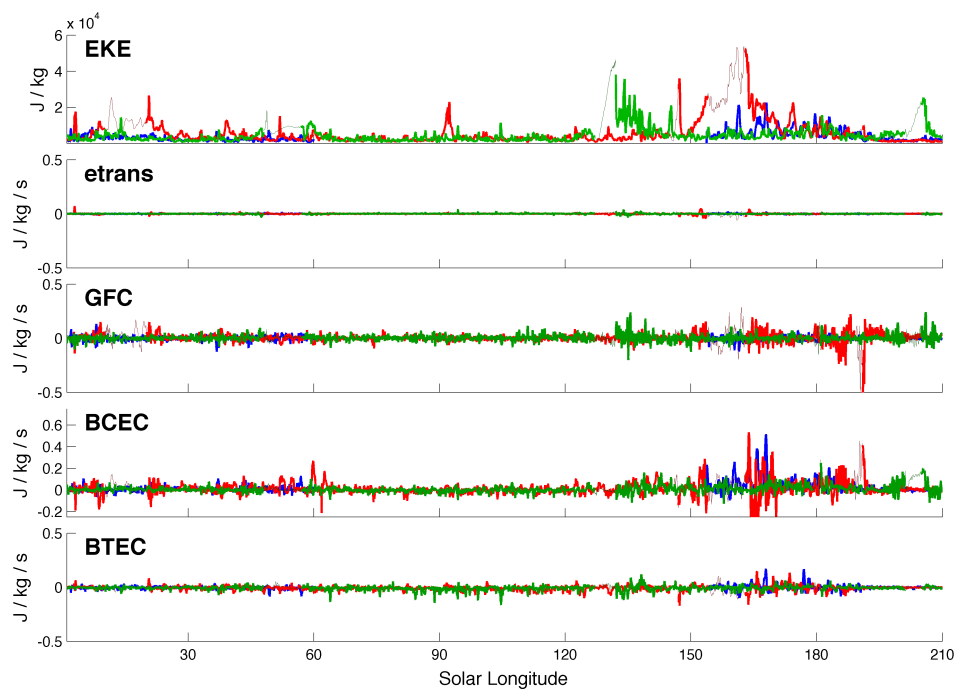


Figure A.71: As in Fig. A.66 but for wavenumber 2.

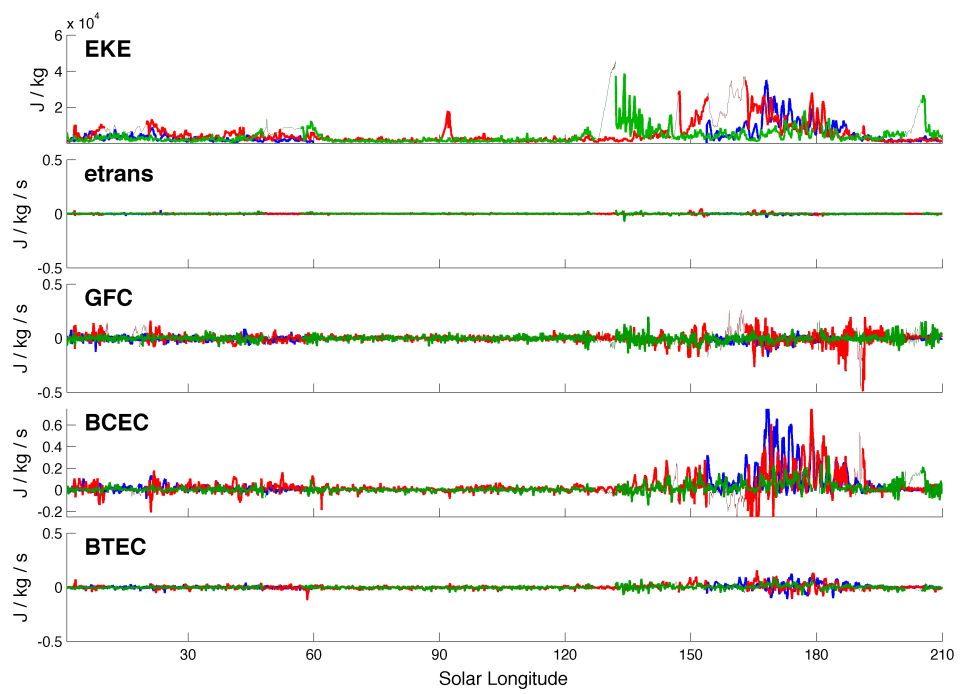


Figure A.72: As in Fig. A.66 but for wavenumber 3.

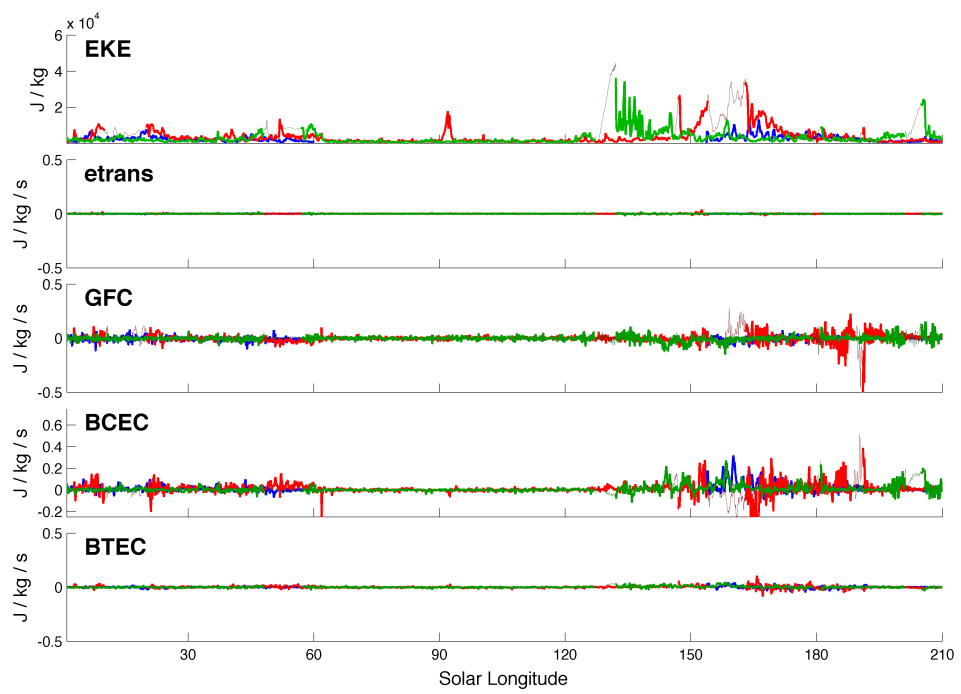


Figure A.73: As in Fig. A.66 but for wavenumber 4.

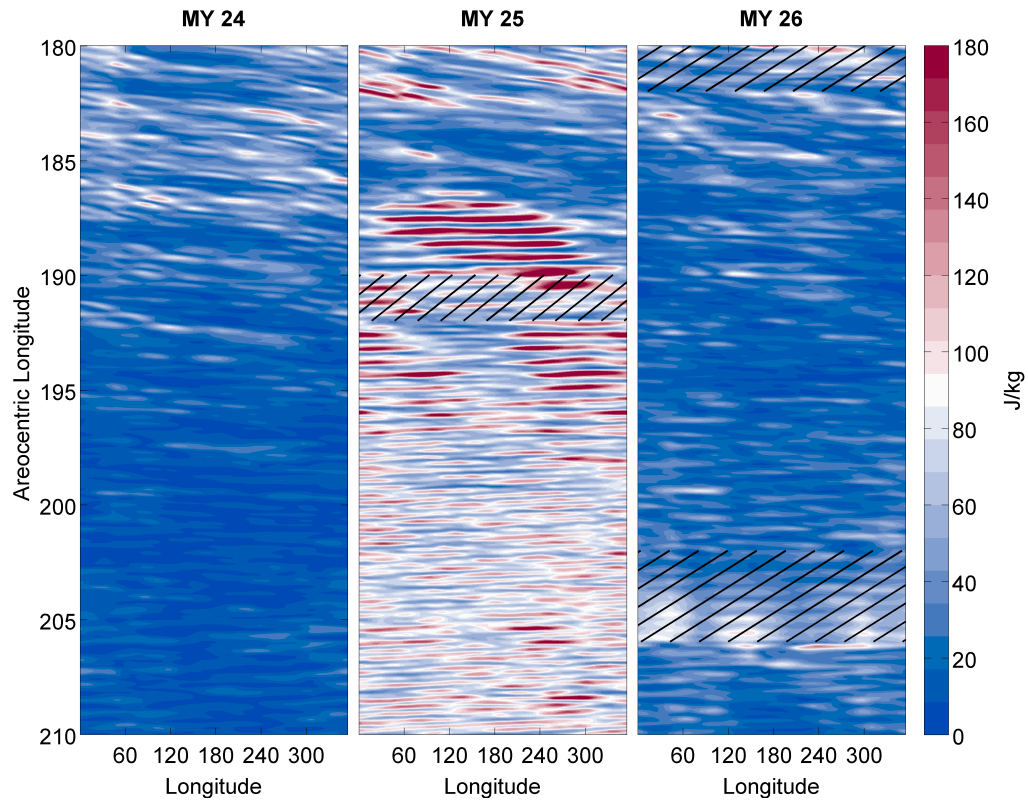


Figure A.74: Hovmöller diagram of EKE at 10 Pa for $L_s = 180^\circ - 210^\circ$ in the $57.5^\circ - 82.5^\circ$ S latitude band. Shown are MY 24 (left), MY 25 (middle), and MY 26 (right). Hatching indicates times of areocentric longitude greater than one degree, when TES retrievals were unavailable, and the analyses are based on a freely running model unconstrained by observations.

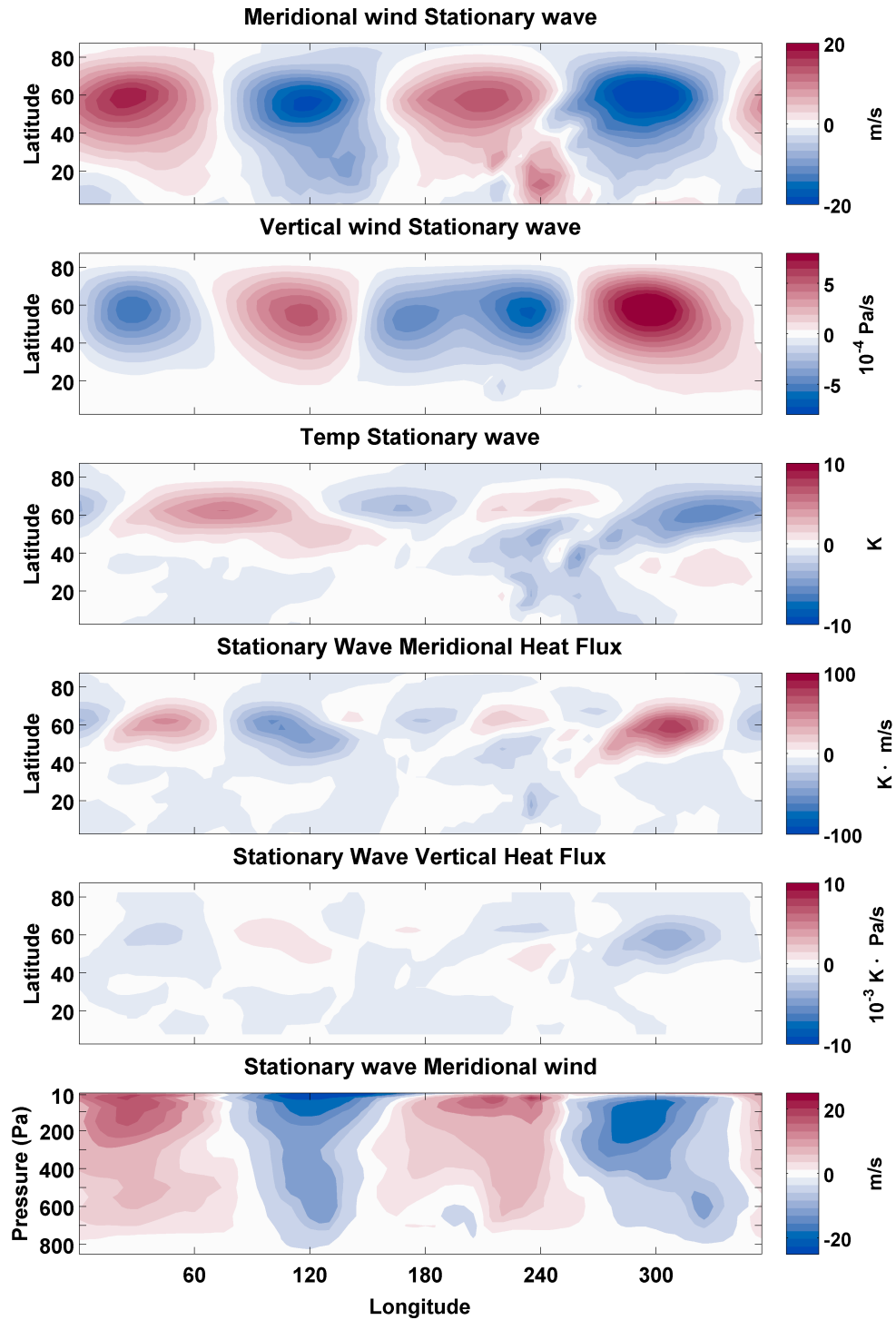


Figure A.75: The meridional wind, vertical wind, and temperature signal with the associated heat fluxes for the stationary wave in the northern hemisphere at 300 Pa for $L_s = 190^\circ - 220^\circ$. The bottom panel is the meridionally averaged meridional wind in the $57.5^\circ - 82.5^\circ$ N latitude band.

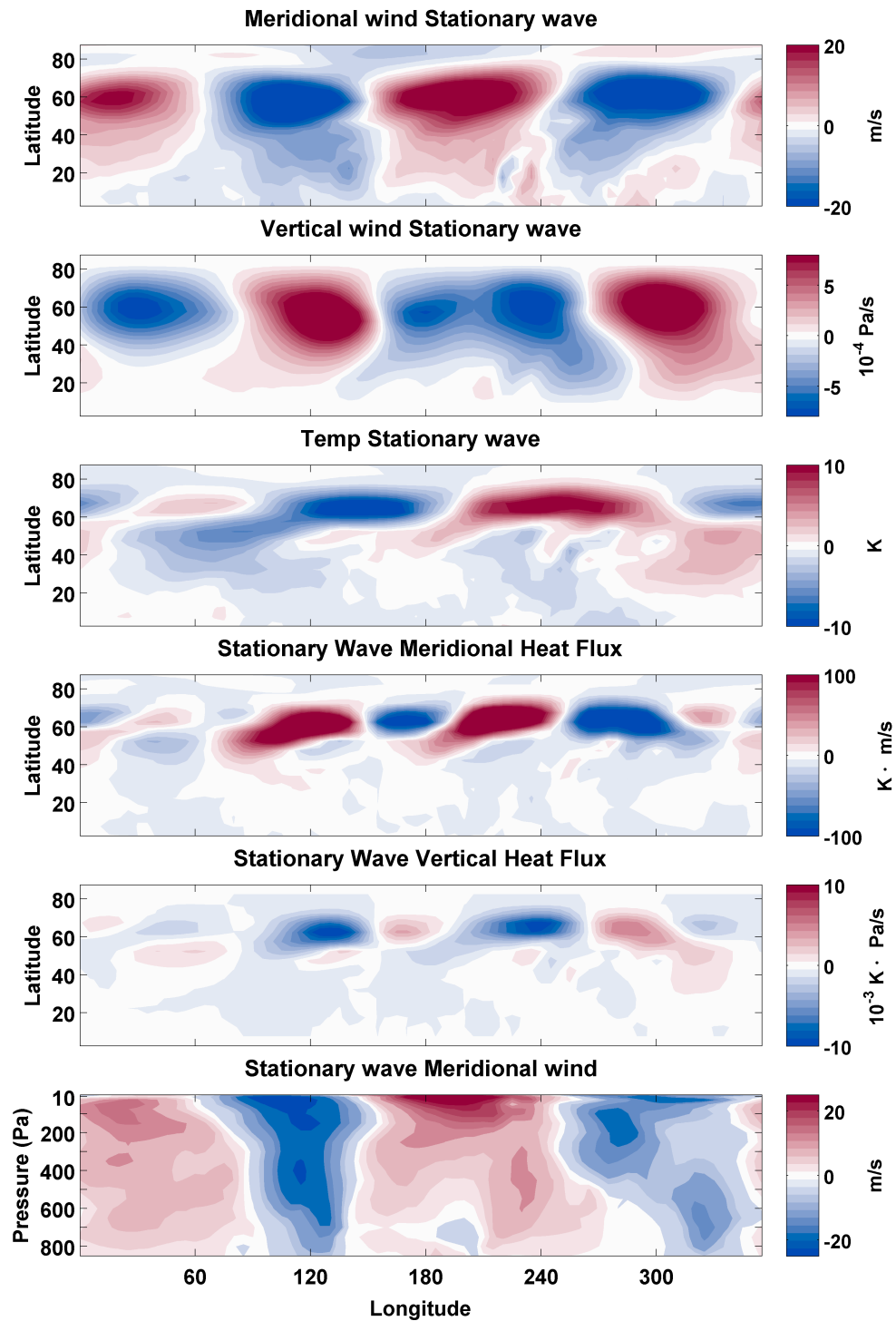


Figure A.76: As in Fig. A.75 but for $L_s = 255^\circ - 285^\circ$.

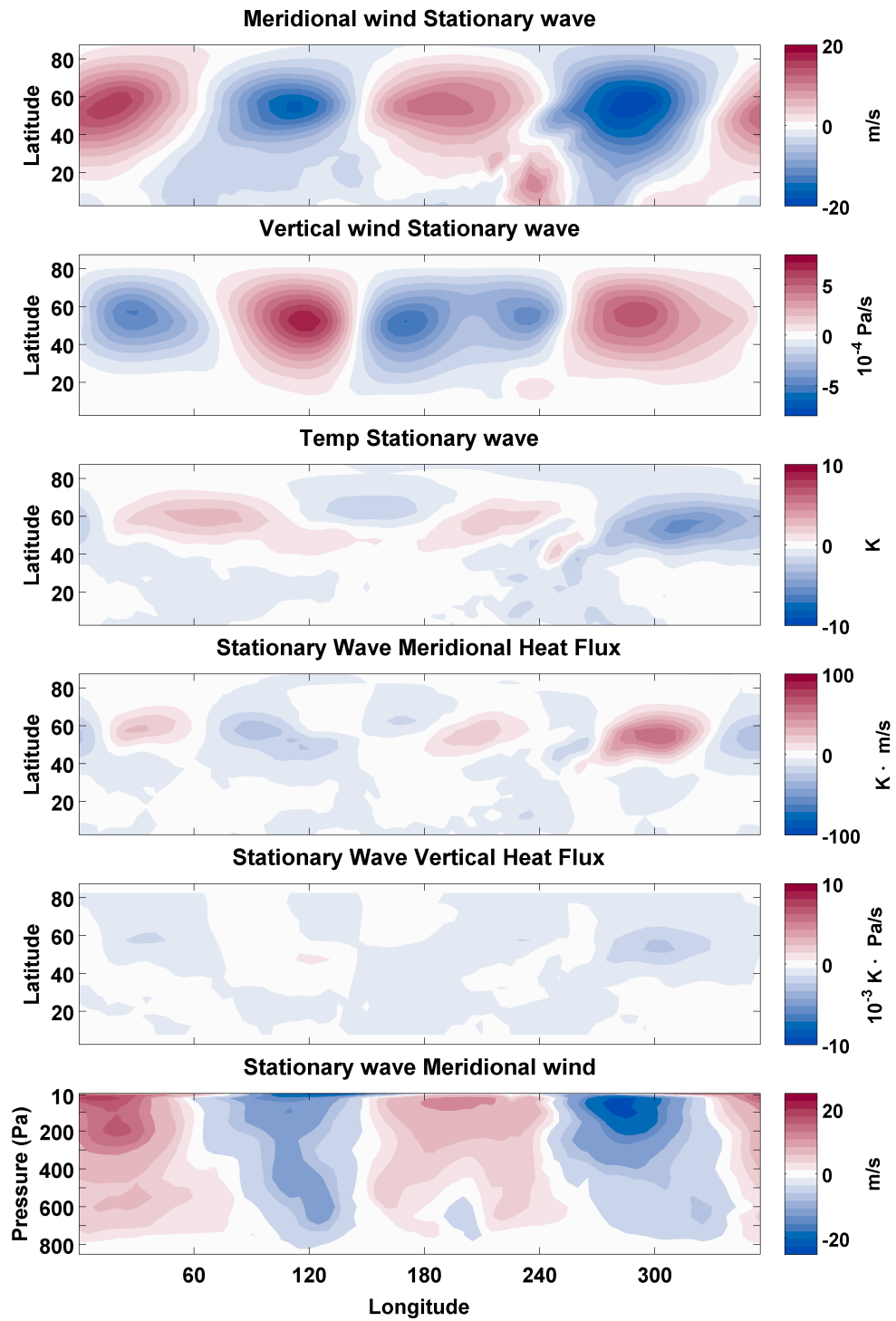


Figure A.77: As in Fig. A.75 but for $L_s = 330^\circ - 360^\circ$.